5-2005

Measurements of the Secondary Electron Emission Properties of Insulators

Clint D. Thomson

MEASUREMENTS OF THE SECONDARY ELECTRON EMISSION PROPERTIES OF INSULATORS

by

Clint D. Thomson

A dissertation submitted in partial fulfillment
of the requirements for the degree

of

DOCTOR OF PHILOSOPHY

in

Physics

Approved:

Dr. John R. Dennison Major Professor	Dr. W. John Raitt Committee Member
Dr. D. Mark Riffe Committee Member	Dr. Jan J. Sojka Committee Member
Dr. Charles Swenson Committee Member	Dr. Laurens H. Smith, Jr. Interim Dean of Graduate Studies

UTAH STATE UNIVERSITY
Logan, Utah

2005

ABSTRACT

Measurements of the Secondary Electron Emission Properties of Insulators

by

Clint D. Thomson, Doctor of Philosophy

Utah State University, 2005

Major Professor: Dr. John Robert Dennison
Department: Physics

Measurements of the electron-induced electron emission properties of insulators are important to many applications including spacecraft charging, scanning electron microscopy, electron sources, and particle detection technology. However, these measurements are difficult to make since insulators can charge either negatively or positively under charge particle bombardment that in turn alters insulator emissions. In addition, incident electron bombardment can modify the conductivity, internal charge distribution, surface potential, and material structure in ways that are not well understood. A primary goal of this dissertation work has been to make consistent and accurate measurements of the uncharged electron yields for insulator materials using innovative instrumentation and techniques. Furthermore, this dissertation reports on the experimental work undertaken by our group to explore insulator charging rates as a function of incident electron energy and fluence. Specifically, these charging studies include: (i) the study of the effectiveness of charge-neutralization techniques such as low-energy electron flooding and UV light irradiation to dissipate both positive and negative surface potentials induced by incident electron irradiation, (ii) the exploration of several noncontacting methods used to determine insulator surface potentials and the insulator

first and second crossover energies that are important in determining both the polarity and magnitude of spacecraft material potentials, (iii) the dynamical evolution of electron emissions and sample displacement current as a function of incident charge fluence and energy with ties to evolving surface potentials as an insulator reaches its current steady state condition, and (iv) the slow evolution of electron yields with continuous incident electron bombardment.

These charging data are explained in the context of available insulator charging models. Specific insulator materials tested included chromic acid anodized aluminum, RTV-silicone solar array adhesives, and Kapton^{TM} on aluminum.

(357 pages)

ACKNOWLEDGMENTS

I am grateful to NASA Marshall Space Flight Center for providing me with the funding to pursue a PhD in physics. I am especially thankful for my advisor, J.R. Dennison, for his continual counsel, encouragement, and optimism. I am indebted to Rob Davies, Neal Nickles, and Albert Chang for leaving to me a great lab, and for showing me the ropes. Vladimir Zavyalov was also a great teacher. He imparted to me many great lessons, and without his data acquisition electronics, I would have been in the lab for several more years.

My fellow graduate students have made life more enjoyable over the last few years. I am thankful to Jason Kite, Alec Sim, and Prasanna Swaminathan for many stimulating conversations that broke up the occasional monotony of lab work and dissertation writing. Also, Jodie Corbridge was a fun lab partner, and because of her scrutinizing glares, I probably broke less equipment than I would have if I had been on my own.

I am grateful to Ralph Carruth and his group at Marshall Space Flight Center for their collaboration and hospitality. I was also grateful to have interacted with other members of the spacecraft charging community, including Rob Frederickson, Leon Levy, Jodie Minor, and Dale Ferguson. These people imparted to me both their resources and invaluable experience.

I am thankful for the Physics Department staff, Deborah Reece, Karalee Ransom, Marilyn Griggs, and Sharon Pappas for helping me with all of my administrative needs, and for providing a small haven where I could catch up on the latest gossip.

I want to thank Lee Pearson and Tim Doyle at Thiokol for providing me with an internship that has, in the end, led to a career away from Utah State.

I am deeply appreciative of Gwena Couillard for her time, wisdom, and kindness.

I want to thank members of my family including my mom and dad for their support, Tige for our fall hunting excursions, and my girls, Kensi, Jaidyn, and Ady, for patiently

enduring a graduate student's lifestyle of poverty. Finally, I want to thank Julie for sticking with me through some tough times. I have finally finished, and easier times lie ahead.

Clint D. Thomson

CONTENTS

LIST OF TABLES

Table Page

Table Page

LIST OF FIGURES

Figure Page

Figure Page

Figure Page

Figure Page

NOMENCLATURE

A	Stopping power coefficient
A_0	Irradiated surface area
a_H	Screened atomic radius
B	Secondary electron escape probability constant
b	Electron energy spectrum electron affinity constant
CF_{det}	Total yield correction factor associated with detector losses
CF_{stg}	Total yield correction factor without stage contribution
d	Insulator thickness
E_0	Incident electron energy
E^{δ}_1	Secondary electron yield first crossover energy
E^{σ}_1	Total electron yield first crossover energy
E^{δ}_2	Secondary electron yield second crossover energy
E^{σ}_2	Total electron yield secondary crossover energy
E_F	Fermi energy
E_g	Band gap energy
E_L	Incident electron landing energy
E^{δ}_{max}	Secondary electron yield maximum energy
E^{σ}_{max}	Total electron yield maximum energy
E_{probe}	Pulsed probing electron beam energy
E_s	Average first collision energy
F	Electric field at sample surface
$f(x)$	Secondary electron transport and escape probability term
G	Ammeter second stage gain
$\hbar$	Planck's constant
$\hbar\omega_p$	Plasmon excitation energy
i	Electron pulse iteration
I_C	Collector current
I_e	Electron gun emission current
I_f	Electron gun filament current
I_g	Grid current
I_{in}	Input current to ammeter
I_{leak}	Electron gun leakage current
I_{max}	Maximum of pulse current
I_0	Incident electron current
$\bar{I}_0$	Mean incident pulse current
I_s	Sample current
I_{stg}	Stage current
J_0	Incident electron current density
k	Chung and Everhart proportionality constant

L	Atomic weight
$\tilde{N}$	Energy spectrum number of emitted electrons
N	Number of pulses
n	Stopping power exponent
$n(x,E_0)$	Secondary electron production term
n^{δ}	Secondary electron yield stopping power coefficient
n^{σ}	Total electron yield stopping power coefficient
p	Normalized plasmon energy ratio
q	Fundamental charge
Q	Charge collected by ammeter
Q_c	Collector charge
Q_0	Incident electron charge
Q_{0N}	Cumulative incident electron charge
Q_{0avg}	Average sample charge per pulse delivered in a series of pulses
Q_s	Sample charge
Q_{sN}	Cumulative sample charge
Q_{SE}	Emitted secondary electron charge
R	Incident electron penetration depth
R_{beam}	Radius of irradiated sample area
R_f	Ammeter feedback resistor of first stage
s	Material density
T	Integrator time constant
t_N	Running time for multiple pulses
V_{out}	Output voltage of integrator
V_s	Insulator surface potential
x	Material depth variable
Yld_{mean}	Multiple pulsed yield mean
Yld_{nostg}	Measured total yield without stage contribution
Yld_{stdev}	Multiple pulsed yield standard deviation
Yld_{stg}	Measured total yield with stage contribution
Yld_{true}	True total yield
Z	Material atomic number
Δ	Radiation induced conductivity power coefficient
Δt	Integration time
α	Sample charge and total yield inverse charge decay parameter
α'	Sample charge and total yield iterative decay parameter
γ	Radiation induced conductivity
γ_0	Innate conductivity
δ	Secondary electron yield
δ_0	Initial secondary electron yield

δ_{max}	Maximum secondary electron yield
δ_{ss}	Steady state secondary electron yield
ε	Average secondary electron excitation energy
ε_0	Permittivity of vacuum
ε_r	Relative dielectric constant
κ	Boltzmann constant
ρ	Insulator resistivity
σ	Total electron yield
σ_0	Initial total electron yield
σ_{max}	Maximum total electron yield
σ_N	Cumulative total electron yield
σ_{ss}	Steady state total electron yield
τ_{RC}	Insulator RC time constant
τ_i	Pulse duration
φ	Material work function
η	Backscattered electron yield
λ_p^2	Electron plasmon correction factor
λ_{SE}	Mean secondary electron attenuation depth
χ	Electron affinity
ω_p	Plasmon frequency

CHAPTER 1

INTRODUCTION

When energetic particles impinge on a solid they can impart their energy, exciting electrons within the material. If this energy is sufficient to overcome surface energy barriers, such as the work function, electron affinity, or surface charge potential, electrons can escape from the material. The extent of electron emission from the material can be quantified as the ratio of incident particle flux to emitted particle flux, and is termed the electron yield. Electron yields are relevant to many technical applications, including: the continued development of electron multiplier detectors (Shih *et al*., 1997), where high-yield dynode materials are desired for more sensitive particle detection; scanning electron microscopy (Reimer, 1985; Seiler, 1983), where low-energy electron emission provides a means for material surface imaging; Auger electron spectroscopy (Belhaj *et al*., 2000), where core-level electron emission provides a signature of surface elemental composition; plasma fusion devices, where low-yield materials such as disordered carbon are desired such that electron emission does not perturb the surrounding plasma; high-current arcing where extensive charge buildup, resulting from electron emissions, produces electrical arcing either through or across insulators; and finally, flat panel displays where electron emission sources must have high yields, and the spacers between anodes and cathodes are required to be insulating and exhibit low secondary electron yields (Schwoebel and Brodie, 1995; Auday *et al*., 2000). The motivation for our studies at Utah State University (USU) comes from NASA's concern for spacecraft charging resulting from energetic particle bombardment and electron emissions from spacecraft surfaces in the space environment (Dennison *et al*., 2003d, 2002, 2001). Specifically, this dissertation concentrates on the electron yield and charging properties of insulator materials resulting from incident electron excitation.

At USU, electron yield measurements are performed in an ultra-high vacuum (UHV) environment for surface contamination control, using a fully enclosing hemispherical grid detection system and electron, ion, and UV incident sources that allow particle species and energy-dependent studies (Dennison *et al*., 2003b; Thomson *et al*., 2003b; Nickles, 2002). Yield measurements on conductors are straightforward since a constant electron current source can be utilized and DC currents coming from the sample can be measured using standard picoammeters. Additionally, by grounding the conductor sample, any charge that leaves or is absorbed into the material can be immediately neutralized to ground. Capabilities for making conductor measurements at USU have been in place for several years now (Dennison *et al*., 2003b, 2002; Nickles, 2002).

The focus of this research has been the development of instrumentation and techniques for measuring the electron-induced electron emission properties of thick- and thin-film insulating materials (Dennison *et al*., 2003d; Thomson *et al*., 2003a, 2003b). Electron yield measurements on dielectrics are more difficult to make than on conductors, since any charge that is deposited in the material cannot easily be dissipated. During measurements of electron emission properties of insulators, charge builds up near the sample surface because of low bulk and surface conductivity. The resulting sample potentials that develop can affect incident electron landing energies, produce energy shifts of the emitted electron spectrum, and consequently lead to significant alterations in the measured electron yields. To minimize insulator charging, pulsed-electron beams coupled with neutralization sources have been implemented. Surface potential and electron yield evolution have also been monitored to determine insulator charging magnitudes and rates.

Most insulator data that exists in the literature was taken decades ago in poor vacuum environments using archaic measurement instrumentation. Consequently, the accuracy of

much of the existing data on both insulators and conductors remains in question. Electron yield measurements made for this dissertation have required the development of novel specialized instrumentation and methods to accommodate pulsed electron-beam sources and short-duration, low-signal measurements (Thomson *et al*., 2003b). As discussed in more detail later in this dissertation, the level of sophistication of the instrumentation and methodologies developed to make these measurements demonstrate significant improvements in comparison to previous studies reported in the literature (see Section 2.2 for summary of previous measurement methods). These improvements have included the development of optically isolated, fast-response, sensitive electronics and various charge-neutralization techniques that include an inexpensive, extremely compact low-energy electron flooding source. An additional improvement has been the development of a measurement methodology that incorporates alternating pulsed measurements and flood-gun neutralization, and minimizes the amount of incident electron fluence required to make electron yield measurements.

Also, key measurements that are not present in the literature have been made on the evolution of electron yields and surface potentials, as a function of incident electron fluence and energy. Additionally, a quantitative study of the effectiveness of UV and electron neutralization sources has been conducted in different incident energy charging regimes and for different insulator materials. Also, methods used to measure electron-irradiation effects on electron emissions have both been developed and tested that include the use of pulsed-electron probing beam techniques as well as continuous electron source methods, such as secondary electron energy spectra shifts in response to evolving surface potentials. Finally, electron emission data has been measured on insulator materials that have never before been studied.

This dissertation reports on the instrumentation, measurement, and analysis of electron-induced electron yields of dielectric materials. Chapter 2 provides an overview of secondary electron emission of insulators. In Section 2.1, descriptions of electron emission quantities such as the total, secondary electron (SE), backscattered electron (BSE) yields, and electron energy spectrum are given, along with definitions for electron-yield emission parameters. In Section 2.2, a summary of previous insulator yield studies is also given, which includes techniques for making pulsed incident electron measurements and surface neutralization. In Section 2.3, a summary of SE yield models is discussed with a description of the creation, transport, and escape mechanisms of SE's within insulators that lead to bulk and surface charging. Bulk and surface charging configurations are discussed based on measurements and calculations of insulator surface potentials and computational models provided in the literature. Finally, analytical tools for the treatment of the rates of sample charge, total electron yields, and evolving surface potentials in response to a pulsed incident electron source are developed.

Chapter 3 provides an overview of the DC and pulsed-yield instrumentation used in this dissertation work. Section 3.1 provides a general description of both the DC and pulsed instrumentation setup used to measure conductor and insulator electron yields and spectra. Section 3.2 examines the instrumentation and settings used specifically for DC yield measurements. Section 3.3 describes the instrumentation used for pulsed-yield measurements, including block diagrams and schematics of the pulsed ammeter and integrator circuitry. Section 3.4 outlines low-energy and high-energy electron source operation in both DC and pulsed modes, with tabulated knob settings for different energies. Finally, Section 3.5 describes the electron and VIS/UV light sources used to neutralize insulators, and also

provides details of a custom-designed, low-energy electron flood gun used to neutralize insulator surfaces.

Chapter 4 provides the methodology used for making pulsed insulator yield and charging measurements. Section 4.1 gives the step-by-step procedure used for taking pulsed-yield data on insulators with minimal charging effects. Section 4.2 provides diagrams illustrating various alternative measurement schemes and analysis algorithms used to calculate electron yields. Section 4.3 describes empirical methods used to determine total, BSE, and SE correction factors used for both DC and pulsed-yield setups. In Section 4.4, a validation of the relative accuracy of the pulsed-yield setup on a conductor material is provided in comparison with results obtained from the DC setup. Additionally, the fractional error of pulsed total and BSE yields are analyzed as a function of incident current magnitude and number of pulses. Section 4.5 describes methods used to monitor insulator charging and surface potentials resulting from electron beam induced surface and bulk charging. Finally, Section 4.6 outlines methods for determining insulator electron yield first and second crossover energies.

Chapter 5 contains experimental data for three insulators used in spacecraft construction: anodized aluminum, RTV-silicone adhesive on copper, and thin-foil Kapton^{TM} on aluminum. Not only is this data useful for spacecraft charging applications, but it also demonstrates yield and spectral measurement capabilities, charging rates as a function of incident electron fluence, novel methods for determining yield parameters, and neutralization method effectiveness as a function of incident electron energy. Section 5.1 provides charging data on anodized aluminum up to the point of dielectric breakdown of the anodized film. Additionally, both charged and uncharged pulsed-yield data is presented. Section 5.2 gives electron yield data on four RTV-silicone samples, with an emphasis on methods for determining the second crossover energy of the materials. Section 5.3 provides electron yield

data on Kapton™-aluminum, and also demonstrates the evolution of electron yield parameters as a function of sample history and electron beam exposure. Additionally, the charging rates of the insulator are analyzed as a function of electron fluence and incident energy. Finally, Section 5.4 gives a summarization of electron yield data for the three sample types, and compares results with those found in the literature.

Chapter 6 provides a list of recommended future studies that have precipitated from this dissertation work. Section 6.1 gives suggestions for instrumentation and computer upgrades, which would increase the speed, accuracy, and capabilities of the present pulsed-yield setup. Section 6.2 proposes future measurements and analysis, which would provide further insights into insulator electron yield and charging models on insulators. Finally, Chapter 7 provides the summary and conclusions for this dissertation.

CHAPTER 2

BACKGROUND

This chapter is divided into three sections that provide background information related to the electron emission properties of conductor and insulator materials. The information presented in this chapter is later used in Chapter 5 in the interpretation and analysis of insulator electron emissions data. Section 2.1 provides basic descriptions of electron yields and energy spectra, characteristic to nearly all materials (conductors and insulators). This includes definitions of total electron, secondary electron, and backscattered electron yields, along with their associated parameters. Section 2.2 provides an exhaustive literature review of experimental electron yield measurements on insulator materials, with a summarization of the measurement techniques used to minimize sample charging. Section 2.3 provides an overview of existing secondary electron yield and energy spectrum models, with an emphasis on dielectric materials. This section also provides a review of models used to predict evolving bulk and surface potentials due to insulator charging, resulting from incident electron irradiation. Finally, a quantitative development of evolving electron yields, sample displacement currents, and surface potentials in response to a pulsed incident electron source is presented.

2.1 Secondary and Backscattered Electron Emission

When a material is exposed to high-energy electron irradiation, electrons are excited from the material, and exhibit a wide range of emission energies ranging from 0 eV up to the incident electron energy. The escape energies of electrons depend on their escape depth as well as the energy-loss scattering mechanisms and potential barriers they experience before leaving the material (discussed more fully in Sections 2.3.2 through 2.3.6). Fig. 2.1 shows a

typical energy spectrum of emitted electrons for gold while being bombarded by an 83 eV incident electron beam. Similar emission spectrum attributes are characteristic of both conductors and uncharged insulators. Generally, for all incident energies, a large population (in the case of Fig. 2.1, >70%) of thermalized electrons are emitted with energies <50 eV. Most of these electrons have suffered numerous inelastic scattering interactions such that they have developed a well-defined thermal energy distribution within the material before they reach the surface and escape. A second large-energy distribution generally exists at energies near the incident beam energy that is comprised of elastically and quasi-elastically scattered electrons.

Emitted electrons can be divided into two categories: i) Secondary electrons (SE); typically lower-energy electrons (<50 eV by convention) that originate within the material, typically produced by numerous inelastic scattering events of the incident electrons or by

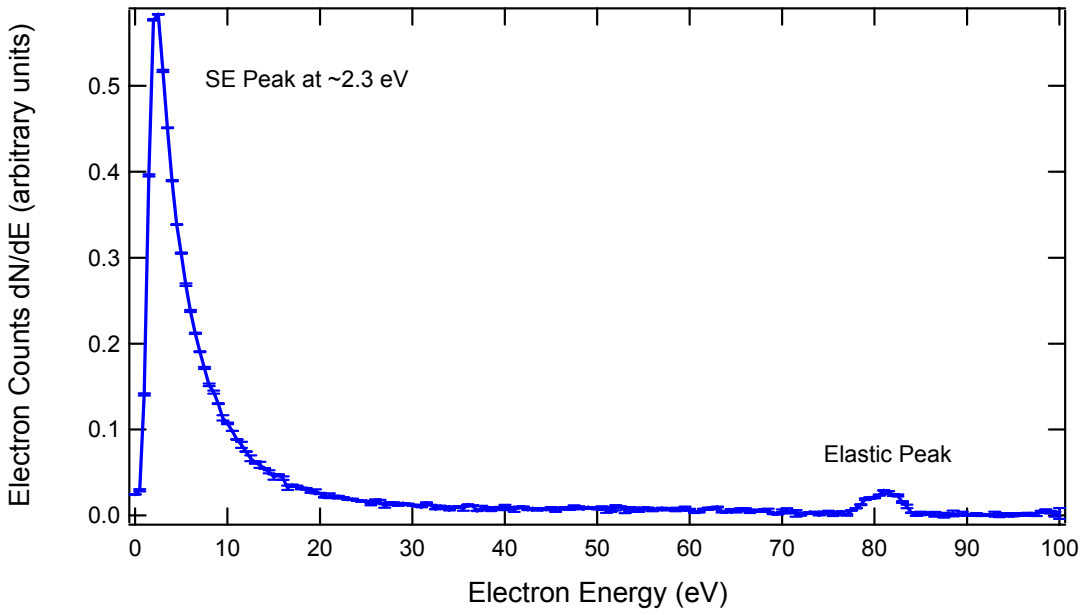

FIG. 2.1. Electron energy spectrum for Au, induced from an 83 eV electron beam. Shown in the spectrum are the SE peak at 2.3±0.5 eV and the elastic peak at 82±1 eV.

higher-energy secondary or backscattered electrons; ii) Backscattered electrons (BSE); typically higher-energy electrons (>50 eV by convention) that originate from the incident electron source, but scatter either elastically or inelastically before leaving the target material (Reimer, 1985; Seiler, 1983). The total yield, σ, BSE yield, η, and SE yield, δ and are defined as the ratios of the sample emitted electron current (or total emitted charge) to the total incident electron current (or total incident charge) as:

$$\sigma \equiv \frac{I_{SE} + I_{BSE}}{I_0} \equiv \frac{\int (I_{SE} + I_{BSE}) \cdot dt}{\int I_0 \cdot dt}, \tag{2.1}$$

$$\eta \equiv \frac{I_{BSE}}{I_0} \equiv \frac{\int I_{BSE} \cdot dt}{\int I_0 \cdot dt}, \text{ and} \tag{2.2}$$

$$\delta \equiv \frac{I_{SE}}{I_0} \equiv \frac{\int I_{SE} \cdot dt}{\int I_0 \cdot dt}, \tag{2.3}$$

where I_0, I_{BSE}, and I_{SE} are, respectively, the total, BSE, SE incident electron currents to and from the sample. For continuous-source measurements, direct measurement of the yields can be measured using sensitive DC ammeters. As an alternative method, the ratios of total incident and emitted charge, or integrated current with respect to time [as shown in Eqs. (2.1) through (2.3)], are useful when making pulsed measurements. For pulsed measurements, the time limits of the integration are the pulse duration of the incident pulse (see Sections 2.2 and Section 3.3).

Plots of the total, SE, and BSE yields as a function of incident beam energy for a gold sample are shown in Fig. 2.2. Referring to the figure, important electron-yield parameters include the maximum total and SE yields, σ_{max} and δ_{max}, along with their associated energies, $E_{max}{}^{\sigma}$ and $E_{max}{}^{\delta}$. Additional important parameters include the first and second crossover energies for total yields, $E_1{}^{\sigma}$ and $E_2{}^{\sigma}$, and for SE yields, $E_1{}^{\delta}$ and $E_2{}^{\delta}$ —energies for which the

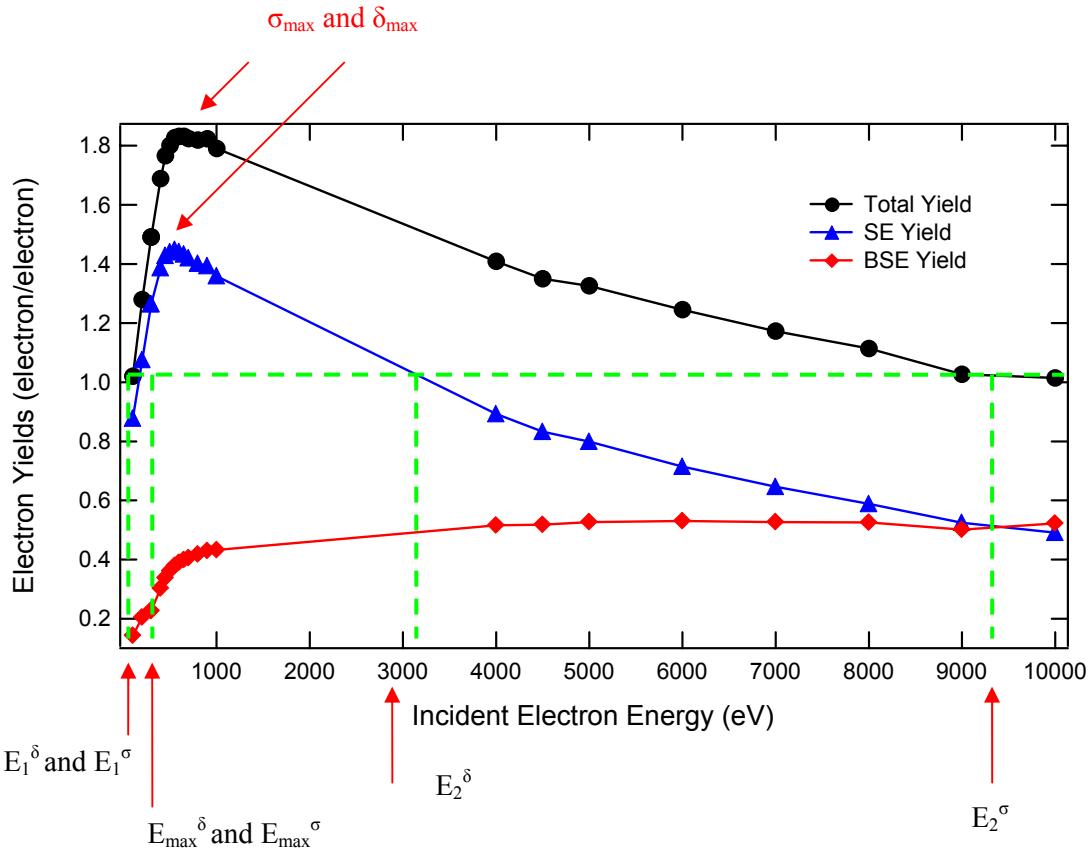

FIG. 2.2. Total (●), SE (▲), and BSE (▼) electron yields for Au as a function of incident electron beam energy. Total yield parameters are σ_{max}=1.8±0.1 at E_{max}^{σ}=600±50 eV. First and second crossover energies were E_1^{σ}=100±20 eV and E_2^{σ}=10000±1000 eV. SE yield parameters were δ_{max}=1.5±0.1 at E_{max}^{δ}=550±50 eV and E_1^{δ}=110±20 eV and E_2^{δ}=3200±200 eV.

electron yield values equal unity. It must be noted there is an ambiguity in the definition of the crossover energies, E_1 and E_2, as presented in the literature, which can cause some confusion. Most studies in the literature fail to discriminate between the SE and total yield crossover energies. In this dissertation, this ambiguity has been clarified by referring to total yield parameters with a superscript of σ, and to secondary yield parameters with a superscript of δ. Generally, for insulators, reported SE and total yield crossover energies range from E_1^{δ} and E_1^{σ}=20-100 eV and E_2^{δ} and E_2^{σ}=500-10000 eV. Typical maximum SE and total yields

can range anywhere from 1-20 (for special cases, >100) at energies of E_{max}^{δ} and E_{max}^{σ}=150-1000 eV (Dennison *et al*., 2003d, 2002; Thomson *et al.,* 2003a; Yong *et al*., 1998; Wong *et al*., 1997; Reimer, 1985; Seiler, 1983; Krainsky *et al*., 1981; Kishimoto *et al*., 1977; Whetten, 1964; Whetten and Laponsky, 1957, 1959; Johnson and McKay, 1953; Mueller, 1945).

As can be seen in Fig. 2.2, total and SE yield curves initially rise with increasing incident beam energy, E_0, up to a few hundred electron volts, and then decline as E_0 is further increased. This initial rise and then gradual decline results primarily because the number of electron-electron excitations increases with increasing E_0, and the maximum incident electron penetration depth, R, also increases with increasing E_0. However, the mean SE attenuation depth, λ_{SE} remains more or less constant (in the absence of charging) regardless of E_0. Hence, for $R \leq \lambda_{SE}$, occurring at E_0 below a few hundred electron volts, the majority of SE's are produced at a depth from which they can escape, producing a maximum SE yield, δ_{max} at an energy, E_{max}^{δ}. Furthermore, since the majority of SE's are produced near the maximum penetration depth, as R is increased to higher energies beyond a few hundred eV, a diminishing number of SE's are able to reach the material surface and escape. This behavior is discussed further in Sections 2.3.2 through 2.3.8. Incidentally, since the total electron yield is dominated by the behavior of the SE yield, it will also exhibit a maximum, σ_{max} and associated E_{max}^{σ}.

The total yield crossover energies, E_1^{σ} and E_2^{σ}, are important parameters since they determine the incident energies for which a material will typically transition from negative ($\sigma<1$) to positive ($\sigma>1$) potentials. Furthermore, the magnitude of insulator charging can depend on a number of other parameters that include the BSE and SE yield magnitudes, incident beam angle (Davies, 1999; Yong *et al*., 1998), substance purity, crystalline structure (Whetten and Laponsky, 1959), temperature (Johnson and McKay, 1953; Johnson, 1948;

Mueller, 1945), insulator thickness (Yu *et al*., 2001; Goto and Ishikawa, 1968; Ishikawa and Goto, 1967), surface cleanliness (Davies and Dennison, 1997; Whetten, 1957, 1959, 1964), surface topography (Yong *et al*., 1998), sample potential (Yi *et al*., 2001), and previous electron irradiation exposure leading to increased defect density and trapped charge (Shih *et al*., 1997; Vigouroux *et al*., 1985; Cazaux, 1999). Numerous conductor electron spectra, yield curves, and yield parameters have been measured at USU and are available on the NASA SEE Charge Collector Knowledge Base (Dennison *et al*., 2002, 2003d). A summary of reported insulator yield values pertinent to this dissertation work is provided later in Section 5.4.

Historically, SE and BSE yields have been measured by either using a sample biasing scheme (to either attract or repel SE's), or by using a retarding field grid detector (biased between 0 V and -50 V). Of these two approaches, the grid/detector scheme is considered to be more accurate, although technically more complicated since all electron current entering or leaving the measuring apparatus needs to be accounted for (Nickles, 2002; Seiler, 1983; Thomson *et al*., 2003b). This often requires the utilization of several sensitive ammeters that can float independently. At USU, a hemispherical retarding field grid detector has been developed to make yield measurements. Further details of how both DC and pulsed-yield measurements are made at the USU facility are discussed in Chapter 3.

Making electron yield measurements on conductors is straightforward since by grounding the sample, charge can be quickly dissipated. Consequently, for conductors, a continuous-emission electron beam and sensitive DC ammeters can be used to measure yields (see Section 3.2). Due to the accumulation of charge during insulator measurements, pulsed-incident electrons sources are typically used when measuring electron yields. Surface potential buildup during the incident electron pulse is an important phenomenon that limits the incident electron pulse widths and frequencies, practical for SE yield measurements on

insulators. This potential is dependent to the total charge deposited on the insulator surface, which is directly related to the electron pulse duration and electron beam intensity (or total electron fluence). This implies a primary limitation on the pulse-measurement system design with regards to the speed and sensitivity of the ammeters used for detecting electron yield currents (refer to Section 3.3). Other limitations arise from the necessity to monitor low-level currents from several sources that are biased over a range of zero to hundreds of volts.

The polarity of insulator charging is most dependent on incident electron energy, but is also dependent upon electron yield parameters, existing insulator surface potential, and electron irradiation history. As described above, positive (negative) charge will build up when the total number of electrons leaving the insulator sample is greater than (less than) the total number of incoming electrons. If the energy of incident electrons is below the insulator total yield first crossover energy, E_1^{σ}, (<100 V for most good insulators) negative charging results. At these energies, relatively few SE's are excited by incident electrons since a minimum energy threshold of a few tens of volts is required to excite electrons beyond the insulator bandgap and surface potential barriers (such as the electron affinity). If the incident electron energy is above the total yield second crossover energy, E_2^{σ} (>1 keV for most insulators) negative charging will also result since incident electrons penetrate deeply into the material (up to several microns), exciting SE's (escape length tens of nanometers) at depths from which they cannot escape. However, if the incident electrons have energies between the total yield crossover energies, E_1^{σ} and E_2^{σ}, more electrons will be emitted from the insulator than are incident, and net positive charging will occur.

A review of material (particularly of conductor) electron emissions behavior is provided by Reimer (1985) and Seiler (1983). Section 2.2 also provides an extensive review of insulator electron yield studies. Section 2.3 elaborates on the mechanisms and models of

insulator SE emission. Finally, in-depth experimental studies of insulator electron emissions and yield parameters, as well as charging behavior, are discussed in Chapter 5.

2.2 Electron Emission Measurements on Insulators

This section contains an extensive review of previous electron yield studies on insulator materials. Insulator electron-induced electron yield measurements began in the 1940's, driven by the development of vacuum tube and electron-multiplier detector technology (Johnson, 1948; Mueller, 1945). Johnson (1948) was probably the first to use a low-amplitude, pulsed incident electron source to measure the SE yields of insulating targets. The pulsed electron beam technique was developed to minimize incident charge exposure and resulting surface potentials caused by electron irradiation. Beam pulsing has been used in conjunction with other methods to control surface potentials, such as using carefully chosen incident energies (near the second crossover energy) to maintain steady-state surface potentials of ~0 V (Girard *et al*., 1992). This technique is used in SEM imaging of insulators. Another technique used to maintain surface potentials at 0 V is to deposit thin metallic films on insulator surfaces, then grounding the surface to dissipate surface charge [also used in SEM imaging of insulators (Reimer, 1985)]. Alternatively, the insulator bulk conductivity has been increased by introducing dopants into the material. Finally, other neutralization techniques have included sample heating, UV irradiation (Bass *et al*., 1998; Levy et al., 1985), and ion and low-energy electron flooding sources (Johnson, 1948; Johnson and McKay, 1953; Kishimoto *et al*., 1977; Krainsky *et al*., 1980, 1981). The details of the pulsed and neutralization techniques relevant to electron-yield measurements are described in more detail in the following paragraphs.

For the pulsed-beam technique, incident electron exposure is typically minimized by using incident pulses <100 μs in time duration, with incident currents on the order of 1-100 nA (Krainsky *et al*., 1980; Kishimoto *et al.*, 1977; Whetten and Laponsky, 1957; Johnson and McKay, 1953; Johnson, 1948). These beam parameters are common to nearly all uncharged insulator electron yield studies. An extensive summary of available insulator yield measurement studies (along with the specific measurement and neutralization techniques used in each study) that have been printed in English are provided in Table 2.1. Insulator yield parameters resulting from these studies that are relevant to this dissertation work are summarized in Section 5.4. In most of the surveyed studies, combinations of incident pulse magnitude and time duration were chosen to fall below a critical charging criterion of ~10^7 electrons/mm^2 per single pulse. In most cases, where this threshold was exceeded, the sample was continuously heated to temperatures >500˚ C while making the measurements to increase sample conductivity and facilitate neutralization (described in more detail below).

The reasoning behind this critical incident charge threshold is discussed further in Section 2.3 where it is explained that an incident electron pulse of 10^6-10^7 electrons/mm^2 (typical for our pulsed setup) is sufficient to produce surface potentials on the order of 0.1-10 V, measured with respect to the grounded sample substrate (refer to Section 2.3.7 for further discussion). In some cases, where low-incident electron doses of ~10^5 electrons/pulse were used, it was demonstrated that a single region of an insulator sample could be pulsed two to three times without significantly altering the insulator SE yield values (Krainsky *et al*., 1981). However, in general, even small incident doses (10^6-10^7 electrons/pulse) can alter insulator surface potentials sufficient to noticeably affect electron yields (see for example data in Sections 5.1 and 5.3). This is especially true in the positive charging energy regime $E_1^{\sigma}<E_0<E_2^{\sigma}$, where positive potentials on the order of 1 V can screen out a significant number

TABLE 2.1. A summary of previous electron yield studies on insulators. Pulsed technique and neutralization methods are included. Studies are arranged in chronological order.

Researcher	Insulator Materials	Insulator Thickness (μm)	Incident Energy (keV)	Incident Current (nA)	Beam Dia. (mm)	Pulse Duration (Rise Time) (μs)	Charge per Pulse (electrons/ mm^2)	Neutralization Technique
Mueller, 1945	pyrex glass	950	0.05-10	5-15	3-4	DC at high temperatures	NA	heat 350-500° C
Johnson, 1948	(BaSr)O on Ni	25	0-2	~10000	1-4	0.2-30 at 0.5-4 kHz rep. rate	10^6-10^9	heat 300-700° C
Johnson and McKay, 1953	MgO single crystals on Ta	350-1650	0-5	~10000	1-4	10-20 at single pulse-60 Hz rep. rate	10^8-10^9	heat 600° C
Whetten and Laponsky 1957	MgO single crystals on W	500	0-4	~1	6	"several μs"	10^4	thermionic Ta filament and heat 750° C
Whetten and Laponsky, 1959	MgO thin films on Pt and W	0.0008	0-4	~1	6	"several μs" to DC	10^4	heat 600° C

TABLE 2.1. (Continued).

Researcher	Insulator Materials	Insulator Thickness (μm)	Incident Energy (keV)	Incident Current (nA)	Beam Diameter (mm)	Pulse Duration (Rise Time) (μs)	Charge per Pulse (electrons/ mm^2)	Neutralization Technique
Fridrikhov and Shul'man, 1960	Mica, glass, Al_20_3, NaCl, others	"several"	0.05-0.25	no info.	no info.	no info.	no info.	heat 300-400° C
Whetten, 1964	alkali halide crystals on W	1000	0-6	10	6	1	10^4	thermionic filament
Ishikawa and Goto, 1967	Pump oils on W	0.0005-0.08	0.05-2.0	100	1.5-2	30 at single and 10 Hz rep rate	10^7	none
Willis and Skinner, 1973	Kapton™ Teflon™, Mylar (metallized)	10-80	0-2.5	1	2.5	1	10^3 (5 mm^2 beam spot)	no info.

TABLE 2.1. (Continued).

Researcher	Insulator Materials	Insulator Thickness (μm)	Incident Energy (keV)	Incident Current (nA)	Beam Diameter (mm)	Pulse Duration (Rise Time) (μs)	Charge per Pulse (electrons/ mm^2)	Neutralization Technique
Kishimoto *et al.,* 1977, 1990	Teflon™, Kapton™, other organic compounds on Al	"few"	0-1.6	<1	no info.	1000	10^7	none
Krainsky *et al.,* 1980, 1981	MgF_2 (fused silica), Kapton™ (Al), Teflon™ on Ag/Inconel	50	0-5	14-33	2	2 (0.2)	10^5	flood gun 5 eV
Yong *et al*., 1998	SiO_2, Kapton™ on Si	2	0.5-2.5	0.01	1-1.5	$3 \cdot 10^4$ at 1 Hz rep. rate	10^7	none
Krainsky and Lesny, 1998	Diamond on Ta	single-crystal	0-5.0	<10	0.1	10 at a 100 Hz rep. rate	10^8	heat 500° C
Thomson *et al.*, 2003a	Anodized Al and RTV-silicone	1.4 μm (Al) and	0.1-5	10-50	1	~5	10^5-10^6	flood gun

of escaping low-energy SE's (refer to Section 2.3.6 for more details on this screening effect). Additionally, beyond the second crossover energy, $E_0>E_2^{\sigma}$ (usually >1 keV for insulators), an insulator will charge negatively up to several thousands of volts (depending on beam energy and incident charge dose), affecting not only the energy of emitted electrons, but also the landing energy of incident electrons (refer to Sections 2.3.6-2.3.7 and 5.2).

Other charging complications can result from electron beam irradiation. For example, it has been hypothesized (and recently measured) that evolving charge profiles within the bulk of insulators, resulting from incident electron irradiation, display alternating negative and positive charge layers (Cazaux, 1986; Cazaux *et al*., 1991; Toth *et al*., 2002; Miyake *et al*., 2003; Osawa *et al*., 2003; Usui *et al*., 2003; Frederickson and Brautigam, 2003). Deep charge layers (>10 nm) cannot effectively be discharged with surface neutralization methods such as electron flooding or UV irradiation, and can produce either accelerating or retarding electric fields to escaping SE's inside the insulator material (refer to Section 2.3.7 and Section 5.3.2 for further details).

Finally, incident electrons with energies of several keV have been shown to cause permanent alterations to glasses, metal oxides, and polymer bonding structures (such as polymer cross linking and chain scissions) at incident charge densities as low as 10^{10} electrons/mm^2, creating additional defects and trap sites for escaping SE's (Reimer, 1985; Vigouroux *et al*., 1985; Krainsky *et al*., 1981; Cazaux, 1999; Jbara *et al*., 2001). These trapped charges also resist surface neutralization methods, because they generally lie well below the surface and are highly localized (Belhaj *et al*., 2000; Vigouroux *et al*., 1985, Cazaux *et al*., 1991). It has been speculated in the literature that charge trapping affects electron yield parameters (Cazaux, 1999; Cazaux *et al*., 1991; Melchinger and Hofmann, 1995; Shih *et al*., 1997), for example, by altering the second crossover energy and total electron yields with

continued electron beam exposure (refer to Sections 2.3.7-2.3.8, 5.2 and 5.3.2). It therefore, also becomes important to consider sample history, specifically previous electron beam exposure and incident energies, when measuring electron yields on insulators. This is discussed more thoroughly in Sections 2.3.7-2.3.8, and experimental data supporting these conjectures are provided in Section 5.3.2. Further considerations of how electron irradiation can permanently alter insulator electrical properties (such as resistivity) are difficult to assess, but are currently being incorporated into the experimental studies conducted at USU (Swaminathan, 2004; Swaminathan *et al*., 2003; Dennison *et al*., 2003a). Nevertheless, to alleviate all these deleterious charging effects, it becomes extremely important to minimize the exposure of the sample to electron irradiation by utilizing low-amplitude, short time duration pulsed electron beams.

Once charge accumulates on an insulator through repeated incident electron pulsing, an effective neutralization method must be employed to return the surface potential to 0 V. Left on its own, an insulator can take several hours to months to fully discharge, depending on its resistivity, thickness, and surface conditions (Swaminathan, 2004; Swaminathan *et al*., 2003; Dennison *et al*., 2003a). Generally, thick (>100 μm), highly-insulating (>10^{12}Ω·cm) targets do not neutralize on their own in a timely manner. However, very thin (<1 μm) insulator films on grounded conductor substrates have been shown to discharge more rapidly (Krainsky *et al.,* 1980, 1981) due to leakage currents to the underlying conductor. In selecting a thin insulator film, it is necessary to choose a thickness greater than both the maximum penetration depth of incident electrons (>1 μm for energies of ~10 keV) and the maximum escape depth of the SE's (10-100 nm for typical insulators) to ensure the incoming and emitted electron current measurements are not corrupted by penetration currents through the sample (Toth *et al*., 2002; Belhaj *et al*., 2000; Seiler, 1983). An alternative but more cumbersome

approach used to control local electron beam charging is to change beam spot positions on the sample with each pulsed measurement (Krainsky *et al.,* 1980, 1981; Seiler, 1983; Wargo *et al*., 1956).

For insulators with high melting points (e.g. SiO_2, MgO, mica, Al_2O_3, diamond, quartz) heating the samples to temperatures ranging from 150-800° C has been show to shorten the neutralization time period significantly (Mueller, 1945; Johnson, 1948; Whetten and Laponsky, 1957). The sample can either be maintained at a higher temperature throughout the measurement process (although higher temperatures have been shown to decrease the yields due to enhanced phonon scattering), or be allowed to cool to room temperature each time a yield measurements is to be taken (Johnson, 1948; Johnson and McKay, 1953). This method is effective in neutralizing both positive and negative charge, and is also effective in dissipating deeply imbedded charge. However, this method can be time consuming, and care must be taken when utilizing the heating method such that the melting points of insulators are not exceeded, especially for polymer materials.

A low-energy (<1 eV) electron flood gun has been shown to be effective in neutralizing surface potentials induced by incident electron with energies $E_1^{\sigma}<E_0<E_2^{\sigma}$ (Whetten and Laponsky, 1957; Krainsky *et al*., 1981, Sections 3.5, and 5.1-5.3). Furthermore, the flooding process is effective in neutralizing positive potentials in a self-regulating manner since once the positive surface is neutralized, low-energy electrons will no longer be attracted to the sample, resulting in a zero net current to the sample. In practice, this technique has also been shown to be much quicker than UV discharging or heating (refer to Section 5.3.3). However, as mentioned above, surface flooding cannot neutralize internal space charge that arises from deep incident electron penetration. Instead, the flooding process deposits electrons on the insulator surface until the combined potential (bulk and surface) is negligible. Hence,

subsequent electron yields may still be altered by internal electric fields even though surface potential is negligible (refer to Section 5.3.2). However, in previous experiments where both flood gun and heat conduction methods were implemented on the same sample, no differences in insulator SE yields were observed up to energies of 4 keV (Whetten and Laponsky, 1957).

Finally, UV sources with energies >4 eV have been shown to stimulate photo-induced conductivity in materials such as Kapton^{TM} and polyethylene, thereby effectively discharging negatively charged insulators (Bass *et al*., 1998; Levy *et al*., 1985). However, UV radiation with energies exceeding the bandgap energy may also induce further charging through the photoelectric effect or through photo-induced currents to the underlying substrate. This method is also limited by the attenuation depth of UV electromagnetic radiation in insulators (e.g. ~10 nm for λ=140-200 nm UV in alkali iodides, Boutboul *et al*., 1998) as well as the insulator's characteristic absorption spectrum, such that deeper bulk charge may not be dissipated effectively. Although some limited testing of UV neutralization sources was conducted in this dissertation work (Section 5.3.3), future studies at USU will determine the effectiveness of this method for different insulators in different energy regimes (refer to Section 6.2.2).

2.3 Physical Models for Insulator Electron Emissions

This section contains an overview of electron emission and charging models for insulator materials. It begins with Section 2.3.1, which gives a brief description of the three-stage model of production, transport, and escape used to describe SE emission from both conductors and insulators. This is followed by Section 2.3.2, which provides a summary of the traditional semi-empirical models used to fit SE yield curves. Then, the three-stage model is elaborated upon further in Sections 2.3.3-2.3.5, with consideration given to the production,

transport, and escape mechanisms of uncharged insulator materials. Next, in Section 2.3.6 it is shown how insulator surface potentials, resulting from electron-induced charging, can affect resulting SE emission spectra as well as electron yields. Section 2.3.7 provides a description the energy-dependent internal charge distributions induced by incident electron irradiation, which lead to these surface potentials. This section is followed by Section 2.3.8, which outlines the theoretical and computational models found in the literature used to predict these internal charge distributions, along with resulting electric fields and potentials at the sample surface caused by electron irradiation. In Section 2.3.9 the modeling equations for evolving electron yields, sample displacement currents, and surface potentials as a function of pulsed incident electron irradiation are developed, and related to DC incident charge, to be used later in the data analysis of Chapter 5.

2.3.1 Overview of the Three-Stage Model

The three-stage electron emission model for both conductor and insulator materials breaks down the complicated electron-material interactions into the following three sequential stages:

1. *Production:* Incident electrons penetrate into and/or backscatter out of the material, exciting a population of secondary electrons as they lose energy to the material. The depth of penetration and number of SE's produced is dependent on the incident electron energy. In addition, higher-energy SE's, produced by the incident electrons, undergo further inelastic scattering events, generating more SE's, with progressively lower energies.
2. *Transport:* A portion of the SE's produced are transported toward the material surface, and undergo further energy-loss mechanisms, dissipating their energy to phonons, plasmons, and other internal inelastic collisions. Most SE's excited deeper within the

material suffer too many energy-loss interactions, and are unable to escape. Due to the diversity and number of scattering processes, the SE transport process has generally been modeled as a diffusion process, where the probability an SE will reach the material surface decays exponentially with creation depth, and varies with the associated SE escape depth of the material (Lye and Dekker, 1957; Dionne, 1975). Dominant SE scattering mechanisms vary from one material to the next, but generally in metals, electron-electron collisions are thought to be the dominant mechanisms, followed by plasmon excitations (Dekker, 1958). For insulators, the large bandgap inhibits electron-electron scattering between SE's that are excited into the conduction band with the valence band electrons of the material, leading to a greater mean escape depth (Grais and Bastawros, 1982). For this reason, the mean escape depth for insulators generally ranges from 10-50 nm, compared to 0.5-1.5 nm for conductors (Seiler, 1983). As a result, the yields for insulators are typically much higher than those of conductors. In some reported cases, the yields of certain insulators can exceed those of standard conductors by as much as a factor of 20 (Seiler, 1983).

3. Escape: SE's that reach the surface are emitted, provided they have sufficient kinetic energy to overcome surface potential barriers. For grounded conductors, the electrons must overcome the material work function. For insulators and semiconductors, the electron affinity must be overcome. Additionally, for insulators, the surface potential induced by incident electron charging provides an additional energy barrier, which must be overcome by escaping SE's (Reimer, 1985; Seiler, 1983).

2.3.2 Traditional Semiempirical Models

The semiempirical SE-yield models that have been developed over the past 50 years have been based on the three-stage model described above, which incorporates the production, transport, and escape components, expressed mathematically as:

$$\delta(E_0) = \int n(x, E_0) \cdot f(x) \cdot dx \,, \tag{2.4}$$

where $n(x,E_0)\cdot dx$ is the production term representing the average number of SE's produced as a function of the incident electron of energy, E_0 in a layer of thickness, dx, at a depth, x, below the surface (Dionne, 1973). Generally, the production term, $n(x,E_0)$ is related to the material stopping power as:

$$n(x, E_0) = -\frac{1}{\varepsilon}\left(\frac{dE}{dx}\right), \tag{2.5}$$

where ε is the average energy required to excite a single SE. The term dE/dx is the rate of energy lost by the incident electron per unit length, and is proportional to the number of SE's produced by an incident electron per unit length. Once a population of SE's are excited, the SE's can undergo numerous scattering events before reaching the surface, such that the SE population takes on a well-defined energy distribution.

The term, f(x) in Eq. (2.4) contains SE transport and escape components, and represents the probability an SE will diffuse to the surface and escape. To first order, SE migration towards the surface can be approximated by an exponential law:

$$f(x) = B\exp(-x/\lambda_{SE}) \,, \tag{2.6}$$

where λ_{SE} is the mean SE escape depth that incorporates trapping probabilities, inelastic, and elastic scatterings. The parameter B is a material-dependent constant that represents the SE escape probability over surface energy barriers (Dionne, 1973). For conductors, B has been related to the work function (Chung and Everhart, 1974), and for uncharged insulators, it has

been related to the bandgap energy and electron affinity (Alig and Bloom, 1978). By combining Eqs (2.4) through (2.6), the general expression for the SE yield can be written as:

$$\delta(E_0) = -\frac{B}{\varepsilon}\int \frac{dE}{dx}\exp(-x/\lambda_{SE})\cdot dx\,. \tag{2.7}$$

Generally, the stopping power term, dE/dx, is expressed as a power of the scattering incident electron energy as:

$$-\frac{dE}{dx} = \frac{A}{E^{n-1}}\,, \tag{2.8}$$

where A is a stopping power coefficient of the material, and n is the stopping power exponent. As will be discussed further below, the stopping power exponent, n, generally ranges between 1 and 2 for most materials.

By integrating Eq. (2.8), and by applying the boundary conditions for the scattering energies and for the incident electron travel depth (energy boundary conditions range from the initial incident electron energy, E_0, to the incident electron scattering energy at a depth x, E(x); spatial boundary conditions range from the surface at x=0 to a depth x), an expression for the incident electron energy, at depth x, in terms of the initial incident electron energy, E_0, can be written as:

$$E^n(x) = E_0^n - Anx\,. \tag{2.9}$$

Integrating to the maximum incident electron penetration range, R, where the incident electron energy goes to zero, yields a relation between R and the stopping power coefficient and exponent:

$$R = \frac{E_0^n}{An}\,. \tag{2.10}$$

A special case of Eq. (2.8) occurs at n=1 where the stopping power becomes independent of scattering energy, and where the primary electrons lose their energy (through the creation of

SE's) at a constant rate as they move through the solid. For this case, the rate of energy loss is related only to the initial incident electron energy, E_0, and maximum electron penetration depth, R, as:

$$-\frac{dE}{dx} = \frac{E_0}{R}. \tag{2.11}$$

Shown in Fig. 2.3 are representative plots of the SE production term, n(E), calculated from Eq. (2.5), and schematically plotted as a function of electron penetration depth and energy. The SE production was calculated using the expressions for the stopping power, given by Eqs. (2.8) through (2.11), with stopping power coefficients of n=1 and n=2 plotted. Also shown is the SE production model provided by Meyza *et al.* (2003) (described later in Section 2.3.8). These models provide an indication of the depths and energies for which incident electrons are deposited and SE's are produced. For insulators, this can provide crude information on the location of the internal charge distributions. Still, much variation exists both for the power-law production model, as well as the Meyza model. For example, it can be seen from these plots for n=1, SE production is constant up to the maximum penetration depth, R. However, for $1<n\leq 2$, most SE's are produced when an incident electron has lost most of its energy, near the maximum penetration depth, R. For the Meyza model, the maximum number of SE's are produced between the surface and maximum penetration depth, R.

An empirically derived expression for the maximum incident electron penetration depth, R, has been determined by Young (1956) over the energy range of 2-40 keV as:

$$\frac{R}{nm} = \frac{1.15\cdot 10^5}{s/(kg/m^3)} \cdot \left(\frac{E_0}{keV}\right)^n, \tag{2.12}$$

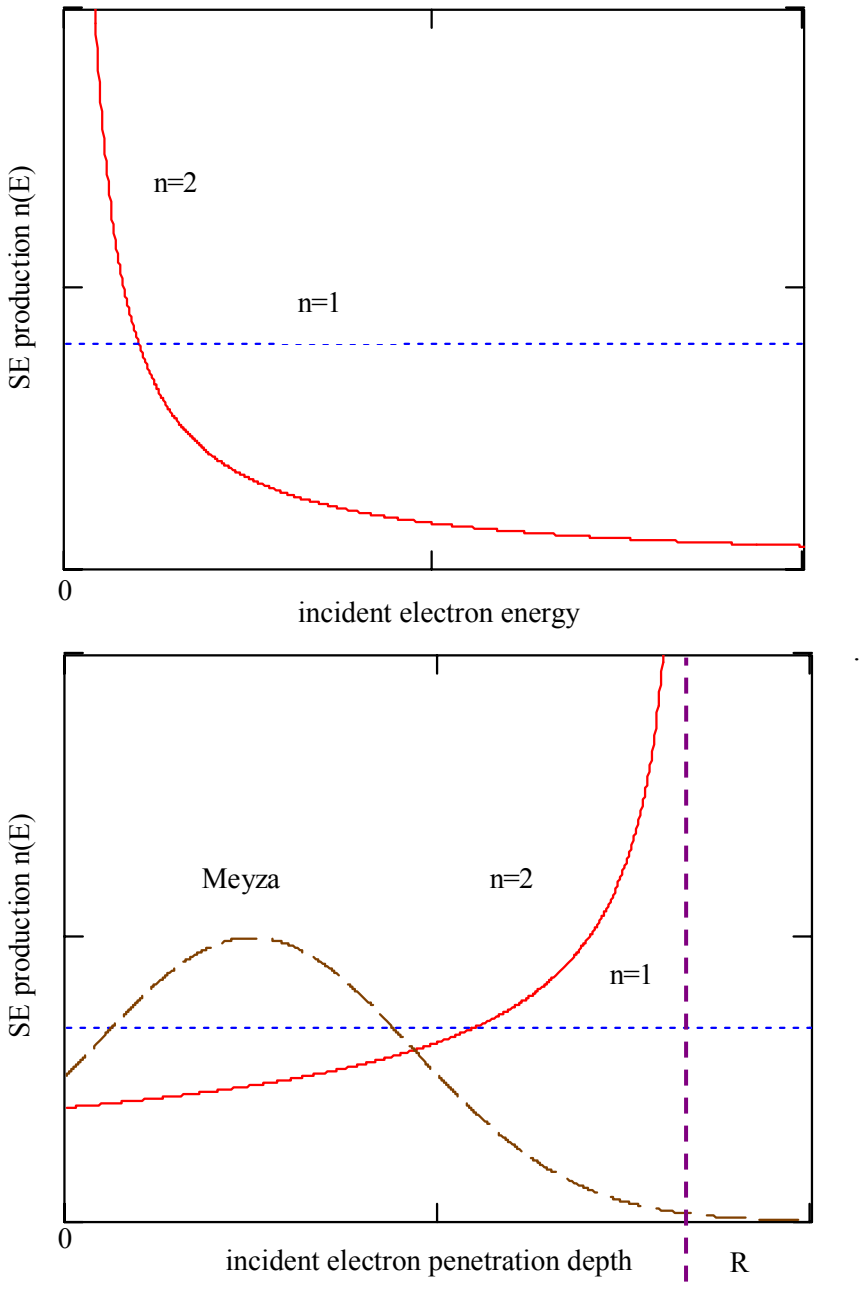

FIG. 2.3. A representation of the average number of SE's produced as a function of incident electron energy (top) and penetration depth (bottom). The function n(E) was calculated using the power-law stopping power given by Eqs. (2.5) and (2.8) through (2.11) with stopping power coefficients of n=1 and n=2 plotted. Additionally, the Meyza model, given by Eq. (2.40), is plotted on the bottom graph. Also shown on the bottom graph is the maximum incident electron penetration depth, R (vertical dashed line).

where s is the material density, and n is the Young's stopping power exponent. Although this expression was determined from the transmission of electrons through thin aluminum foils, Eq. (2.12) (and similar variations of this expression) has been successfully applied to the modeling of many other types of materials (Reimer, 1985; Melchinger and Hofmann, 1995). Fig. 2.4 shows the energy dependence of the maximum penetration range [calculated from Eq. (2.12)] of incident electrons for insulators relevant to this study (i.e., anodized aluminum, silicone adhesives, and Kapton^{TM}). Other similar empirical expressions for the incident electron range, with different values for A and n (ranging from 1-2), can be found elsewhere in the literature (Reimer, 1985; Fitting, 1975; Grais and Bastawros, 1982; Young, 1956). Furthermore, numerous theoretical and computational treatments are also available, which incorporate classical, quantum-mechanical, non-relativistic, and relativistic treatments for the incident electron stopping power term and penetration range, and have been applied to the problem of SE emission (Reimer, 1985; Kanaya *et al*., 1978; Akkerman *et al*., 1992; Akkerman and Akkerman, 1999; Boutboul *et al*., 1996; Battye *et al*., 1974; Ozturk and Williamson, Jr., 1993; Sternglass, 1950). From these studies, it can be shown there exists theoretical grounds for choosing a stopping power exponent that ranges between 1 and 2. Included among the computational studies are the works of Akkerman and Boutboul who have used a Monte Carlo simulation, incorporating several elastic and inelastic scattering mechanisms relevant to electrons (both incident and SE's) over the energy range of 20 eV to 10 keV, to predict stopping powers and electron travel lengths for several alkali halides and polymers (Akkerman *et al*., 1992; Akkerman and Akkerman, 1999; Boutboul *et al*., 1996). In our review of these computational approaches for determining the incident electron penetration range, it has been found that the computational results agree with the empirical range equation, Eq. (2.12), to within ten percent for applicable electron energies ranging from

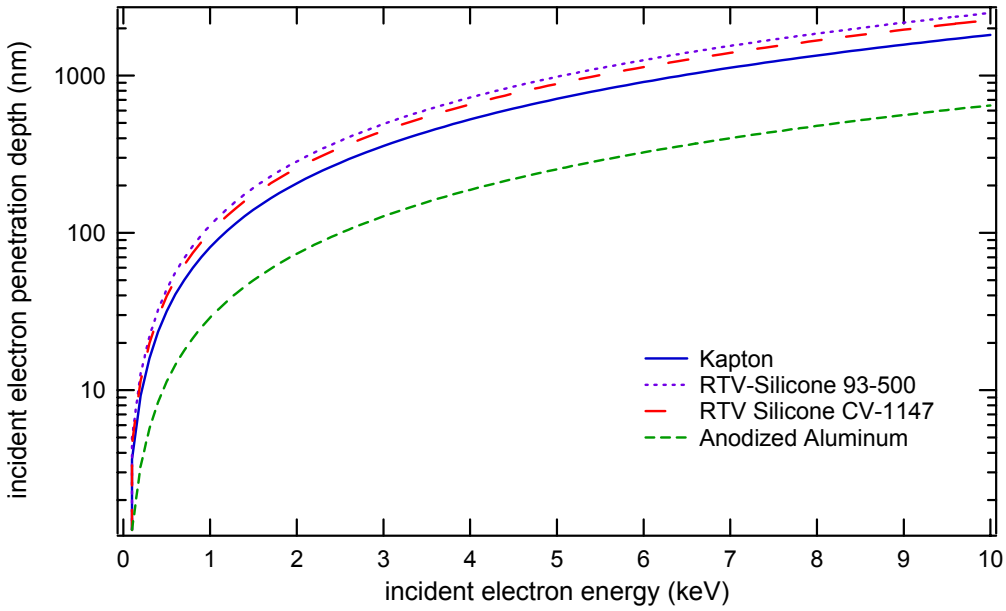

FIG. 2.4. Incident electron penetration depths as a function of incident electron energy for insulators relevant to this study. Depths were calculated using Eq. (2.12) over the range of 100eV to 10 keV.

100 eV to 10 keV (Thomson, 2003c; Akkerman and Akkerman, 1999). However, as will be described in Section 2.3.4, the empirical range equations [including Eq. (2.12)] cannot be extended accurately to electrons with energies <100 eV (e.g., SE's) since the prohibition of higher-energy scattering mechanisms act to lengthen lower-energy electron travel lengths. Finally, in the study of insulator charging, these range equations are important since they give spatial limits over which incident electrons embed themselves into insulator materials.

By integrating Eq. (2.7) from x=0 to x=R, and combining with Eqs. (2.8) through (2.10), an expression for the SE yield is obtained that depends on material parameters: A, B, ε, n, and $\lambda_{SE.}$ This expression is often reduced in terms of the maximum SE yield, δ_{max} and corresponding energy, $E_{max}{}^{\delta}$ by setting the derivative of $\delta(E_0)$ with respect to the incident energy to zero and solving for δ_{max} and $E_{max}{}^{\delta}$. This reduced yield equation then becomes:

$$\delta(E_0) = \frac{B}{\varepsilon}\delta_{\max}\left(\frac{E_{\max}{}^{\delta}}{E_0}\right)^{n-1}\left\{1-\exp\left[-\frac{R}{\lambda_{SE}}\left(\frac{E_0}{E_{\max}{}^{\delta}}\right)^{n}\right]\right\}, \tag{2.13}$$

where the parameters B, ε, and n can be related by the following exponent term:

$$\frac{B}{\varepsilon} = \frac{1}{1-\exp(-R/\lambda_{SE})}, \tag{2.14}$$

and

$$n = \frac{B}{\varepsilon}\left[\frac{B}{\varepsilon} - \frac{R}{\lambda_{SE}}\exp(-R/\lambda_{SE})\right]^{-1}. \tag{2.15}$$

Note from Eq. (2.15), the power exponent, n, can be related to the ratios of R/λ_{SE} and B/ε as shown in Fig. 2.5, where Eq. (2.14) has been substituted into Eq. (2.15), and n is plotted as a function of R/λ_{SE}. From the figure, it can be seen for a given $n(R/\lambda_{SE})$ value, two solutions for R/λ_{SE} exist. For the analysis presented in this dissertation, the higher-value solution of R/λ_{SE} was used since $R>\lambda_{SE}$ represents the physical solution for most incident electron energies. This can be seen by comparing the values for R shown in Fig. 2.4 with the modeled values for λ_{SE} provided later in Section 2.3.4. Hence, once $n(R/\lambda_{SE})$ is determined by fitting SE yield curves with Eq. (2.13), the ratio of R/λ_{SE} can be determined using Eqs. (2.13) through (2.15) as shown in Fig. 2.5. Then, if the maximum penetration depth, R, is determined using, for example, semi-empirical formulations as given by Eq. (2.12) (refer to Fig. 2.4), the mean SE escape depth, λ_{SE}, can be estimated for an insulator material. As will be shown in Section 5.3.2, this analysis was used on Kapton™ to evaluate λ_{SE} as a function of incident electron irradiation.

As mentioned above, the power exponent, n, has been determined both theoretically and experimentally for different materials over different electron energy ranges, but in regards to Eq. (2.13), a few special cases are worth noting since they will be used later in this

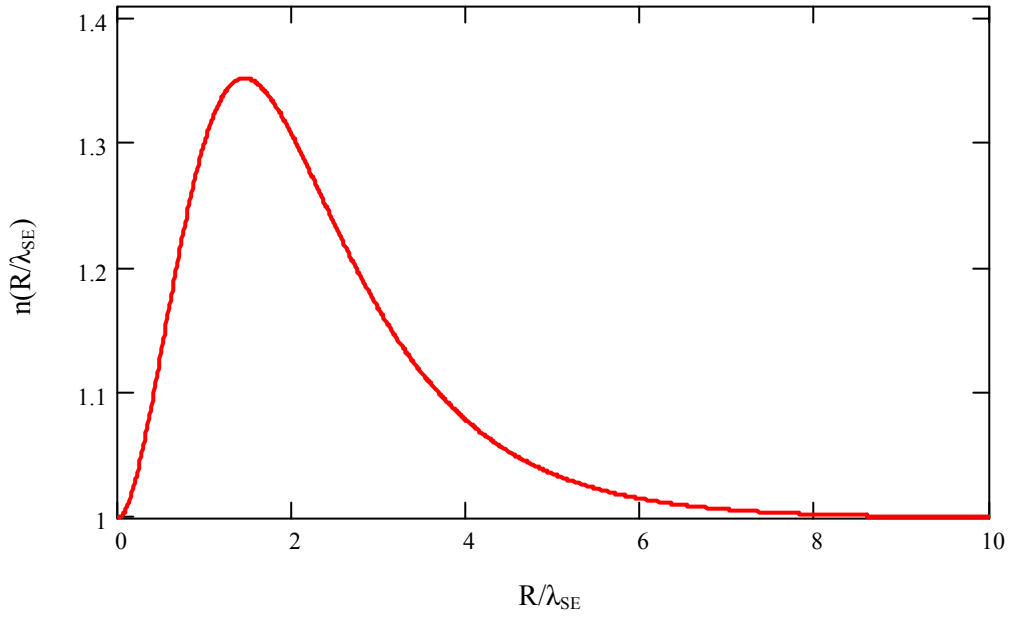

FIG. 2.5. SE yield parameter, $n(R/\lambda_{SE})$, plotted as a function of R/λ_{SE}. Notice for a given $n(R/\lambda_{SE})$ value, two solutions for R/λ_{SE} existed. The higher R/λ_{SE} solution was chosen for the analysis in this dissertation.

dissertation (Sections 5.1 through 5.3). Furthermore, as described above, by determining n (either through experiment or theory), the ratios B/ε, as well as R/λ_{SE} can be calculated from Eqs. (2.14) and (2.15) allowing one to further reduce Eq. (2.13). For example, for Young's model, n=1.35 (determined experimentally by Young on aluminum foils). Given this value, Eqs. (2.13) through (2.15) can be combined to obtain a new SE yield expression given as:

$$\delta(E_0) = 1.114 \cdot \delta_{max} \left(\frac{E_{max}{}^{\delta}}{E_0} \right)^{0.35} \left\{ 1 - \exp\left[-2.28 \left(\frac{E_0}{E_{max}{}^{\delta}} \right)^{1.35} \right] \right\}. \qquad (2.16)$$

From Eq. (2.16) regarding modeling SE yield curve data, one can observe the number of independent fitting parameters has been reduced to two, δ_{max} and $E_{max}{}^{\delta}$. Equation (2.16) is referred to as Young's SE yield model, and is used to fit yield data throughout Sections 5.1 through 5.3. A similar procedure can be applied to obtain the Feldman model (Feldman,

1960), where the power exponent, n, is predetermined based on the material atomic number as:

$$n = \frac{1.2}{(1 - 0.29 \cdot \log_{10} Z)}. \tag{2.17}$$

Continuing along these lines of reason, the Variable-N model is obtained from Eq. (2.13), by allowing n to vary as a third free parameter (along with δ_{max} and E_{max}^{δ}), ranging over all possible values $1<n<2$ while fitting to experimental yield data. As will be demonstrated in Sections 5.1 through 5.3, of these three models, the Variable-N model is found to provide the best fit to experimental data since it includes a third free parameter. An evaluation of these models for both conductor and insulator data is provided in Sections 4.6 and 5.1 through 5.3.

Finally, a fourth yield model provided by Sternglass (1953) incorporates the Bethe stopping power [in contrast to the power-law stopping power of Eq. (2.8)], with several simplifying assumptions, along with Eq. (2.7), to arrive at an alternative reduced yield equation:

$$\delta(E_0) = \frac{E_0}{E_{\max}^{\ \delta}} \cdot \exp\left[2 - 2\left(\frac{E_0}{E_{\max}^{\ \delta}}\right)^{1/2}\right] \cdot \delta_{\max}. \tag{2.18}$$

It must be noted although the Sternglass model is based in large part on theoretical grounds as apposed to the empirical approach of Eq. (2.13), it generally does a poorer job of fitting experimental data (refer to Sections 5.1 and 5.3 as well as Dennison *et al*., 2002, 2003d). Further review of the derivations of the SE yield models presented in Eqs. (2.4) through (2.18) are provided in Nickles (2002), Davies (1999), and Dionne (1973).

Although the models presented above generally do well in fitting conductor SE yield data, they have several shortcomings when modeling insulator data. As described more fully below in Sections 2.3.3 and 2.3.5, attempts have been made to relate SE production and

escape parameters (ε and B) to fundamental insulator electronic properties, such as the bandgap and electron affinity. Furthermore, in Section 2.3.4, it is demonstrated the mean SE escape depth, λ_{SE}, displays a strong dependence on SE energy that, in turn, significantly affects the SE transport and escape probabilities. This is particularly important for insulators where the energy bandgap can play a significant role in the scattering mechanisms allowed for diffusing hot electrons in the conduction band that suffer minimal energy losses per scatter. Furthermore, as described in Sections 2.3.4-2.3.5, SE's in an insulator with energies above the bandgap energy (SE's with energies ranging from ~10 eV to 50 eV) are subject to various other energy-loss mechanisms that include electron-plasmon, electron-hole pair creation, electron-exciton, and electron-phonon inelastic scatterings. However, for SE's with energies below the bandgap energy, all-energy loss mechanisms are prohibited except for electron-phonon scattering, thus altering the SE escape depth and probability (Zavyalov, private communication). Hence, λ_{SE} can display a strong dependence on SE energy that is not accounted for in Eq. (2.13) (refer to Fig. 2.7 in Section 2.3.4).

Finally, the models presented above are not equipped to handle the electron yields from charged insulators. As described in Section 2.3.6, positive and negative surface potentials induced by an electron beam can significantly affect the measured SE, BSE, and total yields by suppressing or accelerating escaping SE's. Furthermore, as explained in Section 2.3.6, negative surface potentials can alter electron yields by both shifting the SE energy distribution to higher energies (such that SE's are accelerated to energies >50 eV), or by altering the impact energies of incident electrons. These results are further demonstrated experimentally in Sections 5.3.2 and 5.3.4. Finally, as explained in Section 2.3.7, even if the insulator surface potential is returned to 0 V with the use of a neutralization source, such as a low-energy flood gun (refer to Section 3.5), latent internal charge distributions can still affect

subsequent electron yields (refer also to Section 5.3.2 and Meyza *et al*., 2003). These charging effects are addressed further in Sections 2.3.6 to 2.3.9. The next three sections focus on SE production, transport, and escape mechanisms for uncharged insulators.

2.3.3 Production Mechanism for Uncharged Insulators

The production mechanism for SE's in uncharged insulators can be adequately described by the expressions for the stopping power and electron yield given by Eqs. (2.5) through (2.18). As described in Section 2.3.2, the stopping power and range equations presented in Eqs. (2.10) and (2.12) have been shown to adequately describe electron depth trajectories for many materials (conductors and insulators) for incident electrons with energies ranging from 100 eV to energies well beyond 10 keV. These range equations are applicable both to conductors and uncharged insulators since, in large part, they depend only on the incident electron energy and macroscopic density of materials (Reimer, 1985; Thomson, 2003a; Akkerman and Akkerman, 1999). For uncharged insulators, the primary difference between the SE production mechanisms, in comparison with conductors, is the additional energy required to excite a population of SE's across the insulator bandgap. This suggests the average energy, ε [refer to Eq. (2.5)], required to excite an SE inside an insulator must be close to the insulator bandgap, $\varepsilon \sim E_g$. Based on the assumption ε is equal to the electron-hole-pair creation energy, Alig and Bloom (1978) have used energy and momentum conservation arguments, along with empirical data for a wide range of insulators, to offer an average SE creation energy as:

$$\varepsilon = 2.8 \cdot E_g , \tag{2.19}$$

where the factor of 2.8 in Eq. (2.19) results from momentum and energy conservation arguments. As indicated above, this treatment for SE production in insulators only applies to

materials that have not been charged. As described in more detail in Section 2.3.7 and in Meyza *et al*. (2003), the ranges of incident electrons in preirradiated insulators can be significantly altered by internal charge distributions and resulting high internal electric fields.

2.3.4 Transport Mechanism for Uncharged Insulators

Once SE's are created in an insulator, many make their way to the surface, undergoing numerous scattering events (and generating further SE's) along the way. As presented in Eq. (2.6), the probability an SE will reach the surface depends on the mean SE escape depth, λ_{SE}, (also referred to as SE travel length throughout this section) and to first order, increases exponentially with creation depth. In general, the mean escape depths for insulators are greater than for conductors and semiconductors (Grais and Bastawros, 1982). This result is true for conductors because the probability for electron-electron and electron-plasmon scattering in the conduction band is greater than it is for insulators due to the greater number of free charge carriers. For semiconductors, although there are fewer charge carriers in the conduction band, the probability for valence electron scattering is greater due to the relatively small energy bandgap (Grais and Bastawros, 1982; Nickles, 2002; Corbridge *et al*., 2003).

For insulators, the relatively small number of hot electrons in the conduction band, along with the relatively large bandgap energy, significantly decreases the probability for electron-electron scattering either with conduction or valence electrons (Grais and Bastawros, 1982). In fact, only SE's with kinetic energies somewhat greater than the bandgap energy can participate significantly in electron-electron scattering, electron-plasmon scattering, or electron-hole recombination. Since the peak of the SE energy distribution lies below a typical insulator bandgap of ~10 eV (see, for example, Fig. 2.1), a significant portion of SE's are prohibited from participating in these energy loss mechanisms. SE's with energies below the bandgap energy can only undergo electron-phonon scattering. Here, although the typical

mean-free-path (~1 nm) for SE-phonon scattering is comparable to other insulator scattering mechanisms (*e.g.*. ionization, electron-plasmon, electron-hole), the energy loss per scatter is on the order of 10^2 -10^4 eV less than for these higher-energy scattering mechanisms (Boutboul *et al*., 1996, 1998, 1999; Akkerman *et al*., 1992, 1994). For example, typical energy losses due to electron-plasmon interactions range between 10-100 eV, while single-scatter electron-phonon energy losses are only on the order of 10-100 meV. Because specific energy loss mechanisms are diminished for SE's in insulator materials, the mean escape depth for SE's typically ranges from 10-50 times higher than for conductors (Seiler, 1983). Fig. 2.6 offers a schematic diagram of the energy loss mechanisms permitted to SE's as well as to incident electrons in insulator materials. As can be seen from the figure, both incident electrons, as well as SE's can undergo both elastic and quasi-elastic scattering, as well as electron-phonon interactions. Furthermore, as discussed above, only higher-energy SE's (>10 eV), as well as incident electrons, can interact with valence electrons and plasmons. Finally, only incident electrons can undergo core electron interactions.

Since the SE travel lengths are difficult to measure directly, most attempts to determine λ_{SE} have been through theoretical or computational studies. Kanaya *et al*. (1978) derived an expression for the most probable SE travel lengths by considering only electron-plasmon interactions as:

$$\lambda_{SE} = \frac{2a_H E_s}{\lambda_p{}^2 p\Delta E \cdot \ln(4E_s / \Delta E)}, \tag{2.20}$$

where a_H is the screened atomic radius, $\lambda_p{}^2$ is a correction factor for incident energies of E_0<1 keV, E_s is the average first collision ionization energy, and p is the normalized ratio of one plasmon-loss energy to the most probable plasmon-loss energy. Furthermore, $\Delta E=28.8(s\nu/L)^{1/2}$ is in units of electron volts, where s is the material density, ν is the valence electron loss, and L is the atomic weight. Since Eq. (2.20) was derived only for electron-

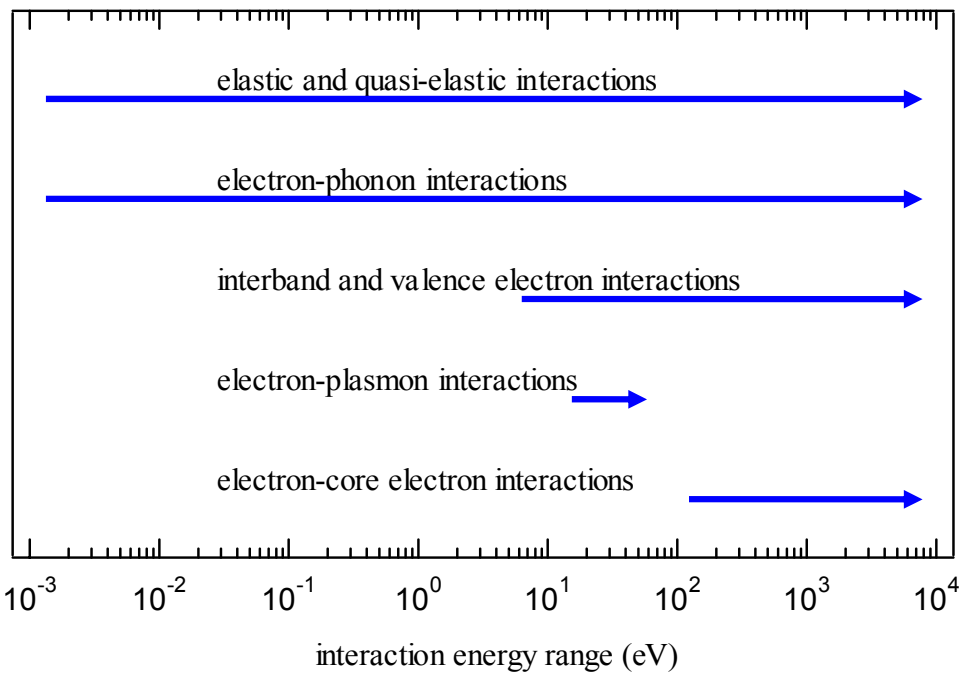

FIG. 2.6. Schematic diagram of the electron interaction energy regimes for an insulator material. These interaction energy regimes apply both to escaping SE's, as well as to penetrating incident electrons. Both incident electrons, as well as SE's can undergo both elastic and quasi-elastic scattering, as well as electron-phonon interactions. Higher-energy SE's (>10 eV), as well as incident electrons can also interact with valence electrons and plasmons. Finally, only incident electrons can undergo core electron interactions.

plasmon interactions, one would expect this expression to describe the travel length only for SE's with energies greater than the elementary plasmon excitation energy, $\hbar\omega_p$ (>10 eV for insulators).

Probably the most extensive computational work on low-energy electron transport in insulators has been conducted by T. Boutboul and A. Akkerman (primary authors), who have performed Monte Carlo (MC) simulations to obtain the inelastic mean free paths (IMFP), stopping powers (SP), travel lengths, and escape probabilities for low-energy electrons in alkali halides and several organic compounds (Boutboul *et al*., 1996, 1998, 1999; Akkerman and Akkerman, 1999; Akkerman *et al*., 1992, 1994). In their studies, they take into account several fundamental scattering mechanisms, as well as the energy dependence of the scattering

cross sections. Their studies cover the transport of electrons over electron energies ranging from <1 eV to >10 keV, and they calculate the inelastic mean free paths (IMFP) and stopping powers (SP) associated with individual, as well as cumulative, scattering mechanisms. Their simulations of electron scattering mechanisms include: electron-screened elastic electron-ion scattering; single-electron core-level and valence-level interband transitions and ionization excitations; electron-plasmon excitations; electron-hole excitation and recombination; and electron-phonon excitations. They use a semiclassical binary encounter theory for core-level excitation estimates, and the first Born approximation, along with an expansion of the imaginary dielectric function, for valence electron excitations.

In agreement with other authors (Battye *et al*., 1974; Cartier and McFeely, 1991), their simulations predict the shortest total MFP's and maximum SP's at energies of ~100 eV, where valence electron interactions (single and collective) are strongest (Boutboul *et al*., 1996; Akkerman *et al*., 1994). Additionally, in this energy regime, the fractional energy loss per scatter ranges between 10-90 percent, hence dissipating a substantial fraction of an electron's energy per scattering event. Due to the short MFP's and high SP's, it follows that near 100 eV the mean electron travel lengths are at a minimum (<1 nm), and steadily grow with increasing and decreasing electron energies on either side of this minimum. For electron energies >100 eV, the electron travel lengths increase as the scattering MFP's of electron-hole, electron-plasmon, and ionization scatterings increase, and as the energetic electrons possess a greater amount of energy to lose (through the excitation and production of more hot electrons) before dissipating all their energy into the material. As a result, the power law approximation provided by Eq. (2.12) provides a good estimate for the electron travel distance at energies >1000 eV. Furthermore, at energies above 10 keV, the simulations of Akkerman and Akkerman (1999) display good agreement with Bethe's nonrelatavistic scattering theory

(Thomson, 2003c). Finally, for electron energies <100 eV, the mean electron travel length once again rises for insulators since the probability for valence electron excitations diminishes, and since the electrons lose relatively little energy through phonon interactions.

Of particular importance to the study of SE travel lengths are the simulations of Boutboul and Akkerman in regards to the MFP's of electrons with energies below the insulator bandgap energy, typically <10 eV. In their models, which are based on electron-phonon interactions in this energy regime, they once again find the electron travel lengths are dependent on electron energy (Akkerman *et al*., 1994). Shown in Fig. 2.7 is a plot of λ_{SE} as a function of SE energy taken from their Monte Carlo simulations (for electron energies 0.5 to 6 eV, below the bandgap, E_g) for CsI, KCl, and NaCl (Akkerman *et al*., 1994). For Fig. 2.7, the mean SE escape depths were calculated from escape probability exponential fits (refer to Eq. (2.6)) performed on the electron escape probabilities provided in Akkerman *et al*. (1994). As shown in the figure, for electron energies ranging from 0.5-6 eV, it was observed that the modeled SE travel lengths increased at a decreasing rate, approaching an asymptotic value near 6 eV. As shown in the figure, the electron travel depth data were fitted with asymptotic-approaching, increasing exponential functions of the form: $\lambda_{SE}(E) = \lambda_{\max} \cdot \left[1 - \exp(-\kappa E)\right]$ over the energy range of 0.5-6 eV. The fitted asymptotes were found to be λ_{max}=35 nm, 9 nm, and 15 nm for CsI, KCl, and NaCl, respectively. The exponential coefficients were found to be κ=0.35 eV^{-1}, 0.70 eV^{-1}, and 0.46 eV^{-1} for CsI, KCl, and NaCl, respectively.

As mentioned previously, these escape probabilities were derived exclusively from electron-phonon interactions for energies ranging from 0.5-6 eV, where this is the dominant SE energy loss mechanism. However, for SE's above the bandgap energy, electron-plasmon interactions contribute significantly to overall SE energy losses. To observe the effects of

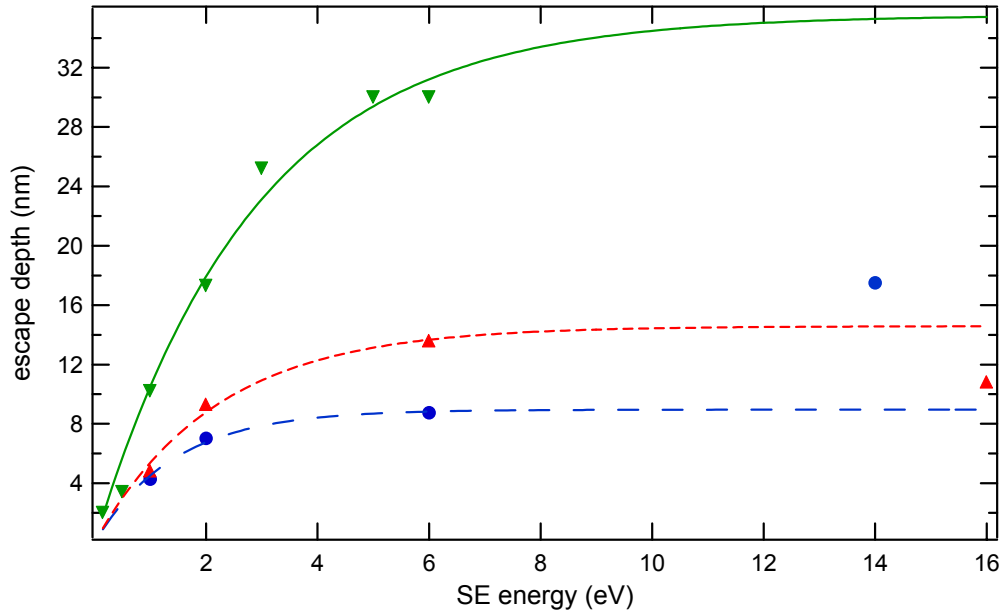

FIG. 2.7. SE transport depths as a function of energy for CsI (▼), KCl (●), and NaCl (▲). Data up to 6 eV was taken from Monte Carlo simulations performed by Akkerman *et al*. (1994) based only on electron-phonon interactions. This data was fit with asymptotic exponential functions as shown. Data beyond 6 eV was taken from Kanaya *et al*. (1978) based on electron-plasmon interactions.

electron-plasmon interactions on higher-energy (>10 eV) SE travel lengths, Eq. (2.20) [along with additional information from Kanaya *et al.* (1978)] was used to calculate estimates for λ_{SE} for KCl and NaCl (data for CsI was not available) in this higher-energy regime. The data points for λ_{SE} were plotted against the material-dependent plasmon cutoff excitation energy, $\hbar\omega_p$ obtained from Pines (1999). Overall, it was found that the electron-plasmon SE travel lengths were in fair agreement with the asymptotic electron-phonon SE travel lengths as can be seen from Fig. 2.7. Specifically, λ_{SE} estimates obtained from Kanaya *et al.* (1978) at the plasmon excitation energy were roughly a factor of 2 higher and a factor of 0.8 lower than those obtained from Akkerman *et al*. (1994) for KCl and NaCl, respectively. However, it must be emphasized, the results obtained from Kanaya *et al.,* (1978) were based exclusively on electron-plasmon interactions. Actual SE travel lengths at energies >10 eV would probably

be lower since other energy-loss mechanisms would contribute to reducing λ_{SE}. Finally, it should be noted the electron affinities for CsI, KCl, and NaCl range from 0.1-0.5 eV, such that most SE's with energies shown in Fig. 2.7 could escape from the insulators, provided the insulator was not positively charged. Additionally, based on typical insulator SE energy distributions (refer to Section 5.3.2), the SE energy peak lies at ~2 eV above the electron affinity. Hence, for an electron-irradiated insulator, the peak energy for SE's internal to the insulator will range between 2-3 eV, and will have mean escape depths corresponding to this energy range. However, from Fig. 2.7, it is observed that the mean SE travel lengths are maximally dependent on SE energy between 2-3 eV, and beyond 6 eV (approaching E_g for each material), the mean travel lengths level out to a constant value. Hence, one would expect λ_{SE} to display strong energy dependence for a large majority of SE's excited in an insulator material.

The results presented in Fig. 2.7 are in agreement with experimental data on the low-energy electron travel lengths reported for CsI (Boutboul *et al*., 1998). In these experimental studies, UV radiation of 140-180 nm (7 eV to 9 eV) was used to excite a population of hot electrons in evaporated CsI thin films on polished CaF_2 substrates. The electron travel lengths were then deduced from the photocurrents measured as a function of insulator film thickness. Since the bandgap energy of CsI is E_g=6.2 eV, these electrons were able to make their way toward the substrate, losing energy primarily through electron-phonon interactions. In their modeling, other scattering mechanisms were neglected since the energy distribution of hot-electrons was not sufficient to excite further significant interband or plasmon excitations. Although in this study, the hot-electron energy distribution was excited by UV radiation instead of electrons, the excited electron population quickly thermalized through multiple scattering events (primarily electron-phonon), such that the final energy distribution depended

little on the initial excitation mechanism (Boutboul *et al*., 1998; Zavyalov, private communication; Dennison, private communication). The experimental results revealed the mean electron travel length for CsI, induced by a 7-9 eV UV source, were on the order of 25±10 nm, in agreement with the calculated asymptotic electron travel length for CsI (35 nm) to within the reported experimental error (refer to Fig. 2.7).

Based on these computational and experimental results, there appears to be a strong energy dependence associated with the SE travel length. Consequently, a single mean escape depth may not be sufficient to adequately fit insulator SE yield data using models built upon the escape and transport probability function, Eq. (2.6). Specifically, these models include Young's model, the Feldman model, and the Variable N model shown in Eqs. (2.13) through (2.17) (and used later to fit insulator data in Chapter 5). As proposed by V. Zavyalov (private communication), and as described further in Section 6.2.3, by incorporating the electron energy dependence into the mean SE escape depth, $\lambda_{SE}(E)$, an improved SE yield model may be formulated that could offer vast improvements in modeling insulators. Unfortunately, in the literature, there exists a vast deficit of both experimental and simulated data that can relate the SE mean travel length to electron energy. However, it may be possible to empirically determine the relationship of $\lambda_{SE}(E)$ and SE energy by measuring a series of SE yield curves (at constant E_0) at stepped suppression grid biases (steps $\leq$ 0.5 V) up to 50 V (Zavyalov, private communication; Grais and Bastawros, 1982). By this method, the SE yield as a function of SE energy could be determined, by fitting the results using Eq. (2.13), and then determining $\lambda_{SE}(E)$ from Eqs. (2.12), (2.14), and (2.15). As described further in Section 6.2.3, an empirical study of the energy-dependent $\lambda_{SE}(E)$ could be the subject of future research at Utah State University.

2.3.5 Escape Mechanism for Uncharged Insulators

Once SE's reach the (uncharged) insulator surface, the probability they will escape is related to the insulator's surface energy barriers, such as the electron affinity, χ. In regards to the SE energy spectrum (refer to Fig. 2.1), only the tail of the SE distribution with kinetic energies greater than the insulator's electron affinity, χ, can escape the solid (Zavyalov, 2003a). As described further below, an insulator's surface energy barrier is further increased in the case of positive charging.

In the electron yield models presented above [Eqs. (2.6) through (2.15)], the escape probability, f(x), is partially governed by the probability coefficient, B, that ranges between 0 and 1 (0: no escape, 1: escape). In the literature, there have been attempts to relate the escape probability coefficient, B, both to the electron affinity and bandgap energy (Alig and Bloom, 1978). Alig and Bloom (1978) used the power-loss model described by Eqs. (2.13) through (2.15), along with the average SE creation energy described by Eq. (2.19), to solve for B in terms of the maximum SE yield, δ_{max}, and energy $E_{max}{}^{\delta}$, as well as to the insulator bandgap, E_g as:

$$B \approx \frac{7\delta_{\max} E_g}{E_{\max}{}^{\delta}}. \tag{2.21}$$

In order to relate B to χ, the authors imposed a free-particle approximation to the excited SE population. They first assumed the probability of an SE escaping (once it had reached the surface) would be zero if $E<\chi$, but equal to $1-(\chi/E)^{1/2}$ if $E>\chi$. Next, they assumed the distribution of electrons in an energy state, E, would be unity if $0 \le E < 1.5 \cdot E_g$ (the factor 1.5 was the energy threshold they reported was required to create an electron-hole pair) since all other energy-loss mechanisms to the SE were neglected (note the authors ignored electron-phonon interactions below E_g). Hence, SE's in this energy state remained in this energy state since all energy-loss mechanisms were prohibited. However, for $E \ge 1.5 \cdot E_g$, further electron-hole pair

creation was allowed, and the unit of energy lost by the SE's was $\varepsilon=2.8\cdot E_g$ from Eq. (2.19). Finally, the density of electronic states per unit energy per unit volume was assumed to be proportional to $E^{1/2}$ in the free-particle approximation. Using these arguments, the authors arrived at an integral expression for B in terms of the ratio of the electron affinity and bandgap energy, of χ/E_g. However, the authors did not explicitly write the integrals in terms of the energy-dependent conditions stated above. Nevertheless, for completeness, the integrals have been solved for here, and are provided as follows:

$$B=\begin{cases} 0 & E\le\chi, \\ 1-\dfrac{\int_{\chi}^{\frac{3}{2}E_g}\chi^{\frac{1}{2}}dE}{\int_{\chi}^{\frac{3}{2}E_g}E^{\frac{1}{2}}dE}=1-\dfrac{\frac{3}{2}E_g\cdot\chi^{\frac{1}{2}}-\chi^{\frac{3}{2}}}{\frac{\sqrt{6}}{2}E_g^{\frac{3}{2}}-\frac{2}{3}\chi^{\frac{3}{2}}} & \chi\le E<\dfrac{3}{2}E_g, \\ 1-\dfrac{\int_{\frac{3}{2}E_g}^{\infty}\chi^{\frac{1}{2}}\cdot e^{-\frac{E}{\varepsilon}}dE}{\int_{\frac{3}{2}E_g}^{\infty}E^{\frac{1}{2}}\cdot e^{-\frac{E}{\varepsilon}}dE}=1-0.503\left(\dfrac{\chi}{E_g}\right)^{\frac{1}{2}} & E\ge\dfrac{3}{2}E_g, E_g>\chi. \end{cases} \tag{2.22}$$

Note, according to the energy conditions outlined by the authors, three energy-dependent solutions exist in Eq. (2.22). For SE's with energies below χ [condition 1 in Eq. (2.22)], the probability coefficient was zero since SE's could not overcome the surface potential barrier. However, for SE's with energies above χ, but below E_g [condition 2 in Eq. (2.22)], or for energies above both χ, but below E_g [condition 3 in Eq. (2.22)], the probability coefficient varied between zero and unity. Using this method, the authors claimed to calculate the escape probability constant to within an order of magnitude of probability constants determined from the semi-empirical expression of Eq. (2.21) for numerous insulators (refer to Alig and Bloom, 1978). Finally, the energy dependence of the escape probability constant in

Eq. (2.22) provides further motivation to develop an energy-dependent SE yield model applicable to insulators as discussed in Section 2.3.4).

An alternative approach for studying the escape of SE electrons from a material's surface potential barriers is provided by the Chung and Everhart (1974) model, which expresses the escaping SE energy distribution in terms of the work function for metals (or electron affinity for insulators). The model starts with a population of SE's that have been excited by incident electrons (or photons or ions), and uses the exponential transport and escape probability expression given by Eq. (2.6) to determine whether an SE created at some depth within the solid will reach the surface (refer to Section 2.3.4). The model also considers surface energy barriers (i.e., work function and electron affinity) such that the energy distribution of emitted SE's is given as:

$$\frac{d\tilde{N}}{dE} = \frac{k}{E_0} \frac{E}{\left(E+\phi\right)^4}, \tag{2.23}$$

where $\tilde{N}$ is the number of emitted electrons, E is the SE energy in electron volts, k is a material-dependent proportionality constant, E_0 is the incident beam energy, and φ is the material work function (for metals). A more thorough explanation of the Chung and Everhart model is provided in Davies (1999).

Although Eq. (2.23) is expressed in terms of the number of electrons, $\tilde{N}$, it can equivalently be expressed in terms of units of electron charge or current by changing the units of the proportionality constant, k. For DC yields on conductors (refer to Section 3.2), it is more useful to express Eq. (2.23) in terms of the collected SE current as:

$$\frac{dI_c}{dE} = \frac{k}{E_0} \frac{E}{\left(E+\phi\right)^4}, \tag{2.24}$$

where I_c is the measured SE current to the collector (in our detector apparatus), and the units for k become $A \cdot eV^3$. For pulsed yields on insulators (refer to Section 3.3), Eq. (2.23) can be expressed in terms of SE charge as:

$$\frac{dQ_c}{dE} = \frac{k}{E_0} \frac{E}{\left(E + \phi\right)^4}, \tag{2.25}$$

where Q_c is the measured SE charge to the collector, and the definition of the material constant, k, has changed from Eq. (2.23) such that it has units of $C \cdot eV^3$. The Chung and Everhart model, as shown in Eq. (2.25), is used in the discussions below (Section 2.3.6) for calculating insulator surface potentials, and is also used in Sections 4.4 and 5.3.2 to fit pulsed insulator SE spectra.

The work function term, φ, in Eqs. (2.23) through (2.25) represents the energy required for a SE to escape from a material's surface. Since the measured SE energy distribution of both conductors and uncharged insulators are similar in shape, with the spectral magnitudes controlled by surface energy barriers (i.e., work function or electron affinity), it seems reasonable to extend the Chung and Everhart model to uncharged insulators by replacing the work function term with the insulator electron affinity, χ. In Section 5.3.2, this model is applied to uncharged insulator SE spectra, and the value of the electron affinity, χ, and material proportionality constant, k, are used to characterize the effects of prior electron irradiation on the emitted SE energy distribution. Finally, as a part of future studies at USU, it would be beneficial to perform a more rigorous review the previous works of Baroody (1950) and Quinn (1962) to determine if the Chung and Everhart model expressed by Eqs. (2.23) through (2.25) can appropriately be extended to insulators by simply replacing the work function term with the insulator electron affinity (refer to Section 6.2.2).

2.3.6 Relationships between Evolving Surface Potentials and Electron Emissions

As described in Sections 2.1 and 2.2, the polarity and magnitude of insulator charging is dependent on the incident electron energy. Between the total-yield crossover energies, E_1^{σ} and E_2^{σ}, the magnitude of insulator charging is positive (since the total yield is greater than one), and the insulator attains a steady-state surface potential of just a few volts (Reimer, 1985). This positive charging increases the insulator surface potential barrier by an amount: $\chi+qV_s$ (q is the fundamental charge and V_s is the surface potential), measured with respect to the bottom of the conduction band, thus filtering a significant portion of the SE energy spectrum by suppressing all but the more energetic SE's (Dennison, private communication; Zavyalov, private communication). Hence, the resulting total electron yield emitted from a positively charged specimen can be expressed as an integral of the uncharged spectrum (taken at the same incident energy) with the integration limits extending from the positive surface potential up to the incident beam energy (Reimer, 1985; Nickles *et al*., 2000). An illustration of this is provided in the top graph of Fig. 2.8, where it is shown that positive surface charging prohibits the escape of lower-energy SE's, thus suppressing the lower-energy portion of the SE spectrum (represented by the shaded area in the figure). Consequently, only the unshaded area of the electron energy spectrum (above qV_s) contributes to the charged electron yield. As explained below, this provides a method for calculating an insulator's positive surface potential by measuring the steady-state (charged) electron yield along with an accompanying electron spectrum at the same incident energy.

For pulsed insulator electron yields, the relationship between the total electron yield and positive surface potential can be expressed in terms of the uncharged electron energy

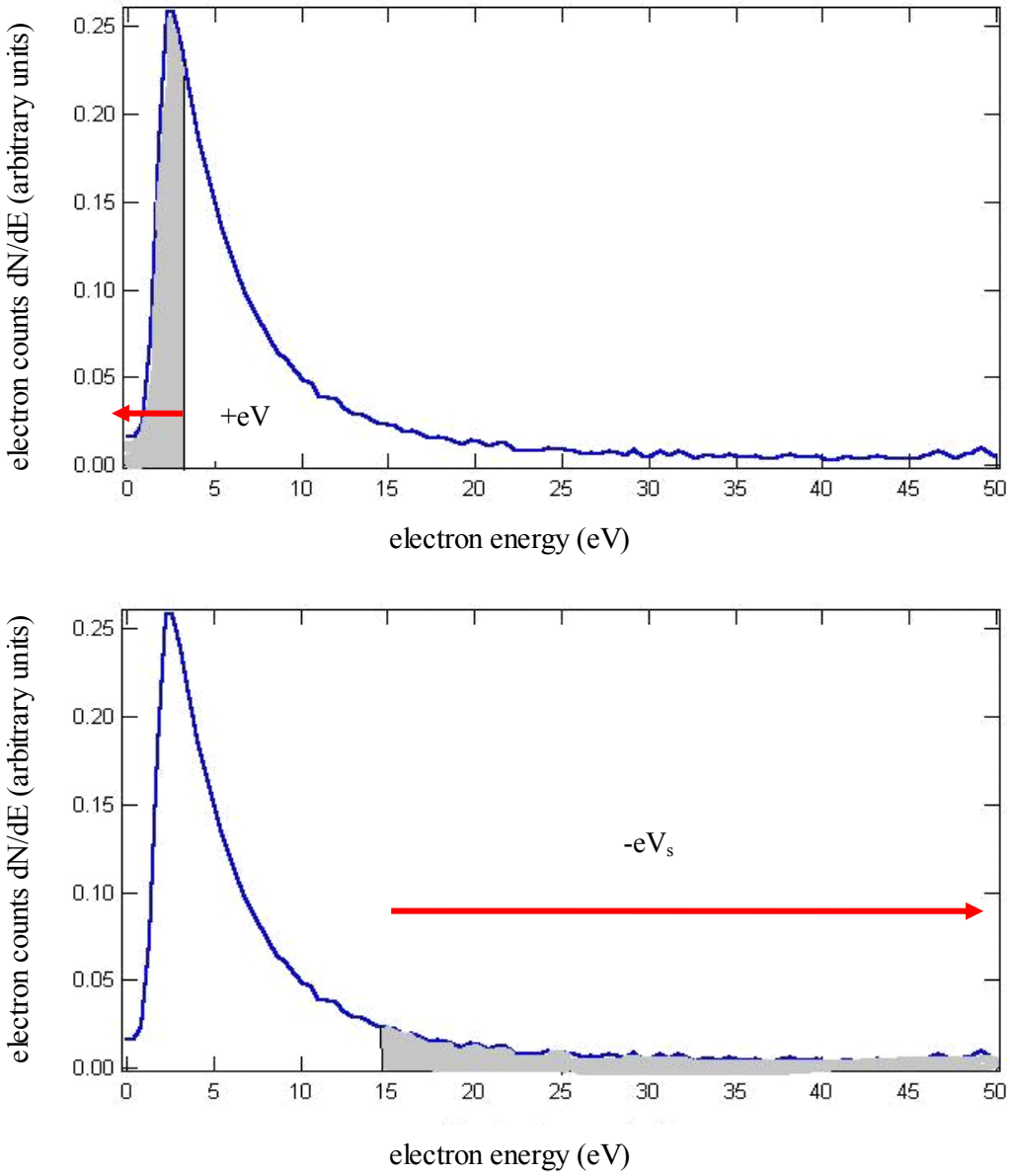

FIG. 2.8. Illustration of reduced SE spectra resulting from insulator surface potentials. (Top) Positive surface charging prohibits the escape of lower-energy SE's, thus suppressing the lower-energy portion of the SE spectrum (represented by the shaded area). (Bottom) Negative surface charging causes escaping SE' to gain kinetic energy, thus pushing the higher-energy portion of the SE spectrum to energies beyond 50 eV.

spectrum, Eq. (2.25), as:

$$\sigma_{ss} \approx 1 = \frac{1}{Q_0}\int_{qV_S}^{E_0} \frac{dQ_c}{dE} dE\,, \tag{2.26}$$

where σ_{ss} is the steady-state total yield (fully charged yield, close to unity), Q_0 is the incident electron charge/pulse, and Q_c is the SE charge (measured by the collector) (Nickles *et al*., 2000). The limits of integration in Eq. (2.26) range from the surface potential energy (only SE's and BSE's with energies greater than qV_s can escape) up to the incident electron energy (elastically or quasi-elastically scattered BSE's will have energies equal to or close to E_0). Finally, the approximate-equal sign in Eq. (2.26) stems from the fact that although the total yield should be equal to unity at steady state, in practice, this is not always the case due to such factors as radiation-induced conductivity and slowly evolving internal charge distributions resulting from continued electron irradiation.

In practice, the steady-state total yield can be measured with a continuous electron beam after allowing sufficient time to charge an insulator to a steady-state current condition. For example, data presented in Section 5.3.4 shows in the positive charging regime, a steady-state condition is achieved within 10 pC of incident charge. However, if the uncharged spectrum is also to be measured on an insulator, as in Eq. (2.26), it must be measured before the steady-state yields using a pulsed incident electron and flood gun neutralization source. The pulsed spectrum is taken prior to the steady-state yield to avoid severe charging effects induced by continued electron bombardment. Finally, as shown in Eq. (2.26), in order to relate the steady-state total yield to the spectrum, it is important to also record the total incident charge, Q_0, with pulsed spectral measurements. This is done by summing all pulsed current signals in the sample/detector apparatus (refer to Section 3.3).

Due to the limitations of most electron-yield measuring setups, it is not feasible to measure total-yield energy spectra up to the incident beam energy, E_0, since this requires

detectors with suppression grids and power supplies that can be biased up to several kilovolts, in a stepped fashion with resolution of <1 V. However, SE spectrum up to 50 eV can easily be measured (refer to Section 5.3.2). Furthermore, since only SE's contribute significantly to the evolution of insulator steady-state potentials in the positive charging regime (due to their low energies, they respond more readily to growing positive surface potentials), the uncharged SE energy spectrum can be equivalently related to the steady-state surface potential as:

$$\delta_{ss} = \frac{1}{Q_0}\int_{qVs}^{50eV} \frac{dQ_c}{dE}\,dE\,, \tag{2.27}$$

where δ_{ss} is the steady-state SE yield (Nickles, *et al*., 2000). Notice the primary difference between Eq. (2.27) and Eq. (2.26) is the upper integration limit, where for the SE yield of Eq. (2.27), the integration is only performed up to 50 eV, which is, by convention, the upper energy limit for the SE spectrum. Hence, Eq. (2.27) should provide a method for determining positive steady-state surface potentials for insulators by measuring the steady-state SE yields δ_{ss} along with the uncharged SE spectrum at a given incident energy (between E_1^{σ} and E_2^{σ}).

The steady-state SE yields are rather simple to measure using a continuous-source incident electron beam (refer to Sections 5.1 through 5.3). Measuring the uncharged SE spectra of insulators is more difficult, and requires a pulsed-incident electron source and neutralization capabilities (refer to Section 5.3.2). However, once uncharged SE spectra are obtained for different incident energies, the Chung and Everhart model, provided by Eq. (2.25), can be used to fit to the spectra, thus determining the material proportionality constant, k and the electron affinity, χ (φ is replaced by the electron affinity for uncharged insulators). Once a fitting function is obtained for the uncharged SE spectral data at different incident energies, it can then be inserted into Eq. (2.27), and the surface potential can be solved for by integration. The symbolic solution of Eqs. (2.25) and (2.27) results in the following polynomial equation:

$$\frac{3qV_s+\chi}{(qV_s+\chi)^3}=\frac{6Q_0E_0\delta_{ss}}{k}+b\,, \tag{2.28}$$

where b is a constant defined in terms of the electron affinity and SE upper integration limit of 50 eV as:

$$b=\frac{\chi+150eV}{\left(\chi+50eV\right)^3}. \tag{2.29}$$

It should also be noted that although Q_0 shows up in Eq. (2.28), the resulting steady-state potentials ultimately do not depend on the incident charge/pulse, since any changes in Q_0 are compensated for in the material constant, k (determined by integrating the uncharged spectrum).

Hence, by determining the positive real root for V_s in Eq. (2.28), the steady-state positive surface potential can be solved for in terms of the steady-state SE yield, incident charge, beam energy, and fitted spectral parameters, k and χ, for incident energies between E_1^{σ} and E_2^{σ}. The symbolic roots for V_s are not written out here due to their length. Instead, this technique is demonstrated in Fig. 2.9 by plotting the positive real solution for the surface potential as a function of the incident electron energy, E_0. For this plot, the incident charge was taken to be Q_0=220 fC, the proportionality constant was k=1.2·10^{-8} C·eV^3, and the electron affinity was χ=3.7 (values were taken from fitted spectral data at E_0=500 eV for Kapton™ from Section 5.3.2). The steady-state SE yields were assumed to remain constant with incident energy for $E_1^{\sigma}<E_0<E_2^{\sigma}$, which is a fair (but not perfect) assumption since the steady-state total yields remain close to unity, and the BSE yields remain fairly constant since they are not strongly affected by the small positive surface potentials that form in this energy regime (SE yields are calculated as the difference between total and BSE yields). However, this assumption is generally not valid for E_0<200 eV since the BSE yields begin to decrease, and surface potential approaches 0 V as the incident energy approaches E_1^{σ} (E_1^{σ}=20-100 eV

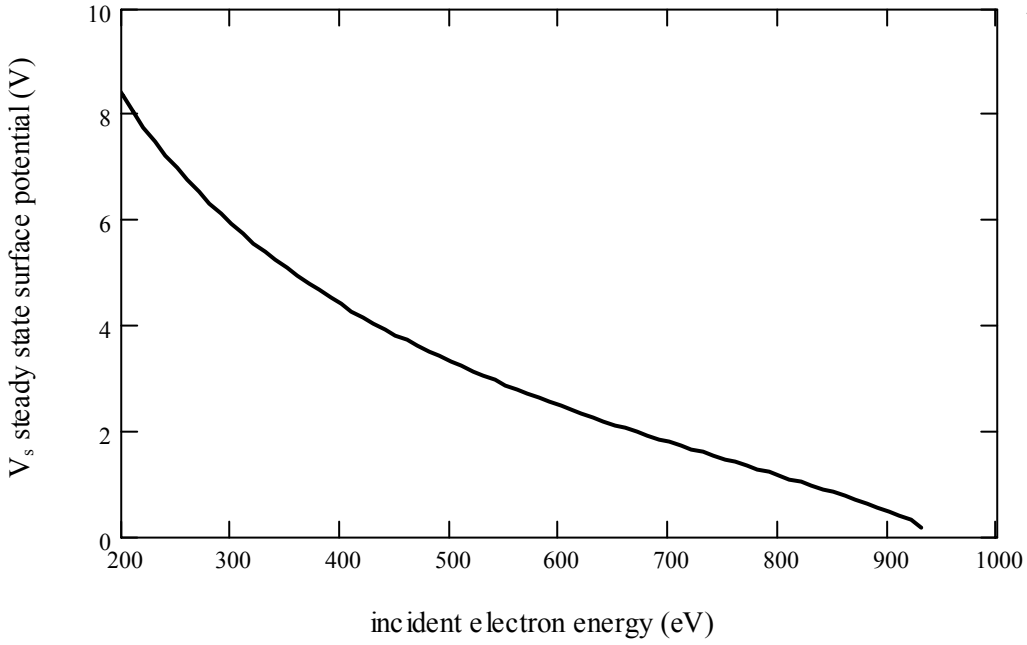

FIG. 2.9. An example of the steady-state positive surface potential plotted as a function of the incident electron energy for $E_1^{\sigma}<E_0<E_2^{\sigma}$. The curve was calculated from Eq. (2.28), using parameters obtained from Kapton™ from Section 5.3.2. The steady-state SE yield was assumed to remain constant with incident energy.

for most insulators). For this reason, the steady-state potential is not plotted below E_0=200 eV in Fig. 2.9. Furthermore, this assumption is not entirely accurate for higher incident energies, since as will be shown in Section 5.3.4, the steady-state SE yields display a slight dependence on incident energy for $E_1^{\sigma}<E_0<E_2^{\sigma}$. Nevertheless, this assumption is sufficient for this example. From Fig. 2.9, it can be seen that as the incident energy approaches E_2^{σ}, the positive surface potential approaches 0 V. This behavior agrees with experimental data, where it is observed that the steady-state potential transitions across zero near the crossover energies, and as will be demonstrated for Kapton™ in Section 5.3.4, E_2^{σ} occurs between E_0=900-1000 eV.

This method for calculating the steady-state positive surface potential for $E_1^{\sigma}<E_0<E_2^{\sigma}$ can be used in conjunction with other methods (such as monitoring shifts in the SE spectral peak, as discussed in Section 4.5) to study positive steady-state surface potentials as a function

of incident energy. It should be noted here, there was not sufficient time in this dissertation work to fully explore these methods experimentally. However, these studies have been proposed as future work at USU in Section 6.2.3.

A similar procedure to that presented above can also be used to monitor the dynamic charging behavior of insulators prior to reaching steady state for incident energies of $E_1^{\sigma}<E_0<E_2^{\sigma}$. As discussed later in this Section 2.3.9, and as demonstrated in Section 5.3.4, the total electron yields approach a value close to unity (SE yields approach a value below unity) as an insulator approaches steady state under a pulsed-incident electron beam. For incident energies between E_1^{σ} and E_2^{σ}, the total yields asymptotically decay from values greater than unity to values near unity as the insulator surface potential charges further positive. However, the BSE yields remain fairly constant as a function of incident energy, typically ranging from values of 0.2-0.5. Since the SE yields are calculated by subtracting the BSE from the total yields, they generally decay from an initial value greater than unity to a steady-state value below unity, ranging from 0.5-0.8, depending on the insulator (refer to Section 5.3.4 for data on decaying SE yields).

To determine the evolving surface potentials, the fractional change in evolving SE yields (at a given energy) are compared to the uncharged fractional SE spectrum area (taken at the same energy). These measurements require two data sets. First, the uncharged pulsed SE spectrum is measured using an alternating pulsed electron source and flood gun neutralization source to ensure the insulator remains uncharged (refer to Section 5.3.2). Then, after these measurements are made, the pulsed SE spectrum from 0-50 eV is fitted with the Chung and Everhart model, Eq. (2.25) to obtain model parameters k and χ. Second, by using a pulsed-yield setup (refer to Section 3.3), small bursts of incident electrons can be delivered to the sample (without intermittent neutralization) such that the charge decay behavior can be

monitored as a function of incident electron fluence (refer to Section 5.3.4). After these measurements are made, the fitted spectrum can then be used to determine the rising surface potentials corresponding to the declining SE yields as the insulator approaches steady state. This is done using the definition of the SE yields, as given in Eq. (2.27). Specifically, the ratio of the integrated partial spectrum versus the full spectrum (integration over different limits) is equated to the ratio of charged SE yield versus uncharged SE yield as follows:

$$\frac{\int_{qV_{si}}^{50eV} \frac{dQ_c}{dE} dE}{\int_{0}^{50eV} \frac{dQ_c}{dE} dE} = \frac{\delta_i}{\delta_0}, \tag{2.30}$$

where qV_{si} is the evolving surface potential corresponding to the i^{th} pulse, δ_i is the SE yield corresponding to the i^{th} pulse (calculated from $\delta_i=\sigma_i-\eta_i$), and δ_0 is the initial, uncharged SE yield value taken on the first pulse.

Similar to above, the surface potential can then be determined by solving for the positive real root of the integrated Chung and Everhart model from Eq. (2.25). The integrated polynomial expression for V_{si} from Eq. (2.30) becomes:

$$\frac{\chi+3qV_{si}}{(\chi+qV_{si})^3} = \frac{\delta_i}{\delta_0} \cdot \left[\frac{1}{\chi^2} - b \right] + b, \tag{2.31}$$

where b is defined by Eq (2.29). Notice the expression for the evolving surface potential in Eq. (2.31) is not dependent on the incident energy, E_0 or the material proportionality constant, k from the Chung and Everhart model. Instead, the surface potential depends only on the material electron affinity and fractional yield. This is consistent with the notion although the measured amplitude of the hot-electron (SE) energy distribution should be affected by E_0 (a higher incident energy allows for a greater number of electrons to be excited into the conduction band), the fractional number of escaping SE's should only be controlled by surface potential barriers (i.e., χ and qV_s). Hence, it follows from the Chung and Everhart model the

integrated SE spectrum is no longer needed to calculate the evolving positive surface potential as a function of electron fluence. Instead, one only needs to know the electron affinity of the insulator under study, and possess charge-decay data of the SE yields. Finally, it can be verified by substituting the definition of δ_0 into Eq. (2.31) (namely, the Chung and Everhart equation integrated from 0-50 eV) when the evolving SE yield approaches its steady-state value, δ_{ss}, the surface potential converges to the expression given by Eq. (2.28).

As was the case above, the symbolic solutions are not given here due to their length. Instead, Fig. 2.10 illustrates the real positive root as a function of the evolving fractional SE yield, δ_i/δ_0 (top graph). Also shown in Fig. 2.10 is the inverse solution of Eq. (2.31), where the fractional SE yield is plotted as a function of rising positive surface potential (bottom graph). For these plots, an electron affinity value of 3.7 eV (taken from Section 5.3) was used for the calculations. Both of these plots are useful for the following reasons: first, expressing the surface potential in terms of the evolving SE yield allows one to calculate the evolving surface potential from SE yield measurements (as is done in Section 5.3.4); second, expressing the fractional SE yield in terms of the surface potential allows one to determine the percentage of escaping SE's as a function of rising positive surface potentials.

As can be seen from the graph displaying $V_{si}(\delta_i/\delta_0)$, V_{si} is positive in polarity, and increases as the fractional SE yield decreases. This is consistent with observations, where the positive surface potential increases until the SE yield reaches its steady-state value. As can be seen from the graph displaying $\delta_i/\delta_0(V_{si})$, as the positive surface potential increases, the fractional escaping SE yield decreases, which is again consistent with experimental observation. Furthermore, the evolution of the SE yield is initially rapid as the surface potential increases, since the majority of SE's have energies <10 eV, and hence, positive surface potentials of only 10 V can suppress a vast majority of escaping SE's (~80 percent in

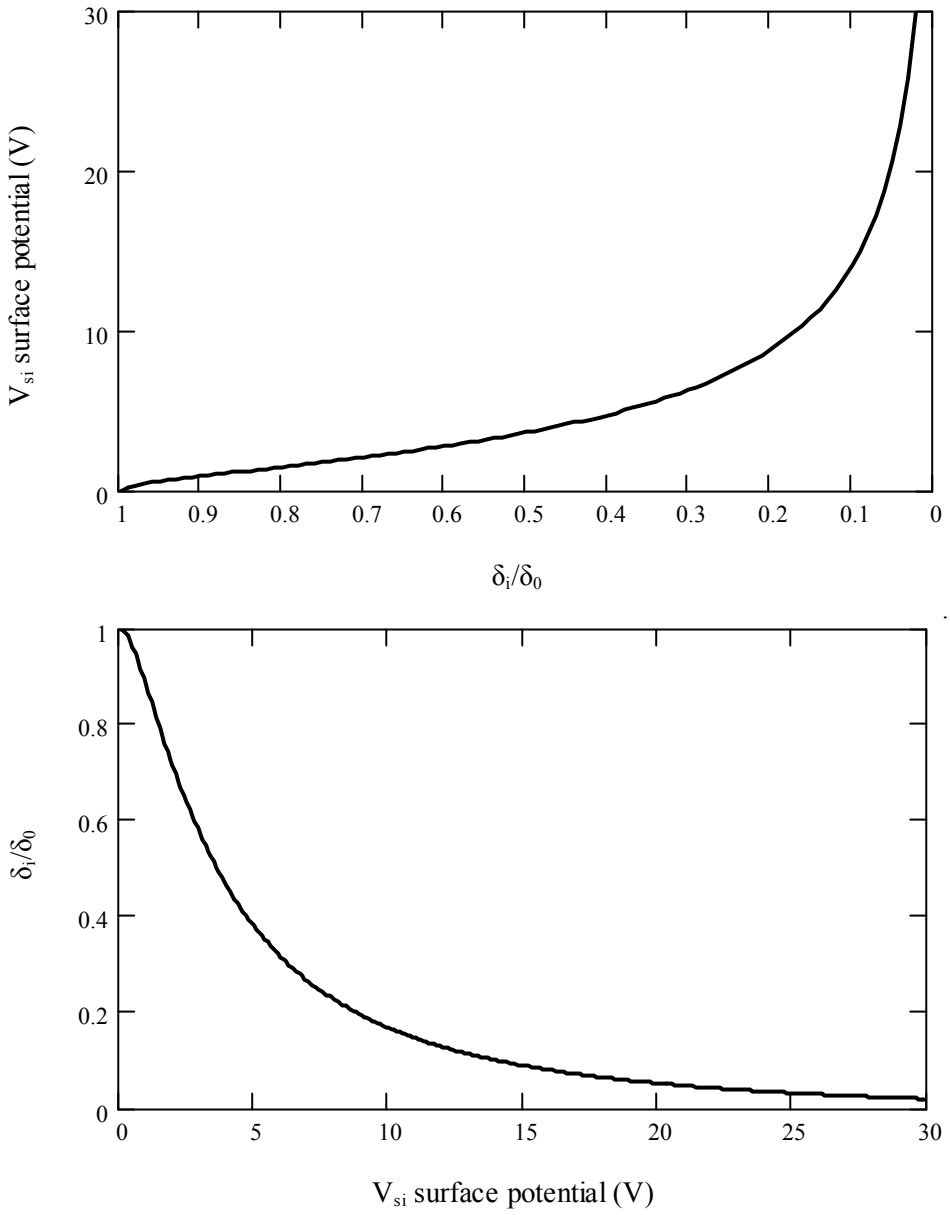

FIG. 2.10. An example of the relationship between the evolving positive surface potential and fractional SE yield for $E_1^{\sigma}<E_0<E_2^{\sigma}$. Plotted are the surface potential as a function of fractional SE yield (top), and the fractional SE yield as a function of positive surface potential (bottom). Curves are calculated using Eq. (2.31). Between the crossover energies, typical fractional SE yields for insulators approach values of 0.2-0.6, corresponding to positive surface potentials of 4-10 V.

this plot). In practice, typical fractional SE yields for insulators approach steady-state values of 0.2-0.6, such that typical positive surface potentials approach values ranging from 0-10 V (refer to Section 5.3.2 and 5.3.4 for further data). This method for determining V_{si} is demonstrated further on a Kapton^{TM} sample in Section 5.3.4, where the evolving surface potential is studied along with the evolving total and SE yields as a function of incident electron fluence and energy.

In the above discussions, only the effects of positive surface charging on electron yields for incident energies $E_1^{\sigma}<E_0<E_2^{\sigma}$ have been addressed. It is also necessary to study the effects of negative surface charging on total, SE, and BSE yields for higher incident energies, $E_0>E_2^{\sigma}$. For these incident energies, there are two main charging regimes that affect the electron yields. First, there is a fast charging regime that occurs at relatively low levels of incident electron irradiation, well before the insulator has reached its steady-state condition. In this regime, the insulator charges negatively (since for $E_0>E_2^{\sigma}$, the total yield is less than unity) to potentials that may significantly affect the escape energies of SE's (e.g., V_s=0 V to -50 V), but do not significantly affect the landing energies of incident electrons ($E_0-|qV_s|$) sufficient to alter the total yields. Hence, the relative magnitudes of the SE and BSE yields are changed, but the total yields are not. Specifically, the BSE yield magnitudes are increased such that they approach the total yield magnitudes, and the SE yields are diminished towards zero. This charging regime is particularly relevant for pulsed yields on insulators since each incident pulse (~10^{-13} C) will induce negative surface potentials with magnitudes on the order of 0.1-1 V (refer to Section 5.3.4). Hence, after 100 pulses, negative surface potentials can range from 10-100 V. Although in most cases these potentials will not affect the total yields significantly, they are sufficient to significantly alter the escape energies of SE's. Because the

changes to the SE and BSE yields are rapid, this negative charging mechanism has been termed the fast negative charging mechanism throughout this dissertation.

This fast negative charging mechanism occurs because the rising negative surface potentials that develop under small incident electron doses are sufficient to accelerate escaping SE's to energies >50 eV, and hence, despite their origin, are registered as BSE's by electron yield detection systems (since 50 eV is, by convention, the measurement energy cutoff between SE's and BSE's). This effect is illustrated qualitatively in the bottom graph of Fig. 2.8, where it can be seen from the SE energy distribution as the negative surface potential grows in magnitude, the SE energy distribution is slowly pushed to the right to higher escape energies. As can be seen from the figure, after a few volts of negative charge, relatively few SE's have been accelerated to energies >50 eV. However, near V_s=-50 V, the entire SE population has been accelerated beyond 50 eV such that the measured SE yield becomes zero, and all electrons are detected as BSE's. At this point, the measured BSE yield magnitude becomes equal to the total yield magnitude. Incidentally, this effect was unexpectedly observed while measuring Kapton™ yield data, as discussed later in Section 5.3.2. Further efforts at USU will concentrate on developing UV neutralization techniques capable of neutralizing negative charging for $E_0>E_2^{\sigma}$. Once we have developed such neutralization techniques, we will be able to measure accurate SE and BSE yields beyond E_2^{σ}, and eliminate the effects of this fast charging mechanism.

The effects of the fast charging phenomenon on the evolving SE yields (prior to steady state) can be expressed mathematically in a manner similar to the expressions given above for positive charging, in terms of the fractional evolving SE yield as:

$$\frac{\int_0^{50eV-|qV_{si}|}\frac{dQ_c}{dE}dE}{\int_0^{50eV}\frac{dQ_c}{dE}dE}=\frac{\delta_i}{\delta_0}, \tag{2.32}$$

where the integral in the numerator represents the right-shifting SE spectrum induced by the rising negative surface potential, V_{si}. The integral in the denominator represents the full uncharged SE spectrum. The ratio of these integrated spectra is equal to the ratio of the charging SE yield versus the uncharged (initial) SE yield value, or the fractional number of SE's with energies <50 eV. From the arguments provided above, one would expect the fractional SE yield to approach zero as the surface potential approaches -50 V.

The solution for the evolving negative surface potential, in terms of the fractional SE yield, can be found by integrating Eq. (2.32) to obtain the following third order polynomial:

$$\frac{\chi+150\text{eV}-3\left|qV_{si}\right|}{\left(50eV+\chi-\left|qV_{si}\right|\right)^{3}}=\frac{\delta_i}{\delta_0}\cdot\left[b-\frac{1}{\chi^2}\right]+\frac{1}{\chi^2}, \tag{2.33}$$

where b is defined by Eq. (2.29). Fig. 2.11 illustrates the negative real surface potential solution to Eq. (2.33). Also, shown in Fig. 2.11 is the inverse solution to Eq. (2.33), where the fractional SE yield is plotted as a function of the magnitude of the negative surface potential. As with the analysis presented above for positive charging, a hypothetical electron affinity value of 3.7 eV (taken from Section 5.3) was used in the calculations.

From the figure displaying $V_{si}(\delta_i/\delta_0)$, it can be seen the magnitude of the negative surface potential starts at zero, but slowly increases to 50 V as the fractional SE yield decreases towards zero (or as SE's are measured as BSE's by the detector). From the figure displaying $\delta_i/\delta_0(V_{si})$, it is observed that the fractional SE yield approaches zero as the magnitude of the negative surface potential approaches 50 V. The evolution of the SE yield is at first slow, as the tail end of the SE spectrum is pushed to energies >50 eV, but then changes rapidly as the negative surface potential magnitude approaches 50 V. This behavior is consistent with the spectral diagram displayed in Fig. 2.8, where one would expect the change in the measured SE yields to be most dramatic when the SE spectral peak (occurring near 2

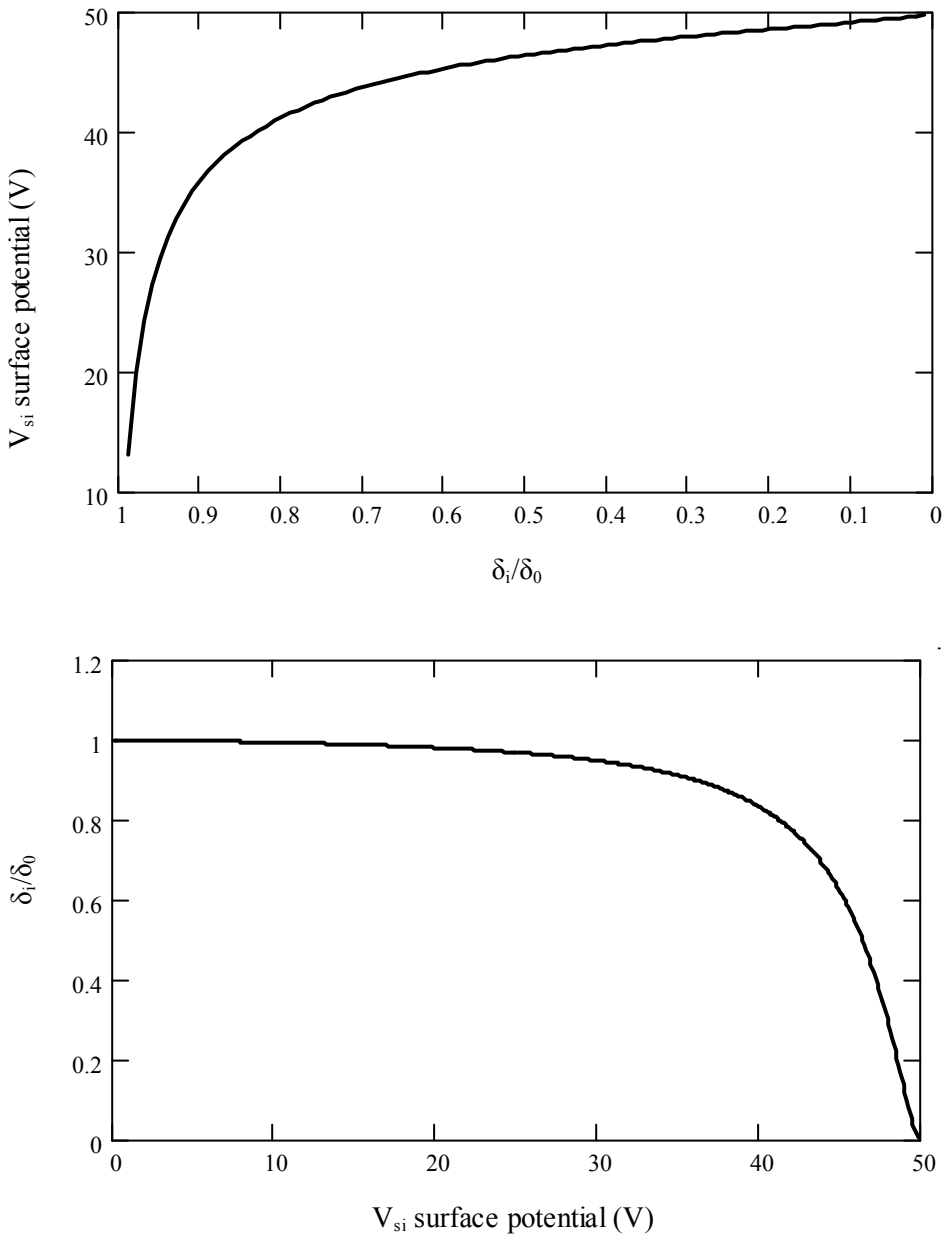

FIG. 2.11. An example of the relationship between the evolving fractional SE yield and fast negative surface potential for $E_0>E_2^{\sigma}$. Plotted are the surface potential magnitudes as a function of fractional SE yield (top) for negative charging, and the fractional SE yields as a function of surface potential magnitude (bottom). Curves are calculated using Eq. (2.33). Typical fractional SE yields for insulators approached 0 as the negative surface potential approached 50 V.

eV) is pushed towards 50 eV by a surface potential near -50 V. This behavior is also consistent with data presented in Section 5.3.2, where measured SE yields approached zero and measured BSE yield magnitudes approached values corresponding to the total yield magnitudes for $E_0>E_2^{\sigma}$.

As mentioned above, there exists a second negative charging regime that also occurs at incident electron energies of $E_0>E_2^{\sigma}$, and is referred to in this dissertation as the slow charging regime. This charging regime occurs under continued electron bombardment at negative surface potentials exceeds 50 V in magnitude (such that the SE yield has already decayed to zero, resulting from the fast charging scenario described above), and the measured BSE yield is equal to the total electron yield. As the insulator is further irradiated by electrons, and as the surface potential continues to grow, the landing energies of incident electrons are diminished by the retarding field of the insulator from initial values of E_0 delivered by the electron source to less energetic values, E_L by the time they reach the insulator. As the electrons continue to impinge on the insulator with lessened kinetic energy, the total yields slowly increase from values less than unity towards values approaching unity (Reimer, 1985). The negative insulator surface potential also continues to grow in magnitude until the insulator either undergoes dielectric breakdown, or until the landing energies of the incident electrons reach a value equal to the second crossover energy, $E_L=E_2^{\sigma}$. At this point, an ideal insulator (with zero leakage current) will have reached its steady-state potential where no net current enters or leaves the insulator, and the total yield is unity. This charging regime is termed slow since it may require a significant amount of incident electron irradiation (in terms of a pulsed doses) for this steady-state condition to be reached. For example, consider an ideal insulator with a typical crossover energy of $E_2^{\sigma}=2$ keV that is irradiated by an incident electron source of $E_0=12$ keV. Provided the insulator does not undergo dielectric breakdown

first, the charged surface potential required to achieve steady-state condition would be V_s=-10 kV. If each incident pulse altered the surface potential by only -0.1 V, it would take ~100,000 pulses (a total of ~10^{-8} C) to fully charge the insulator. Hence, in terms of our pulsed-yield setup, this process is indeed very slow. However, for a continuous incident electron source of 10 nA (typical of our DC setup as described in Section 3.2), the steady-state potential would be reached in approximately 1 s.

For ideal insulators, Reimer (1985) has expressed the negative surface potential resulting from this slow charging mechanism in terms of the incident electron landing energy, E_L, and the incident beam energy, E_0. This expression has been termed the total yield equation, and is given as follows:

$$E_L = E_0 - \left| qV_s \right|, \tag{2.34}$$

where q is the fundamental electron charge, and V_s is the negative surface potential. Using Eq. (2.34), the evolving negative surface potential can be determined using a technique set forth by Reimer (1985). This technique takes advantage of the fact that the incident electron landing energy, E_L, will continue to decrease as the sample is charged further negative, and if the landing energy can be determined, the surface potential can then be calculated using Eq. (2.34). This landing energy can be ascertained indirectly by monitoring the rise in the total yield values with continued negative charging, and then by determining the landing energies corresponding to the rising total yields from the total yield curve (refer, for example, to Sections 5.3.2 and 5.3.4). However, to use this technique, the accuracy in the total yield values must be very good since even small changes in the yields due to charging, systematic errors, or random uncertainties can equate to large changes in the corresponding landing energies determined from the total yield curve (refer to Section 5.3.4 for further details). In a like manner, Eq. (2.34) can also be used to determine the total yield second crossover energy,

E_2^{σ}, since the steady-state surface potential (indicated by a total yield of unity) can be expressed in terms of Eq. (2.34) by setting $E_L=E_2^{\sigma}$. This relationship is used later in Sections 4.6 and 5.2 as a method for determining E_2^{σ} for insulators.

In practice, the relationship expressed in Eq. (2.34) with $E_L=E_2^{\sigma}$ does not always correspond to the steady-state condition, since all insulators exhibit a finite resistance that alters the steady-state surface potential in response to an incident electron beam (Reimer, 1985). The effective resistance of all insulators will decrease due to the radiation induced conductivity (RIC). RIC induced by a continuous incident electron beam can be approximated by the empirical expression:

$$\gamma = \gamma_0 \left(\frac{10^8 J_0 E_0}{Rs} \right)^{\Delta}, \tag{2.35}$$

where γ_0 can be taken as the innate conductivity, J_0 is the incident current density in A/cm^2, R is the incident electron penetration depth in units of centimeters [see Eq. (2.12)], s is the material density in g/cm^3, and Δ is a material-dependent power coefficient that ranges between 0.5-1 (Nunes de Oliveira and Gross, 1975). This finite resistance acts to lower the measured surface potential, and hence increases the steady-state landing energy to a value above E_2^{σ} as calculated by Eq. (2.34) (Reimer, 1985). Also, the leakage currents due to RIC will act to lower the steady-state total yield to a value below unity as given by (Reimer, 1985):

$$\sigma_{ss} = 1 - \frac{E_0 - E_L}{eI_0\gamma}, \tag{2.36}$$

where I_0 is the incident electron current.

Despite the apparent simplicity of Eq. (2.34) for predicting steady-state negative surface potentials in the slow negative charging regime, several other anomalous experimental results have been reported that cannot be explained by the total yield equation charging model given above. For example, often the polarity and magnitude of the steady-state surface

potential measurements under a continuous electron beam do not correspond to values predicted by the total yield approach of Eqs. (2.34) (Melchinger and Hofmann, 1995). Additionally, E_2^{σ} values as determined by Eq. (2.34) change with current density and radiation time (see Sections 5.2 and 5.3.2) (Cazaux, 1999; Jbara *et al.,* 2001). Jbara *et al.* (2001) reported that measured E_2^{σ} values drifted from 3.5 keV to 2.5 keV when the incident current (DC source) was increased from 1 nA to 10 nA on MgO, while the incident beam energy was kept constant at E_0=20 keV. According to the authors, this lowering of E_2^{σ} was attributed to alterations of the MgO material properties by the creation of additional electron traps (and the enhanced ability to retain electron charge) generated by the increased electron irradiation (Jbara *et al*., 2001). Consequently, although the total yield model presented in Eq. (2.34) can provide a good approximation for E_2^{σ} for highly-insulating dielectrics, additional influences such as radiation-induced conductivity and material micro-structural alterations caused by continuous incident electron irradiation can alter the measured electron emission properties.

In summary, the relationships between insulator surface potentials and escaping electrons fall under two general charging regimes: positive charging for incident energies between the crossovers, $E_1^{\sigma}<E_0<E_2^{\sigma}$, and negative charging for incident energies, $E_0>E_2^{\sigma}$ (incidentally, negative charging also occurs at incident energies, $E_0<E_1^{\sigma}$, but this case has not been treated here). Within both these charging regimes, methods have been shown for determining both the evolving and steady-state surface potentials based on the SE spectral and SE yield data. Both the steady-state and non-steady-state (pulsed) methods described above provide noncontacting probing methods that can be used to study both positive and negative sample surface potentials in various incident energy regimes, and with sensitivity that may not be attainable using other methods such as commercial noncontacting potential probes (Swaminathan, 2004; Swaminathan *et al*., 2003; Dennison *et al*., 2003a). Furthermore, the

steady-state methods described above can also be compared to other noncontacting electron beam methods for determining positive and negative surface potentials as described further in Sections 4.5, 4.6, and 6.2. Finally, the pulsed method described above, combined with studies of the evolving electron yield and sample displacement current (described below in Section 2.3.9), provide methods for studying the dynamic charging behavior of insulator materials as a function of incident electron irradiation, prior to reaching a steady-state condition. These methods are used further to evaluate the dynamic charging behavior of Kapton^{TM} under pulsed incident electron bombardment in Section 5.3.4.

2.3.7 Electron Radiation Induced Charge Distributions in Insulators

Previous studies of insulators have shown the internal charge distributions (both evolving distributions, as well as static charge distributions), resulting from incident electron irradiation, form multiple alternating positive and negative charge layers (Meyza *et al*., 2003; Melchinger and Hofmann, 1995; Cazaux, 1999; Cazaux *et al*., 1991; Miyake *et al*., 2003; Osawa *et al*., 2003; Usui *et al*., 2003; Frederickson and Brautigam, 2003; Frederickson *et al*., 2003; Frederickson and Dennison, 2003). The spatial and charge-polarity configurations of these layers can depend on a number of factors that includes the magnitude of electron yield, electron yield crossover energies (particularly E_2^{σ}), material resistivity (both innate and radiation-induced conductivity), dielectric strength, electron trapping and detrapping rates, incident electron penetration depths, mean SE escape depths, and incident electron fluxes and energies. Not until recently have quantitative methods been developed to simulate and measure internal charge distributions as a function of the material and environmental variables described above (Meyza *et al*., 2003; Miyake *et al*., 2003; Osawa *et al*., 2003; Usui *et al*., 2003; Frederickson and Brautigam, 2003; Frederickson *et al*., 2003; Frederickson and

Dennison, 2003). Nevertheless, qualitative (and to some extent, quantitative) assessments of the internal charging trends, common to most insulators, can be estimated based on knowledge of incident and SE electron energies, energy-dependent travel depths, and insulator surface potentials.

As has been shown in Figs. 2.4 and 2.7, the incident electron penetration range, as well as the mean SE escape depths, can be calculated for insulators, leading to approximations for the regions where insulators will accumulate positive or negative charge distributions. For example, for an insulator (previously uncharged) that is first exposed to incident electron irradiation, one would expect an SE depletion region to occur between the insulator surface and the SE travel depth, λ_{SE} (10-50 nm into the material), since, regardless of the incident electron energies and penetration depths, SE's that are excited near the surface will be able to escape. For SE's created farther into the material ($>\lambda_{SE}$) where they cannot escape, just as many excited SE's will travel towards the surface as will travel further into the material (in the absence of internal electric fields). Furthermore, one would expect an incident electron deposition region to occur somewhere between the surface and the maximum incident penetration depth, R (10 nm to >1 μm depending on the incident energy). The net charge in these regions will ultimately depend on the number of electron vacancies versus trapped electrons that will in turn depend on, among other things, incident electron energy, material SE travel depth, λ_{SE}, and the maximum incident electron penetration depth, R. Provided below are four charging scenarios that give a qualitative sketch of a few of the complex charge distributions that can develop in insulators based on incident electron energy considerations, incident electron and SE travel lengths, and resulting internal electric fields and surface potentials.

Scenario I: Single Positive Charge Distribution for Total Yield σ>1: Here, the incident electron beam is between the crossover energies, $E_1^{\sigma}<E_0< E_2^{\sigma}$, such that the total yield is σ>1, and the incident electron penetration depth is on the order of the SE travel length $R\sim\lambda_{SE}$. From Figs. 2.4 and 2.7, it can be seen that the approximate relevant energy regime for this scenario is $E_0<1$ keV, where both the incident electron penetration depth and SE travel length are <100 nm. Since the incident electron deposition region and the SE travel lengths coincide, a single net positive charge distribution is formed (since σ>1) at depths ranging from the insulator surface to ~100 nm. The magnitude of this positive charge layer is on the order of $Q_{net}=Q_0(\sigma-1)$, where Q_0 is the incident charge.

Even if the incident electron penetration range were to exceed the SE travel length in the positively charging regime $E_1^{\sigma}<E_0< E_2^{\sigma}$ (for example, for insulator with crossover energies ranging from 1-5 keV), the above charging scenario could still be achieved. This would occur if the trapped electron/hole mobility were increased through enhanced radiation-induced conductivity and/or by high internal electric fields ($>10^6$ V/m) between the oppositely charged layers. For example, for a beam radius much greater than the incident electron penetration depth, $R_{beam}>>R$ or SE escape length, $R_{beam}>>\lambda_{SE}$ (such that edge effects can be excluded), the magnitude of the internal electric field, F, resulting from the net charge (positive in this case) deposited in the sample under pulsed electron irradiation can be approximated as follows:

$$F_N \approx \frac{\sum_{i=1}^{N} Q_{0i}\left(\sigma_i - 1\right)}{A_0 \varepsilon_0 \varepsilon_r}, \tag{2.37}$$

where Q_{0i}/A_0 is the incident charge density delivered on the ith pulse (typical incident charge doses for our pulsed setup are $\sim10^{-13}$ C/mm^2 per pulse), σ_i is the total yield value on the ith pulse (total yields will decrease due to positive charging as discussed below in

Section 2.3.9), and the summation accounts for the growing charge distribution with each incident pulse. Based on Eq. (2.37), for a typical insulator with an initial total yield of $\sigma>2$ (refer to Chapter 5 for insulator total yield values), the internal electric field could exceed magnitudes of 10^6 V/m after ~100 pulses. Hence, two opposing charge distribution layers, comprised of a positively charged SE depletion region and negatively charged incident electron deposition region, could readily recombine under these electric field magnitudes, even without the assistance of radiation-induced conductivity.

Scenario II: Double Positive/Negative Charge Distribution for Total Yield $\sigma>1$: Here, the incident electron beam energy is between the crossover energies, $E_1^{\sigma}<E_0< E_2^{\sigma}$ such that the total yield is again $\sigma>1$. However, for this case it is assumed the incident electron penetration depth is sufficiently greater than the SE travel length, $R>\lambda_{SE}$, or that internal electric fields are not strong enough to result in recombination of the positively and negatively charged layers. Hence, a double charge distribution (positive-negative) is formed where the positively charged region, from SE depletion, occurs between the surface and λ_{SE}, and a negatively charged region, from embedded incident electrons, occurs between the surface and R. This scenario also assumes field-assisted radiation-induced conductivity does not cause the separate distributions to diffuse into one (at least on the time scales of the experiment). For this charging scenario, the simple Dynamic Double Layer Model (DDLM) has been presented in the literature (Cazaux, 1986, 1999; Melchinger and Hofmann, 1995) to predict ensuing internal electric fields and potentials. Cazaux (1999) provides an approximate solution for the change in insulator surface potential as a function of the incident charge, Q_0, total yield ,σ, sample thickness, d, electron irradiation area, A_0, and SE and incident electron travel depths as:

$$V_s = \frac{Q_0(\sigma-1)d}{\varepsilon_0\varepsilon_r A_0} - \frac{\sigma Q_0\lambda_{SE} + Q_0 R}{2\varepsilon_0\varepsilon_r A_0}, \tag{2.38}$$

where in deriving this expression, it has been assumed the electron beam radius, R_{beam} is much greater than d, R and λ_{SE} (for these studies, R_{beam} was on the order of 0.5 mm, whereas insulator thicknesses ranged from 1-50 μm, as given in Chapter 5). Furthermore, from Eq. (2.38), it can be seen the first term dominates if the insulator thickness, d, is much greater than R or λ_{SE} (R generally did not exceed ~1 μm for the incident energy regimes of this dissertation, as shown in Fig. 2.4). For example, for a typical incident energy of E_0=1 keV, the magnitude of the positive surface potential of an insulator with a thickness of 10 μm would only be further diminished by ~10% by including the second term in Eq. (2.38), as apposed to only using the first term. For these reasons, it is often appropriate in our studies at USU to neglect the second term in Eq. (2.38), since most insulators we study have thicknesses >10 μm (refer to Sections 5.2-5.3), such that Eq. (2.38) can be further simplified to:

$$V_s \approx \frac{Q_0(\sigma-1)d}{\varepsilon_0\varepsilon_r A_0}. \tag{2.39}$$

Finally, it should be noted Eqs. (2.38) and (2.39) are equally as valid for approximating the change in surface potential of negatively charged insulators for σ<1, since as σ decreases below unity, the surface potentials becomes negative. The results for the evolving surface potential as a function of incident charge, determined using Eq. (2.39) along with Eq. (2.31), are further evaluated below in Section 2.3.9.

Scenario III: Additional Negative Surface Charge Layer for Total Yield σ>1: In practice, an additional negative charge layer would be expected to form at the insulator surface for *Scenarios I* and *II* given above. This negative surface layer would be comprised of SE's that would be unable to escape the positive surface potential barrier resulting from the insulator having σ>1 (Cazaux *et al*., 1991). The returning SE's that contribute to this negative surface layer are responsible for the relatively low positive

steady-state surface potentials (ranging from 1-10 V), which form under positive charging conditions between the crossover energies (refer to Section 2.3.9 below). This additional charge layer at the surface is further contributed to if the sample is flooded with low-energy electrons (from a flood gun as described in Section 3.5), which are used to neutralize the net positive potential at the surface. The thickness of the additional charge layer is determined by the penetration depth of the returning electrons. The penetration depth of such electrons with <10 eV energy is <50 nm as illustrated in Fig. 2.7; however, this depth may be lengthened by high internal electric fields just beneath the surface. Given this additional layer, the electric fields can still remain high inside the insulator. However, this additional negatively charged layer opposes the electric fields emanating from the SE depletion region, such that the electric field is weak (or negligible if the insulator has been neutralized using an electron flood gun) beyond the insulator surface into the vacuum.

Thus, even if the surface potential measured 0 V, strong internal electric fields could still exist below the surface, and act to accelerate penetrating electrons and retard further SE transport towards the surface (electric field lines point from the SE depletion layer towards the surface). This scenario is relevant to pulsed-yield measurements, where one might expect the maximum yields of the insulator to be diminished with repeated electron exposure, even after the surface has been neutralized with an electron flooding source. Another possible outcome of repeated electron irradiation and flood-gun neutralization is that the electron-rich layer at the surface causes subsequent SE excitation and escape to occur primarily near the surface, and not from further within the material, thus diminishing the material dependence of total electron emission behavior. If this were the case, this would cause the SE energy distribution to spread to higher energies since

SE's excited near the surface would not undergo as many energy-loss scattering events before escaping. Clearly, from these qualitative arguments, it is difficult to predict the effects that these charge distributions would have on electron emission behavior. However, key measurements to test these scenarios would be to monitor the behavior of SE yields as a function repeated electron irradiation, particularly after the surface potential has been neutralized with an electron-flooding source (refer to Section 5.3.2).

Scenario IV: Double Positive and Negative Charge Distribution for Yield $\sigma<1$: Here, the incident electron beam is beyond, $E_0>E_2^{\sigma}$ such that $\sigma<1$, and the incident electron penetration depth is greater than the SE travel length, $R>\lambda_{SE}$ such that charge-distribution recombination does not occur (if it does, a single net negative charge distribution evolves, similar to *Scenario I* above). Hence, a double charge distribution (positive-negative) forms, similar to *Scenario II* above. A positive charge layer occurs down to a depth λ_{SE} from SE depletion, and a negative charge region occurs down to a depth R from embedded incident electrons. However, a large number of SE's are created too deep within the material to escape (thus, $\sigma<1$) such that the magnitude of the negative charge region exceeds the positive charge region, and the resulting net surface potential is negative. Also for this scenario, the maximum incident electron penetration depth, R, can greatly exceed λ_{SE}, reaching maximum depths >1 μm. Here, the DDLM (Cazaux, 1999, 1986; Melchinger and Hofmann, 1995) provides a representative model for calculating the internal electric fields. Additionally, Eqs. (2.38) and (2.39) give an adequate estimate for determining the negative surface potential as a function of incident charge, provided the limiting assumptions of the equations are met (see discussion above).

For this scenario, at $E_0>E_2^{\sigma}$ the magnitude of the surface potential is not self regulated as was the case for $E_0<E_2^{\sigma}$ for *Scenarios I-III*. Hence, the net negative charge

distribution will continue to grow as a function of incident electron irradiation either until the insulator undergoes dielectric breakdown, or until the steady-state condition is met (where $E_L=E_2^{\sigma}$ as described as the slow negative charging mechanism above in Section 2.3.6). However, prior to arriving at a steady-state condition (or even after arriving at a steady-state condition), the relative depths of the internal charge distributions can change. For example, as the insulator approaches steady state, internal electric fields can become sufficiently high ($>10^5$ V/m) such that they retard the penetration of subsequent incident electrons, thus pushing the peak of the deposited incident electron negative charge region closer to the surface (Meyza *et al*., 2003). This also restricts the region for subsequent SE generation closer to the surface, and establishes an accelerating electric field that assist SE's diffusing towards the surface, thus altering the escape probabilities and energies of SE's. If the electric field between the negative internal charge distribution and insulator surface becomes sufficient, dielectric breakdown may initiate towards the vacuum. Levy (private communication) has reported observing the arcing of insulators from the bulk into the vacuum after irradiating the insulator with >20 keV electrons. Also, the effects of permanent damage resulting from the collapse of internal charge distributions towards the surface have been observed using SEM imaging (Song *et al*., 1996).

Figure 2.12 shows qualitative diagrams of the four charging configurations presented above. Although these qualitative scenarios provide a rough guide for estimating internal charging as a function of energy, further computational analysis and experimentation are required to more accurately predict the relationships between internal charge distributions and resulting surface potentials and electron yields. Additionally, as was described in the above scenarios, as charge layers build up inside the insulator, the dynamics between electron penetration and SE emission become more complicated as strong internal electric fields begin

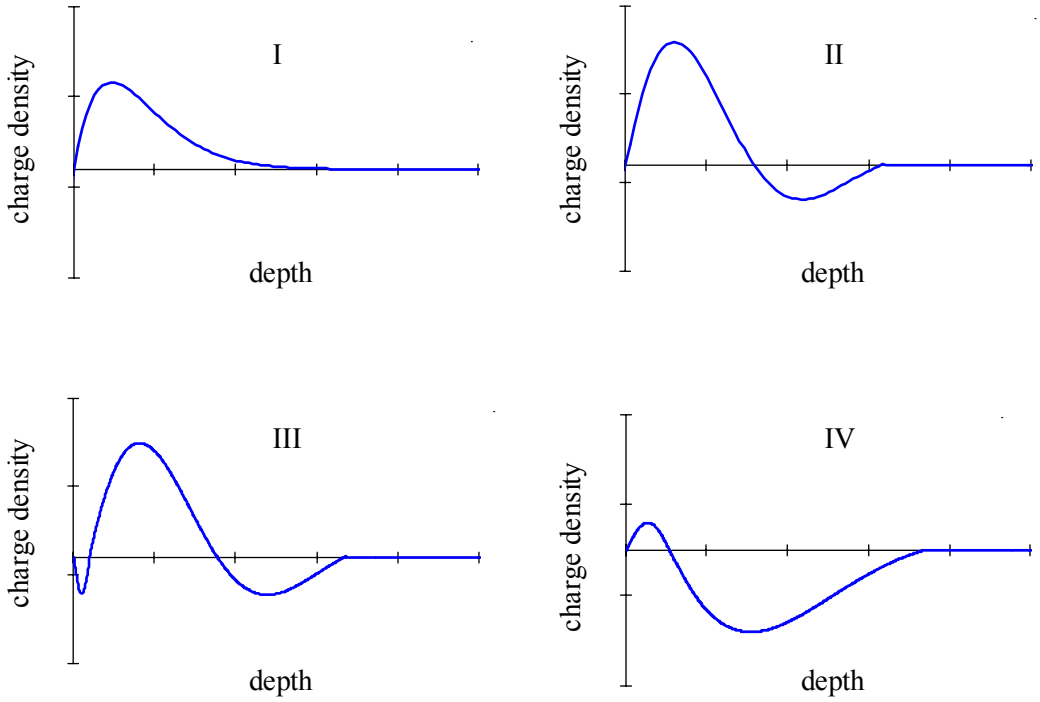

FIG. 2.12. Qualitative diagrams of the positive and negative internal charge distributions as a function of depth. Shown are (top left) positive charging Scenario I, (top right) positive charging Scenario II, (bottom left) positive charging Scenario III, and (bottom right) negative charging Scenario IV.

to alter incident electron trajectories, charge population diffusion behavior, field and radiation assisted conductivities, and SE transport and escape. Additionally, field induced dielectric breakdown, towards the surface or substrate, can further alter electron yields, surface potentials, and internal charge distributions. These alterations continue even after the insulator has reached a steady-state situation under continued incident electron irradiation (Meyza *et al*., 2003).

Finally, the charging scenarios presented above have been developed in the absence of any external conducting surfaces or applied electric fields. For the measurements made at Utah State, external electric fields are provided by the suppression and inner grid of our

detector apparatus that can further add to the complexity of ensuing insulator surface and bulk charge distributions (Meyza *et al*., 2003). For example, as explained in more detail in Section 4.5, by providing a positive potential to the detector grids surrounding the sample, SE's trapped on the insulator surface can overcome positive surface potential barriers, and escape. Additionally, although a small effect, the surrounding electric field from a positive conductor can act to effectively decrease the surface electron affinity of uncharged insulators, thus lowering surface potential barriers for escaping SE's (Boutboul *et al*., 1999; Cazaux, 1999).

Hence, incident electron currents and energies, sample history, and external electric fields can all affect internal charge distributions (and fields), in turn, altering incident electron penetration depths, as well as SE transport and escape. These internal charge distributions can take several days to months to fully discharge, and the insulator's material and electronic structure may be permanently altered, thus changing electron emission properties. Presently, only a few computational and theoretical studies have been developed to begin to address the dynamic charging problems related to internal charging, evolving surface potentials, external applied electric fields, and electron emissions (Meyza *et al*., 2003; Frederickson and Brautigam, 2003; Frederickson *et al*., 2003; Frederickson and Dennison, 2003; Kotera and Suga, 1988; Song *et al*., 1996). None, so far, have incorporated the effects of material degradation evoked by radiation-induced defect creation and discharge damage that act to permanently alter the electrical properties of the material. Clearly, these complex issues are not well understood, and merit additional investigation. Presented in Section 2.3.8 is a more detailed description of the models that exist in the literature used to predict internal charge distributions, internal electric fields, surface potentials, and electron emission behavior.

2.3.8 Models for Internal and Surface Charge Distributions, Electric Fields, and Potentials

As mentioned in Section 2.3.7, a simple model for evaluating a double charge layer distribution, induced by incident electron irradiation, has been presented by Cazaux (1999, 1986) and Melchinger and Hofmann (1995), and has been termed the Dynamic Double Layer Model (DDLM). The double charge distribution presented in these models consists of a positive layer associated with the SE depletion region, and a negative layer associated with the incident electron deposition region, and are used to simulate evolving surface potentials and electron emissions as a function of electron fluence and incident energies. Cazaux (1999) used a 1-D planar approximation for the SE depletion region and incident electron deposition region, consisting of a positive uniform charge distribution extending from the surface to λ_{SE}, and a negative charge distribution extending from the surface to a depth R. The author also considered SE transport, trapping, detrapping, and escape, as well as the image charge response of the underlying conductor substrate. Melchinger and Hofmann (1995) developed a 3-D DDLM by treating both positive and negative charge distribution volumes as cylinders, each containing a constant charge density. These cylinders made up capacitive terms with dimensions that did not change with irradiation time. However, the total charge density that made up these layers was allowed to vary with time. By fitting to capacitive, yield, and charge parameters, the authors were able to predict evolving bulk and surface potentials as a function of time, displaying reasonable agreement with experimental data. They also found the charging behavior was highly dependent on both current density and incident energy. Although the DDLM models are simplistic compared to more complex charge distributions that have been experimentally measured or computationally modeled (Meyza *et al*., 2003; Miyake *et al*., 2003; Osawa *et al*., 2003; Usui *et al*., 2003; Frederickson and Brautigam, 2003; Frederickson *et al*., 2003; Frederickson and Dennison, 2003), they are easy to implement and

have been successful in predicting time-dependent steady-state surface and bulk potentials under continuous-source incident electron irradiation (Melchinger and Hofmann, 1995).

Although not directly related to the DDLM's, further comments are warranted concerning the studies of Cazaux (1999) and Melchinger and Hofmann (1995) on metal-oxide materials. Specifically, these authors have successfully applied their DDLM models to provide explanations for the anomalous charging behavior exhibited by metal oxide insulators. Specifically, these insulators charge negatively under continuous incident electron irradiation between the crossover energies, where positive charging is predicted from pulsed-yield data where $\sigma>1$ (refer to Section 5.3.1). Furthermore, Cazaux (1999) provides arguments for the raising of the steady-state surface potentials for metal oxides at incident energies above E_2^{σ} [as presented in Eq. (2.34)] due to radiation-induced trapping effects. According to the author, under continued electron bombardment, incident electrons permanently alter metal oxide materials by generating oxygen vacancies, which lead to additional trapping and scattering centers, which inhibit SE transport to the surface. This causes the total electron yields to diminish, hence lowering E_2^{σ} with continued electron irradiation. The lowering of E_2^{σ} causes the magnitude of the negative surface potential to increase, as predicted by Eq. (2.34). Incidentally, for metal oxides, this raising of the surface potential is in opposition to the effects of radiation-induced conductivity and leakage currents, which would act to decrease the measured surface potential as determined by Eq. (2.34).

Cazaux (1999) goes on to explain metal oxides exhibit further anomalous behavior under continuous electron irradiation resulting from radiation induced electron trapping and scattering, along with the ensuing buildup of charge layers. For example, as mentioned above, for incident beam energies between the crossover energies, $E_1^{\sigma}<E_0<E_2^{\sigma}$, positive charging is predicted since $\sigma>1$ as measured with the pulsed-yield technique (refer to Section 5.1).

However, Cazaux argues (and experimental evidence shows) metal oxides will display negative surface potentials under continued electron irradiation at incident energies, $E_1^{\sigma}<E_0<E_2^{\sigma}$ (when a positive surface potential is expected). Again, this is attributed to the lowering of electron emissions resulting from alterations to the metal-oxide structure under electron beam bombardment. These claims are important since they are in agreement with the experimental measurements made in this dissertation work (see Section 5.1).

Melchinger and Hofmann (1995) compare the results of their DDLM model to measured steady-state surface potential data on singe-crystal Al_2O_3 (sapphire) (surface potentials were measured by the shift in Auger spectra lines). In agreement with their experimental data, the DDLM predicts three steady-state charging regimes:

Regime I with $E_1^{\sigma}<E_0< E_2^{\sigma}$, constant-slowly increasing negative potential <10 V that is relatively time independent, in clear contradiction to pulsed-yields where $\sigma>1$ and positive charging should ensue [but in agreement with the arguments of Cazaux (1999) and our own experimental findings, see Section 5.1].

Regime II with $E_2^{\sigma}<E_0<10$ *keV*, moderately increasing negative surface potential <25 V with increasing energy, in contradiction to Cazaux (1999), where the surface potential is predicted to increase due to radiation induced trapping and scattering.

Regime III with $E_0>10$ *keV*, severe negative charging >500 V, increasing with incident energy, consistent with Eq. (2.34). The authors also show (both with experimental data and with their model) the magnitude and trend of evolving surface potentials beyond 10 keV is highly dependent both on incident current and energy, related to the competition between radiation-induced conductivity and radiation induced defect and electron-trap formation. For example, their experimental data at E_0=9.4 keV shows a steady relaxation of the negative surface potential from approximately 100 V to <10 V in

a 20-min. time period when irradiated with an incident current I_0=5 nA. In contrast, they find the negative surface potential steadily rises beyond 500 V at I_0=31 nA and the same incident energy, consistent with radiation induced trapping effects described by Cazaux (1999). However, at E_0=15 keV and I_0=48 nA, the sample once again displays a relaxation of the negative surface potential, consistent with radiation-induced conductivity effects. These results show metal-oxide materials exhibit anomalous charging behavior, unlike other insulators, which warrant further experimental investigation (refer to Section 6.2.1).

Although the DDLM's have been shown to be successful in interpreting and predicting experimental surface potential and electron yield data, an obvious limitation of these models is they are based upon a rigid internal charge distribution geometry that cannot change with continued electron irradiation. In many cases, these simple double-layer charge distributions do not adequately represent the true complex internal charge distributions and electric fields that are induced by electron irradiation. Meyza *et al.* (2003) has presented a 1-D (R_{beam}>>R) time dependent model for charging insulators under continuous electron irradiation for alumina, Al_2O_3, that includes no presumptions about the spatial structure of the internal charge distribution. The model improves upon the simple DDLM's by allowing for multiple positive and negative charge layers that can move, change shape, and charge density, both below and above E_2^{σ}.

Their model begins with an empirical expression for the SE generation rate as a function of depth, related to the maximum incident penetration depth by the following Gaussian distribution [compare to Eqs. (2.5) and (2.8), and refer to Fig. 2.3]:

$$\frac{n(x,E_0)}{\mathring{A}} = 0.146\left(\frac{E_0}{keV}\right)^{-0.3}\exp\left[-7.5\left(\frac{x}{R}-0.3\right)^2\right], \qquad (2.40)$$

where the SE creation distribution peak is shifted by 0.3R (empirically derived) from the surface into the target material. As a side note, the Gaussian distribution of Eq. (2.40) is quite different from the power-loss model presented in Eq. (2.8) as illustrated in Fig. 2.3. The model then utilizes basic material and electrical properties, along with the summation of all relevant currents (i.e., incident electron, SE, BSE, radiation-induced conductivity, electric-field attenuated, electron-hole, and electron-trapping currents) relevant to SE production, transport and escape, to calculate the resulting time-dependent internal charge distribution in the insulator. Furthermore, they apply a series of attenuation probabilities to the transport of holes and SE's, related to their respective mobility under the influence of internal electric fields, electron-hole recombination rates, and charge trapping probabilities to localized electron states. All of these attenuation probabilities affect the mean SE travel (or escape) lengths used to model electron yields in insulators [refer to Eqs. (2.13-2.15)]. By combining all electron/hole current contributions along with their associated attenuation probabilities, they are able to model internal charge distributions, electric fields, and surface potentials that are in good agreement with experimental evidence (refer to Sections 5.1 and 5.3.4).

In particular, their calculations show a steady-state solution involving triple-layer charge distributions (configuration -+-, similar to *Scenario III* above) for Al_2O_3 at E_0=1 keV (σ>1), and $J_0=10^{-5}$ A/cm^2. After 50 ms ($5\cdot10^{-9}$ C/mm^2), their simulations show internal electric fields peak to values $>10^6$ V/m between the SE depletion region and incident electron deposition region, while surface potentials remained positive at 4-5 V (consistent with insulator pulsed-yield surface potentials between the crossover energies, as shown in Sections 2.3.6 and 2.3.9). However, the authors do not allow for the possibility of dielectric breakdown in the case where the internal electric fields exceed ~10^6 V/m, which would cause the internal charge distributions to collapse into a single net-positive charge distribution. Finally, the

authors demonstrate at E_0=1 keV, the evolving charge distributions become much more complex in the presence of an external electric field supplied by a biased grid. This could have important implications to our work if the inner detector grid in our detector apparatus is used to discriminate between SE's and BSE's (refer to Sections 3.1 and 6.1.1).

For E_0=30 keV, their calculations show an initial incident electron deposition layer extends evenly over a depth >4 μm, but this negative region soon creates high internal electric fields that limit further incident electron penetration into the material. Once electron penetration is limited, a double negative charge distribution is created with one distribution peaking at ~0.8 μm beneath the surface, and another layer peaking <100 nm from the insulator surface. Additionally, a positive SE depletion region forms at a depth of ~500 nm resulting from field-enhanced SE transport towards the surface. Finally, an additional SE depletion region occurs within the first 10 nm of the surface. Hence, the overall charge distribution for this incident energy takes on the configuration of (+-+-). Given this charge distribution, the peak electric field within the material after 100 ms radiation at $J_0=10^{-5}$ A/cm^2 (10^{-8} C/mm^2) is ~10^6 V/m, and the steady-state negative surface potential is ~20 kV, a value much higher than that measured by Melchinger and Hofmann (1995) in this same energy regime (see discussion above). This clearly demonstrates the impending complexities associated with predicting internal charge distributions of electron-irradiated insulators, and reveals a condition where the simple DDLM model fails to accurately represent the true geometry of the internal charge distributions and their resulting electric fields and surface potentials.

Finally, one other finding from the simulations of Meyza *et al.* (2003) is worth noting since it is directly applicable to this dissertation work. In their study, the authors present the time-dependent behavior of the total electron yield for charging regimes associated with $E_1^{\sigma}<E_0<E_2^{\sigma}$ ($\sigma>1$, positive charging) and $E_0>E_2^{\sigma}$ ($\sigma<1$, negative charging). Specifically, for

E_0=1 keV at $J_0=10^{-5}$ A/cm^2, their model predicts it takes ~1 μs (10^{-13} C/mm^2) for the total yield to decrease from a value of ~2.4 to its steady-state value of unity, caused by the recapture of SE's by the positive surface potential. For E_0=30 keV, with the same current density, it takes ~25 ms ($2.5\cdot10^{-9}$ C/mm^2) for the total yield to rise from ~0.5 to its steady-state value of unity, caused by the retarding of the incident electron incident energy towards E_2^{σ}. These results clearly illustrate the dependence of the charge-decay rate at which an insulator will arrive at a steady-state condition, dependent on the incident electron energy, E_0. As explained in Section 2.3.6, these energy regimes (i.e., E_0=1 keV, σ>1and E_0=30 keV, σ<1) represented both the relatively rapid positive charging regime, and slow negative charging regime. The charge-decay time constants for these regimes can also be estimated using the electron-escape models presented in Section 2.3.6, as well as the models developed for pulsed charging rates in Section 2.3.9, below. Furthermore, as will be shown in Sections 5.1 and 5.3.4, these simulation results are consistent with measured charging rates for anodized aluminum and Kapton^{TM}-aluminum under pulsed electron irradiation in both the positive and slow negative charging regimes.

2.3.9. Evolving Electron Yields, Sample Currents, and Surface Potentials by a Pulsed Incident Electron Source

Thus far, several models have been presented that describe both the evolving and steady-state surface potentials of insulators resulting from electron irradiation. However, in this dissertation and in the literature, models have not yet been presented that describe the changes in evolving surface potentials, sample displacement currents, and electron yields in response to a pulsed incident electron source, prior to arriving at a steady-state condition. The aim of this section is to develop the necessary models that will be used to characterize the

rates of charging of insulators for our pulsed-yield setup as a function of electron fluence and incident electron energy later in Chapter 5.

First, consider an insulator irradiated by a low-amplitude, continuous electron source. One would expect the sample displacement current, I_s, to evolve with time until a steady-state potential is achieved. The evolution would depend on the time-dependent total electron yield, $\sigma(t)$, as follows:

$$I_s(t) = I_0 \cdot (\sigma(t) - 1), \tag{2.41}$$

where the sample current, $I_s(t)$, depends on the incident current, I_0, as well as on the time dependent total yield. As written in Eq. (2.41), if $\sigma(t=0)>1$ (that is, $E_1^{\sigma}<E_0<E_2^{\sigma}$), the initial sample displacement current would be positive (net electron current away from the sample), but if $\sigma(t=0)<1$ ($E_0<E_1^{\sigma}$ or $E_0>E_2^{\sigma}$), the net sample current would be negative (net current into the sample). For both negative and positive charging, when the steady-state condition is achieved, the yield will be ~1, and from Eq. (2.41), the sample displacement current will be zero.

In a similar manner, for a pulsed incident electron source, the sample displacement charge, Q_s, (deposited or emitted) can be expressed as a function of the incident charge and total yield as:

$$Q_{si} = Q_{0i}(\sigma_i - 1), \tag{2.42}$$

where the index i represents the pulse number (i=1 for the first pulse), Q_{0i} is the incident electron charge corresponding to the i^{th} pulse (Q_0 will stay more-or-less constant for a stable electron source), and σ_i is the yield corresponding to the i^{th} pulse. As with the continuous-source case presented above, the total yield will approach a value close to unity, and Q_{si} will approach a value close to zero as the sample charges to steady state. Furthermore, as mentioned above in Section 2.3.6, if there are leakage currents for $E_0>E_2^{\sigma}$, the total yield will

approach a value less than unity, and the steady-state sample charge will deviate slightly from zero. However, for the treatment presented below, leakage currents have been neglected

For our experimental pulsed-yield setup (refer to Section 3.3), the incident charge is obtained by measuring a short-duration current pulse, and then integrating current over the full pulse duration as:

$$Q_0 = \int_0^\infty I_0(t) \cdot dt \,, \tag{2.43}$$

where the upper limit of the integral is allowed to go to infinity for convenience, since in practice, the current pulse goes to zero very quickly (typically within 10 μs for our experimental setup, refer to Section 3.3) and contributes no more to the integral. This upper integration limit is arbitrarily chosen during experiments, and is only required to encompass the incident pulse. Furthermore, I_0 is generally kept more-or-less constant for a measurement sequence involving many incident pulses.

The cumulative incident charge, Q_{0N}, delivered by numerous incident electron pulses can be expressed in terms of Eq. (2.43) as the sum of each incident pulse up to the N^{th} pulse as:

$$Q_{0N} = \sum_{i=1}^{N} Q_{0i} = \sum_{i=1}^{N} \int_0^\infty I_{0i}(t) \cdot dt \,. \tag{2.44}$$

Likewise, the cumulative sample displacement charge, Q_{sN}, (captured or emitted) from the sample over repeated incident pulses (up to the N^{th} pulse) can be related to the incident electron charge using Eqs. (2.42) through (2.44) as:

$$Q_{sN} = \sum_{i=1}^{N} Q_{si} = \sum_{i=1}^{N} Q_{0i}(\sigma_i - 1) = \sum_{i=1}^{N} \int_0^\infty I_{0i}(t)dt \cdot (\sigma_i - 1) \,. \tag{2.45}$$

As will be shown below, it is useful to relate the pulse number index, i, and cumulative incident charge, Q_{0N}, to an average incident current, $\bar{I}_0$, and pulse-duration time, τ,

such that direct comparisons can be made with DC charging data. To do this, an average current/pulse must be defined that corresponds to the DC current that would be delivered to the sample if a continuous electron source were used. To do this, first an average incident charge/pulse is defined from the cumulative charge calculated from Eq. (2.44) as:

$$\bar{Q}_0 \equiv \frac{Q_{0N}}{N} = \frac{1}{N}\sum_{i=1}^{N} Q_{0i} \ . \tag{2.46}$$

For convenience, the incident pulse is treated as a square-wave pulse, and the average incident current per pulse, $\bar{I}_0$, is calculated from Eq. (2.46) as:

$$\bar{I}_0 = \frac{\bar{Q}_0}{\tau_i}, \tag{2.47}$$

where τ_i is the time duration of each incident pulse that is generally constant throughout a pulsing sequence, and can be controlled by the trigger pulse sent to the electron source (typical values for τ_i were 5 μs in this dissertation work). Finally, the cumulative charging time, τ_N, can be calculated by simply summing up the time durations of each incident pulse as:

$$\tau_N = \sum_{i=1}^{N} \tau_i \ . \tag{2.48}$$

Furthermore, an average sample displacement current can also be calculated in a similar manner as:

$$\bar{I}_s = \frac{\bar{Q}_{s0}}{\tau_i} = \frac{\frac{1}{N}\sum_{i=1}^{N} Q_{si}}{\tau_i} \ . \tag{2.49}$$

Conversely, when making DC current measurements, one may find the total sample displacement charge deposited (or emitted) by a constant continuous-source electron beam using Eq (2.41) as:

$$Q_s(t) = \int_0^t I_s(t) \cdot dt = I_0 \int_0^t \left(\sigma(t) - 1\right) \cdot dt \, , \tag{2.50}$$

where t is the irradiation time, and it is assumed the incident current remains constant.

So far, the evolution of the sample charge and current in Eqs. (2.41) through (2.50) have all been dependent on the evolution of the total yield. Hence, it is important to develop an expression for the evolving total yield as a function of incident pulsed charge. From the data (shown later in Sections 5.1 and 5.3.4), it is found that the yield decays more-or-less exponentially with pulse number (or deposited charge, or time) so that an expression for the total yield that meets the temporal boundary conditions is given as:

$$\sigma_i = 1 + (\sigma_0 - 1) \cdot \exp\left[-\alpha' \cdot (i-1)\right], \tag{2.51}$$

such that when i=1, the total yield is equal to the uncharged yield, σ_0, and as i approaches infinity, the total yield approaches a value close to unity. Alternatively, the total yield can be expressed as a function of the cumulative incident charge as:

$$\sigma_i = 1 + \left[\sigma_0 - 1\right] \cdot \exp\left[-\alpha \cdot \left(\sum_{i=1}^{N} Q_{0(i-1)}\right)\right], \tag{2.52}$$

where for i=1, the summed charge term is forced to zero. The exponent α has units of inverse coulombs, and is a decay constant related to the charging time constant of the sample and system (discussed in more detail below). The decay constant α in Eq. (2.52) can be related to α' (for i=N) in Eq. (2.51) by equating the exponent terms as follows:

$$\alpha = \frac{\alpha'(N-1)}{\sum_{i}^{N} Q_{0(i-1)}} = \frac{\alpha'(N-1)}{Q_{0(N-1)}}, \tag{2.53}$$

where again, the summed charge term is forced to zero for i=1. From Eq. (2.53), it can be seen if the incident charge, Q_{0i}, is kept constant, the expression for α reduces to $\alpha \approx \alpha'/Q_0$. As shown in simulation (Meyza *et al.,* 2003) and experiment (refer to Sections 5.1 and 5.3.4), the decay constant, α, is energy dependent. One would expect it to be relatively large for energies $E_1^{\sigma} < E_0 < E_2^{\sigma}$, since positive surface potentials need to rise only to a few volts to trap the

majority of escaping SE's, thus achieving a steady-state condition very quickly. However, above E_2^{σ}, the steady-state condition is dependent on raising the negative surface potential such that either the SE distribution is pushed above 50 eV (fast negative charging mechanism), or the landing energy of incident beam is decreased to a value close to E_2^{σ} (slow negative charging mechanism). For $E_0>E_2^{\sigma}$, since the total electron yield is lower, and surface potentials must reach several hundred to thousands of volts to reach steady state, one would expect the time constant to be much smaller. A comparison of the energy-dependent quantities for α as well as time constants is provided in Section 5.3.4.

For pulsed yields, the evolving total yield can also be approximated by combining Eqs. (2.47) and (2.52) as:

$$\sigma_N \approx 1+\left[\sigma_0-1\right]\cdot\exp\left[-\alpha\cdot\overline{I}_0\cdot\tau_N\right]. \tag{2.54}$$

Likewise, the total yield can also be approximated as a function of time for DC incident current as (approximate):

$$\sigma(t) \approx 1+\left[\sigma_0-1\right]\cdot\exp\left[-\alpha\cdot I_0\cdot t\right], \tag{2.55}$$

where α is related to the incident DC current and charging time constant of the dielectric. Finally, with these expressions for the total yield, the evolving sample charge expressed in Eqs. (2.42), (2.45), and (2.50) can be rewritten in terms of pulse number, cumulative charge, or time as:

$$Q_{sN} = Q_{0N}\cdot\left[\sigma_0-1\right]\cdot\exp\left[-\alpha'\cdot(N-1)\right], \tag{2.56}$$

$$Q_{sN} = Q_{0N}\cdot\left[\sigma_0-1\right]\cdot\exp\left[-\alpha\cdot\left(\sum_{i=1}^{N}Q_{0i}\right)\right], \tag{2.57}$$

$$Q_s(\tau_N) \approx \overline{I}_0\tau_N\cdot\left[\sigma_0-1\right]\cdot\exp\left[-\alpha\cdot\overline{I}_0\tau_N\right]. \tag{2.58}$$

From Eqs. (2.57) and (2.58), it can be seen the decaying charge equations can be expressed in terms of a charge-decay time constant, rather than the decay constant, α, as:

$$Q_s(\tau_N) \approx \overline{I}_0 \tau_N \cdot [\sigma_0 - 1] \cdot \exp\left[-\frac{\tau_N}{\xi}\right], \tag{2.59}$$

where the charge-decay time constant, ξ, has been defined as:

$$\xi = \frac{1}{\alpha \cdot \overline{I}}. \tag{2.60}$$

Rewriting the charge equation in terms of a charge-decay time constant will be useful later in Sections 5.1 and 5.3.4 for comparing the charge-decay rates of our pulsed-yield measurements to the modeled and measurements DC decay rates reported in the literature.

The charging equations given by Eqs. (2.56) through (2.58) can be used in combination with the integrated Chung and Everhart equations, Eqs. (2.31) and (2.33) to estimate the positive and negative surface potentials that evolve with incident electron pulsing. Specifically, for positive charging for $E_1^{\sigma}<E_0<E_2^{\sigma}$, Eq. (2.31) can be combined with Eq. (2.52) to obtain an equation for the evolving positive surface potential in terms of the evolving total yield as:

$$\frac{\chi + 3qV_{sN}}{(\chi + qV_{sN})^3} \approx \frac{1 + [\sigma_0 - 1] \cdot \exp\left[-\alpha \cdot \left(\sum_{i=1}^{N} Q_{0i}\right)\right] - \eta_0}{\sigma_0 - \eta_0} \cdot \left[\frac{1}{\chi^2} - b\right] + b, \tag{2.61}$$

where b is defined by Eq. (2.29). Also, in Eq. (2.61), the definition of the SE yield has been employed (δ=σ-η), where the initial BSE yield, η_0, is assumed to remain constant (as will be shown in Section 5.3.4, this is a fair assumption). Likewise, for the fast negative charging regime for $E_0>E_2^{\sigma}$ (described above in Section 2.3.6), a similar expression for the evolving negative potential in terms of the evolving SE yield can be written in terms of Eq. (2.33) and (2.52) as:

$$\frac{\chi+150\text{eV}-3\left|\text{qV}_{si}\right|}{\left(50eV+\chi-\left|\text{qV}_{si}\right|\right)^3}=\frac{1+\left[\sigma_0-1\right]\cdot\exp\left[-\alpha\cdot\left(\sum_{i=1}^{N}Q_{0i}\right)\right]-\eta_i}{\sigma_0-\eta_0}\cdot\left[b-\frac{1}{\chi^2}\right]+\frac{1}{\chi^2}, \quad (2.62)$$

where $\left|\text{qV}_{si}\right|$ is the magnitude of the negative surface potential on the ith pulse. In this case, η_i is also monitored as a function of pulse number since it will evolve along with the SE yield as higher-energy SE's gain energy above 50 eV due to the increasing negative surface potential (refer to discussion in Section 2.3.6).

An alternative approach to solving for the evolving surface potential involves treating the insulator as a charging parallel-plate capacitor, with one electrode being the charging insulator surface, and the other electrode being the conductor substrate, which matches the surface charge with an opposing charge layer. As discussed in Section 2.3.7, for our experimental setup with no external electric fields (originating from the hemispherical grid), it is appropriate to impose a simplified limiting case, where the edge effects of the internal charge distribution are neglected. This limiting case is justified for the following reasons: first, the net charge distribution (positive or negative) in the insulator exists over the region of incident electron penetration, R, and SE escape, λ_{SE}, not extending more than a few microns into the insulator for energies (E_0<30 keV) relevant to our setup (refer to Figs. 2.4 and 2.7); second, the insulator thickness, d, is generally much greater than either R or λ_{SE} such that the charged insulator region can be treated as a thinly charged sheet separated from the substrate by an uncharged insulator (note this assumption would not be relevant for the anodized Al alloy studied in Section 5.1 since the anodized layer thickness was only ~1 μm); third, the electron irradiated area is generally much greater than the insulator thickness, R_{beam}>>d such that edge effects can be neglected (this assumption would not hold for insulators approaching ~1 mm in thickness). Having made these assumptions, the change in the magnitude of the surface potential on the i^{th} incident pulse (measured with respect to the grounded sample

holder) can be estimated by modifying Eq. (2.39) to accommodate a pulsed incident electron source, as:

$$V_{si} \approx \frac{Q_{0i}\left(\sigma_i - 1\right)}{A_0} \cdot \frac{d}{\varepsilon_0 \varepsilon_r} . \tag{2.63}$$

Eq. (2.63) applies for both positive and negative charging, since when $\sigma>1$, the change in surface potential is positive, and when $\sigma<1$, the change in surface potential is negative. Then, using Eq. (2.63), the cumulative surface potential resulting from repeated incident pulses can be written as:

$$V_{sN} \approx \sum_{i}^{N} V_{si} . \tag{2.64}$$

An example of the calculated evolving positive surface potential as a function of cumulative incident charge is shown in Fig. 2.13. In the figure, Eqs. (2.61) and (2.64) have been used to estimate positive surface charging, with the equation parameters taken from Kapton™ at E_0=500 eV (refer to Section 5.3.4), with χ=3.7 eV, σ_0=1.6, η_0=0.29, $Q_0=1\cdot10^{-13}$ C, d=8 μm, A_0=0.8 mm^2, and ε_r=3.4. The evolving total yields were also taken from fitted Kapton™ data at E_0=500 eV that will be presented later in Section 5.3.4. A similar plot for the fast negative charging mechanism, using Eq. (2.62), was not performed since data for the evolving SE yield as a function of incident charge was not acquired in this energy regime (this could be a subject of future study in our lab). From Fig. 2.13, it can be seen that for positive charging, the steady-state surface potentials calculated from Eqs. (2.61) and (2.64) agreed to within an order of magnitude throughout the range of cumulative charge. Furthermore, it can be seen from Fig. 2.13, as stated above, for $E_1^{\sigma}<E_0<E_2^{\sigma}$, positive surface potentials plateau at just a few volts (in the case of Eq. (2.61), at ~3 V). The results obtained from Eq. (2.61) were considered to be much more accurate since they did not rely on assumptions made for the

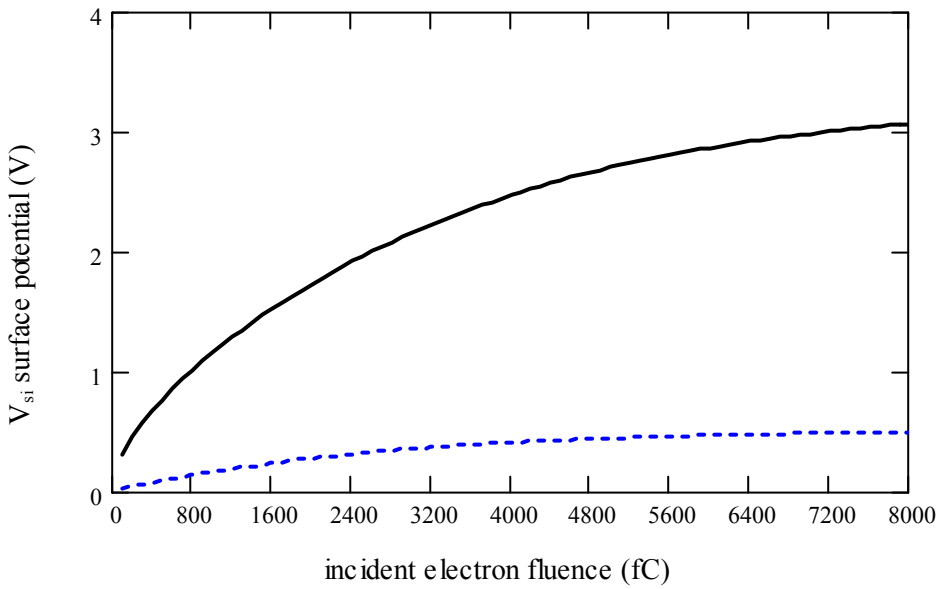

FIG. 2.13. An example of the calculated evolving positive surface potentials as a function of cumulative incident charge. Surface potentials were calculated from Eq. (2.61) (solid line), and from Eq. (2.64) (dashed line). Calculations agreed to within an order of magnitude, although estimates from Eq. (2.61) were considered to be more accurate.

charging geometry factors, A_0 and d. These values are difficult to determine accurately since the actual charge distribution geometry inside the insulator is unknown. For this reason, Eq. (2.61) was used instead of Eq. (2.64) for calculating evolving positive surface potentials in this dissertation. Further data and analysis of these charge decay studies are provided for Kapton™ in Section 5.3.4.

CHAPTER 3

INSTRUMENTATION

This chapter begins in Section 3.1 with an overview of the USU equipment and facilities used to measure electron yields. A more detailed description of the DC-data acquisitioning setup is given in Section 3.2, used to make conductor yield measurements. Modifications to the DC setup are described in Section 3.3 that have allowed pulsed-yield measurements on insulator materials. Next, a description of the characterization and operation of the electron guns in DC and pulsed mode are presented in Section 3.4. Finally, charge neutralization sources used to discharge insulator materials are described in Section 3.5.

3.1 General Experimental Setup

For this dissertation work, the primary instrument for making electron yield measurements was a versatile ultra-high vacuum (UHV) chamber known as the FATMAN chamber (shown in Fig. 3.1) that has extensive surface analysis, sample characterization, and measurement capabilities (Thomson *et al*., 2003b; Dennison *et al*., 2003b; Nickles, 2002; Chang *et al*., 2000a). This chamber can simulate diverse space environments including controllable vacuum ($<10^{-10}$ to 10^{-3} Torr), ambient neutral gases conditions, and electron, ion, and solar irradiation fluxes. The chamber is currently equipped with three electron guns, two ion guns, various photon sources, SEM, Auger spectroscopy, and a flood gun neutralization source (Thomson *et al*., 2003b; Dennison *et al*., 2003b). For UHV measurements, the chamber is pumped using turbomolecular, magnetic ion, and titanium sublimation pumps to base pressures ranging from 10^{-10} to 10^{-8} Torr. Nickles (2002) provides a more complete description of the overall chamber specifications and capabilities.

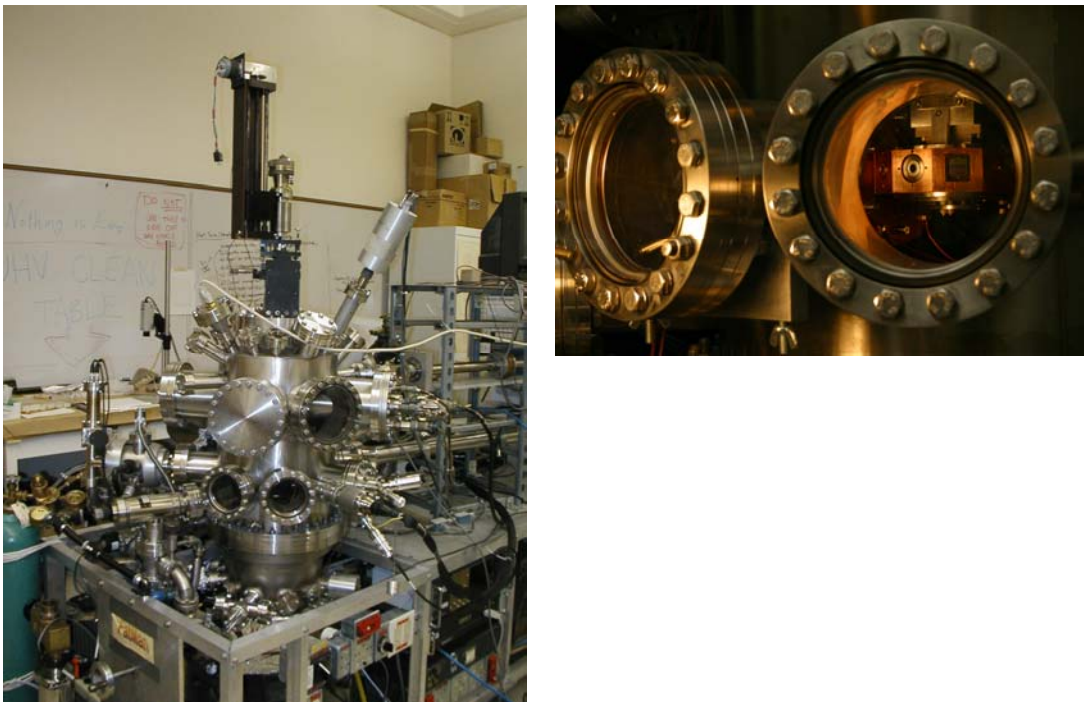

FIG. 3.1. USU FATMAN ultra-high vacuum chamber for making electron emission measurements. Inset (top right) shows the sample stage through the chamber view-port window.

The sample stage, shown in Fig. 3.2, holds 11 samples that can be positioned before various sources, and is detachable for rapid sample change out. The primary detector for electron emission studies is a custom hemispherical grid-retarding field analyzer that fully encloses the sample under study (Nickles, 2002; Chang *et al*., 2000a). The hemispherical grid detection system, shown in Fig. 3.2, has been carefully calibrated (both through calculation and measurement) to account for detector losses, allowing yield accuracies with systematic errors <5% (discussed more fully in Section 4.3). The incident electron (or ion) beam enters into the detector assembly through a tubular aperture in the back of the detector housing. A suppression grid within the detector is used to discriminate between BSE's (energies >50 eV) and SE's (energies <50 eV), by applying a 0 V or -50 V bias. By ramping the grid bias,

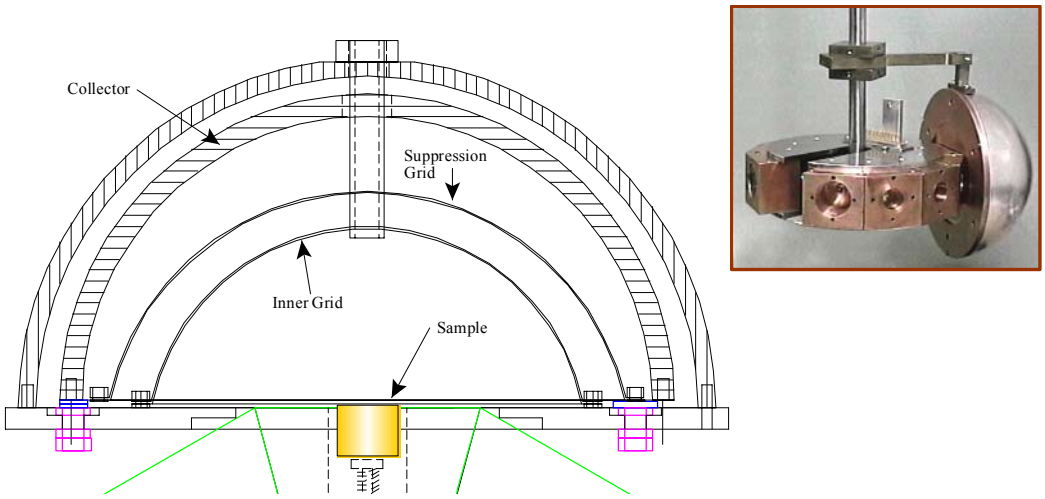

FIG. 3.2. (Top right) Sample carousel and hemispherical detector used to make electron yield and spectral measurements. The sample carousel was capable of holding 11 samples at a time. The detector apparatus rotated independently with respect to the sample stage, and could fully enclose each sample for electron, ion, or photon-induced electron yields. (Bottom left) Cross section of detector apparatus shows collector, suppression grid, inner grid, and sample.

energy spectra of the emitted electrons can also be measured using this detector with an energy resolution of 1.5±0.4 eV, limited by non-uniformities in the suppression grid (Nickles, 2002). Potentials on the suppression grid are controlled using a Keithley 230 voltage supply controlled via GPIB interfacing by a computer for both DC and pulsed-yield measurements.

An inner grid (tied electrically to the stage) sits between the suppression grid and the sample to shield the incoming electron beam and sample from electric fields generated by the suppression grid (see Fig. 3.2). The electron collector always remains at a +50 V bias with respect to the suppression grid both to ensure all electrons passing through the grid reach the collector, and also to ensure any SE's emitted from the collector are returned to the collector. The collector potential is supplied by a standard AC-driven power supply for the DC-yield setup, and with batteries for the pulsed-yield setup (refer to Sections 3.2 and 3.3 for descriptions of the two setups). More information on details of the vacuum chamber, sample

stage assembly, and detector apparatus are provided in the dissertation work of Nickles (2002). Other detectors in the FATMAN chamber include a standard Faraday cup detector, an electrostatic hemispherical analyzer, a cylindrical mirror analyzer, and a time-of-flight micro-channel plate detector.

As described in more detail in Chapter 5, samples were thin insulator layers, sheets, and films that were adhered to 10.0±0.1 mm diameter Oxygen Free High Conductivity (OFHC) copper cylinders using a UHV adhesive containing fine silver powder to provide electrical contact between the films and substrate. Conductor samples were cleaned using acetone and methanol immediately before introduction into the vacuum. Additionally, conductor samples were sputtered *in situ* with argon to remove adsorbed contamination monolayers. Sample cleanliness was confirmed using Auger spectroscopy. Most insulator samples were cleaned only with methanol before introduction into the vacuum; no ion sputtering or Auger spectroscopy was performed, which could cause damage and charging to the sample surfaces.

Two principal electron guns were available for making yield measurements. The first was a low-energy gun (STAIB Model EK-5-S) with an operating energy range of 50 eV to 5 keV and pulsing capabilities from 1μs to continuous emission. The other was a high-energy gun (Kimball Model ERG-21) with an operating energy range from 4 keV to 30 keV and pulsing capabilities from 20 ns to continuous emission. Both guns provided monoenergetic electron beams with beam currents ranging from 0.1 nA to 10 μA, and beam spot diameters ranging from 200 μm to 3 mm, depending on the gun and energy. Details of electron gun characterization and operation for both DC and pulsed-yield measurements are provided in Section 3.4.

For conducting samples, electron guns were operated in continuous emission mode, and DC currents were measured with standard ammeters sensitive to several tens of picoamperes. For pulsed measurements on insulators, the electron guns delivered 5 μs (shorter pulse durations of 1 μs were achievable), 1-100 nA incident pulses. As stated above, two separate electrical setups were developed for DC and pulsed-yield measurements. A simple schematic, applicable to both DC and pulsed-measurement setups, is shown in Fig. 3.3. For both setups, sensitive ammeters were tied independently to the electron collector, suppression grid, sample, and sample stage for electron current detection. Both DC and pulsed measurements and data retrieval were fully computer automated, using GPIB interfacing and a DAC card (Iotech Model Daqboard 200A) under Labview™ control. A more complete description of the DC-system and pulsed-system setup is available in Sections 3.2 and 3.3.

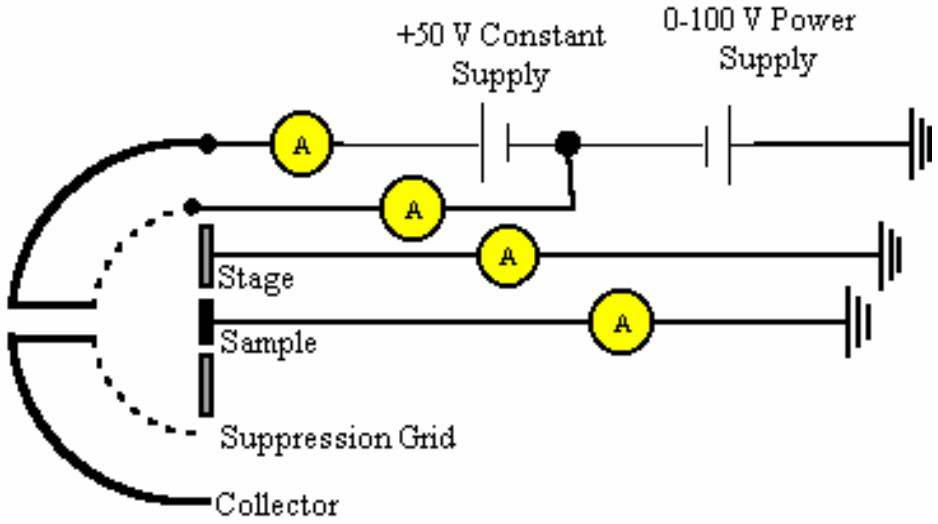

FIG. 3.3. Basic schematic for DC- and pulsed-yield measurements. The suppression grid was biased to discriminate between SE's and BSE's and to take energy spectral measurements. The incident electron beam entered through the detector aperture tube. Collector, suppression grid, sample, and stage currents were measured independently to calculate electron yields.

3.2 DC-Yield Measurement Setup

The DC yield setup built at USU has proven to be both an accurate and versatile system for the absolute measurements of electron yield properties of conducting materials. An overview of the setup is provided in the following paragraphs, and is illustrated in the block diagram shown in Fig. 3.4. A more detailed description of the setup is given in Nickles (2002).

For DC yield measurements, the electron guns were operated in continuous emission mode (see Section 3.4) at typical incident currents of 20-40 nA (current densities <10 $\mu A/cm^2$). The electron beam was incident at a normal angle to the samples, and entered the detector cavity through a tubular aperture in the back of the detector housing. The detector/sample assembly was comprised of four electrically isolated components: an electron collector, suppression grid, sample, and stage. The stage component included sample-stage, inner-grid, and other stray conducting components electrically tied together. The suppression grid could be biased between ±110 V using the Keithley 230 variable power supply (GPIB controlled via Labview). The collector potential floated at +50 V with respect to the suppression grid, supplied by a Lambda LM-130-60 AC-driven power supply. Sample and stage were usually tied to ground through separate picoammeters, but could be floated and biased if needed.

DC-current signals were measured independently for the collector, suppression grid, sample and stage. Two separate circuit schemes existed for measuring the DC current signals. Generally, the sample and stage currents (along with Faraday cup and UV photodiode currents and sometimes the suppression grid) were sent through the patch-panel circuitry, while the HGRFA circuit was reserved for the collector and grid currents. The patch-panel circuitry consisted of five custom-designed isolated ammeters, equipped with internal biasing

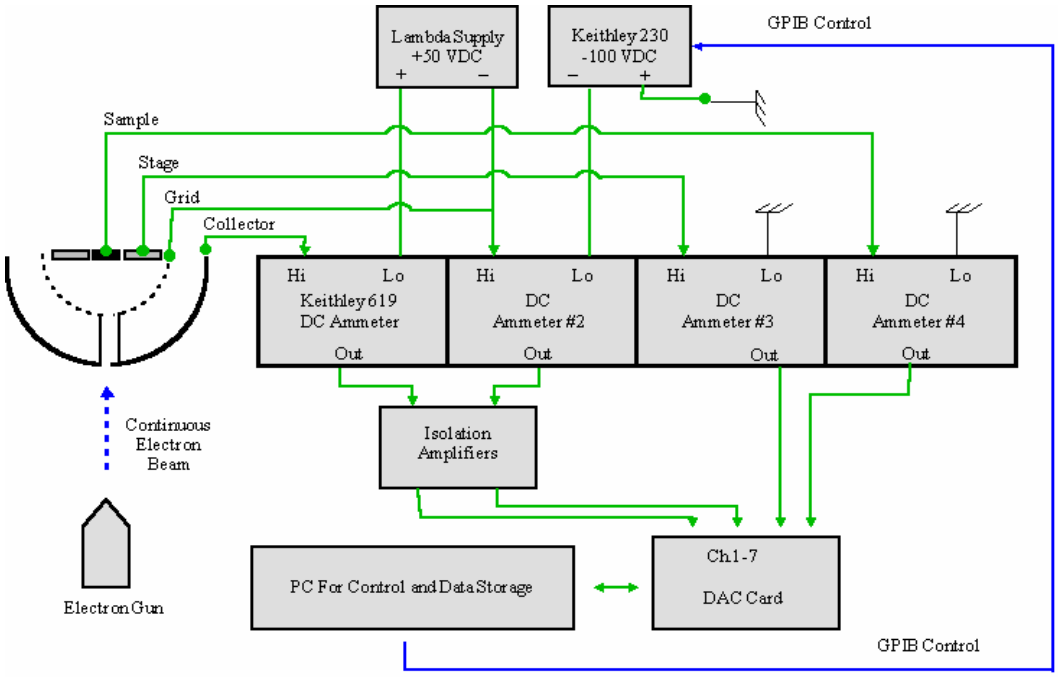

FIG. 3.4. DC-yield measurement block diagram for conductors. A continuous-emission electron beam <50 nA was used to excite electrons from the sample. Emitted electrons were captured by the collector. The suppression grid was used to discriminate between SE's and BSE's, or to measure electron energy spectra. Signals were captured with sensitive ammeters, and then sent to a computer for yield analysis. Labview was used to automate the data acquisition and analysis process.

capabilities (±60 VDC) or external biasing (with isolation up to 2 kV). The hemispherical grid retarding field analyzer (HGRFA) circuitry, built around a commercial Keithley 619 electrometer, had two channels that floated with respect to the Keithley 230 power supply potential.

Each patch panel ammeter was built around a current-to-voltage converter (Analog Devices 546) integrated-circuit with resistive feedback gain chosen to provide ±50±0.01 nA current range and resolution (Nickles, 2002). The current signal for each ammeter was sent through a unity-gain, non-inverting inductively-coupled isolation amplifier (Analog Devices 202) with 2 kV isolation to protect the computer DAC card in situations where the sample,

stage or Faraday cup were biased. The overall maximum bandwidth for each ammeter was ~1 kHz.

The HGRFA circuitry utilized triaxial cables (for additional noise reduction) that carried collector (and sometimes suppression grid) current signals to the Keithley (Model 619) electrometer. The electrometer was powered through a 110 VAC isolation transformer (isolation to 4000 V rms) so it could be floated with respect to the Keithley 230 power supply. The voltage output signals from the Keithley 619 passed through unity-gain isolation amplifiers (Burr Brown ISO121 with isolation of 3500 V rms) before going to the computer DAC card.

The computer DAC card was an Iotech Model Daqboard 200A with 8 usable differential analog input channels and 16-bit analog-to-digital conversion with a 100 kHz sampling rate. For each measurement, 10,000 samples were acquired over a period of 100 ms for each channel, and then averaged (standard deviations were also calculated for error). Yields were then calculated in Labview as ratios of the collector current to the total incident current [refer to Eqs. (2.1) to (2.3)]. Full Labview diagrams used for data acquisitioning and electrometer control are provided in Nickles (2002).

For yield calculations, the total incident current was determined by one of three ways: i) by directly monitoring the electron gun emission current through the gun controller (only available for the Kimball gun); ii) by measuring the total gun current using the Faraday cup; or iii) by simply summing the sample, suppression grid, collector and stage currents (conservation of charge method). All three methods were shown to produce results for the total incident current consistent to ~3% (Nickles, 2002). Of these methods, the third (charge conservation) method was more expedient, and was therefore implemented most often. Using

this method, the DC-yields were measured and calculated in terms of the collector, sample, stage and suppression grid currents as:

$$\sigma = \frac{I_c}{I_0} = \frac{I_c}{I_c + I_s + I_{stg} + I_g\left(0V\right)}, \tag{3.1}$$

$$\eta = \frac{I_c}{I_c + I_s + I_{stg} + I_g(-50V)}, \tag{3.2}$$

where σ was the total yield (0 V suppression grid bias), η was the BSE yield (-50 V suppression grid bias) and I_0, I_c, I_s, I_{stg}, and I_g were the total incident, collector, sample, stage, and suppression grid currents, respectively. SE yields were calculated as the difference between the total and BSE yields as:

$$\delta = \sigma - \eta\,. \tag{3.3}$$

The data acquisitioning and yield calculation processes were automated using Labview such that yield measurements (and their associated errors) took only a few minutes for each incident beam energy (Nickles, 2002) (refer to Fig. 2.2 as an example). In measuring the electron yields, the electron gun (STAIB gun for lower energies, Kimball gun for higher energies, and ion gun for ion yields) was adjusted to the desired beam energy, and the filament current was also set. Then, emission grid and focus settings were attuned to obtain the desired beam spot profile and current density. These settings had been predetermined for each incident energy such that this entire process took no more than a couple of minutes (see Section 3.4 for further details on electron gun operation). After setting up the electron gun, the sample/detector angular, vertical, and horizontal positions were optimized while continuously monitoring collector, sample, suppression grid, and stage currents. This optimization was performed such that the magnitudes of the collector and sample currents were maximized while stage current was minimized. This process was only performed at the beginning of a measurement set (took roughly 1-5 minutes for DC measurements), and

required no further adjustment when the electron gun energy, emission grid, and focus settings were modified. The horizontal/vertical electron gun deflection settings were then fine tuned while again maximizing (minimizing) collector and sample (stage) currents. Typically, these adjustments were also performed only once, and did not change significantly with energy, emission grid, and focus modifications.

Finally, after optimizing for electron yield measurements, DC-energy spectra for a given energy could be measured without any further modifications. This was done by stepping up the suppression grid potential with the Keithley 230 power supply, and measuring the collector current (refer to Fig. 2.1 as an example). As with the yield measurements, this procedure was fully automated using Labview [further details are provided in Nickles (2002)].

As described further in Section 3.3, a similar pulse measurement scheme for the insulating materials was developed and tested. However, pulsed yields were measured using an entirely separate data acquisition circuitry setup, utilizing sensitive, optically-isolated, and fast-response ammeters.

3.3 Pulsed-Yield Measurement Setup

Although an entirely different measuring circuit was used for pulsed-yield measurements, the basic block diagram was much the same as for the DC setup. Comparisons of Figs. 3.4 and 3.5 show key differences were the addition of a timing control circuit, electron gun pulsing circuitry, and more sophisticated current measuring circuitry. This section provides an overview of these innovative instrumentation enhancements.

Fig. 3.5 provides a block diagram of the pulsed-yield measurement setup. As can be seen in the figure, a digital TTL signal from the computer DAC card was used to activate a timing circuit that delivered a simultaneous trigger to both a Tektronix 115 pulse generator

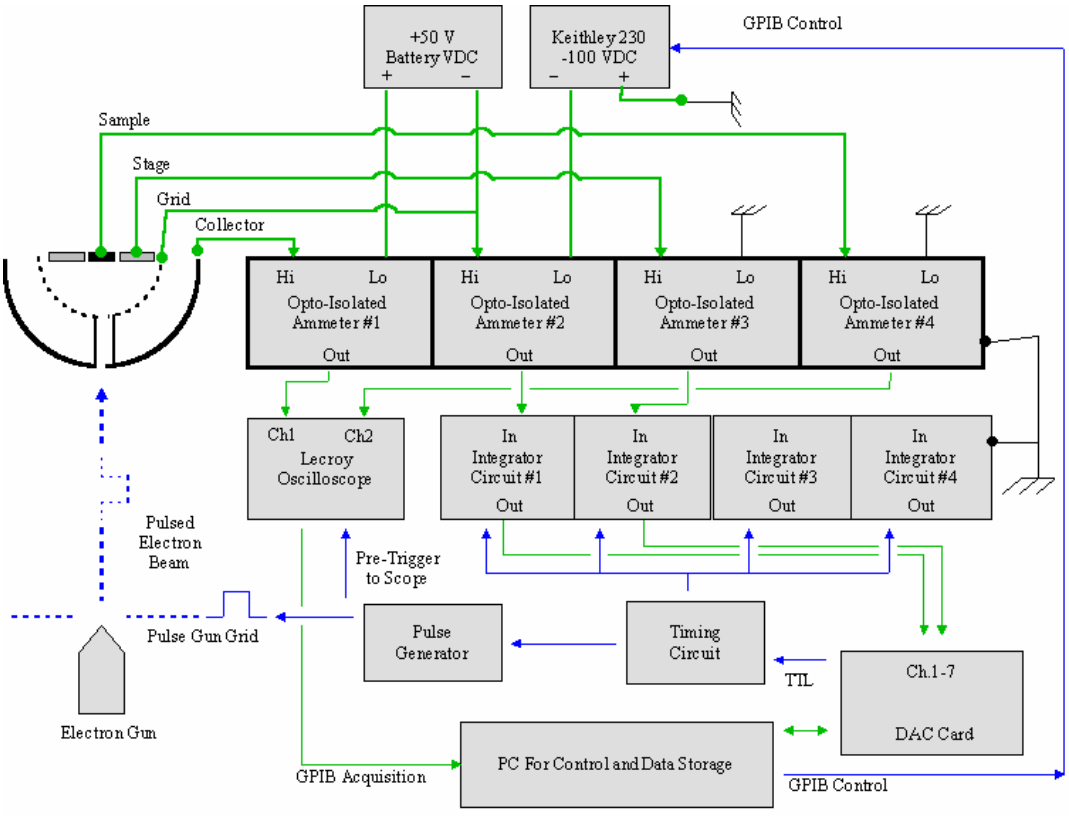

FIG. 3.5. Pulsed-yield measurement block diagram for insulators.

and integrator circuitry. The pulse generator sent a square-wave pulse (typical pulse duration of 5 μs and 100 ns rise time) to one of the two electron guns (see Section 3.4 for details on electron gun operation) that emitted an electron-beam pulse with an amplitude ranging from 10-100 nA to the sample. As with the DC setup, current signals from the collector, suppression grid, sample (sample displacement current for insulator samples), and stage were measured independently using sensitive ammeter circuitry. However, ammeters used for pulsed measurements were optically isolated, fast (1-10 μs rise time), and sensitive ($1 \cdot 10^8$ V/A to $2 \cdot 10^6$ V/A) with low internal noise (0.6-3 nA noise level). Generally, an ammeter amplification of $2 \cdot 10^7$ V/A (with a response time of ~4 μs) was used for signal processing.

These signals were captured using either a 500 MHz LeCroy digital storage oscilloscope, or by integrator circuitry. Details of the current measuring circuitry are provided in more detail in Thomson *et al*. (2003b) and Zavyalov (2003b). As with the DC setup, the pulsed-data acquisition and analysis setup was fully automated using Labview. Details of the Labview Virtual Instrumentation (VI) control program are given in Thomson (2003d).

For the pulsed setup, additional measures were taken to eliminate system noise, especially noise in the frequency bandwidth of 0.1-1 MHz (since the Fourier transform of the current pulses lay in this bandwidth). The fast-response ammeters along with the Lecroy digital oscilloscope were invaluable tools in diagnosing both noise magnitudes and frequencies. As with the DC setup, the Keithley 230 power supply (controlled using GPIB interfacing to the computer) was used to bias the suppression grid. Although the Keithley power supply contributed some noise to the system, it was retained for its computer-interfacing capabilities (especially useful in spectral measurements where the grid was biased in a stepped fashion). However, to eliminate further system noise caused by AC-driven power supplies, the collector was floated with respect to the suppression grid at +45 V using a series of rechargeable NiH 9 V batteries. By using a battery supply in place of the Lambda power supply (used for DC measurements), it was found the noise level was reduced by ~2 orders of magnitude. The Keithley 230, along with the sample, stage, collector, and suppression grid vacuum chamber wiring outputs were routed to the pulsed-circuitry setup using a series of SPDT gold-plated terminal switches, enclosed in grounded aluminum boxes for electromagnetic shielding as shown in Fig. 3.6.

To further shield the circuitry from electromagnetic noise, computer monitors and the Lecroy oscilloscope were placed in a metal-plated instrumentation rack that reduced the system noise by ~100 nA (see Fig. 3.7). All currents were carried using Triax cabling (yellow

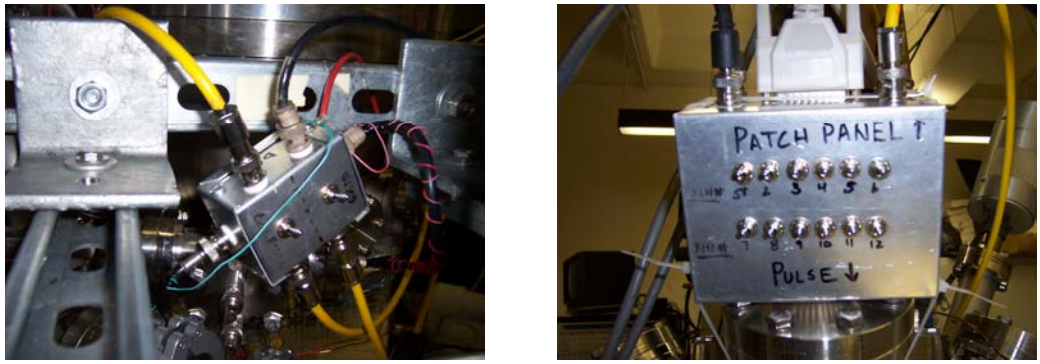

FIG. 3.6. Switch boxes for pulsed vs. DC measurement circuitry. (Left) Grid and collector switch box. (Right) Sample and stage switch box. Aluminum cases were equipped with triaxial cable connectors, and were tied to chamber ground to shield signal circuitry.

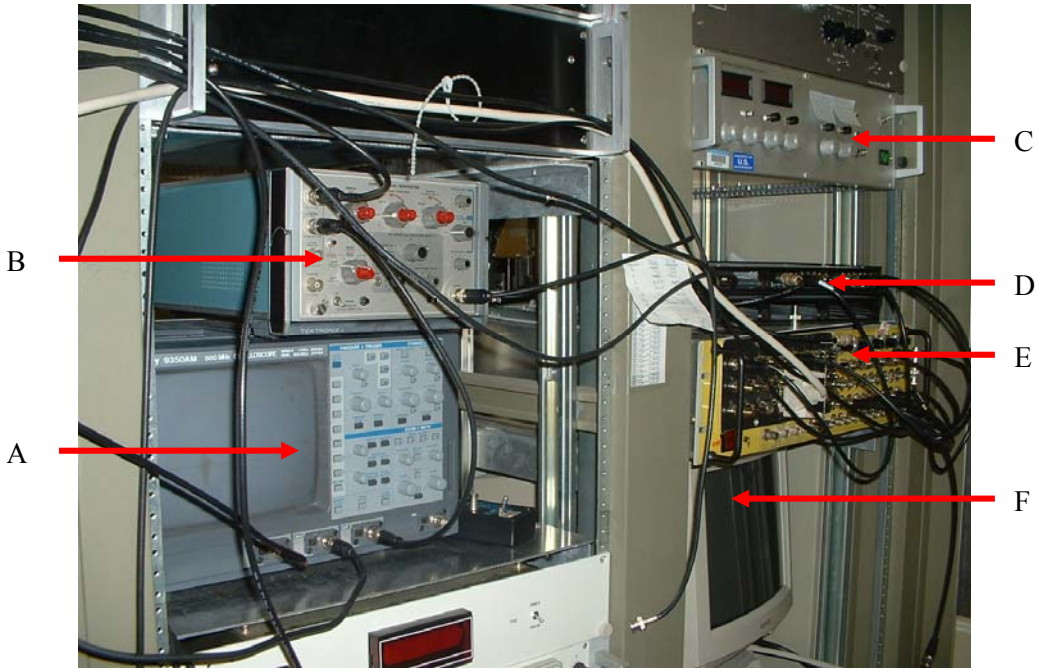

FIG. 3.7. Instrumentation in the electronics rack. (A) Lecroy digital storage scope and (B) Tektronix pulse generator used for collector and sample signal capturing and electron gun pulsing. Also shown are the (C) STAIB gun controller, (D) DAC card interface box, (E) DC ammeter circuitry box, and (F) computer. Instruments were mounted in the conducting rack to avoid electromagnetic interference with cabling and ammeter box.

cables in Fig. 3.9), with the signal carried on the inner wire, the inner shield tied to the signal potential, and the outer shield tied to earth ground. Precautions were taken to tie all cable shielding to a single-ground point located on the ammeter box, to minimize noise associated with ground loops. A block diagram of the pulsed-setup cable shielding and grounding scheme are shown in Fig. 3.8. All ammeter and integrator circuitry, along with the timing circuit and collector battery supplies, were enclosed in a grounded aluminum box that was carefully designed to shield the internal circuitry from external as well as internal electromagnetic noise caused by circuit cross-talk and circuitry power supplies. Fig. 3.9

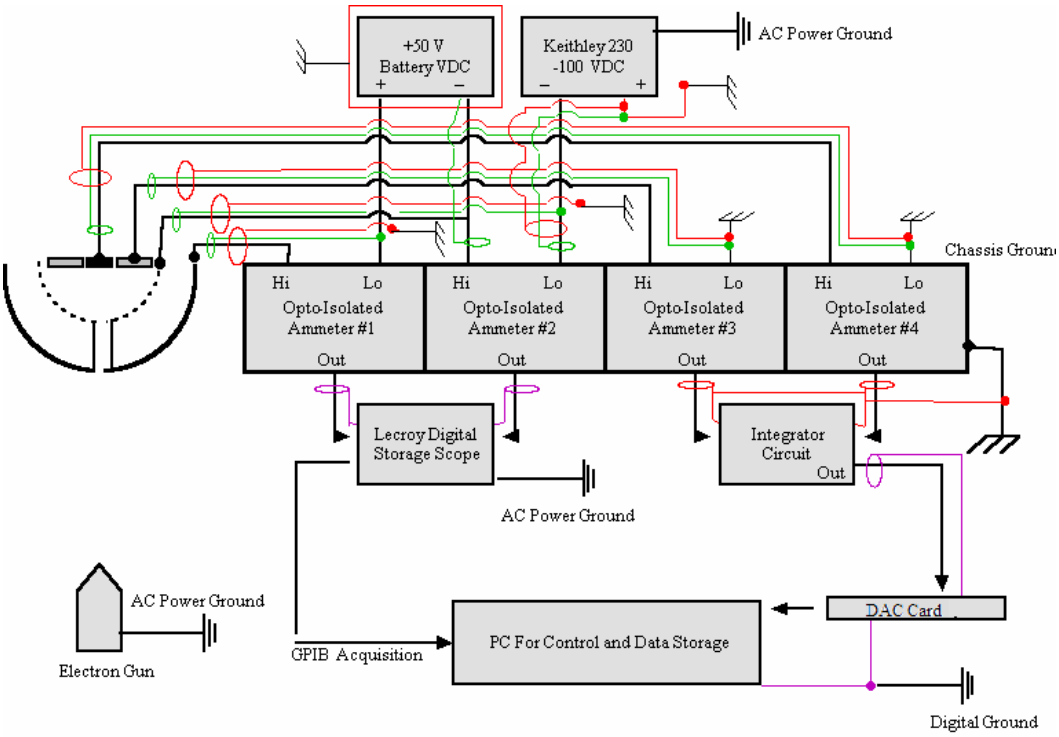

FIG. 3.8. Simplified pulsed-yield block diagram showing grounding and shielding scheme. The timing circuit and pulse generator have been omitted from this diagram for simplicity. Current signals were carried with Triax cabling with the inner shield at the signal potential, and the outer shield at ground. All ground connections for signals were terminated at the ammeter box. High-powered equipment as well as the computer were put on different AC power line circuits for noise control.

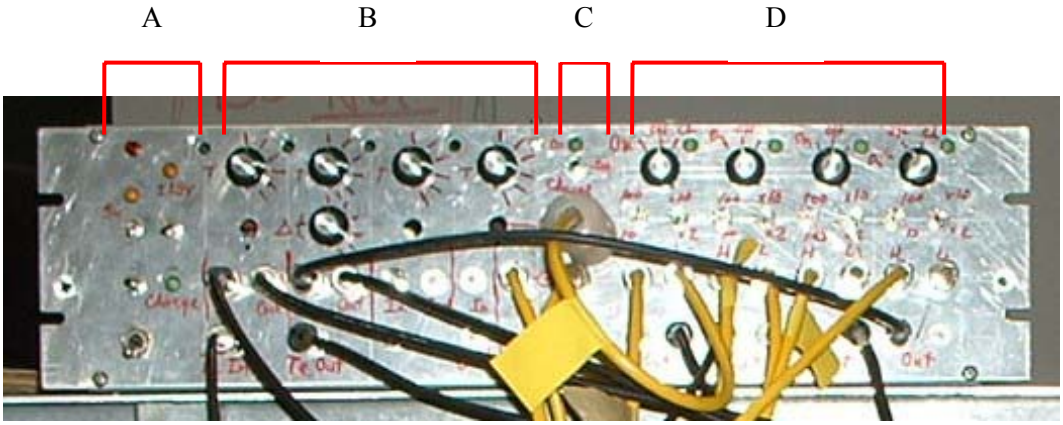

FIG. 3.9. Front panel of the ammeter box used for pulsed-yield measurements. (A) Switches on the left controlled power to ammeter circuits, integrator circuits, and battery charger. Also shown are (B) four integrator circuits with switches to control integration times and time constants (see Table 3.4), (C) power and charging switch to ammeter circuitry, and (D) four ammeters with switches to control the gains for the 1st and 2nd stages (see Table 3.3).

shows the front panel of the ammeter/integrator box. The inside of the ammeter box is shown in Fig. 3.10. Finally, all high-powered equipment (vacuum pumps, guns, gauges, etc.) were placed on a different AC power-line circuit than measurement apparatus (ammeters, integrators, oscilloscope, computer, etc.), and low-pass AC line filters were installed to reduce any high-frequency noise loaded on the AC power lines. After making these alterations, final noise levels for the pulsing circuitry was <20 nA (<5 nA with the Keithley 230 power supply disconnected) over the frequency range of 0.1-1 MHz. A summary of the noise contributions for different laboratory equipment before and after noise reduction modifications are given in Table 3.1. Suggestions for further noise reduction and signal cleanup are discussed in Section 6.1.2.

Once the collector, suppression grid, sample and stage current signals were measured with the ammeters, two general methods existed for signal processing and yield calculation. The first method involved taking ratios of the peak maxima using Eqs. (3.1) to (3.3), referred

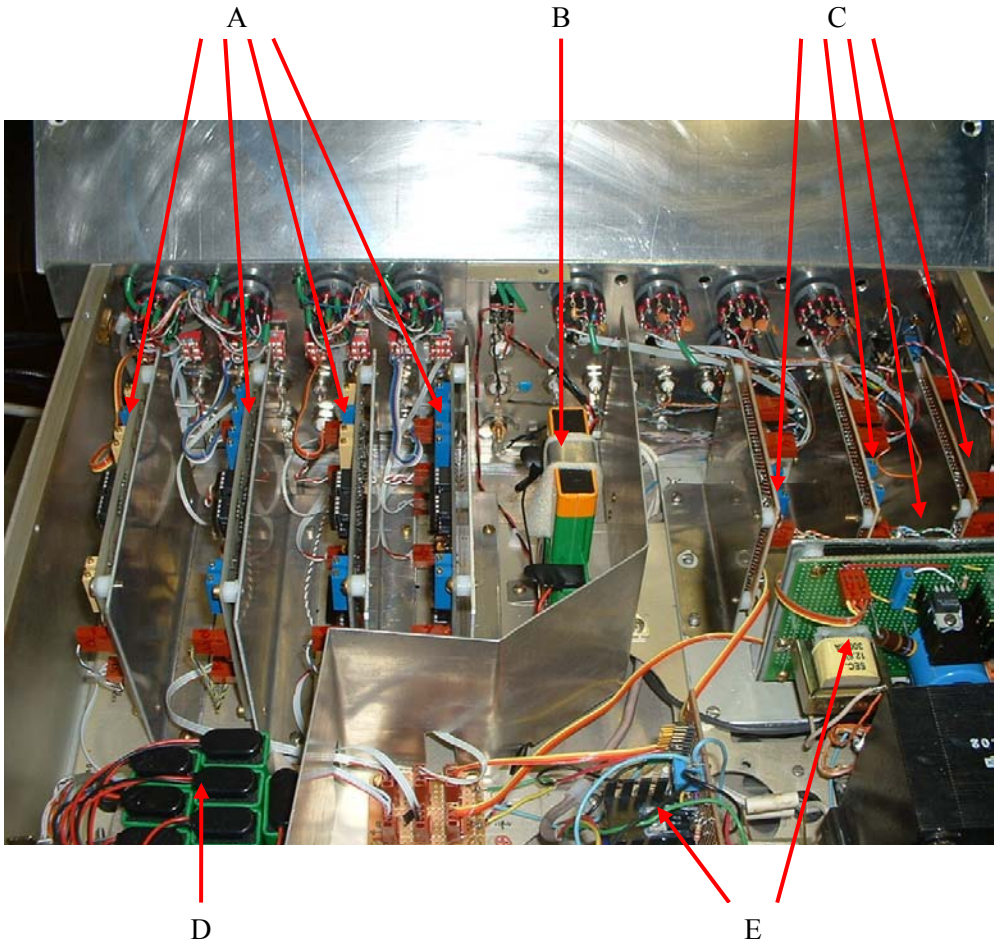

FIG. 3.10. Inside of the ammeter box used for pulsed-yield measurements. Shown are (A) the four ammeters circuits, (B) a battery power supply used to bias the collector to +45 V with respect to the suppression grid, (C) four integrator circuits, (D) a floating battery power supply for stage 1 of the ammeters, and (E) AC-driven power supplies used to power integrator and ammeter circuitry. Also, aluminum plate plating was used throughout the box to shield sensitive electronic circuitry from electromagnetic noise and crosstalk.

to as the current-profile method (see Sections 4.2 and 5.3.2 for details on the implementation of this method). However, this method could only be used if the pulse durations (typical signals duration were 5 μs) exceeded the ammeter rise and fall times (a total of ~9 μs for the $2 \cdot 10^7$ ammeter setting). Also, the pulse profiles emitted from the electron guns were required to be square such that a plateau maximum could be captured. In order to accommodate

TABLE 3.1. Measured noise-level contributions on the pulse-measuring circuitry from various lab instruments.

Instrument	Noise Amplitude Prior to Reduction	Noise Amplitude After Reduction
Lambda Power Supply	>1 μA	0 μA
DC-Patch Panel (on)	>1 μA	0 μA
Computer Monitor	~100 nA	<5 nA
Ion and Convectron Gauge Controller	~25 nA	0 nA
Keithley 230 Supply (low side of grid)	~20 nA	~20 nA
Lecroy Oscilloscope	~20 nA	5 nA
Turbo Pump	<1 nA	<3 nA
Mechanical Pump	<1 nA	<3 nA
Flood Gun and Controller	<1 nA	<3 nA
Ion Pump	<1 nA	<3 nA

shorter-duration pulses (as well as nonuniform pulses), and to minimize the effects of random noise on the measurement, another method for yield calculation was utilized that involved integrating the current signals with respect to time to obtain the total signal charge. By doing this, the response time of the ammeters, with respect to the signal duration, became less important. Although the magnitudes of the measured signals depended on the response time of the ammeters, the area under the current signals remained unchanged. Using this integration method, yields were calculated from ratios of total charge as

$$\sigma = \frac{Q_c}{Q_0} = \frac{\int I_c dt}{\int I_c dt + \int I_s dt + \int I_{stg} dt + \int I_g(0V) dt}, \tag{3.4}$$

$$\eta = \frac{Q_c(BSE)}{Q_0} = \frac{\int I_c dt}{\int I_c dt + \int I_s dt + \int I_{stg} dt + \int I_g(-50V) dt}, \tag{3.5}$$

$$\delta = \sigma - \eta . \tag{3.6}$$

Signals were integrated using one of two methods: either the pulses were captured on the LeCroy digital storage oscilloscope, and then sent to the computer (via GPIB interfacing)

for computational integration; or signals were sent to one of four integrator circuits (described in more detail below), and then a DC output voltage was sent to the computer DAC card. Fig. 3.11 shows a typical sample and collector pulse as captured with the oscilloscope. Table 3.2 summarizes the oscilloscope settings for measuring 5 μs, 10-100 nA electron pulses. Further details on methods for yield measurement and calculation are given in Section 4.2.

The ammeter, integrator, and timing circuitry was designed and built by Vladimir Zavyalov. Further details on the instrumentation are presented in Zavyalov (2003b). To achieve ammeters with both the sensitivity (100 pA) and speed (~1 μs) for making pulsed measurements, both shunt and feedback ammeters were initially designed and built, and their performance results were compared. A short summary of these initial ammeter designs is described as follows:

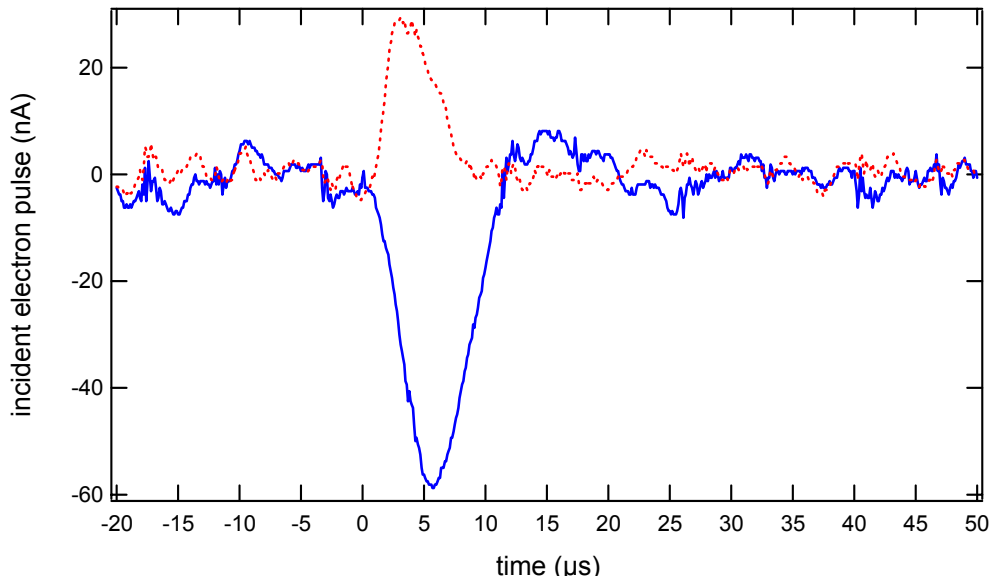

FIG. 3.11. Typical electron current pulse profiles for the sample (dot) and collector (solid). Incident pulses were 5 μs, 50 nA on Au at E_0=800 eV. Similar pulsed signals were obtained for stage and suppression grid signals. Delayed rise and fall times were caused by the system capacitance and ammeter response times.

TABLE 3.2. LeCroy 9350AM 500 MHz Oscilloscope settings for pulsed yields.

Scope Setting	Setting Value
Trigger Setup	Edge Triggering, Positive Slope, Ext. 10, DC Coupling DC 50 Ω, Holdoff: off, Normal
Time Settings	10 μs/div., 20 μs delay
Amplitude Settings	0.2-1.0 V/div, 0 offset

i) A shunt picoammeter was built using a Burr-Brown OPA 602 operational amplifier (Zavyalov, 2003) with input resistances of 100 kΩ and 1 MΩ (both resistors were tried). At an amplifier gain of 10^6 V/A, the internal noise level was found to be ~4 mV (4 nA), comparable to the noise level generated by our vacuum system. However, due to the stray capacitance of the input cables (~100 pF), combined in parallel with the input resistance of the ammeter, the resulting response time of the ammeter ranged from 10-100 μs, which was not adequate for our measurements. Consequently, this approach was not pursued further.

ii) A single-stage resistor-feedback operational amplifier was built using an Analog Burr-Brown OPA 602 operational amplifier (Zavyalov, 2003). The single-stage amplifier included a feedback resistor of 10^7 Ω along with a compensating capacitor in the feedback loop chosen to match the input RC time constant. With a gain of 10^6 V/A this amplifier had an internal noise level of ~1 mV (1 nA) and a bandwidth of roughly 250 kHz (rise time of ~2 μs). Both the amplification and response time parameters of this amplifier outperformed the shunt ammeter, so further development of this approach was pursued.

The final version of the ammeters (four were built) were composed of three stages, and were equipped with optically coupled isolation amplifiers. The stages and the circuit

schematics of the opto-isolated ammeter are outlined in Zavyalov (2003). The first ammeter stage was built using a low-noise, low-leakage operational amplifier. The feedback resistance for this stage was chosen to range between 10-100 kΩ to optimize the signal-to-noise ratio, as well as the ammeter response time. This provided a selectable gain of 10^4 to 10^5 V/A (selectable on the front panel as shown in Fig. 3.9) at 200-400 kHz bandwidth. The second ammeter stage transferred the voltage signal from the first transimpedance stage to the third amplifying stage through optical coupling. Analog optocouplers provided ~2.6 kV isolation between the floating signals and output ground with low nonlinearity of 0.01%. Optical coupling was achieved through a light emitting diode (LED) with two matching photodiodes detecting optical signals from the same LED. To maintain isolation, the input and output op amps on either side of the optocouplers were operated with separate power sources (not shown in the schematic). In order to maintain low-noise operation and to avoid electromagnetic coupling, batteries were used to power the circuit's front end. The overall gain for the second stage was 2-10 V/A (selectable on the front panel as shown in Fig. 3.9), with an overall bandwidth of DC-1MHz, limited primarily by the capacitance of the optocoupler photodiodes.

Finally, the third amplifier stage was composed of a standard inverting voltage amplifier, with an additional gain of 100 V/A and a bandwidth ranging from DC-63 MHz. The overall gain of the three-stage ammeter ranged from $2 \cdot 10^6$ to $1 \cdot 10^8$ V/A (selectable on the front panel as shown in Fig. 3.9), with an internal noise level of 0.6-3.0 nA and a maximum bandwidth ranging from 35-350 kHz. Table 3.3 summarizes the different selectable amplification settings along with associated noise levels and response times.

Integrator circuits were used as a method to capture the voltage outputs of the ammeters. In order to convert a short impulse voltage signal from an ammeter to a DC output voltage, which could then be recorded by the computer through a data acquisition board, a

TABLE 3.3. Ammeter gain settings with corresponding response times and maximum frequency bandwidth. Values could be selected on the front panel of the ammeter box (see Fig. 3.9).

Overall Gain (V/A)	Feedback Resistance (kΩ)	2nd Stage Gain (V/A)	Rise Time (μs)	Settle Time (μs)	Bandwidth (kHz)	Input Noise (nA)
$2x10^6$	10	x2	1	1.4	350	3
$1x10^7$	10	x10	2	3	175	3
$2x10^7$	100	x2	4	5	90	0.6
$1x10^8$	100	x10	10	15	35	0.6

switched integrator circuit was used. A description of the integrator and sample-and-hold circuitry is given in Zavyalov (2003). For the integrating stage, a precision integrating amplifier was chosen. This amplifier was based on a low-bias current FET op amp with integrating capacitors, and low leakage FET switches—all incorporated on the same chip. Since the complete circuit was on a single chip, this particular amplifier eliminated many of the problems commonly encountered in discrete designs, such as leakage current errors, stray capacitance interference, voltage offset drift, and noise pickup. High quality metal-oxide internal capacitors with excellent dielectric characteristics provided high temperature stability and low nonlinearity of ~0.005% that was especially important for short integration times. TTL/CMOS-compatible timing inputs controlled the integration period, as well as the hold-and-reset functions to set the effective transimpedance gain and reset (discharge) the integrator capacitor. The overall transfer function of the integrator was:

$$V_{out} = \frac{Q}{T} \cdot R_f G = \frac{\Delta t}{T} \cdot I_{in} R_f G \,, \tag{3.7}$$

where Q was the total charge, T was the integrator time constant, R_f was the ammeter feedback resistor of the ammeter first transimpedance stage, G was the second stage gain, Δt was the

integration time, and I_{in} was the measured current at the ammeter input (see Table 3.3). The integration time, Δt, was selected to be longer than or equal to the current impulse duration, and the integrator time constant was selected independently over a range of 4-100 μs (see Fig. 3.9). Table 3.4 summarizes the different selectable integration times and time constants.

To increase the integrator DC hold time, a monolithic sample-and-hold circuit was used as an output stage of the integrator. This circuit utilized BI-FET technology to obtain ultra-high DC accuracy with fast acquisition of the signal and low droop rate (Zavyalov, 2003). It operated as a unity-gain follower with accuracy of ~0.002 percent. The droop rate was set by an external capacitor chosen for our applications as 0.1 μF, and was expected to be ~0.3 mV/s. The data acquisitioning time was controlled primarily by the computer's speed to execute Labview commands, and was estimated to be ~500 ms. The total output signal change during data acquisition was expected to be less then 0.01 percent, and did not depend on the integration time chosen.

TABLE 3.4. Integration times, Δt, and integrator time constants, T, with associated integration capacitors. Values could be selected on the front panel of the ammeter box (see Fig. 3.9) and were chosen to be greater than the pulse-width duration.

Integrator Time Constant		1	2	3	4	5	6
T	C (pF)	40	60	100	160	220	1000
	T (μs)	4.0	6.0	9.0	15.5	21	92
Integration Time		1	2	3	4	5	6
Δt	C (nF)	0.33	0.47	0.62	1.0	1.9	10
	Δt (μs)	5.5	6.5	8.5	12.5	21.5	104

Finally, to control the proper operation of the switched integrator and sample-and-hold circuit, a simple digital pattern generator was used (Zavyalov, 2003). This generator created TTL level digital signals to control the RESET, INTEGRATE, and SAMPLE switches at a rate controlled by a trigger signal that originated from the computer DAC card, controlled by Labview. A detailed summary of the circuitry, which includes several written reports and electrical schematics, is provided in Zavyalov (2003).

3.4 Electron Gun Operation and Characterization

For measuring both insulator and conductor electron yields with our detection apparatus, it was important to use mono-energetic low-amplitude electron sources that exhibited highly stable beam current emission on the order of 10 pA. Moreover, the electron sources needed controllable spot sizes, with diameters ranging from 0.1-10 mm, as well as stable beam positioning. The desired beam current amplitudes were to range from 1-100 nA, kept to a minimum to avoid contamination effects and charging (Davies and Dennison, 1997). Also, it was important to be able to measure electron yields over a wide energy range, starting from the first crossover energies, E_1^{δ} and E_1^{σ} (<100 eV), to energies well beyond E_2^{δ} and E_2^{σ} (>10 keV). Furthermore, for insulator measurements, it was imperative to choose sources with pulsing capabilities with magnitudes <100 nA and durations <10 μs. These requirements were governed by the insulator charging rates (discussed more fully in Sections 5.1 and 5.3.4), especially at energies $E_1^{\sigma}<E_0< E_2^{\sigma}$. For example, in Section 2.3 it was estimated a single 5 μs pulse at 10-50 nA ($\sim 10^{-13}$ C/mm^2 or $\sim 10^6$ electrons/mm^2) could alter an insulator's surface potential anywhere from 0.1-1 V. These small potentials were sufficient to alter total and SE yields in the positive charging regime after just a few pulses (refer to Sections 2.3.9, 5.1, and 5.3). Hence, it was important to stay well within this charge limit. Also, as summarized in

Section 2.2, most previous pulsed-yield studies found in the literature stayed well within this charge density limit. Furthermore, in addition to choosing a low-amplitude pulsing source, it was preferred to have electron sources that emitted uniform pulse profiles (for example square-wave pulses) such that pulse peak plateaus could be monitored as a function of time.

Two electron guns used for both DC and the pulsed-yield measurements were the STAIB Model EK-5-S gun, spanning energies ranging from ~50 eV to 5 keV, and the Kimball Model ERG-21 gun, spanning energies ranging from 4 keV to >20 keV. These guns fulfilled the requirements described above with one exception (as will be discussed further below): the STAIB gun did not emit uniform pulses such that pulse peak plateaus could not be monitored as a function of time to calculate electron yields.

During yield measurements, electron-beam parameters such as the beam energy, emission current, beam spot-size dimensions, and beam positioning were optimized to obtain the most accurate yield measurements. For both DC and pulsed yields, emission currents from the guns ranged between 1-100 nA (depending on the measurement set). Additionally, beam spot dimensions were kept to a minimum and the beam direction was maintained with critical precision (<0.5 mm variation at the sample face). Optimization of the electron beams required manipulation of vertical, horizontal, and angular translation of the sample stage as well as adjustment of the energy, focusing, deflection, suppression grid, and filament current gun controls. Sample stage adjustments varied from one sample to the next, but are not covered in this section (see Sections 3.2 and 4.1 for further details on electron beam optimization procedures). However, details of the DC and pulsed-emission control settings for both STAIB and Kimball guns were independent of sample selection (except for horizontal and vertical deflection settings), and are outlined in the paragraphs that follow.

All DC operation settings were determined for both the STAIB and Kimball guns, before pulse-yield optimization was performed. The general procedure for DC optimization went as follows. First, the beam energy was set and the filament current was adjusted. Both guns provided monoenergetic electron beams with energy resolution of $\Delta E/E<1\cong10^{-4}$ for the Kimball gun at 5 keV, and $\Delta E/E<1\cong10^{-3}$ for the STAIB gun at 5 keV. Furthermore, after waiting roughly 60 seconds after adjusting the beam currents, both guns continued to provide beam current stability with <1% variation over a time span of ~30 min. Typical operating filament currents ranged from 1.40-1.50 A for the STAIB gun, and 1.50-1.60 A for the Kimball gun. Second, rough adjustment of the grid-potential settings was performed to obtain emission currents on the order of 1-100 nA (depending on the experiment). Third, the beam spot size was monitored on a phosphor-screen while focus settings were adjusted to minimize the diameter. For both guns, the target diameter of the spot-size was <1 mm. With the Kimball gun, this target was easily met since beam-spot sizes (as determined by sharp-edge beam profiling) were determined to range easily between 0.2-1 mm in diameter. For the STAIB gun, spot sizes tended to increase with decreasing energy such that below 400 eV, the spot size exceeded 1 mm (generally ranged from 0.5-3 mm). For the Kimball gun, spot sizes were easily maintained below 1 mm for operating energies ranging from 5-20 keV. Below 5 keV, electron beam stability was difficult to maintain for the Kimball gun. It should be mentioned that, although reasonable estimates for the beam spot size could be obtained by using the phosphor screen, as described above, in the future, a more careful beam characterization study should be conducted in future work to accurately determine the spot sizes as a function of incident energy. As will be described later in Section 5.3.4, variations in the beam spot size resulted in errors in the charge-decay analysis as a function of incident electron current density.

After focus and grid adjustments were made, the electron beam was directed into the Faraday cup module to measure the beam current, and gun current emission was adjusted for the specific experimental conditions. Further details of the Faraday cup module are contained in Nickles (2002). For the STAIB gun, this adjustment was best performed by altering the filament current (optimal operating currents between 1.40-1.50 A) since grid and focus settings were interdependent. For the Kimball gun, beam current adjustment was best performed by fine-tuning the grid potential. DC operation settings for the STAIB and Kimball guns are given in Tables 3.5 and 3.6, respectively.

After DC-emission settings were optimized, the pulsed-emission settings for each of the guns were found. The STAIB gun controller possessed two pulsing options (each with separate BNC inputs) that both acted to momentarily lower the grid suppression potential to emit electron pulses. The first front-panel TTL input led to a precision potentiometer that controlled the output of a fast-acting potentiometer tied to the grid. This potentiometer was capable of emitting pulses ranging from DC to 1 ms in duration. The second pulsing input (on the back of the controller), designed for a 5-15 V input, provided capacitor-resistor coupling to the grid, and was optimized for 1-2 μs (500 ns pulse rise time) pulse durations. For insulator measurements, the back-panel pulsing input was used for the shorter pulsing time duration.

To pulse the STAIB gun, the controller was first adjusted for optimal DC emission (as shown in Table 3.5). Then, grid and focus knob settings were increased such that the electron beam was fully suppressed. The pulse generator then provided a 5 μs, 12-13 V square wave that momentarily lowered the grid potential of the gun. A few problematic features of the STAIB gun were that the grid and focus knob settings were coupled such that by adjusting one, the other also changed. If more emission current was needed, the grid knob setting was not adjusted further, but the filament current, I_f, of the gun was increased until the amplitude

TABLE 3.5. STAIB gun settings for DC measurements. Typical filament currents ranged from 1.40-1.50 A. Gun current emission levels were adjusted by adjusting the filament current.

Beam Energy (eV)	Grid Knob	Focus Knob
80	1.00	0.56
90	1.00	0.56
100	1.00	0.56
150	1.10	0.64
200	1.28	0.76
250	1.34	0.82
300	1.41	0.89
350	1.50	1.02
400	1.54	1.06
450	1.62	1.17
500	1.68	1.26
600	1.52	1.63
700	1.98	1.63
800	1.98	1.63
900	1.98	1.63
1000	1.98	1.63
1200	2.24	1.95
1500	2.48	2.28
2000	3.80	3.84
3000	4.43	4.53
4000	4.40	4.52
5000	4.50	4.55

of the emitted electron pulse became adequate for measurements. STAIB pulsed-emission settings are given in Table 3.7. Pulse-generator settings for STAIB gun pulsing are shown in Table 3.8. The full pulsed-yield measurement procedure, including optimization and adjustment of gun controller settings, are provided in Section 4.1.

By increasing pulse width durations sent to the STAIB gun (from the pulse generator), it was found as the pulse duration exceeded ~2 μs, the pulse profiles emitted from the gun became nonuniform. The manufacturer's reported optimal pulsing range was 1-2 μs. Beyond this pulsing range, the emitted pulses displayed a negatively sloped plateau as shown in Fig.

TABLE 3.6. Kimball gun settings for DC and pulsed-yield measurements. Settings for DC measurements were the same as for pulsed measurements except the Blanker option that was disabled on the controller. The filament current, I_f, was kept constant at all energies. Current emission, I_e, from the gun was controlled by adjusting the Grid potential. The measured leakage current, I_{leak}, from the gun (while fully suppressed) was below the noise level for all energies. Typical signal currents to the collector, I_c, and sample, I_s, are also given for these settings.

Beam Energy (keV)	I_f (A)	Grid (V)	I_e (μA)	Align. Knob	Lens Knob	Blank Knob	I_{leak} (nA)	I_c (nA)	I_s (nA)
6	1.6	40	2.5	-39/16	0.04	39	<0.5	20	20
8	1.6	50	1.4	-36/38	0.36	39	<0.5	20	20
10	1.6	60	1.3	-57/56	1.05	39	<0.5	20	25
12	1.6	60	1.0	-54/86	0.88	45	<0.5	15	25
14	1.6	90	1.1	-49/84	0.28	60	<0.5	15	25
16	1.6	100	2.5	-66/108	0.29	68	<0.5	25	60
18	1.6	110	3.6	-77/114	0.27	68	<0.5	25	60

TABLE 3.7. STAIB gun settings for pulsed measurements. Pulse magnitudes were adjusted by altering the filament current, I_f. Approximate beam diameters as measured on the phosphor screen are given for each energy. Measured pulsed signal currents to the collector, I_c, and leakage currents, I_{leak}, from the gun (while in full-suppression mode) are also shown.

Beam Energy (keV)	Grid Knob	Focus Knob	Beam Dia. (mm)	I_f(A)	I_c (nA)	I_{leak} (nA)
0.1	2.91	2.14	>3	1.45	50	<0.01
0.2-0.3	2.91	2.14	2-3	1.43	50	<0.01
0.4-1.0	2.91	2.14	1-2	1.41-1.42	50	<0.01
1.1-1.5	3.00	2.18	<1	1.43-1.44	50	0.01
1.6	3.15	2.47	<1	1.43-1.44	50	0.01
1.7	3.25	2.60	<1	1.43-1.44	50	0.01
1.8	3.43	2.70	<1	1.43-1.44	50	0.01
1.9	3.50	2.71	<1	1.43-1.44	50	0.01
2.0-2.2	4.80	4.10	<1	1.47	50	0.16
3.0	7.06	6.39	<1	1.53	50	0.18
4.0	7.02	6.30	<1	1.53	50	0.21
5.0	7.81	7.19	<1	1.53	50	0.18

TABLE 3.8. Tektronix 115 Pulse Generator settings for STAIB and Kimball gun pulsing.

Pulse Generator Setting	Value
STAIB Amplitude (Multiplier)	4.0 (1.0) — outputs 13 V to STAIB
Kimball Amplitude (Multiplier)	4.5 (0.5) — outputs 5 V to Kimball
DC Offset	Preset: 0 V
Pulse Polarity	Positive
Rise/Fall Time (Multiplier)	100 ns/100 ns (1)
Pulse Period	1 ms
Pulse Width	5 μs
Mode	Manual or External
Trigger	Burst

3.12. As can be seen from the figures, STAIB pulse profiles ranging from 2-10 μs were measured using two different ammeter settings: $2 \cdot 10^6$ V/A with a 1 μs response time, and $1 \cdot 10^7$ V/A with a 4 μs response time (see Section 3.3 and Zavyalov (2003b) for details on the ammeters). For both ammeters, the shape of the electron gun pulse profiles were observed to be at first somewhat symmetric for t<2 μs, but then declined for the rest of the pulse duration. Due to the relatively poor pulse profiles of the gun beyond a pulse width of 2 μs, the pulse maxima could not be used to calculate pulsed-yields. Instead, for the STAIB gun, pulse profiles had to be integrated with respect to time to obtain total accumulated signal charge, and then the appropriate ratios of total charge were used to determine the yields (as discussed in Section 3.3).

Finally, it was found even while fully suppressed, the STAIB gun still emitted small (but measurable) DC leakage current, I_{leak}, that increased with increasing beam energy. Considerable efforts were made to minimize this leakage current (by adjusting grid/focus suppression settings), but were not entirely successful at all energies. The magnitude of the leakage was on the order of 10-200 pA, and increased with increasing gun energy. Measured values of I_{leak} for optimum gun settings for a range of energies are listed in Table 3.7. It was

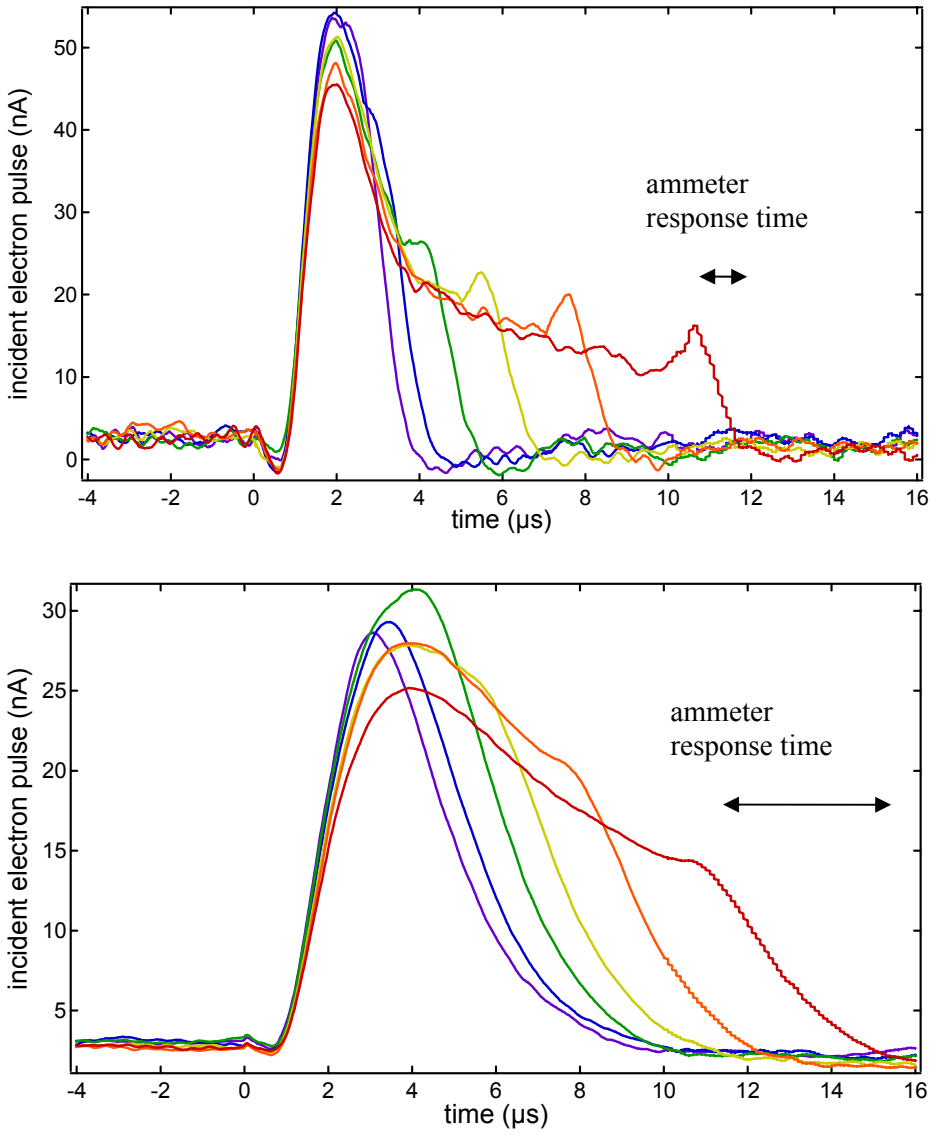

FIG. 3.12. Pulse profiles for the STAIB gun at 1 keV as measured by the Faraday cup. Similar profiles were seen in sample current profiles. Two ammeters were used with 1 μs (top) and 4 μs (bottom) response times. Pulse widths supplied by the generator were 2 μs (purple), 3 μs (blue), 4 μs (green), 5 μs (yellow), 7 μs (orange), and 10 μs (red) duration square waves. As seen in the figure, electron pulse profiles emitted from the gun were not square or symmetric in time.

important to minimize the leakage current so it would not contribute to insulator charging between pulses.

Pulsed settings for the Kimball gun were identical to the DC settings (summarized in Table 3.6), except the Blanker switch was enabled. The Blanker switch provided internal deflection of the beam such that electrons could not exit the gun aperture (providing full cutoff of the emission current). The gun was capable of pulsing from 20 ns to DC emission. To pulse the gun, the Blanker cutoff voltage was increased until DC current emission went to 0 nA. The Blanker cutoff voltage depended on operating energy, but was independent of all other gun-controller settings. A 5 V TTL trigger from the pulse generator (see Table 3.8) was used to trigger the gun. The amplitudes of the incident pulses could be adjusted by changing the Grid potential settings. To ensure the electron beam was completely suppressed (and no leakage currents were present), sample current was monitored on the oscilloscope screen with a scope setting sensitive to <0.1 nA. For all energies, no leakage current was measurable above the system noise level (see Table 3.7).

The pulse profiles emitted by the Kimball gun were square (any curvature was due to the response time of the ammeters), and the pulse duration could be completely controlled by the pulse width setting on the pulse generator. The practical range of the Kimball gun pulse durations was limited only by the ammeter response times (see Table 3.3). The minimum pulse durations, dictated by the response times of our ammeters, ranged from 500 ns to 1 μs. Representative pulse profiles for the Kimball gun are shown in Fig. 3.13. For pulse durations exceeding ~10 μs, the magnitudes of the current pulse profiles could be used to calculate the electron yields, referred to as the current-profile method (see Section 4.2). As mentioned above, this was in contrast to the STAIB gun, where relatively poor pulse-profile

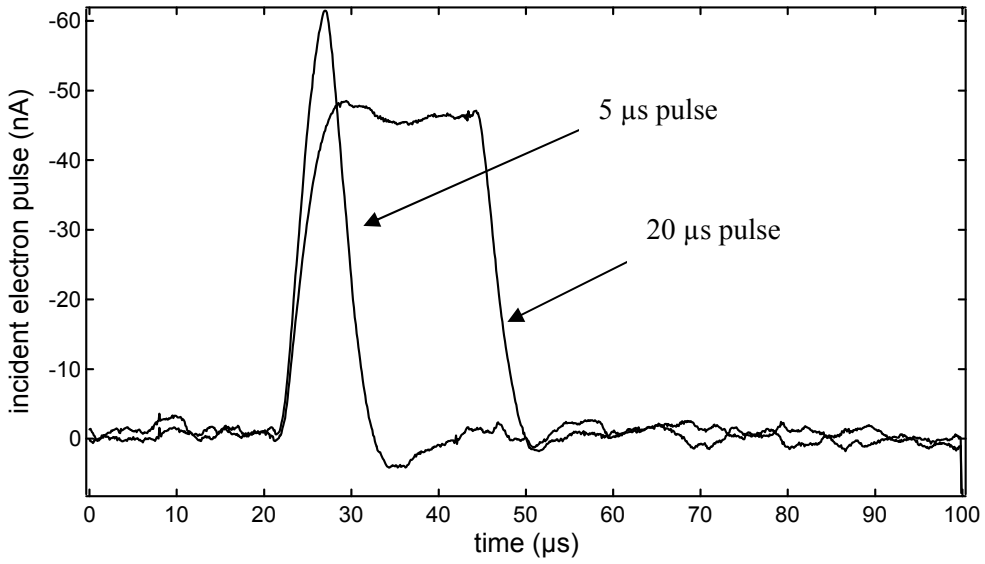

FIG. 3.13. Sample-current pulse profiles for the Kimball gun at 10 keV. Pulse widths supplied by the generator were 5 μs and 20 μs-duration square waves. In contrast to the STAIB gun (see Fig. 3.12), electron pulse profiles emitted from the gun were both symmetric and square in time such that maxima of the pulse peaks could be used to calculate electron yields. The ammeter response time for these measurements was approximately 4 μs.

characteristics made it necessary to calculate yields using a charge-integration method (see Section 4.2).

Finally, as outlined in Section 6.2.3, it would be an interesting future study to calculate insulator electron yields with the Kimball gun using the pulse peak amplitudes, and by varying the pulse duration. Specifically, the charging rates of the insulator could be monitored by using a pulse >100 μs in duration, and by measuring the decay of the plateau with time. These results could be compared with measurements presented in Section 5.3.4, where the charging rates of Kapton^{TM}-aluminum were monitored as a function of incident electron pulse.

3.5 Charge Neutralization Sources

Methods for insulator charge neutralization included a low-energy flood gun used primarily to neutralize positive insulator charging and various lamp sources that extended into the UV, used to neutralize negative charging. Descriptions of the experimental setup for these sources are provided below. Experimental data demonstrating the effectiveness of neutralization are described more fully in Sections 5.1 to 5.3.

The low-energy electron flood gun source was mounted adjacent to the sample (separated from the samples by 11 mm, center of gun aperture to center of sample) in the sample block module as shown in Fig. 3.14. The gun exhibited a wide beam spot and an energy range of a ~1 eV to >100 eV. The gun was composed of a Kimball Physics hairpin tungsten filament (on a CB104 ceramic base), a Wehnelt can extractor, a biasing anode grid, and a grounding grid. The small size (~2 cm long by 0.6 cm dia.) and relatively low cost (parts were ~$100) allowed the possibility of a number of guns to be built for each sample module or to be built for other research studies underway by our group at USU (Dennison *et al*., 2003a; Swaminathan, 2004; Swaminathan *et al*., 2003). Further details of the gun assembly are shown in Fig. 3.15. Details of the sample module design are found in Nickles (2002).

A simple electron gun power supply was custom designed at USU for the gun. Pictures of the controller external panel and internal wiring are shown in Fig. 3.16. An electrical schematic of the controller is shown in Fig. 3.17. As presently designed, the controller allows the Wehnelt can, filament, and anode grid to float to a maximum of -12 VDC using a standard AC-to-DC power supply, although this supply could be replaced with one of a higher voltage to increase the gun's maximum electron energy. The floating potentials of the can, filament, and anode were independently adjusted with 10 kΩ to 25 kΩ 10-turn, wire-

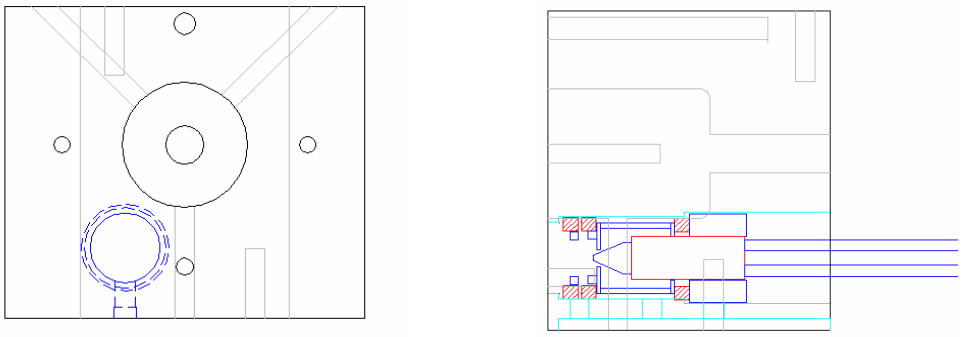

(a) (b)

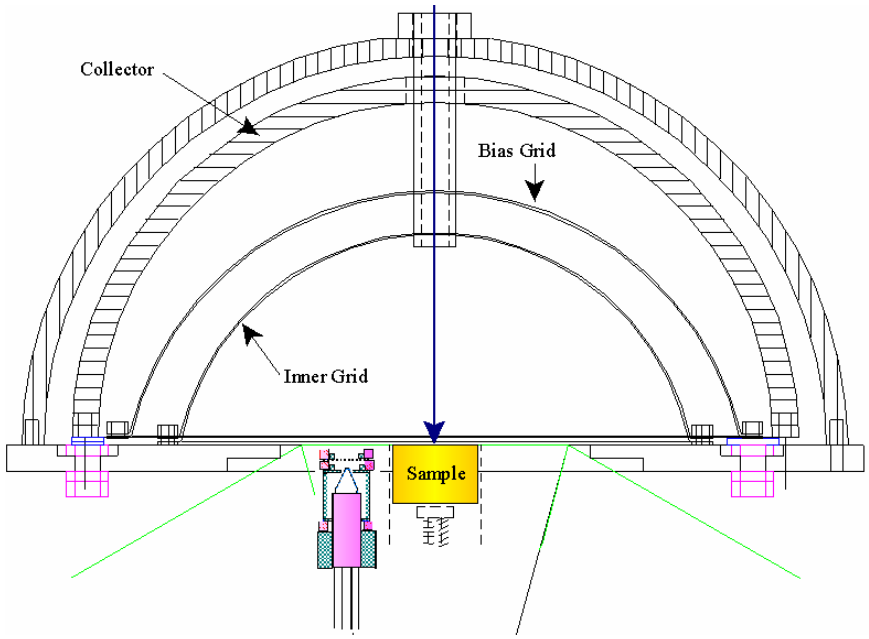

(c)

FIG. 3.14. Details of the electron flood gun in the sample block module. Design drawings of top view (a) and side view (b) of the electron flood gun inside the sample module. Insulating ceramic parts are identified in red, conducting parts are indicated in blue, modifications to the sample module are indicated in light blue and the existing sample module is indicated in black. Diagram (c) showing the assembly diagram for the electron flood gun mounted in a sample module surrounded by the hemispherical grid retarding field analyzer. For scale, the inner grid has a 31.5 mm radius.

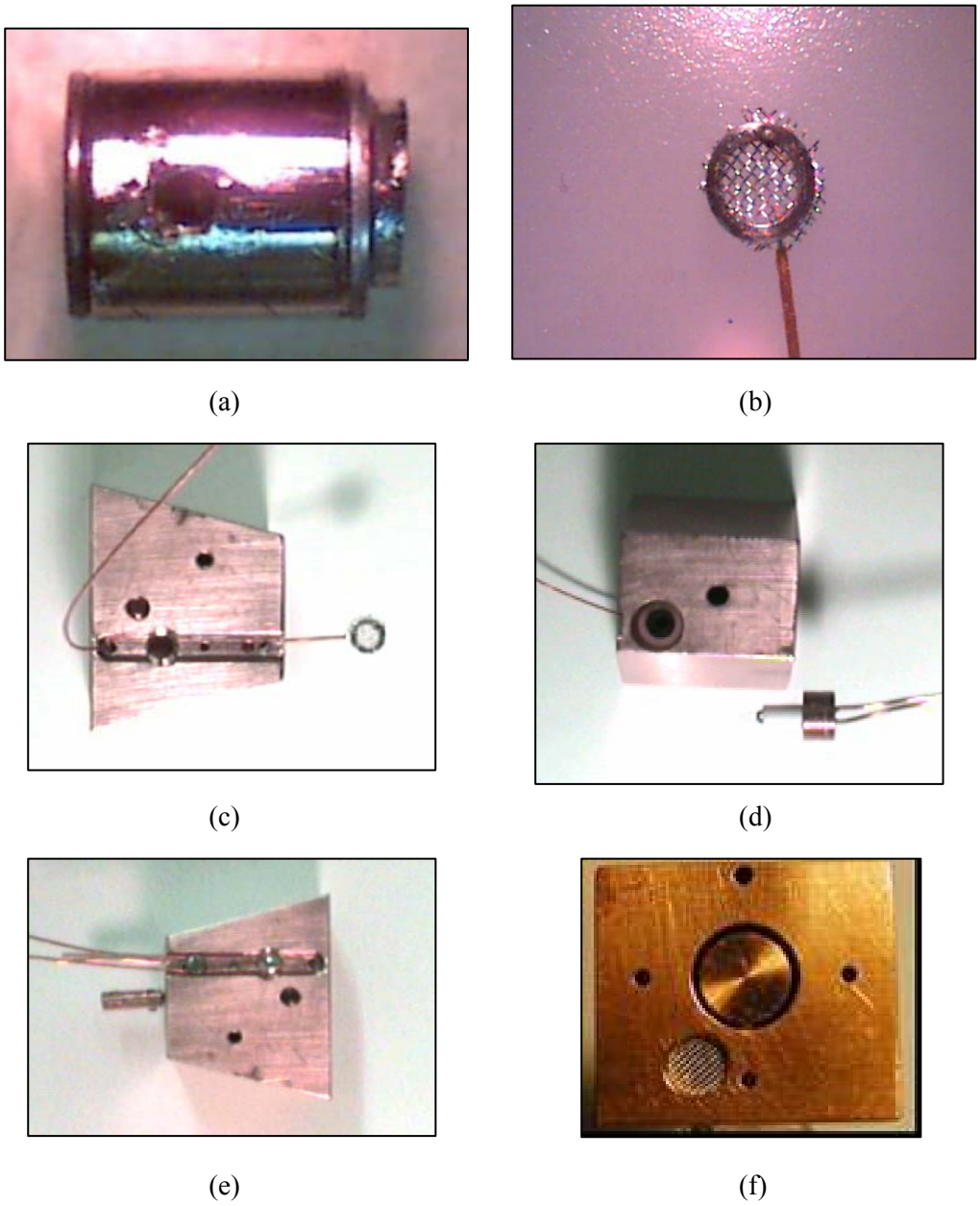

FIG. 3.15. Details of the electron flood gun assembly. (a) Assembled Wehnelt can (7 mm in length) with threaded (#0-80) hole for electrical contact screw. (b) Grid anode (5 mm dia.) with electrical contact wire. (c) Sample block module (side view) with grid anode being inserted. The narrow groove provides a track for anode, and Wehnelt can wires along with the electrical screw-terminal and the set screw that secures the full mechanical assembly inside the module. (d) Sample block module (bottom view) and tungsten filament on ceramic base, mounted in a copper ring ready for insertion into module. (e) and (f) Fully assembled sample block modules (side view and top view).

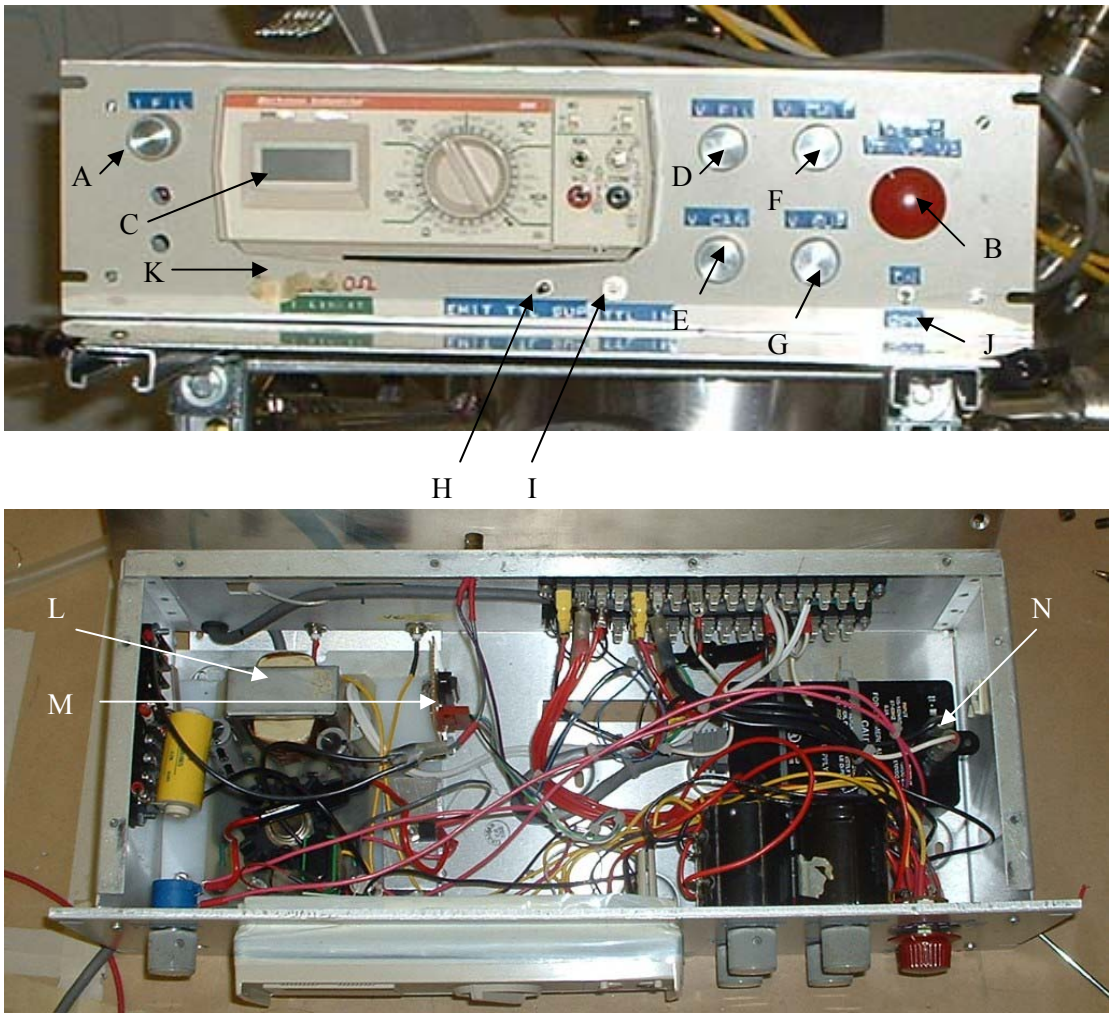

FIG. 3.16. Outside (top) and inside (bottom) of flood gun controller. (Top) The filament current control potentiometer (A) is at the left. The red knob (B) selects the control voltage displayed on the voltmeter (C). The filament voltage (D), Wehnelt can (extractor) voltage (E), anode emission voltage (F), and anode suppressor (G) voltage are set by the four potentiometer knobs. A switch (H) at the bottom center is used to select the voltage placed on the Wehnelt can (extractor); the selections are emission, suppression or TTL control. An input for a TTL control signal (I) is to the right of the switch. Switch (J) provides power to the controller. Switch (K) selects a 2 Ω resistor in series with the filament. (Bottom) Filament 5 VDC power supply (L) is at the left. TTL-controlled relay (M) is to the right of the filament power supply. The 12 VDC floating power supply (N) is mounted at the right of the controller.

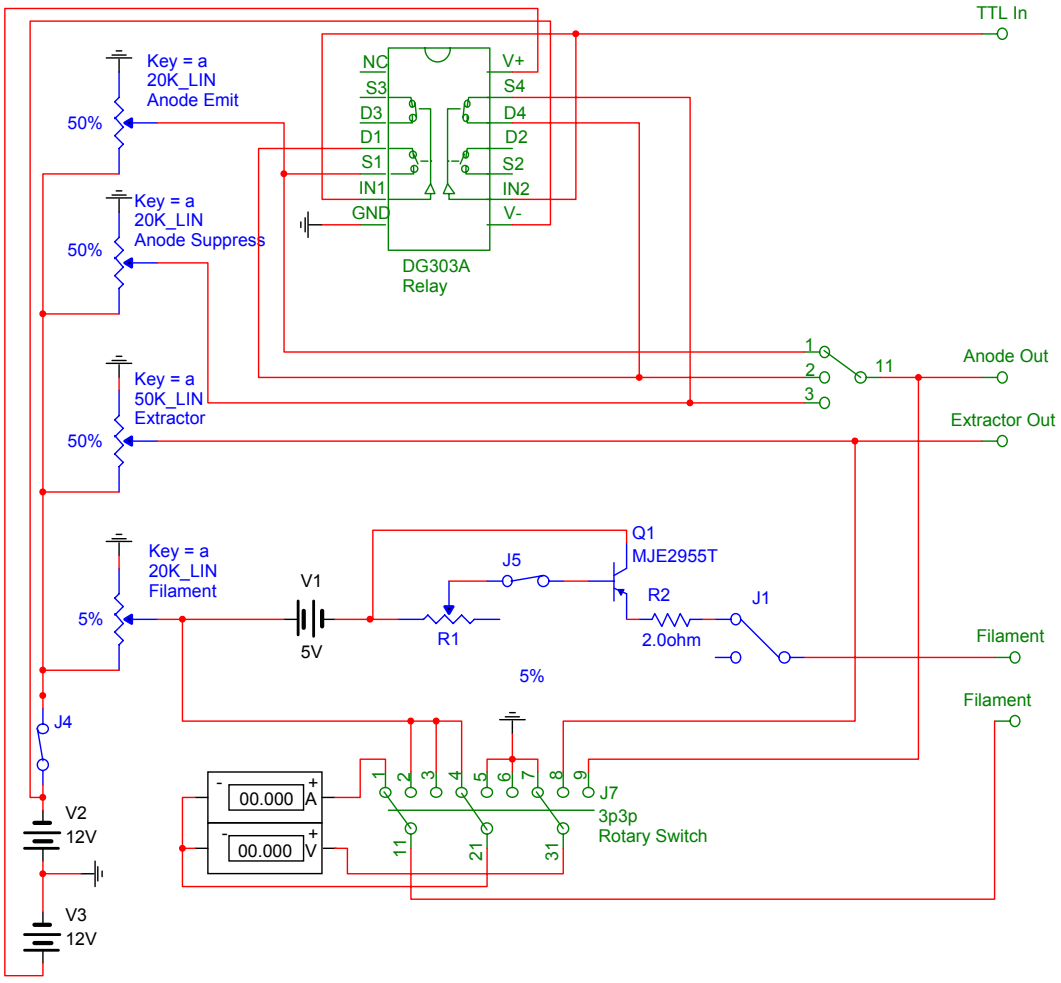

FIG. 3.17. Electrical schematic of the flood gun controller.

wound precision potentiometers. Additionally, the anode potential could be switched, either manually or remotely, using a TTL input between acceleration and suppression modes that could also be independently adjusted. Switching was accomplished using either a manual toggle switch, or an integrated circuit switching relay driven by a TTL input signal. This provided beam blanking capabilities for alternating pulse/flooding measurements. The filament was powered using a 5 V, 3 A (maximum) DC supply. The current to the filament was controlled using a simple bipolar junction PNP transistor (Fairchild MJE2955T), with the

base current controlled with a 10 kΩ potentiometer. Current overloading of the filament was prevented by placing a 2 Ω, 10 W high-powered resistor in series with the filament.

For purposes of sample neutralization, the flood gun was operated by floating the Wehnelt can and filament to a negative potential, and then applying a less negative potential to the anode grid. Table 3.9 summarizes the settings typically used during pulsed measurements such that gun emission current remained ~100 nA (as measured by collector). Between pulsed-yield measurements, the anode potential was switched from suppression to emission mode (controlled with a TTL trigger) for a few seconds between each incident electron pulse to neutralize positive surface charge. This process was self regulating such that once the positive insulator was neutralized, the low-energy electrons were no longer attracted to the surface, and a steady-state current corresponding to a near-zero surface potential was achieved.

The amount of flood gun current drawn to the sample was dependent on the gun's filament current and anode potential, as well as the sample potential. A series of simulations were conducted to model the performance of the electron flood gun using the program SIMION 7. The intent of the simulations was to predict behavior of the electrons and their effectiveness at neutralizing charged insulators over a range of operational beam energies. Fig. 3.18 shows results of a simulation of electron trajectories for electron flood gun at very low beam energy, as used in the FATMAN hemispherical grid retarding field analyzer. The plot demonstrates even at a low sample surface potential of 0.5 V, low-energy electrons on the order of 1 eV are attracted to the surface and can facilitate neutralization. Similar simulations under different sample and flood gun acceleration potentials were performed, and indicated by performing slight physical alterations to the gun, such as the addition of an annular focusing ring, the flood gun could provide a focused low-energy electron beam. Such alterations

TABLE 3.9. Flood gun operation settings for alternating pulse/flood sequencing.

Controller Setting	Setting Value
Filament Current	1.24-1.25 A
Filament Floating Potential	-1 V
Wehnelt Can Potential	-2.5 V
Anode Potential (suppression)	-8 V
Anode Potential (emission)	0 V

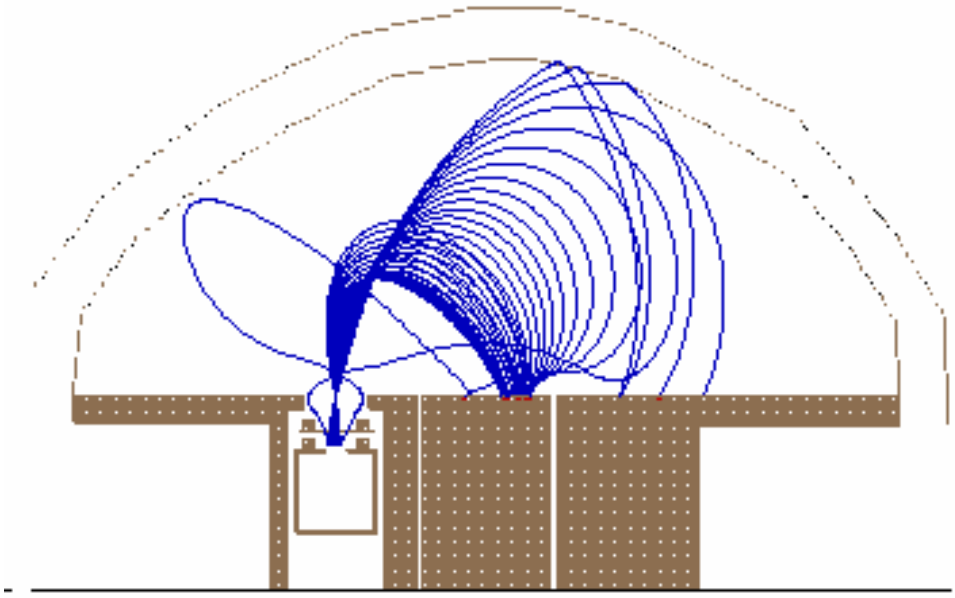

FIG. 3.18. A SIMION 7 simulation of the flood gun inside the detector cavity. The gun sits adjacent to a positively charged sample (center) at +0.5 V and retarding grid (outer hemisphere) at -1 V. The filament electron energy was 0.2 eV, suppression grid bias was -1 V, can bias was -2 V, and anode grid bias was 4 V. Blue lines are electron trajectories for various electron emission angles over the face of the emission aperture. This simulation demonstrates that even low sample surface potentials can attract electrons and undergo neutralization.

may provide additional future uses for the gun such as low-energy electron emission studies (see Section 6.1.1) or the charge storage insulator studies currently underway at USU (Dennison *et al*., 2003a; Swaminathan, 2004; Swaminathan *et al*., 2003).

Additional measurements were performed to test the effectiveness of the flood gun. A gold sample was placed in the sample module next to the gun, and sample current was monitored as the sample was biased to positive potentials ranging from 0 V to +50 V for three different anode potentials, while maintaining a constant filament current of 1.3 A. Plots of sample current as a function of sample bias for three different extraction potentials are shown in Fig. 3.19. Each data set was fitted with an asymptotical exponential function of the form: $I_{0V} + I_{\max}\left(1 - e^{-aVs}\right)$. At a sample potential of 0 V, the current drawn from the flood gun varied from 6-75 nA, depending on extraction potential. This indicated even at very low positive potentials for a flooding duration of 1 s, the flood gun would deliver 4-5 orders of magnitude of electron charge to an insulator than a typical 5 μs, 50 nA incident electron pulse containing ~10^6 electrons. In addition to measuring the sample current, crude energy spectra of the flood gun were taken by stepping the retarding grid as shown in Fig. 3.20. The spectra showed emitted electron energies ranged from 2-4 eV. From these initial diagnostic measurements, it was expected the flood gun would be effective in neutralizing charge buildup accrued during an incident electron beam pulse at energies between the crossover energies. The positive surface potentials that formed in this energy regime would accelerate low-energy electrons towards the surface until the surface was neutralized. However, beyond E_2^{σ}, effective neutralization was not expected since the insulator was expected to charge negative such that low-energy electrons would be repelled.

Since the flood gun was not expected to be very effective in neutralizing negative charge, other methods were explored to neutralize the insulator in this charging regime. UV

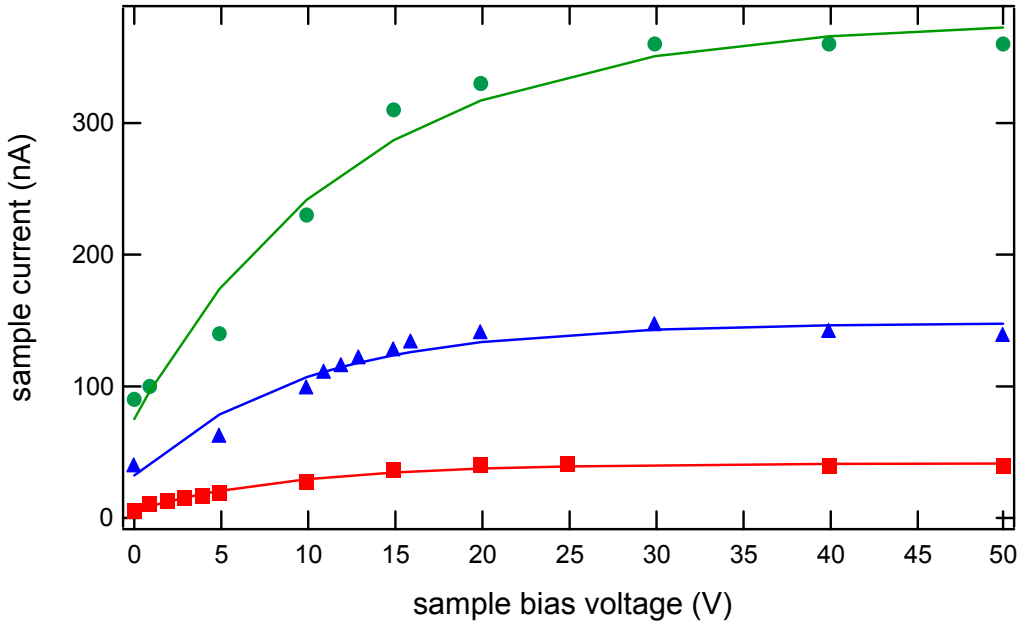

FIG. 3.19. Flood gun current to a biased Au sample. The filament current was 1.3 A for all data; only the gun extraction potential is varied from 4 V (●), 3 V (▲), and 2 V (■). Sample current ranges from 5.5 nA to 75 nA at a 0 V sample potential, and from 42 nA to 380 nA at saturation. Curves are least-squares asymptotic exponential fits.

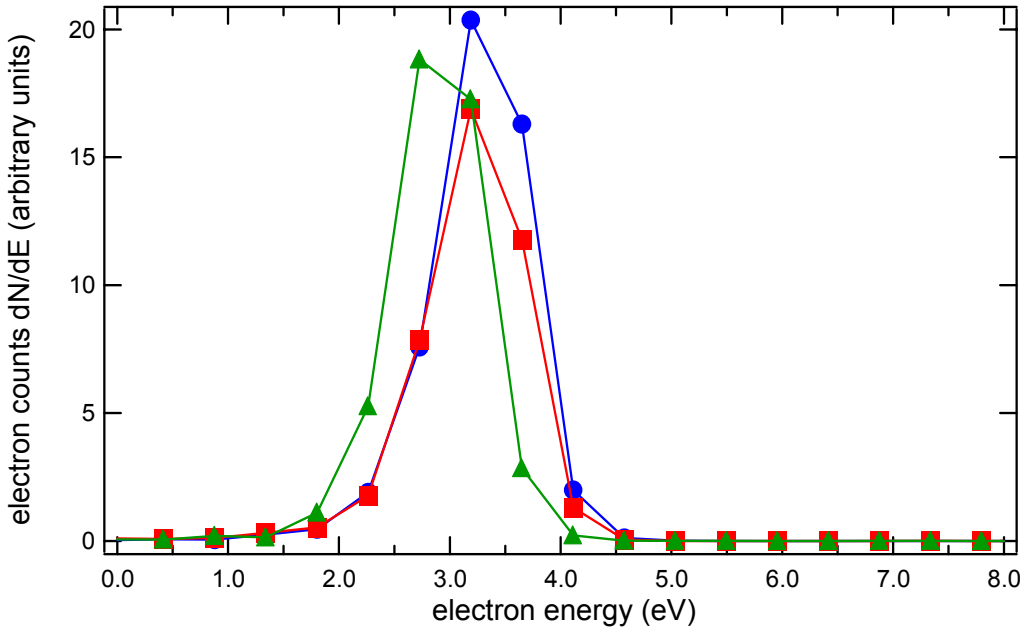

FIG. 3.20. Flood gun emission spectra as measured by the collector. The suppression grid potential was stepped in 0.5 eV increments and the sample potential was kept at 0 V. The filament current was 1.3 for all data; only the gun extraction potential is varied from 3.5 V (●), 3 V (▲), and 2.5 V (■).

sources with energies at a fraction of the insulator band gap (<10 eV) have been shown to be effective in discharging insulators such as Kapton™ and polyethylene by stimulating photo-induced conductivity (Bass *et al*., 1998; Levy *et al*., 1985), and the incident photon flux is not affected by sample potential. Consequently, a series of lamps including a mercury-gas, tungsten-filament, and UV LED array (peak energy 3.1 eV) were mounted next to a quartz view port with a focusing lens to irradiate insulator samples inside the chamber. Energy spectra of these different sources are shown in Fig. 3.21. Measured intensities of the focused beams at the sample faces ranged from 1-35 mW/cm^2. Discharging measurements on Kapton™-aluminum using the flood gun, mercury, and tungsten lamps are evaluated in Section 5.3.3.

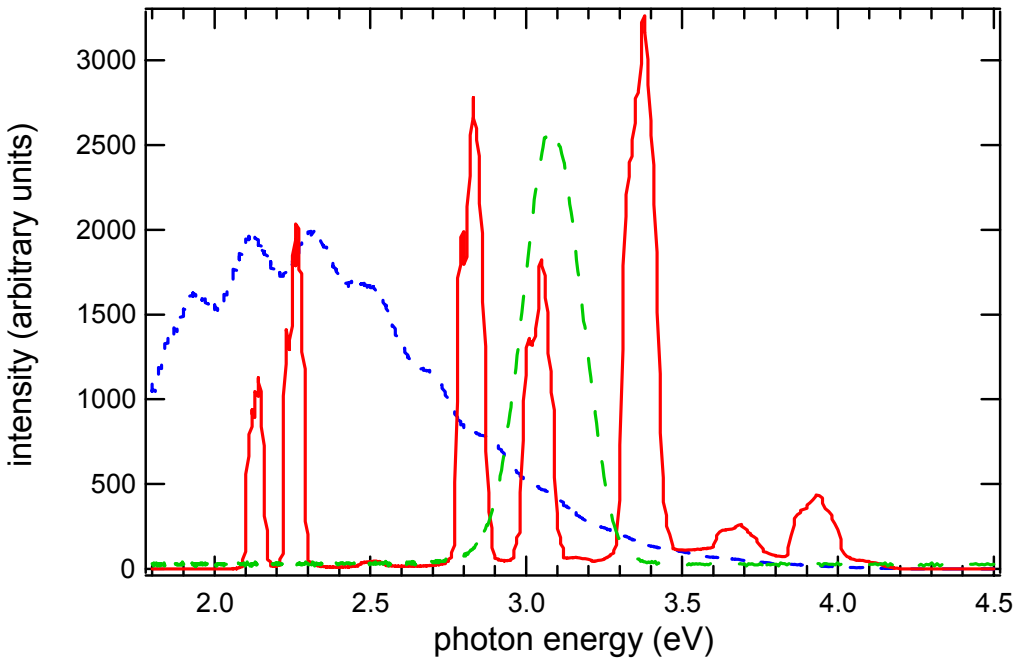

FIG. 3.21. Tungsten (short dash), LED array (long dash), and mercury (solid) lamp energy spectra. The mercury lamp spectrum extended to energies up to 4 eV. Energies >4 eV have been shown in the literature to be effective in discharging negatively charged insulators (Bass *et al*., 1998).

CHAPTER 4

PULSED-YIELD MEASUREMENTS

This chapter begins with Section 4.1, which outlines the general procedure used to measure pulsed-yields along with time estimates for each step. Section 4.2 describes in more detail the pulsed-yield procedure, and also provides alternative methods for pulsed-yield measurement and analysis, along with methods to monitor insulator charging effects on electron yields. Section 4.3 describes the empirical derivation of correction factors used for both pulsed-yield and DC-yield measurements, related to current losses inside the detector apparatus. In Section 4.4, pulsed yields taken on conducting titanium are presented, and are compared to DC measurements on the same material to validate the pulsed-measurement technique. Section 4.5 describes methods for monitoring insulator charging by monitoring DC SE spectra, pulsed displacement current, and pulsed yields. Finally, Section 4.6 describes methods that were explored to measure the first and second crossover energies, important to spacecraft charging and scanning electron microscopy applications.

4.1 General Pulsed-Yield Measurement Procedure

Although different methods were explored for measuring pulsed insulator electron yields (see Section 4.2), the adopted general procedure involved alternating electron pulses with flood gun neutralization. Precautions were taken to minimize the amount of electron beam exposure prior to taking yield measurements. During the electron beam optimization procedure, this was particularly complicated since as few incident pulses as possible were used to center the electron beam through the detector aperture tube and onto the sample. The general procedure used for making pulsed electron yields was as follows:

1. Prior to taking any measurements, all battery power supplies used in the pulse-yield setup were charged. Batteries were used to power the ammeter circuitry, as well as to float the collector at +45 V with respect to the suppression grid. All batteries were internal to the ammeter box, and could be charged by simply throwing a switch (see Section 3.3 for details on the ammeter circuitry). Fully charged batteries typically provided 4 hours of operation before needing to be recharged. The charging process took 8-10 hours.
2. One of the vacuum chamber ion gauges was turned on briefly to ensure the chamber pressure was sufficiently low for electron gun operation. However, ion gauges were never left on during measurements since they emitted stray electron current (~100 pA at the sample surface) into the chamber. Hence, the gauges could corrupt the yield measurements or charge insulator samples. This procedure took roughly 1 minute.
3. System noise levels were checked by turning on all measurement circuitry (ammeters, integrators, oscilloscope, computer and monitor). Channels one and two of the oscilloscope were monitored to check the system noise level. Significant noise above ±5 nA was traced back to its source and eliminated. Diagnosing the system noise could take anywhere from 1-15 minutes depending on the noise level and familiarity with laboratory equipment.
4. With the flood gun turned on but left in full-suppression mode, the DC offsets for the integrator circuitry (stage and suppression grid signals were generally sent through the integrators circuits, while collector and sample signals were sent through the storage oscilloscope) were determined using the mean of 100 measurements, and then entered into the Labview VI [see Thomson (2003d)]. These offsets originated from small errors in the zero adjustment of the integrator and ammeter circuits (adjustable with

potentiometers mounted to the circuit boards) that needed manual readjustment on occasion, but for day-to-day measurements were most easily corrected using the Labview data acquisitioning process. This procedure took roughly 15 minutes, and in the future can be fully automated using Labview, eliminating both operator time input and error.

5. After checking the chamber pressure, the electron gun (either the STAIB gun or Kimball gun) was turned on, but left in full-suppression mode (see Section 3.4 for electron gun operation settings). This included increasing of the filament current to its operating level such that the thermionic emission current could stabilize (see Section 3.4). For the Kimball gun, both the Blanker and grid settings were also fully suppressed. Additionally, for the STAIB gun, the grid/focus settings were fully suppressed and the beam energy was kept at 0 eV. Once the filament was increased, the gun was allowed to sit for a few minutes to ensure filament current emission stability. This entire process took ~5 minutes for each energy setting, and may be further streamlined by computer automating gun controller settings.
6. The detector aperture and extension arm were visually aligned with the electron gun's firing trajectory through the view ports of the chamber. For the STAIB gun, the glow from the electron gun filament (emitted from the gun aperture, visible with the room lights off) was used to further align the electron trajectory with the detector aperture tube. The glowing filament provided a small ~0.5 cm dia. disk that could be centered on the detector aperture tube by adjusting sample stage angular and x,y,z translational settings. Optimal angular and translational settings were recorded for subsequent sample block positioning. This procedure took roughly 5 minutes.

7. Once visually aligned, the electron gun was readied for firing. For the Kimball gun, the grid potential was decreased (but Blanker potential was still left at its full suppression potential). For the STAIB gun, the beam energy was increased to 400-500 eV. Once ready, the electron gun was pulsed repeatedly [using the Labview Virtual Instrumentation, Thomson (2003d)] with a pulsing period of 1 s while x/y deflection settings on the electron gun controller were adjusted to maximize the collector and sample pulsed signals on the oscilloscope. As few pulses were used as was possible (10-20 pulses in most cases) for this optimization procedure to minimize sample exposure to the electron beam. Once the gun was optimized on the sample, the pulsing was stopped, and the gun was left once again in full suppression mode. Once optimized, the sample-stage angular and translational settings, as well as the electron gun controller deflection settings, were not changed throughout the remainder of the experiment. However, other electron gun settings such as grid, focus, filament, and Blanker were adjusted appropriately for different gun energies (see Section 3.4). This optimization procedure took only a few minutes.
8. The sample was then flooded with the flood gun for 1-2 minutes to dissipate any surface charge that had accumulated during the optimization procedure (see Section 3.5 for flood gun operation settings).
9. With the electron beam optimized, pulsed measurements were taken at different incident energies, typically using 10 pulses per measurement [selectable with the Labview VI, see Thomson (2003d)]. These pulses were integrated (using either the integrator circuitry or by computation integration in Labview), and then yields were calculated and averaged. Additionally, raw data was exported for collector, sample, suppression grid, and stage integrated charge, as well as sample and collector raw

pulsed signals for further analysis. Between each electron pulse, the sample was flooded for 1-2 seconds (flood time selectable in the Labview VI) to avoid charging. Additionally, after each series of pulsed measurements, the sample was flooded for an additional 1-2 minutes. Suppression grid biases were also selected in the Labview VI: 0 V biasing was used for total-yield measurements, and -50 V biasing was used for BSE-yield measurements. Once total and BSE yields were measured for a given energy, the electron gun energy was increased manually, and other electron gun settings such as grid and focus settings were manually adjusted appropriately (see Section 3.4). However, precautions were always taken to adjust grid potential settings (in addition to focus settings on the STAIB gun and Blanker settings on the Kimball gun) prior to increasing beam energy such that the gun always remained fully suppressed. Sample stage x, y, z, and angle settings were not adjusted after the initial sample positioning optimization. Electron beam deflection settings were also not adjusted after the initial electron gun optimization. The entire yield measurement, acquisition, and flooding sequence took roughly 5 minutes at a given energy. Adjusting the gun controller energy and settings took an additional 2-5 minutes.

Section 3.4 contains further information on electron gun operation. Section 4.2 provides additional detailed information on other measurement and analysis schemes used for pulsed-yield and spectral measurements. Finally, Thomson (2003d) contains information on the Labview software used to automate the yield measurements.

4.2 Electron Yield and Spectral Analysis

For the majority of the experimental work presented in this dissertation, only one or two general measurement and analysis approaches were implemented for taking insulator yields. The routine procedure was outlined in Section 4.1. However, several other approaches were explored, and deserve to be documented since each method demonstrated unique advantages and disadvantages, and may be useful in future studies. For example, some methods offered efficient streamlined data acquisitioning, while others offered capabilities for system diagnostics and sample charging monitoring. For the purposes of this dissertation, methods for pulsed-yield measurements fell into two general categories: charge-integration methods and current pulse-profile methods. With the charge-integration methods, pulsed electron current signals, which were captured with fast-response ammeters, were integrated to obtain values of electron charge. This integration was performed using either the integrator circuitry, or by capturing the signals with the oscilloscope, and then performing computational integration (see Section 3.3). These values of charge were then used to calculate electron yields by taking ratios of the collector charge to the total incident electron charge as shown in Eqs. (3.4) through (3.6). With the current pulse-profile method, pulsed electron current signals were measured by the fast-response ammeters and then captured on the oscilloscope. The pulse maxima were then used to calculate yields as the ratios of the collector current to total incident current as shown in Eqs. (3.1) through (3.3).

Both the charge-integration and current-profile methods demonstrated their own respective advantages and disadvantages. The charge-integration method inherently provided noise reduction of the signals, since the cumulative sum of all random noise with respect to time approached zero. Additionally, signal integration did not depend on circuitry response time or non-uniform electron gun emission profiles. Hence, this method was ideal for pulse

widths of 5 μs emitted by the STAIB gun (see Section 3.4 for a description of the emission characteristics of this gun). However, it was also important to develop capabilities to analyze pulse-profiles as a function of time in order to provide information on electron gun emission profiles (see Section 3.4), system noise diagnostics (see Section 3.3), signal frequencies diagnostics, pulse plateau analysis, and sample charging monitoring (see Sections 4.5, 5.3.2 and 5.3.4). The current pulse-profile method was uniquely tailored for these types of analysis. Also, by monitoring pulse profiles as a function of time, the pulse maxima (or plateaus) were used to calculate electron yields in a similar fashion to the DC method, by taking ratios of electron current. However, yield calculations involving the current pulse-profile method required incident pulses with durations (>5 μs), good electron gun emission profiles (see Section 3.4), low system noise (<10 nA), and fast ammeters response times (<2 μs).

For each of these charge-integration and pulse-profile methods, various measurement and analysis schemes were tested and employed (and automated using Labview) for studying electron yields and spectra, as well as sample charging. Block diagrams for these analysis schemes are shown in Figs. 4.1-4.4 and 4.8-4.9. More in-depth explanations are contained in the following paragraphs.

For the charge-integration method, three different acquisitioning and analysis schemes were explored. For the first of these schemes, as shown in Fig. 4.1, the collector, sample, stage, and suppression grid electron pulse signals, measured with the fast ammeters, were sent to four integrator circuits, and the resulting DC-voltage signals (0-5 V) were imported to the computer using four channels on the DAC card (refer to Section 3.3). Using Labview, the DC offsets for these voltage signals (caused by offsets in the ammeter and

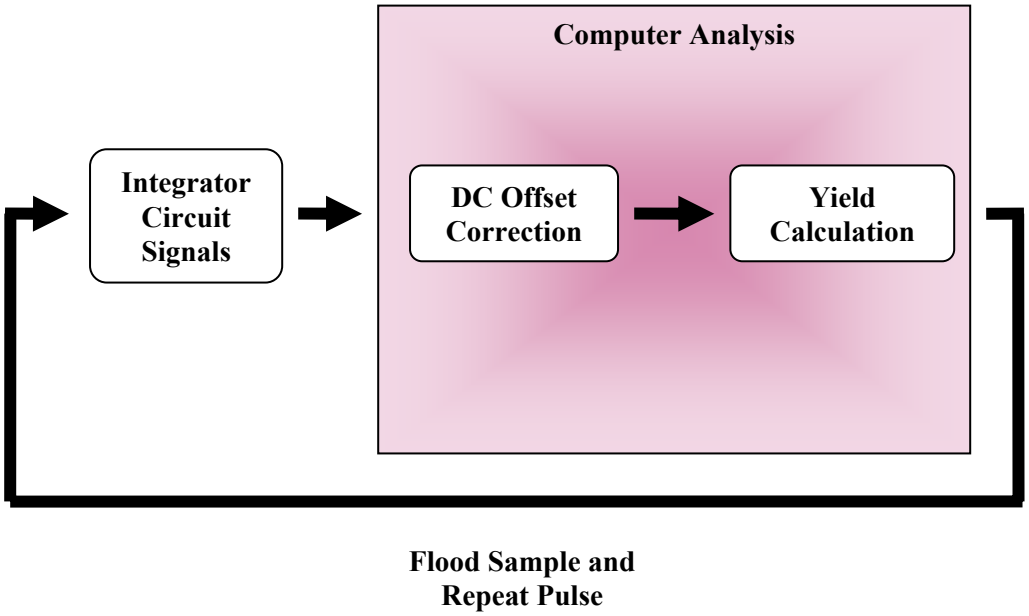

FIG. 4.1. First measurement and analysis scheme for charge-integration yield calculations. For each incident pulse, measured collector, sample, stage, and suppression grid signals were sent through the integration circuitry, and then to the computer where DC-offset correction and yield calculation were performed.

integrator circuitry, and determined at the beginning of each experiment) were corrected for, and then yields were calculated. The sample was then flooded for surface neutralization, and another incident pulse was repeated. This scheme provided a quick method for making yield measurements without the use of the oscilloscope, but at the cost of signal-profile information and analysis versatility that included sample charging and noise diagnostics. Additionally, yields were very sensitive to integrator and ammeter DC offsets, which were difficult to diagnose using this scheme, and could change during the measurement process. Hence, it was preferred to send the most important signals (collector and sample) through the oscilloscope, and reserve the use of the integrator circuits for stage and suppression grid signals. In future studies the exclusive use of the integrator circuits for all four signal sources (collector, sample,

stage, and suppression grid) may be well suited for rapid turn-around insulator yield measurements, but in most cases it was not adequate for this dissertation work.

The second and third charge-integration schemes (block diagrams shown in Figs. 4.2 and 4.3, respectively) utilized both the oscilloscope and integrator circuitry. Collector and sample signals were measured with the ammeters, and then sent to the two channels on the digital storage oscilloscope, where full-pulse profiles were exported to the computer via GPIB interfacing. Then, using Labview, signal unit conversion (from voltage to current) was performed using the user-selected ammeter gain setting ($2 \cdot 10^6$, $1 \cdot 10^7$, or $2 \cdot 10^7$ V/A). The imported waveforms were then adjusted for DC offsets, and then integration of the signals was performed [see Thomson (2003d)]. Stage and suppression grid pulses were measured with the ammeters, and processed through the integrator circuitry and computer DAC card, similar to the first scheme, except voltage signals were converted back to values of electron charge using the ammeter gain settings and integrator time constant settings (usually T=15.5 μs for a 5 μs pulse). Once all signals had been integrated, yields were calculated using Eqs. (3.4) through (3.6). The collector and sample signals constituted the most important components in the yield calculation since their values were generally at least an order of magnitude larger than stage or suppression grid signals in total-yield measurements. Additionally, the sample displacement current signal provided direct information on sample charging rates as a function of electron fluence (refer to Section 5.3.4). Therefore, using the oscilloscope for the collector and sample signals, and the integrator circuitry for stage and grid signals provided a good compromise between data acquisition convenience and versatility for more in-depth yield and charging analysis.

A key difference existed between the second and third charge-integration schemes. For the second scheme, raw collector and sample traces, captured during each pulse/flooding

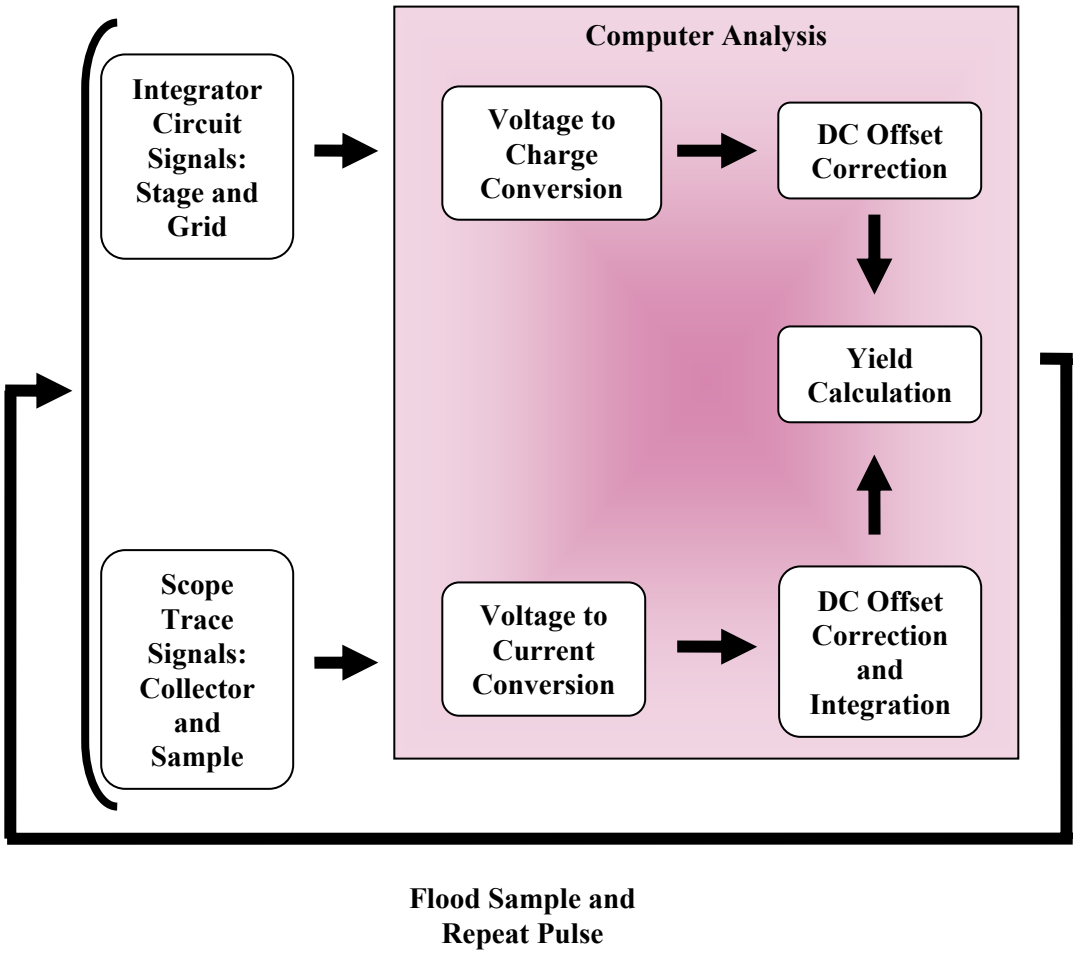

FIG. 4.2. Second measurement and analysis scheme for charge-integration yield calculations. For each incident pulse, measured stage and suppression grid signals were sent through the integration circuitry, while collector and sample signals were sent through the storage oscilloscope. All signals were then used to calculate the electron yield. This process was repeated several times for each energy, and electron-flood neutralization was employed between each measurement.

iteration, were carried through the entire integration/yield calculation process. In this way, a single yield value existed for each pulse iteration, and all yields were combined in the end to determine a mean value and error (standard deviation of the mean). However, this scheme often suffered from relatively high sample and collector-signal noise that could contribute significant random error (6-15 percent for I_0=15-40 nA in a single total-yield measurement,

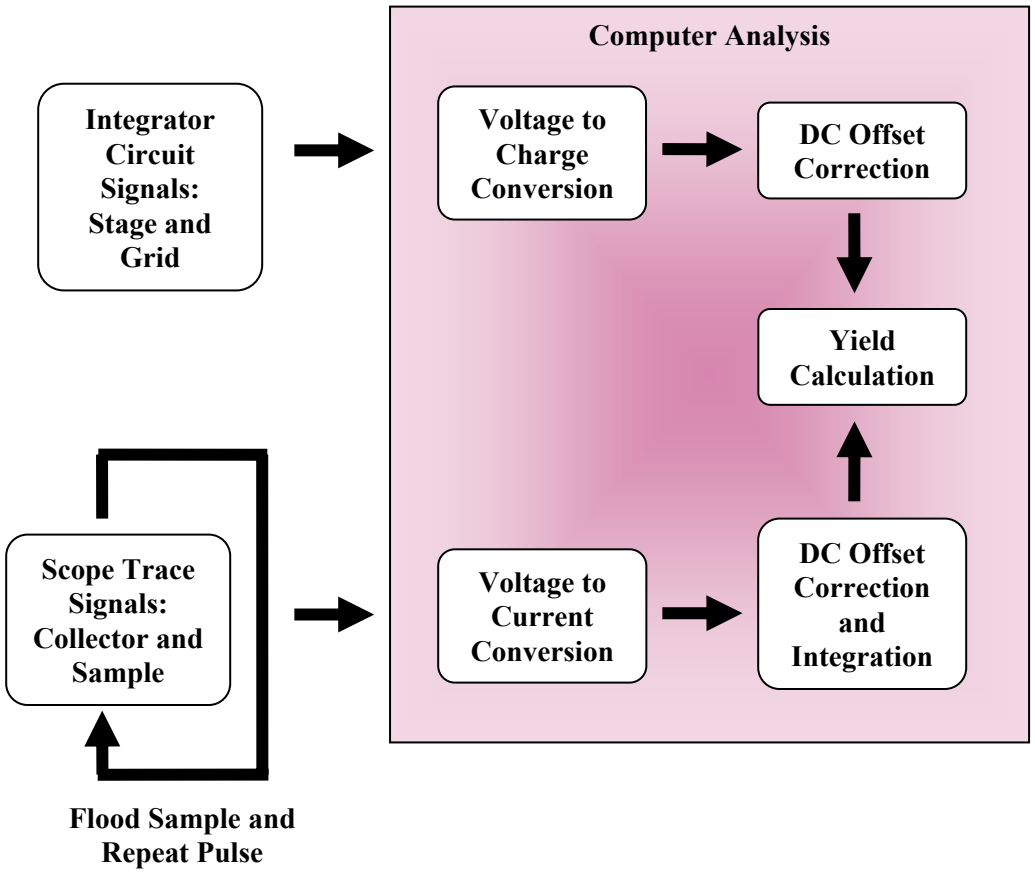

FIG. 4.3. Third measurement and analysis scheme for charge-integration yield calculations. For each incident pulse, measured stage and suppression grid signals were sent through the integration circuitry, while collector and sample signals were sent through the storage oscilloscope. Collector and sample electron pulse signals were improved by averaging scope traces point-by-point before any signal integration or yield calculations were performed. Electron-flood neutralization was employed between each incident pulse.

see Section 4.4). For the third scheme, multiple collector and sample waveforms (flooding performed between each pulse) were combined through raw trace point-by-point averaging (performed with either the LeCroy oscilloscope or with Labview) before the integration/yield calculation process was performed. The point-by-point error could also be propagated through the integration algorithm to obtain a total-charge error value. In this way, pulsed signals were cleaned up significantly before any integration or yield calculations were

performed. However, a significant drawback to the third scheme was the electron gun current emission could drift throughout the course of a measurement (changing pulse-signal amplitudes), and only one yield value was produced at the end of the pulse/flood iteration loop such that evolving yields (resulting from sample charging) could not be extracted from the data. Since it was important to monitor evolving yields as a function of electron fluence, the second analysis scheme was preferred for most of the measurements in this dissertation.

Note, a method very similar to the second charge-integration scheme was also used to perform pulsed-spectral measurements as shown in the block diagram in Fig. 4.4. For spectral measurements, single-pulse signals from the collector were integrated (as described above) for successive applied suppression grid potentials (supplied by the Keithley 230 power supply, and automated with Labview). Generally, ten single-pulse/flood gun iterations were taken for each suppression grid potential setting, and then values for total charge were combined by calculating the mean and standard error of the ten measurements. Since this mean charge value depended on both the energy distribution of emitted electrons as well as on the total incident current, it was crucial that the electron guns were maintained at stable emission current during the course of the experiment (a full spectrum could take as long as 30 min.). This was achieved by allowing the gun to sit for roughly 5 min. at the operating filament current (using full current emission cutoff for the gun) before beginning pulsed spectral measurements.

Before describing methods for the current pulse-profile analysis, the yield-calculation and pulse-signal integration algorithms used in the charge-integration analysis are outlined as follows:

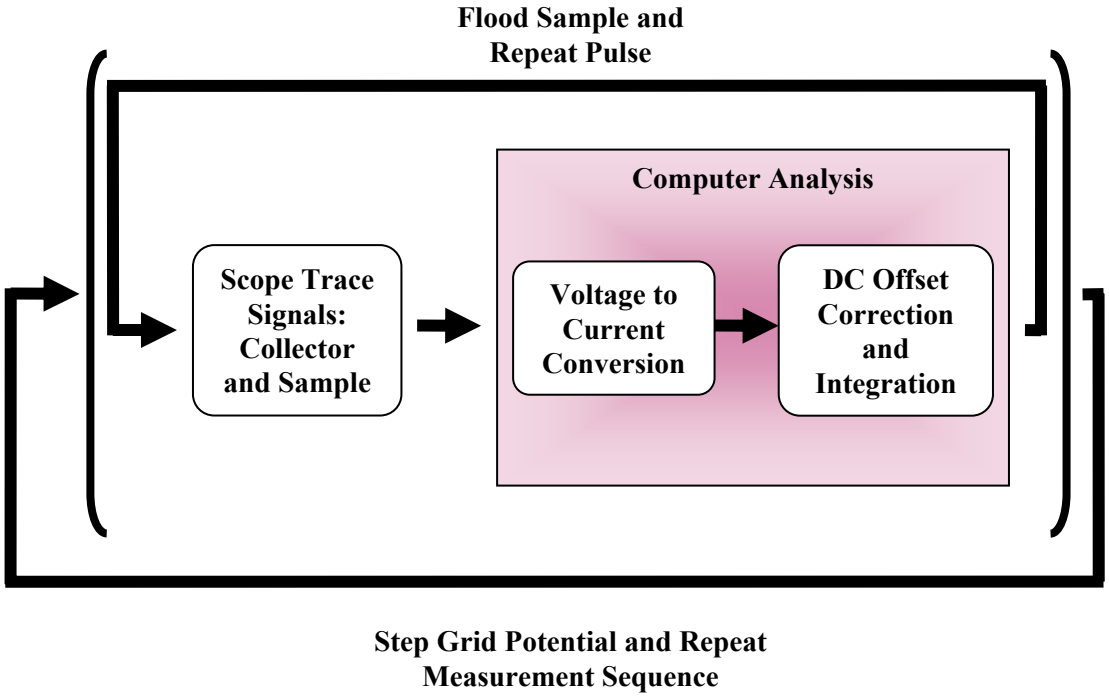

FIG. 4.4. Spectral measurement and analysis scheme for charge-integration analysis. This scheme was similar to the second charge-integration yield analysis method shown in Fig. 4.2, where the collector and sample signals were sent through the storage oscilloscope and then integrated to find the total electron charge. This process was repeated several times, and electron-flood neutralization was employed between each incident pulse. After several pulse iterations, the suppression grid potential was stepped to a higher (negative) potential, and the pulsing sequence was resumed.

1. Pulsed signals originating from both the integrator circuitry and oscilloscope were corrected by their respective DC-offsets. For integrator-circuit signals (usually stage and suppression grid signals), the mean DC-offset values were obtained at the beginning of each experiment by running 50-100 measurements with the electron guns fully suppressed, but all other instrumentation turned on (including the flood gun in full-suppression mode and all pulse-data acquisition circuitry). Each mean offset value was subtracted from its respective charge signal (usually stage or suppression grid) before yield calculations were performed.

2. DC-offset corrections for oscilloscope signals (usually collector and sample) were completely automated in Labview [see Thomson (2003d)]. The offset correction process involved averaging subsections of the waves before and after the pulse signal (0-15 μs before and 60-100 μs after), and shifting the entire waveform by the difference of the mean offset from 0 nA on the y-axis, as demonstrated in Fig. 4.5. After correcting for DC-offsets, numerical integration of the signal was performed in Labview. For further noise reduction, the last 20 points (this number of data points was arbitrarily chosen) of the integrated waveform were averaged to obtain the final integrated charge value as demonstrated in Fig. 4.6. The Labview Virtual Instrument algorithms used for DC-offset correction and pulse-signal integration is described in more detail in Thomson (2003d).
3. Furthermore, for the 2^{nd} charge-integration scheme, pulsed-yield calculations were performed in two ways. For pulsed-total yields, the stage contribution was excluded from the total incident electron current denominator term [see Eq. (3.4)], since the stage background noise contributed a significant amount of error (as much as 100 percent for ten averaged measurements) in the yield calculation (these large noise errors may be eliminated in future work as explained in Section 6.1). However, for pulsed BSE yields, the suppression grid potential of -50 V turned SE's back towards the sample and sample block such that a significant portion were collected by the stage surfaces; hence the stage signal/noise ratio increased by roughly an order of magnitude. Hence, for BSE yields, the stage error was reduced sufficiently, and was used in the yield calculation (e.g., BSE fractional error ranged from 10-20 percent for I_0=40-50 nA for ten measurements at E_0=400 eV, refer to Section 4.4). Consequently,

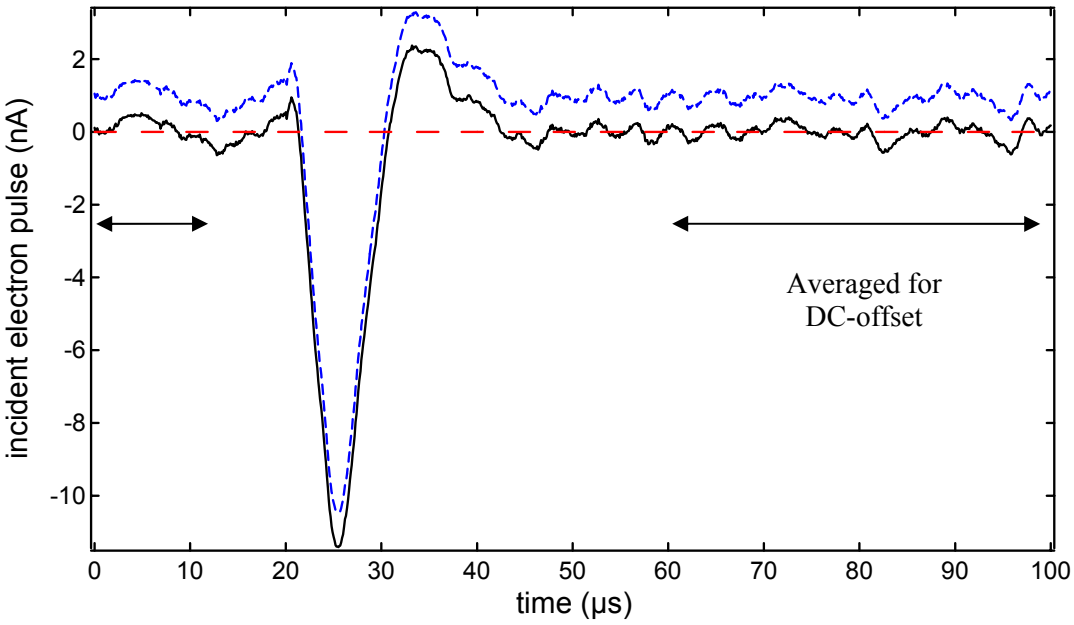

FIG. 4.5. Collector pulse signal demonstrating DC-offset correction. Pulse duration was 5 μs at E_0=1000 eV on a gold sample. Arrows show subsections of the traces that were averaged to perform the DC-offset shifting of the entire original waveform (dash) to 0 nA (solid).

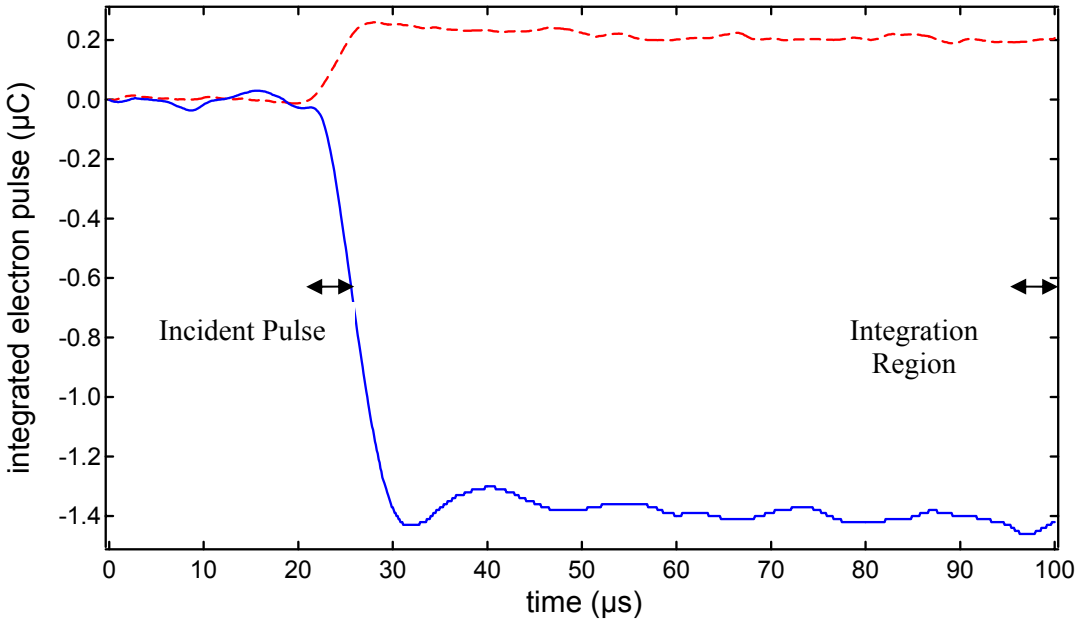

FIG. 4.6. Integrated pulsed-signal curves for the sample (dash) and collector (solid). The incident pulse duration was 5 μs at E_0=200 eV on an anodized aluminum (insulating) sample. The last 20 points of each integrated wave were averaged to obtain the final integrated charge values.

as discussed further in Section 4.3, two separate correction factors existed for the pulsed total and BSE yield calculations used in this dissertation.

4. As described above for the second charge-iteration method, after each incident electron pulse iteration the electron yield was calculated. After numerous pulsing iterations, the final combined yield was calculated one of three ways. Often, when electron flooding was used between each incident electron pulse, charging distortions to the yield were insignificant (as demonstrated in Section 5.3.2). In this case, it was adequate to combine electron yields by calculating a mean value and standard error. However, in cases where the flood gun was not implemented (or was not effective, e.g., $E_0>E_2^{\sigma}$) sample charging on the yields were significant with repeated incident pulsing as shown in Fig. 4.7. In this case, a judicial choice of either a linear or decaying-exponential fit [see Eq. (2.51)] was used to estimate the first uncharged yield value. An example of these fitting methods to charging yields is shown in Fig. 4.7.

As described above, the current pulse-profile method was used for square-wave pulses with durations >5 μs such that the total pulse width exceeded the ammeter rise and fall times (~1 μs for the $2\cdot10^6$ V/A gain and ~4 μs for the $2\cdot10^7$ V/A gain). As described in Section 3.4, the STAIB gun pulse profile was not square in time such that this method could only be used for the Kimball gun. With the current-profile method, the maxima of the current pulses were used to calculate yields. The plateau of the signals were either averaged or fitted (depending on their charging rates or slopes) to obtain the maximum currents. Two current-profile schemes were explored and are shown in the block diagrams Figs. 4.8 and 4.9. For the first current-profile scheme, yields were calculated for each pulse iteration, and then combined by calculating a mean yield and standard error (Fig. 4.8). For the second current

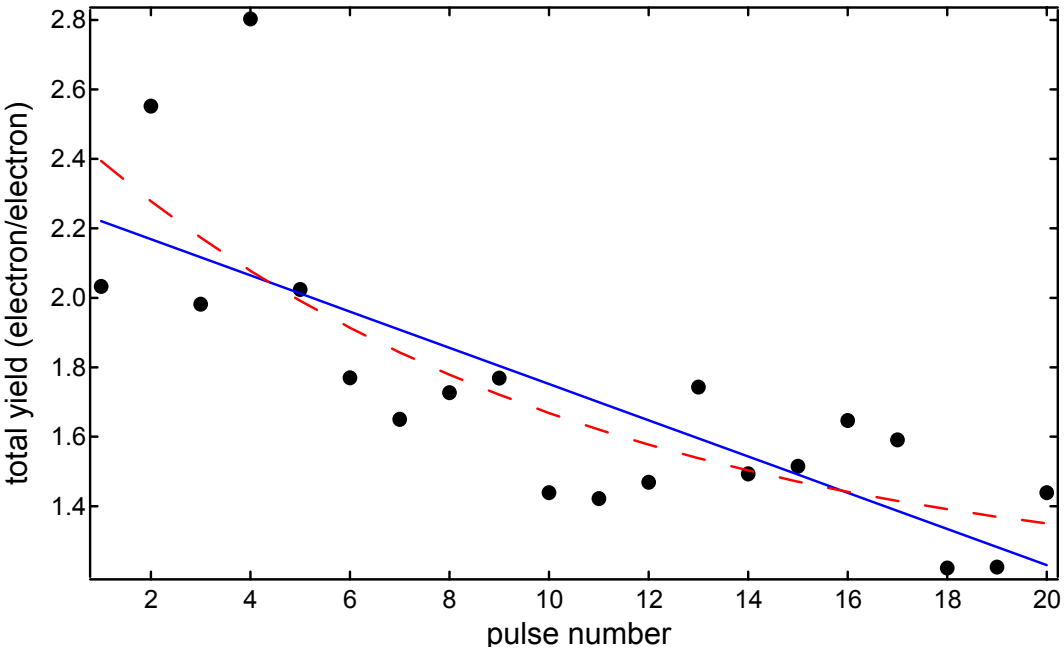

FIG. 4.7. Linear (solid) and exponential (dash) fits to decaying yields (due to charging) as a function of pulse number. Pulse durations were for 5 μs at 500 eV on anodized aluminum. Both methods provided estimates for uncharged-yield values (the first pulse). In this case, linear estimates for the initial yield were 2.3±0.1, and exponential estimates were 2.4±0.2, as determined by Eq. (2.51).

pulse-profile scheme, individual traces were combined point-by-point before any yields were calculated (Fig. 4.9). With the second current-profile scheme, signal noise levels were significantly reduced, but at the cost of losing sample charging information (showing up as decays in the pulse plateau maxima). A further drawback for both of these schemes was only two pulsed signals (collector and sample) could be measured at any given time by the two-channel oscilloscope. Consequently, grid and stage contributions to total incident current had to be neglected, and the appropriate correction factor had to be applied to the data to account for these current losses in the yield calculation (see Section 4.3). Nevertheless, these methods (particularly the first scheme) provided a valuable method for monitoring yield evolution as a function of electron pulse duration. Fig. 4.10 shows collector and sample signals for

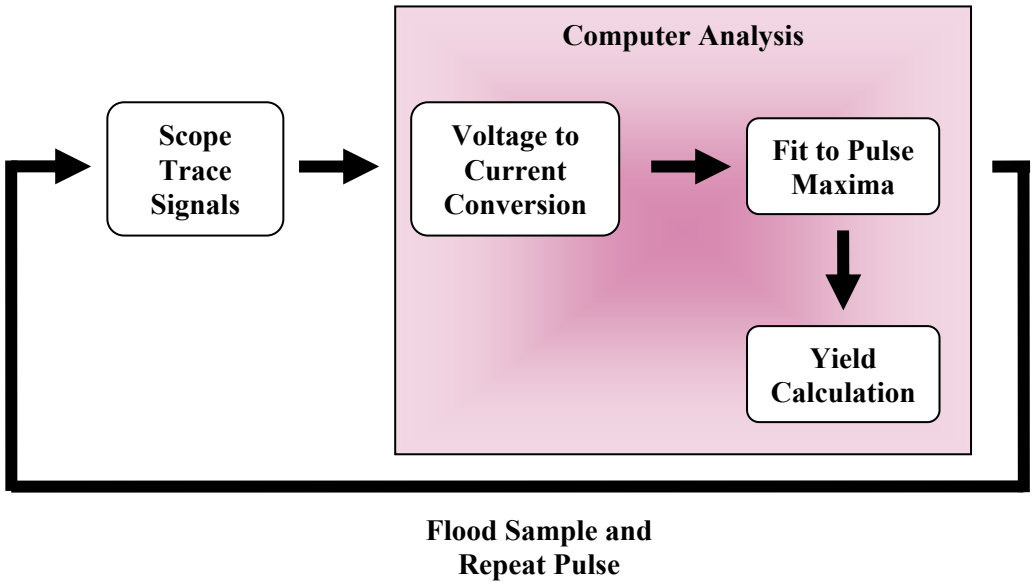

FIG. 4.8. First measurement and analysis scheme for current pulse-profile yield calculations. For each incident pulse, measured collector and sample signals were sent through the storage oscilloscope and then to the computer where yields were calculated by taking ratios of the pulse-peak maxima. After this sequence, electron-flood neutralization was employed, and a new pulse measurement was repeated. Finally, all yields were combined by calculating a mean and standard error.

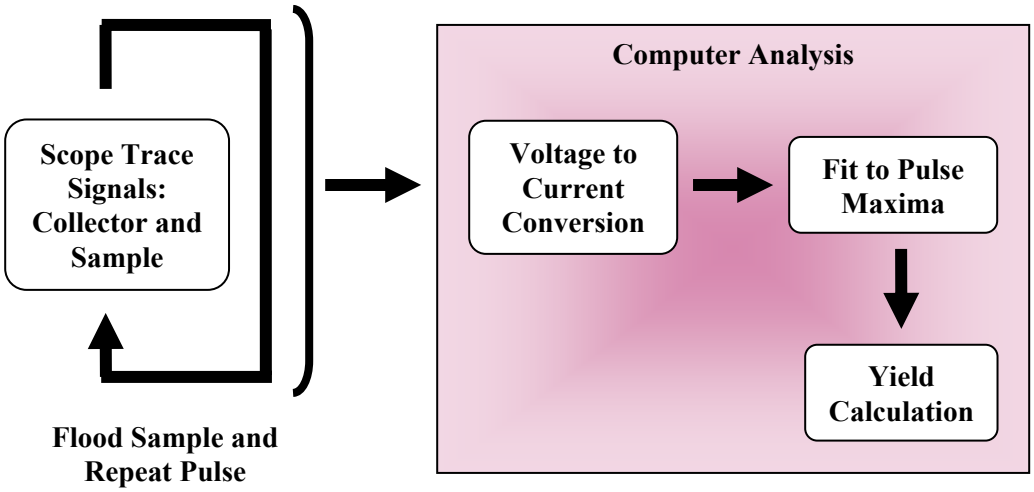

FIG. 4.9. Second measurement and analysis scheme for current pulse-profile yield calculations. For each incident pulse, measured collector and sample signals were sent through the storage oscilloscope. Numerous electron pulse signals were combined through point-by-point averaging of scope traces for signal cleanup before yield calculations were performed by taking ratios of the pulse peak maxima. Electron-flood neutralization was employed between each incident pulse.

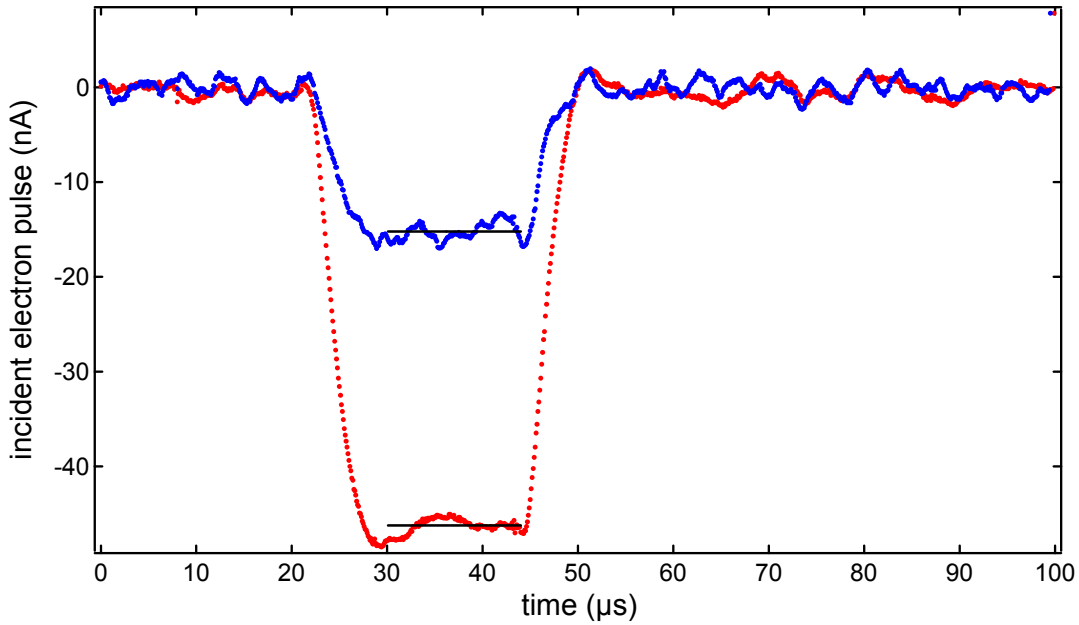

FIG. 4.10. Collector (-15 nA peak) and sample (-46 nA peak) pulse signals from a 20 μs incident electron pulse at E_0=10 keV. Ten single-pulsed signals were combined for each of the shown pulses using the second current-profile analysis scheme (Fig. 4.9). Signal plateaus were averaged (solid lines) and were found to vary by fractional errors of ±4 percent for the sample current (-46±2 nA) and 13 percent for the collector current (-15±2 nA).

a 20 μs incident pulse at E_0=10 keV from the Kimball gun, where the second current-profile analysis scheme has been used. In this case, averages of the plateaus were later used to calculate electron yields in Section 5.3.2.

Pulsed electron-yield and spectral data using these techniques on insulator samples are demonstrated in Chapter 5.

4.3 Absolute Electron Yields: Measurement Correction Factors

It has been well established that small changes in the absolute magnitude of electron yields can have substantial effects on spacecraft potentials (Dennison *et al*., 2001; Davies and Dennison, 1997; Chang *et al*., 2000b, 2000c). In order to predict the extent of spacecraft differential charging in spacecraft charging codes, it is mandatory to accurately determine

absolute total, SE, and BSE yield parameters such as the maximum total and SE electron yields, σ_{max} and δ_{max}, and their corresponding energies, $E_{max}{}^{\sigma}$ and $E_{max}{}^{\delta}$, as well as the first and second crossover energies, $E_1{}^{\sigma}$ and $E_2{}^{\sigma}$, at which the material transitions between positive and negative charging. Previous experimental studies have determined values for these parameters for some materials, but most measurements were taken in poor-quality vacuums, and were susceptible to contamination effects. Furthermore, most electron yield data is taken by methods that do not provide a true measure of SE yields, and the resulting data from these setups are then referenced to previous standards (Holliday and Sternglass, 1957). Furthermore, past attempts to calibrate detector systems have only been partially successful (Reimer and Drescher, 1977; Thomas and Pattison, 1970). Consequently, existing electron yield data that have been corrected against previous standards may be correct in a relative sense, but the absolute accuracy remains uncertain.

Traditionally, the most common method used to determine SE yields for conductors has been to measure the incident electron-induced sample current at 0 V sample bias, and then to subtract the sample current at +50 V sample bias, where most SE's have returned to the positive sample (Nickles, 2002). A standard scanning electron microscope is able to take this type of measurement without modification. However, the electric field lines between the +50 V sample and the closest grounded surfaces—typically the sample holder—do not necessarily return all SE's to the sample surface (Nickles, 2002). Davies (1999) studied a similar situation, and estimated the error in the absolute SE yield to be as high as 20 percent. Alternately, hemispherical or cylindrical electrostatic energy analyzers have energy-dependant transmission functions (Nickles, 2002), while photomultiplier tubes or channel plate detectors exhibit both energy and current dependant efficiencies and substantial modification of amplification with detector lifetimes and vacuum conditions.

Several investigators have chosen to use retarding grid analyzers for these reasons (Sternglass, 1953; Thomas and Pattison, 1970; Reimer and Drescher, 1977; Holliday and Sternglass, 1957). However, accurate absolute yield measurements using such grid analyzers require corrections for scattering off the grids and other detector surfaces, as well as for other geometrical factors. Spherical or hemispherical retarding grids are most common, as their radial electrostatic fields provide better energy resolution (Sternglass, 1953; Thomas and Pattison, 1970; Reimer and Drescher, 1977; Holliday and Sternglass, 1957). Corrections for spherical grids that fully surround the sample are much simpler to determine than those for hemispherical grids (Sternglass, 1953; Jonker, 1951). However, at USU, we have used a hemispherical grid to facilitate the use of a sample carousel for increased sample throughput (see Section 3.1 and Nickles, 2002).

It has been essential in our experimental investigations at USU to provide calibrations for absolute insulator electron yield measurements, with a target systematic uncertainty of <5 percent for total, SE, and BSE yields. Much of this work for DC yields has already been performed. Previous to these insulator studies, Nickles and Dennison (Nickles, 2002) arrived at a set of correction associated with total, SE, and BSE measurements performed using the USU FATMAN setup. In their studies, determination of the correction factor values were based on detailed numerical modeling of the grid corrections for our detector apparatus (see Nickles, 2002), as well as comparisons with previous yield measurements by other investigators where available. It must be noted that since the publication of the dissertation work of Nickles (2002), the SE and BSE correction factors used in our laboratory have been further modified, based on corrections to the original numerical calculations, as well as from experimental work performed by Chang and Dennison (Dennison, 2003e). An overview of

these numerically calculated current losses associated with the detector apparatus is summarized below.

The numerical calculations were based on Eqs (3.1) through (3.3), where in making yield measurements with our detector apparatus, not all electrons emitted from the sample were gathered by the collector, thus making the measured yield values artificially low. Instead, some electrons were lost to other surfaces before they were collected. The largest correction was attributed to the opacity of the grids, accounting for ~75 percent of the full correction factor. Smaller blocking corrections of ~5 percent of the full correction factor were based on the geometries of the detector not subtended by the hemispherical grids (~10 percent of the detector's total surface area), and kept electrons from not reaching the collector. This included electrons lost out of the detector aperture tube, or those that hit other detector surfaces before reaching the collector.

The third largest correction was for BSE's reflected from the collector. Coating the collector with colloidal graphite that has a particularly low BSE yield of 0.07 (Sternglass, 1953) is a standard method used to reduce this correction; in our case, this contribution to the full correction factor was reduced to ~4 percent. Essentially all SE's that were excited from the collector surface were returned to the collector since the suppression grid was always held at –50 V with respect to the collector. Also, many high emission angle BSE's had trajectories that return them to the collector before reaching the suppression grid. Finally, additional higher-order correction terms involved multiple SE or BSE scatters within the detector, accounting for the last ~16 percent of the full correction factor. It must be noted that in all previous studies in the literature we reviewed, these higher-order corrections corresponding to absorption and scattering (within the detector apparatus) were neglected (Nickles, 2002; Reimer and Drescher, 1977; Thomas and Pattison, 1970). Overall losses within the detector

apparatus lowered the measured SE electron yields by ~11.5 percent, and BSE yields by ~45 percent. Best estimates for the numerically derived detector correction factors for total, SE, and BSE yields are summarized in Table 4.1. Although a total yield correction factor was not provided by Nickles (2002) or in subsequent SE and BSE correction factor studies, this value was estimated in Table 4.1 by using SE and BSE correction factors (shown in the table) along with measured total and BSE data taken at E_2^{σ}.

In this dissertation, it was important to continue the efforts pursuant to obtaining accurate corrections by empirically verifying previous numerically-determined DC-yield correction factors, as well as to also establish those important correction factors related specifically to pulsed-yield measurements. The remainder of this section is dedicated to studies performed to further establish both the DC and pulsed-yield systematic uncertainties and correction factors inherent to the FATMAN chamber. The extent of the random uncertainties, pertaining specifically to pulsed-yields, is discussed further in Section 4.4.

The systematic errors associated with pulsed yields existed in two general categories that included errors associated with detector losses and errors associated with the method for calculating pulsed electron yields. As shown in Table 4.1 (as provided by Nickles, 2002), there existed a set of SE and BSE correction factors associated with the hemispherical retarding grid analyzer that applied to both DC and pulsed-yield measurements on both conductor and insulator samples (for total yields, referred to as CF_{det} below). In addition to the detector correction factor, a second correction factor existed exclusively for pulsed-yield measurements, corresponding to the exclusion of the stage-current contribution to the calculation of total electron yields (for total yields, referred to as CF_{stg} below). As described in more detail in Section 4.2, the stage-current contribution was excluded in pulsed total-yield measurements due to the high noise in the measured signal, but was included in BSE yield

TABLE 4.1. Summarization of empirically and numerically derived correction factors for total, SE, and BSE yields due to losses in detector apparatus. Values for the empirical total-yield correction factor, determined at $E^{2\sigma}$, were consistent with the numerically derived value to within 3 percent.

Electron Yield	Empirical Correction Factor	Numerical Correction Factors
Total Yield	1.15	1.18
SE Yield	Not yet determined	1.15
BSE Yield	Not yet determined	1.40

measurements where the stage signal was sufficiently large to obtain a good reading [refer to Eqs. (3.4) to (3.5)]. Empirical studies of these correction factors performed for this dissertation work are explained in detail below.

In order to experimentally validate the numerically modeled detector correction factors of Nickles (2002), a series of measurements were performed on gold (two different sets of data), stainless steal alloy (SS316), and graphitic amorphous carbon samples to empirically verify the total-yield correction factor. To do this, the total electron yield was monitored along with the sample current as the electron beam energy was traversed across E_2^{σ}. This was done to determine the measured total yield value associated to a net zero sample current, corresponding to the sample's steady-state condition. When the steady-state condition is reached, the total yield should equal unity. However, deviations from unity are associated with detector losses, and hence provide a value for the detector correction factor at E_2^{σ}. In order to study these relationships better, the total yield was plotted as a function of the sample current as shown in Fig. 4.11, and displayed a linear relationship for energies near E_2^{σ}. By this method, as E_2^{σ} was traversed, the sample current, I_s, was expected to approach 0 nA, and the total yield correction factor could be determined.

While performing this analysis, it was found the beam energy increment, as well as the beam current magnitude, primarily affected the slope of the linear relationship between total yield and sample current, but the zero-crossing remained unchanged by these parameters. This occurred because increasing the beam current increased the sample current with increasing beam energy, but did not affect the total yield value (to first order, yields are independent of incident current). Likewise, by increasing the beam energy increment, the sample current and total yields changed at different rates, affecting the slope of the linear relationship. However, neither fluctuations in the beam current nor beam energy increment affected the incident energy at which the sample reached steady state. Nevertheless, to minimize the number of varying parameters while measuring the total yield dependence on sample current, the electron beam energy was increased at a fairly constant rate of 50-100 eV per increment, and the beam current at different energies was kept constant (to within 10 percent).

As shown in Fig. 4.11, as the sample current traversed 0 nA, the total yield was somewhat less than unity. It must be noted the measured sample current remained relatively free from errors associated with the detector apparatus. Although SE's and BSE's can reflect off the grids, and BSE's can reflect from the collector or other collector surfaces (described above) and return to the sample, this error has been shown in numerical calculations to account for <2 percent of the original emitted sample current induced by the incident electron beam (Nickles, 2002). Consequently, the deviation of the total yield from unity (the factor required to force the total yields to unity) at the point where the sample current crossed 0 nA was taken to be the total yield correction factor at $E_0=E_2^{\sigma}$. Furthermore, as shown in Fig. 4.11 and as summarized in Table 4.2, the empirically determined total-yield correction factor was consistent for the four samples studied to within 2 percent. From these results, it seemed

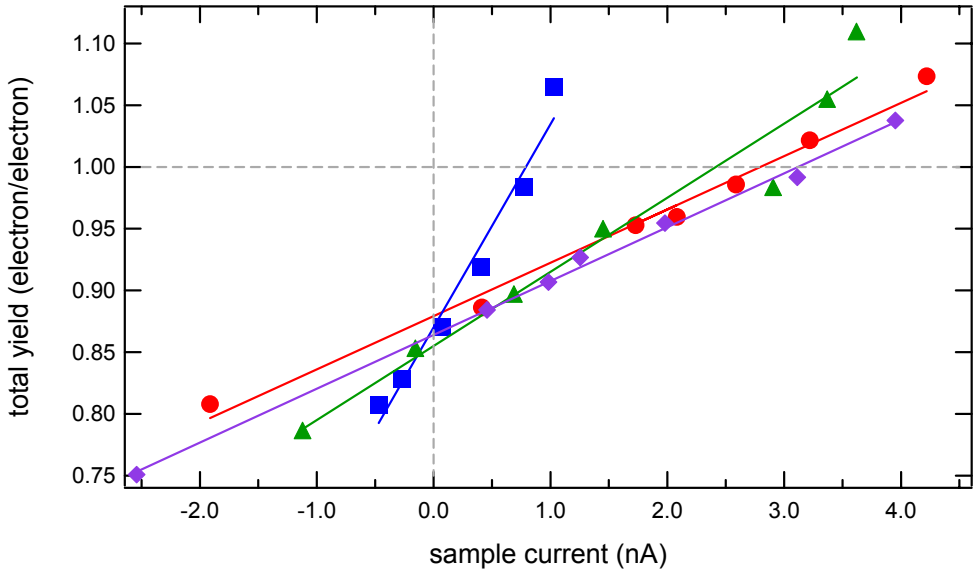

FIG. 4.11. Linear fits to total yield as a function of sample current to determine the correction factor associated with detector losses. Data shown is for gold data set #1 (■) gold data set #2 (▲), stainless steal alloy SS316 (●), and graphitic amorphous carbon (♦). Error bars have been omitted for visual clarity. At E_2^{σ}, the sample current should be 0 nA, and the total yield should be one. Fit results are summarized in Table 4.2.

reasonable to conclude the correction term was material independent (as it should be), and it could be applied to all materials (both conductors and insulators). Furthermore, it was assumed this correction factor was dependent only on detector-associated losses, and was not dependent on the incident beam energy. This assumption was used in all further analysis presented throughout the remainder of this dissertation (as explained in Section 6.2.2, this assumption is proposed as a subject for future investigation at USU). Finally, as shown in Table 4.1, the measured total-yield correction factor agreed with the numerically determined value (both determined at E_2^{σ}) to within 3 percent. Due to this small discrepancy between empirically and numerically derived total-yield correction factors, in subsequent analysis presented in this dissertation, the empirically derived total-yield correction (1.15) was used to adjust measured total yields all incident energies, and the numerically derived BSE correction

TABLE 4.2. Empirically determined correction factors for total yields due to losses in detector apparatus. Fitted correction factors are shown in Fig. 4.11.

Material	Setup	Correction Factor
Gold Data Set #1	DC	1.14±0.01
Gold Data Set #2	DC	1.17±0.01
Stainless Steal Alloy	DC	1.15±0.01
Graphitic Amorphous Carbon	DC	1.160±0.003
Combined Correction		*1.15±0.02*

(1.40) was used to adjust measured BSE yields. After total and BSE yield measurements were adjusted, SE yields were calculated from the corrected total and BSE yield values.

As mentioned above, for pulsed total yields, there existed a second correction factor associated with excluding the stage current contribution from the total-yield calculation. The stage current was excluded due to the small signal-to-noise ratio in the signal. Excluding the stage current contribution from the total-yield calculation was expected to artificially raise pulsed total-yield calculations by decreasing the value of the total incident current in the equation's denominator [see Eq. (3.4)]. It must be noted this raising effect resulting from the stage-signal exclusion was in opposition to the lowering effect of detector-losses. The stage correction factor was expressed as the ratio of the total yield, hypothetically measured with the stage contribution, $\mathrm{Yld}_{\mathrm{stg}}$, over the total yield measured without the stage contribution, $\mathrm{Yld}_{\mathrm{nostg}}$:

$$CF_{stg} = \frac{Yld_{stg}}{Yld_{nostg}}. \tag{4.1}$$

Equivalently, combining Eq. (4.1) with Eq. (3.1), it can also be shown the stage correction factor can be expressed as the ratio of the stage current over the total incident current as:

$$CF_{stg} = 1 - \frac{I_{stg}}{I_0}. \tag{4.2}$$

The stage correction factor, CF_{stg} was calculated using Eqs. (4.1) and (4.2) using extensive data sets for numerous conducting materials. Over 200 current readings (including I_{stg} and I_0) were taken from gold, stainless steal alloy SS316, molybdenum, and titanium data sets over a wide range of incident energies, ranging from 100 eV to 20 keV. From this data, it was observed for a well-optimized electron beam, the averaged fraction of the stage current contribution to the total incident current was 10±1 percent (error was the standard deviation of the mean), independent of incident beam energy. Thus, from Eq. (4.2), the stage correction factor can be written for all materials at all incident energies as:

$$CF_{stg} = 0.90 \pm 0.01. \tag{4.3}$$

Coincidentally, the lowering effect of the stage correction factor in total pulsed yields acted to cancel (almost exactly) the raising effect of the detector-loss correction factor (given in Table 4.1), such that by combining the two correction factors, the complete correction for pulsed total yields was found to be:

$$CF_{stg} \cdot CF_{det} = 1.03 \pm 0.02. \tag{4.4}$$

This result led us to conclude raw total pulsed yields calculated without the stage current were representative of the true (completely corrected) total yields:

$$Yld_{nostg} \approx Yld_{true} \tag{4.5}$$

to within a few percent error. Consequently, the raw pulsed total-yield data (calculated without the stage) needed no corrections during the analysis.

This conclusion was empirically tested using a method similar to that described above, where the raw total yields (calculated without the stage signal) were plotted as a function of sample current near E_2^{σ}. These tests were performed both on conductor and insulator

materials, using both the DC and pulsed setups, where total yields were plotted against DC sample current for the DC setup, and against the integrated sample displacement current for the pulsed setup. Plots of the linear fits to these data sets are shown in Fig. 4.12. The fit results for the correction factors are summarized in Table 4.3. As can be seen from the table, the correction factors did not vary significantly with material type (conductor or insulator) or measurement setup (pulsed or DC), and were close to unity (to within 1 percent), in agreement with Eq. (4.4). These results confirmed the relationship shown in Eq. (4.5), indicating for total pulsed yields measured without the stage current, no correction factors needed to be applied to the raw data.

In summary, pulsed-total yields were measured and calculated without the use of stage current contributions, while BSE yields were measured with the stage current. No correction factors were applied to the raw total pulsed-yield data (measured without the stage current contribution) since the stage and detector correction factors were shown to cancel out each other to unity [to within 3 percent from Eq. (4.4)]. Additionally, for both pulsed and DC total yield measurements, measured without the stage current, the systematic uncertainty was empirically determined to be within 1 percent (refer to Table 4.3). However, for pulsed and DC BSE yields, as well as for DC total yields, the stage-signal contribution was included in the total yield calculation, and correction factors shown in Table 4.1 were applied to the data to correct for detector losses. These correction factors were determined from previous numerical studies (Nickles, 2002), and were tested empirically as shown in Figs. 4.11 and Table 4.2. From these empirical tests, the systematic uncertainty associated with the DC total yield detector correction factor was shown to be within 2 percent for the four material data sets studied (refer to Table 4.2), and was found to agree with numerically derived values to

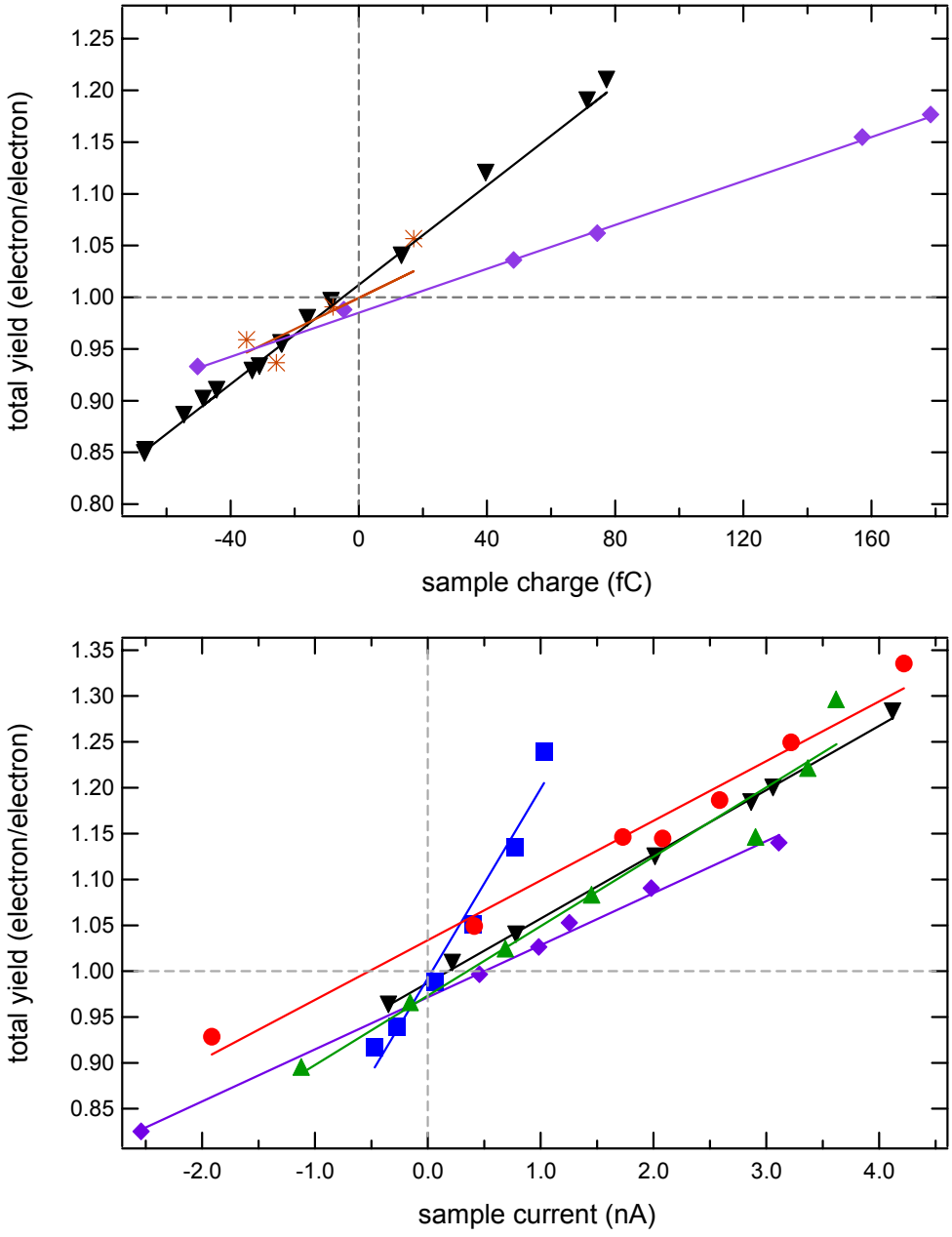

FIG. 4.12. Linear fits to total yield as a function of sample charge and current to determine the combined detector and stage correction factor. (Top) Pulsed total yield fits vs. sample charge for titanium (▼), graphitic amorphous carbon (♦), and Kapton™-aluminum (∗). (Bottom) DC total yield fits vs sample current for gold data set #1 (■) gold data set #2 (▲), stainless steal alloy SS316 (●), graphitic amorphous carbon (♦) and titanium (▼). Error bars have been omitted for visual clarity. For all materials and measurement setups, the combined correction factor was close to unity, to within 1 percent. Fit results for the combined correction factor are summarized in Table 4.3.

TABLE 4.3. Empirical determination of the complete total-yield correction factor calculated without stage current contributions. Fits to DC and pulsed data are shown in Fig. 4.12.

Material	Setup	Correction Factor
Gold Data Set #1	DC	1.01±0.01
Gold Data Set #2	DC	1.03±0.02
Stainless Steal Alloy	DC	0.97±0.01
Titanium Alloy	DC	1.013±0.003
Graphitic Amorphous Carbon	DC	1.028±0.003
Titanium Alloy	Pulsed	0.99±0.02
Graphitic Amorphous Carbon	Pulsed	1.02±0.02
Kapton on Aluminum	Pulsed	1.01±0.07
Combined Correction		*1.01±0.01*

within 3 percent. Finally, for both DC and pulsed setups, absolute SE yields were calculated using the corrected total and BSE yields using Eqs. (3.3) and (3.6). In conclusion, based on the results presented in this section for both DC and pulsed-yield setups, the systematic error associated with our absolute total-yields were well within our target systematic uncertainty of 5 percent. However, further empirical work remains to be done to validate the numerically derived SE and BSE correction factors (presented in Table 4.1), as well as to determine the possible energy dependence of the total-yield correction factor (assumed to be energy independent in this dissertation work). This work is further discussed in Section 6.2.2, and is presently being explored at USU. Further analysis of the random uncertainties associated with the pulsed-yield setup is discussed in Section 4.4.

4.4 Validation of Pulsed Measurements with DC Measurements

As discussed in Sections 4.1 and 4.2, repeated pulsed measurements were required to statistically determine electron yields and associated uncertainties. However, by making repeated measurements, the samples were also expected to charge, thus altering electron

emission properties. Furthermore, even after neutralizing the insulator surface, it was not known whether insulator electron properties would remain unchanged after repeated electron beam exposure. Consequently, it was important to be able to predict the statistical uncertainty of yield measurements with respect to repeated pulses as well as incident pulse magnitude such that electron yield accuracy could be balanced with electron beam exposure. To gain insight into the magnitude of the random uncertainties of our pulsed-yield measurements without insulator charging distortions, total and BSE yields were initially taken on a conducting titanium alloy sample.

On the titanium sample, error diagnostics for the pulsed-yield system were performed by taking 100 single-pulse total and BSE yield measurements at E_0=400 eV, with pulse duration of 5 μs and current magnitudes of 5 nA, 15 nA, 40 nA, 50 nA, and 80 nA. For total yield measurements, the stage current contribution was excluded due to a low signal-to-noise ratio (refer to Sections 4.2-4.3), but for BSE yields, all signal contributions were incorporated into the yield calculation. Results for the percent fractional error as a function of pulse number for both total and BSE yields are shown in Fig. 4.13, and depended both on the signal amplitude and on the number of pulsed measurements. Data were fitted using standard statistical analysis as:

$$\%FE(N) = \frac{100}{\sqrt{N}}\left(\frac{YLD_{stdev}}{YLD_{mean}}\right), \tag{4.6}$$

where N was the number of pulsed measurement, YLD_{stdev} was the yield standard deviation, and YLD_{mean} was the yield average. The ratio of the standard deviation over the yield was the fitting parameter. Additionally, the percent fractional error as function of incident current was fitted with a simple power law of the form A^n as shown in Fig. 4.14, and was expected to scale inversely with the incident current magnitude since the yield fractional error was

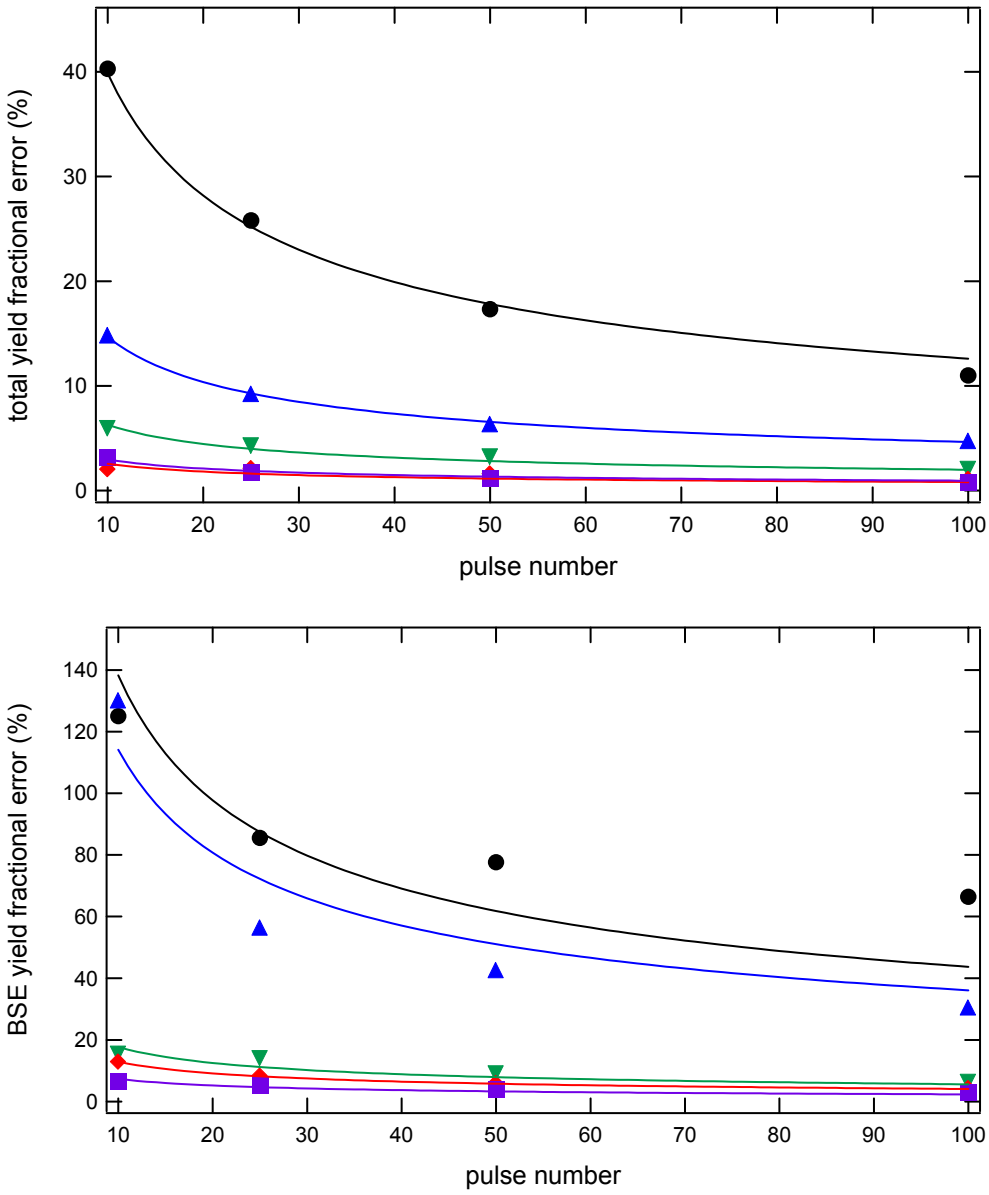

FIG. 4.13. Fractional error as a function of number of pulses for different incident pulse magnitudes. Total yields (top) and BSE yields (bottom) were taken with the low-energy STAIB gun at E_0=400 eV on conducting titanium at 5 nA (●), 15 nA (▲), 40 nA (▼), 50 nA (♦), and 80 nA (■) impulse magnitudes. Curves are least-squares fits to the data based on Eq. (4.6).

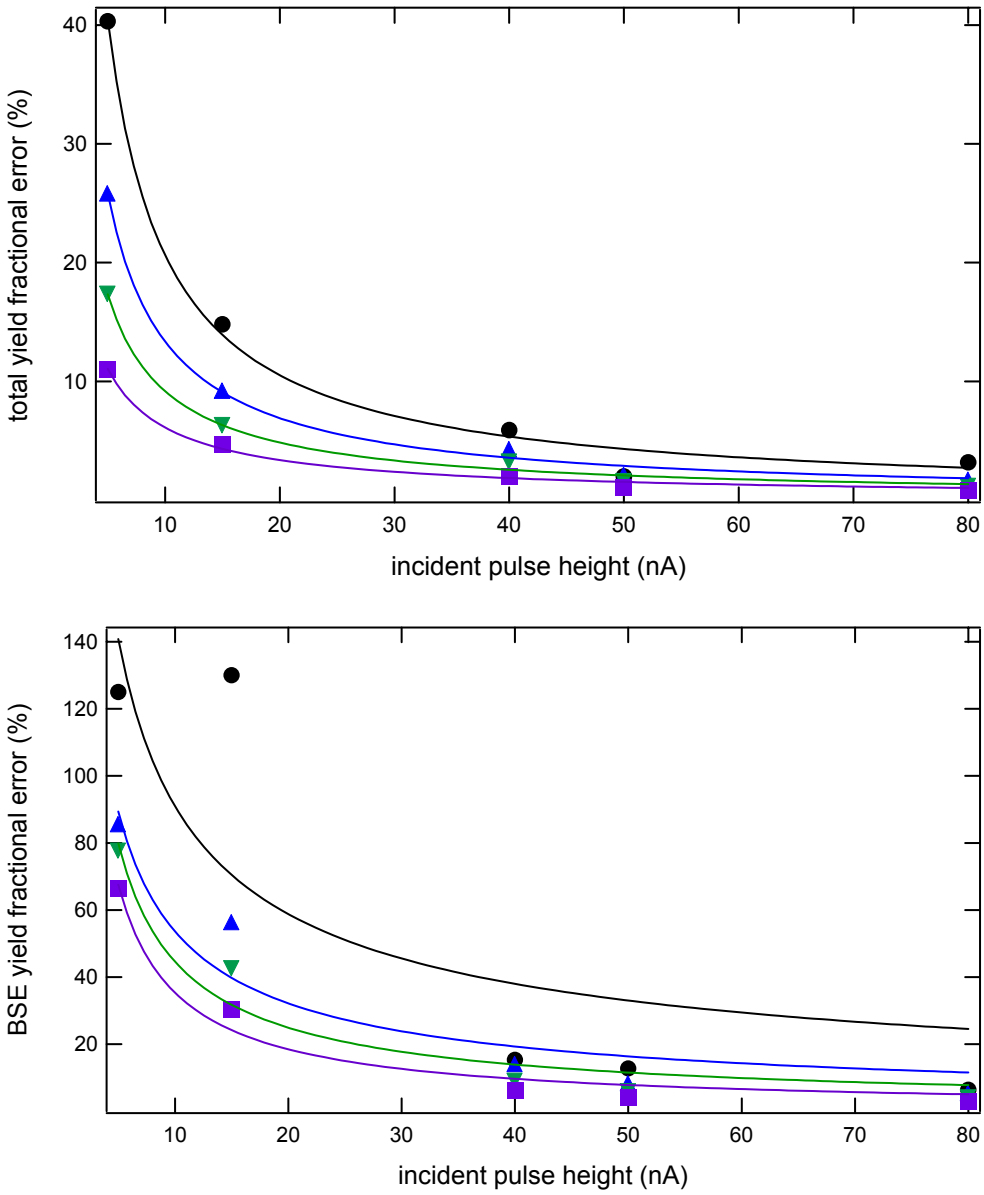

FIG. 4.14. Fractional error as a function of incident pulse magnitude for different number of pulses. Total yields (top) and BSE yields (bottom) were taken with the low energy STAIB gun at E_0=400 eV on conducting titanium using 10 pulses (●), 25 pulses (▲), 50 pulses (▼), and 100 pulses (■). Data were fitted with a power-law function of the form A^n. It was found, in general, the fractional yield errors varied inversely with incident pulse magnitude.

assumed to scale directly with the inverse of the system signal/noise ratio. As expected, the fractional yield error depended more strongly on incident pulse magnitude (scaled roughly inversely with pulse magnitude) than on number of measurements (scaled inversely to the root of the number of measurements). This showed improvements to electron yield accuracy, while minimizing the sample's exposure to the incident electron beam, could be obtained more readily by increasing the beam current as apposed to taking repeated measurements.

In this dissertation, total yield data were generally taken using ten pulses/measurement at 20-50 nA pulse magnitude (~10^6 electrons/mm^2 per pulse), such that the percent fractional errors ranged from 6-15 percent. BSE yields were generally taken at 50-100 nA pulse magnitude such that the errors ranged from 10-20 percent (refer to Figs 4.13 and 4.14). These errors remained fairly consistent for energies below and beyond E_2^{σ}, but increased in the energy regime E_2^{σ}±100 eV, where the total yield was close to unity, due to the diminished collector current signal. Additionally, the SE yield error remained close to the total yield error up to ~5 keV since in this energy regime the SE contribution to the total electron yield was much larger than the BSE contribution. Above 5 keV, SE and BSE emission contributed more or less equally to the total yield; such that (during measurements) the incident beam current was generally increased (see Section 3.4 on electron gun operation) to 50-80 nA to reduce the SE yield error. Finally, the total, SE, and BSE yield errors were also expected to depend on material (since yields varied with material); therefore, these diagnostic measurements were only meant to provide a rough gauge for yield uncertainties.

To test the absolute accuracy of the pulsed-yield setup, pulsed yields were taken on titanium using both the low-energy (100-5000 eV) and high-energy (5000-20000 eV) electron guns and compared with measurements taken with the DC-yield setup (see Sections 3.2 to 3.3 for setup schematics). Results for these comparisons are shown in Fig. 4.15, and displayed

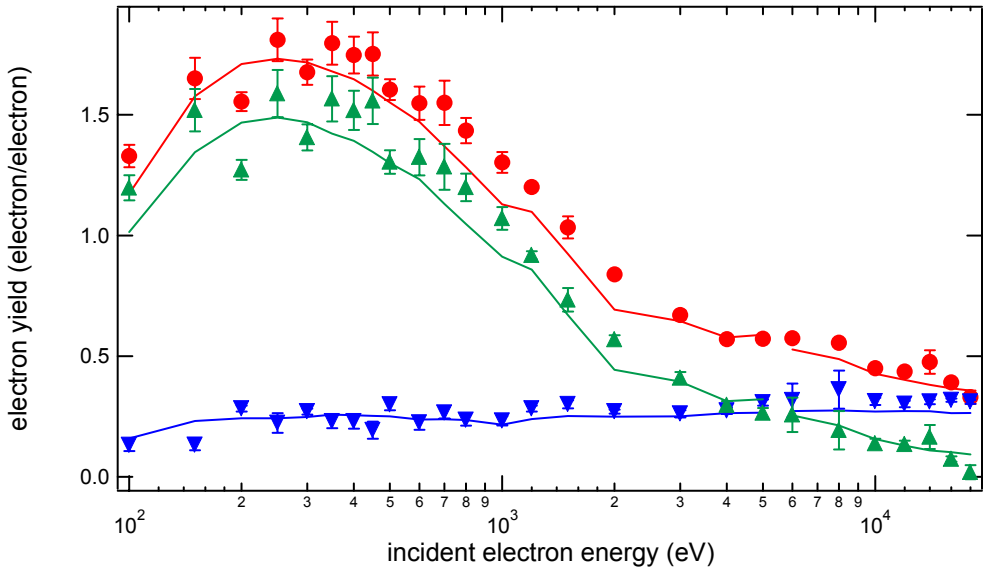

FIG. 4.15. Comparison of pulsed total (●), SE (▲), and BSE (▼) yields with DC (solid lines) yields for titanium. Each data point was the mean of 10 pulses (standard error as bars), of time duration 5 μs and magnitude 40 nA.

average (maximum) discrepancies of: total 10 percent (20 percent), SE 10 percent (20 percent), and BSE 15 percent (20 percent) yields over the incident electron energy range. Additionally, using the high-energy electron gun, pulsed-yield data were taken using 5 μs and 20 μs pulses, and yields were calculated using both the charge-integration and current pulse-profile schemes (refer to Section 4.2). For the charge-integration method (on both the 5 μs and 20 μs pulses), 10 pulses were used to calculate the yields, whereas with the current pulse-profile method (20 μs pulses), 10 pulses were combined and the average of 100 points on the current peak plateau were used to obtain a pulse maximum (see Section 4.2). A comparison of the pulsed-yield results are shown in Fig. 4.16, and showed average (maximum) discrepancies of: total 10 percent (15 percent), SE 13 percent (30 percent), and BSE 30 percent (80 percent) yields over the energy range. Finally, a pulsed SE spectrum was taken on titanium at E_0=400 eV (shown in Fig. 4.17) demonstrating the full automation of pulsed-

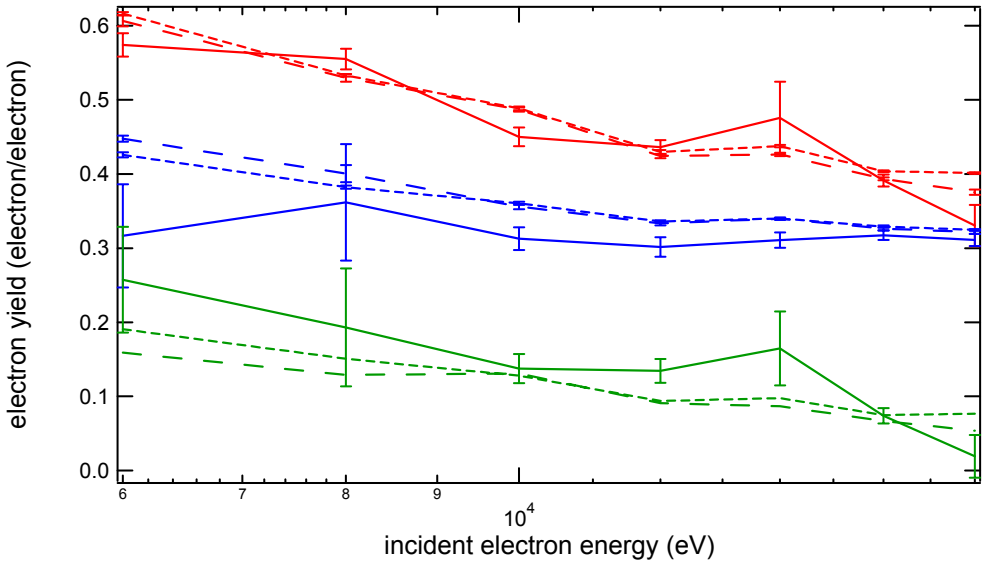

FIG 4.16. Comparison of pulsed high-energy data taken with the Kimball gun on titanium using different measurement approaches. Shown are total (red), SE (green), and BSE (blue) yields measured with 5 μs charge integration (solid), 20 μs charge integration (long dash), and 20 μs current profile (short dash) methods (see Section 4.2). Each data point was the mean of 10 pulses (standard error as bars) with pulse magnitude of 40 nA.

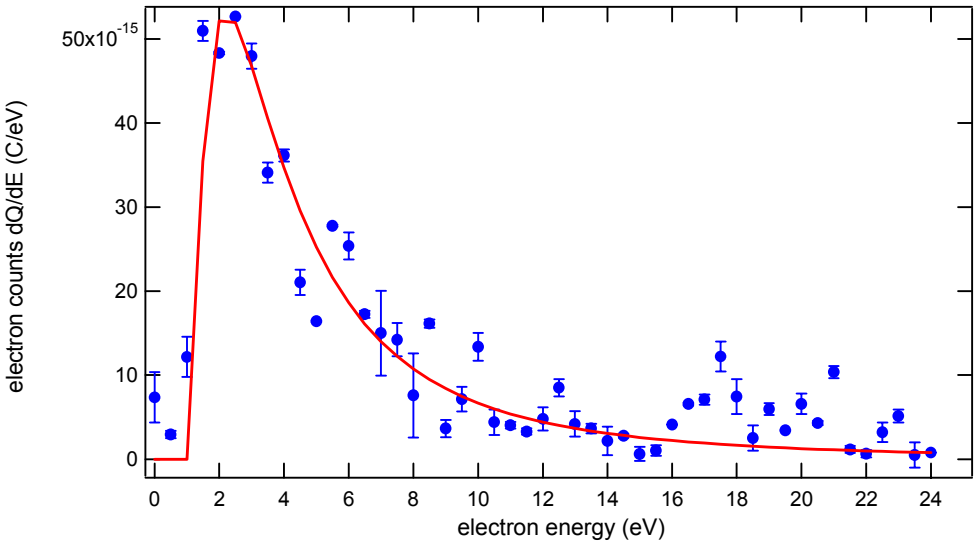

FIG 4.17. Pulsed-yield SE spectra on titanium at 400 eV. Each data point was the mean of 10 pulses (standard error as bars), of time duration 5 μs and magnitude 40 nA. Pulsed-data acquisition and suppression grid biasing were fully automated. Spectrum was fit with the Chung and Everhart model, Eq. (2.25) (Chung and Everhart, 1974).

yield measurements and suppression grid biasing for taking energy-resolved electron emission measurements.

4.5 Monitoring of Sample Charging

Since the FATMAN chamber was not equipped with a surface potential probe to directly measure insulator surface potentials, other indirect methods were developed to monitor insulator charging in response to incident electron irradiation. These methods included techniques to measure both steady-state charging behavior under a continuous incident electron beam, as well as the dynamic charging behavior under a pulsed incident electron beam. Specifically, these methods included: (i) measuring the evolution of the total electron yield and sample displacement current as a function of repeated incident electron pulses (refer to Sections 2.3.9 and 5.3.4); (ii) the calculation of both steady state and charging insulator surface potentials using uncharged SE spectra combined with DC, as well as pulsed electron beams (refer to Sections 2.3.6, 2.3.9, and 5.3.4); (iii) the use of shifting DC SE emission spectra to determine the positive and negative steady-state surface potentials, induced by continuous electron irradiation (refer to Section 5.1 and 5.2) and; (iv) the use of a probing pulsed incident electron beam used to determine high-negative steady-state potentials induced previously by a continuous-source incident beam energies $>E_2^{\sigma}$ (referred to as the mirror method in Section 4.6 and 5.2).

Of these four methods, the shifting DC spectrum [method (ii) above] method will be discussed in detail in this section. More in-depth discussions of the other methods are found elsewhere in this dissertation. The monitoring of the evolution of the total electron yields and sample displacement current as a function of incident electron pulse [method (i) above] is outlined in Section 2.3.9 with data provided in Section 5.3.4. Hence, only a brief description

will be given in this section. The combination of uncharged pulsed SE spectra with steady-state and pulsed yields [method (iii) above] is also discussed in more detail in Sections 2.3.6 and 2.3.9, and will only be given a short description in this section. Furthermore, applications of the pulsed probing mirror method [method (iv) above] for determining negative surface potentials and E_2^{σ} is covered in greater depth in Sections 4.6 and 5.2.

Concerning method (i) from above, both the total electron yields and integrated sample displacement current, Q_s, evolved with repeated electron pulses. Figure 4.18 demonstrates the response of the total electron yield and integrated sample displacement current in response to repeated 5 μs, ~50 nA (~10^6 electrons/pulse) incident electron pulses at E_0=500 eV (below E_2^{σ}), as well as E_0=3000 eV (above E_2^{σ}) on a Kapton^{TM}-aluminum sample (this and more data is presented in Section 5.3.4). For the data shown in Fig. 4.18, no neutralization was performed between incident pulses. As can be seen from the figures, both the total yield and displacement current responded dramatically to incident electron fluence for energies below E_2^{σ}, but showed little change at energies above E_2^{σ}. As described in Section 2.3.9 and demonstrated in Section 5.3.4, the decay constants for the evolving total yields and sample displacement currents were equivalent. Changes in the total yield and Q_s were most dramatic between E_1^{σ} and E_2^{σ} since positive charging occurred in this energy regime, and even small changes in the positive surface potential can trap a significant portion of the SE population (the peak energy is at ~2 eV as described in Section 2.1) (Nickles *et al*., 2000). Above E_2^{σ}, negative sample charging lowered the landing energy of incident electrons through electric-field repulsion. However, these charging effects were rather small (compared to the positive charging regime) since numerous pulses were required to significantly alter the landing energies of the incident electrons, and growing negative surface

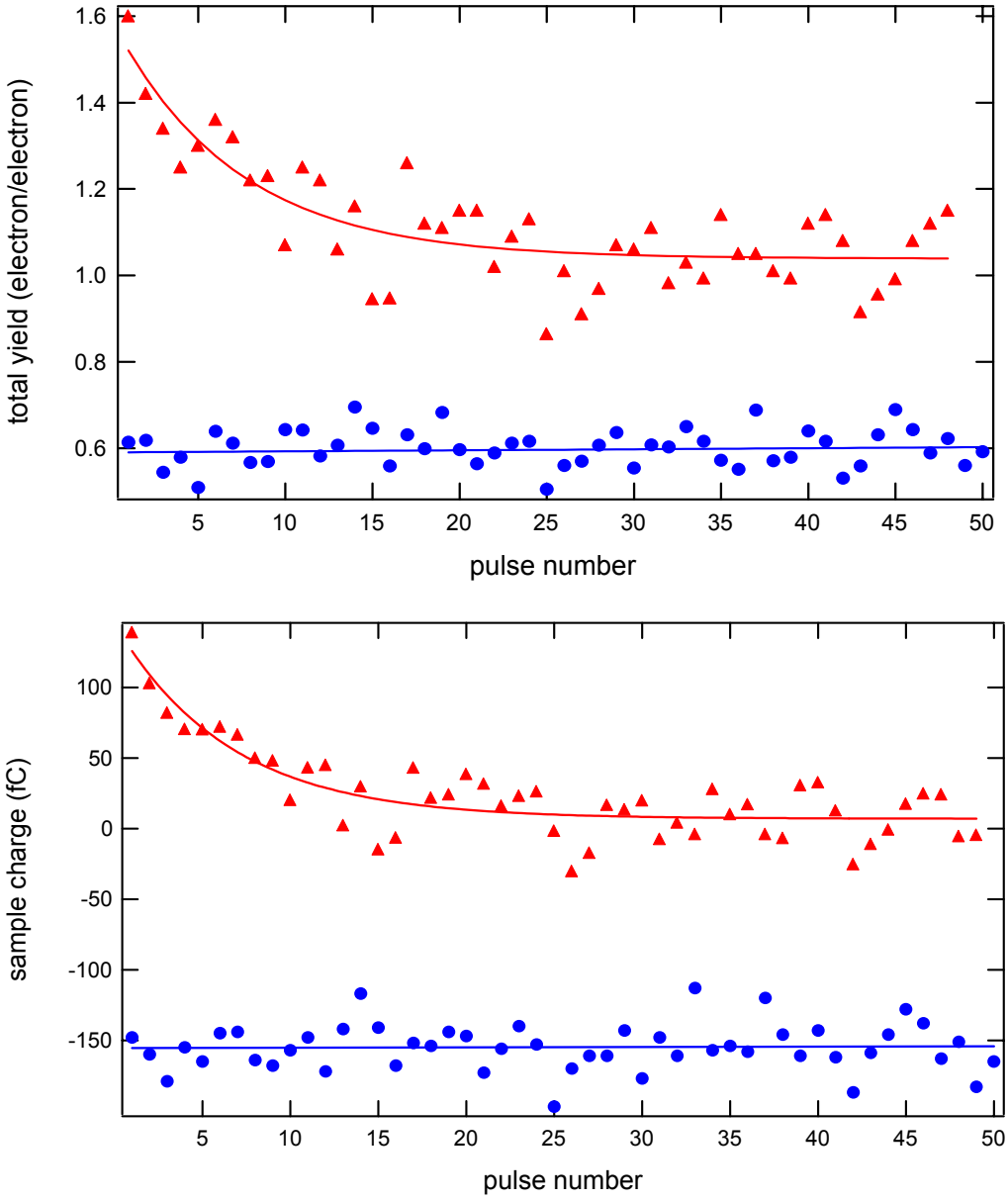

FIG. 4.18. Evolution of total electron yield (top) and sample displacement current (bottom) as a function of pulse number due to sample charging. Each pulse consisted of ~10^6 electrons. Data shown is for insulating Kapton™-aluminum at 500 eV (▲) (below E_2^{σ}) and 3000 eV (●) (above E_2^{σ}), in response to 5 μs, ~50 nA incident electron pulses. Data is fitted with decaying exponential functions. No neutralization techniques were employed between electron pulses. Quantitative analysis for these and other curves are provided in Section 5.3.4.

potentials did not significantly alter the total electron yields. A complete data set along with quantitative analysis for these curves on Kapton™-aluminum is provided in Section 5.3.4.

Monitoring sample charging through these types of pulsed measurements was useful in three ways. First, by monitoring the evolution of electron yields during routine measurements, the effects of incident electron exposure on electron yield could quickly be assessed, and the appropriate neutralization source (such as the electron flood gun) could be utilized to discharge the sample and return the yields to their original uncharged values. Additionally, the effectiveness of discharging techniques could be evaluated by comparing the yields before and after neutralization. These types of studies are explored in Sections 5.1 and 5.3.3. Second, the evolution of sample displacement current as a function of electron fluence provided a method to evaluate pre-steady insulator charging rates in response to pulsed incident electron irradiation. The models used to evaluate such data were developed in Section 2.3.9, and were applied to experimental data in Section 5.3.4. Third, as mentioned in method (ii) above, by combining the evolving total yield data with the uncharged SE spectra taken at the same incident energy, the evolving positive surface potentials were calculated as outlined in Sections 2.3.6 and 2.3.9. These calculations are demonstrated on Kapton™ in Section 5.3.4, and have been proposed as continued future work at USU (refer to Section 6.2.3).

As previously mentioned in method (iii) above, measuring shifts associated with the DC SE spectral emission peak provided a technique for determining the sample surface potential induced by a continuous-source electron beam. As further explained in Section 4.6, this technique can also be used to determine the crossover energies of insulator materials (refer to Sections 4.6 and 5.1-5.2). Under a continuous-source electron beam, an insulator quickly charges to steady state, and the sample surface potential goes either positive (for energies

between E_1^{σ} and E_2^{σ}) or negative (for energies below E_1^{σ} or above E_2^{σ}). These sample potentials can have considerable effects on SE escape kinetic energies as measured by the SE emission spectra. As explained in Section 2.1, typically a material with 0 V surface potential displays a SE emission peak near 2 eV (see, for example, Fig. 2.1). However, if the sample potential becomes negative, the surface potential barrier will be lowered, and a repulsive electric field will accelerate escaping SE's away from the sample surface. The increased energy of escaping SE's can be observed in the SE spectra by a right-shifting of the SE emission peak to higher energies (Nickles *et al*., 2000; Girard *et al*., 1992; Jbara *et al*., 2001; Mizuhara *et al*., 2002). Alternatively, if the sample surface is positive, the surface potential barrier will increase and inhibit lower energy SE's from escaping the sample surface. In this case, an external positive potential must be applied, for example, by a surrounding grid to pull the full distribution of SE's away from the attracting surface potential of the sample. Hence, for positive surface potentials, a typical SE spectrum will show an SE peak left-shifted to apparent negative kinetic energies.

Incidentally, future modifications must be made to our present detector apparatus in order to observe this left shifting of the suppressed SE spectrum, which results from positive charging. This is the case since our detector apparatus has an inner grid (tied to the sample stage) that sits between the sample and the suppression grid used to extract SE's from the positively charged sample (refer to Section 3.1). Hence, with our present detector design, an SE spectra influenced by a positively charged sample would appear to decrease in the magnitude (instead of shifting to the left) since only higher-energy electrons could escape the sample, pass through the inner grid and suppression grid, and arrive at the detector (refer to Fig. 4.20 below). If we wish to observe the left shifting of the SE spectrum resulting from a positive surface potential, we must electrically tie the inner grid (along with the sample stage)

to the suppression grid. However, our present detector was not intended for this type of rewiring, and as a result, the inner grid cannot be biased to positive potentials >30 V. Future alterations to our detector have been proposed to electrically isolate the inner grid from the stage such that it can be biased independently (see Section 6.1.1). Such alterations will allow us to more effectively study positive surface potentials using the SE spectra. Electron emission spectra measured with the inner grid grounded (the sample stage was also grounded) along with spectra measured with the inner grid (and sample stage) electrically tied to the suppression grid, are demonstrated further below.

The use of SE emission spectra for monitoring sample potentials (both positive and negative) was tested first on a conducting gold sample such that the sample potentials could be controlled better by biasing the sample using a DC power supply. These measurements were made while irradiating the gold sample with a continuous ~30 nA incident electron beam at 1 keV. Although demonstrated on a conductor, this same method was used later on insulating samples to determine surface potentials induced by continuous electron beam charging (see Sections 5.1 and 5.2).

A comparison of two emission spectra measured with the inner grid both grounded and tied to the suppression grid, while the sample was biased to -5 V is shown in Fig. 4.19. For these spectra, the incident beam energy was E_0=1 keV and grid biasing steps were 0.5 V. Several features of this graph should be noted. For the spectrum taken with the grounded inner grid, a false SE emission peak was observed at 1.8 eV caused by SE emission from the inner grid, excited from the scattering of sample BSE's. However, with the inner grid tied to the suppression grid, this second SE peak disappeared since SE's originating from the inner grid were mutually discriminated by both inner-grid and suppression-grid potentials, similar to sample SE's. For the default detector configuration (inner grid grounded), the position of

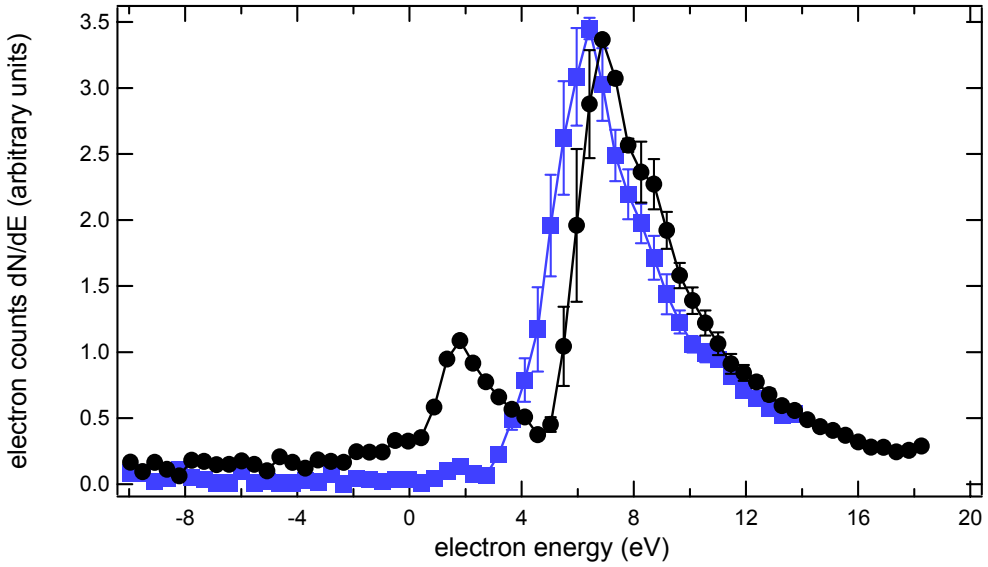

FIG. 4.19. SE spectra of negatively biased gold (-5 V) with inner grid both tied to the suppression grid (■) and grounded (●). Grid bias steps were 0.5 V, E_0=1 keV, and I_0≈30 nA. A second peak (at 1.8 eV) appeared in cases where the inner grid was grounded, as BSE's originating from the sample scattered off the inner grid and created additional SE's. Sample SE peak maxima occurred at 6.4 eV (■) and 6.9 eV (●). Surface potential analysis is summarized in Table 4.4.

this false SE peak was not noticeably affected by the sample potential, and so it was used as a reference potential to determine the inherent kinetic energy of SE's. In this manner, it served as a benchmark from which to reference the charged sample SE emission peak in order to determine the value of the sample potential. For example, when emitted SE's are repelled by a negatively biased sample, as is the case in Fig. 4.19, the SE distribution peak is right shifted to a kinetic energy corresponding to the applied sample potential in addition to the SE's own inherent kinetic energies [(sample bias)+(inherent SE kinetic energy)]. In Fig. 4.19, the SE peak maxima occurred at 6.4 eV (for the inner grid tied to the suppression grid) and 6.9 eV (for the grounded inner grid). Hence, after accounting for the inherent SE kinetic energies of 1.8 eV, the shifted spectra were consistent with the applied sample voltage (-5 V) to within 0.4 V and 0.1 V respectively. These results are summarized in Table 4.4.

TABLE 4.4. A comparison of DC SE spectral methods for determining sample potentials on a gold conducting sample. Methods are identified by their respective figure numbers. All measurements were taken at incident beam energies of E_0=1 keV, incident beam currents of ~30 nA, and suppression grid bias steps of 0.5 V. Measured sample potentials were calculated by the shifts in the sample SE spectral peak with respect to the grid SE peak occurring at 1.8 eV.

Method Description	Applied Sample Potential (V)	SE Peak (eV)	Grid Peak (eV)	Measured Sample Potential (V)	Discrepancy (V) (and % error)
Inner Grid Tied to Suppression Grid, Figs. 4.19 and 4.22.	-5.0	6.4	None	-4.6	0.4 (8%)
	+5.0	-3.3		+5.1	0.1 (2%)
Grounded Inner Grid, Positive Potential, Figs. 4.20 and 4.21.	+1.5	1.8 eV (Original SE Spectra)	Not Separated From Sample	+1.0	0.5 (33%)
	+2.0			+1.5	0.5 (25%)
	+5.0			+3.4	1.6 (32%)
Grounded Inner Grid, Negative Potential, Fig. 4.23.	-2.0	4.6	1.8 eV	-2.8	0.8 (40%)
	-5.0	6.9	1.8 eV	-5.1	0.1 (2%)
	-10.0	11.9	1.8 eV	-10.1	0.1 (1%)
	-15.0	16.9	1.8 eV	-15.1	0.1 (1%)

Figure 4.20 shows additional emission spectra for the case where the gold sample was biased positively, and the inner grid was grounded. Again, the suppression grid bias steps were 0.5 V, and the incident beam energy was and E_0=1 keV. As explained above, without modifying the detector, the positive surface potentials could not be measured by observing the left shifting of the sample SE peak since the inner grid shielded the sample from the suppression grid extraction potentials. Instead, the magnitudes of the SE distributions were suppressed, and the sample SE peaks occurred at 1.8 eV. It should be noted the SE distributions shown in Fig. 4.20 were composed of both sample and inner-grid SE contributions, similar to the inner grid SE peak occurring in the negatively-biased configuration (shown in Fig. 4.19). The magnitude of the SE distribution decreased with increasing sample potential since only electrons with kinetic energies greater than the applied

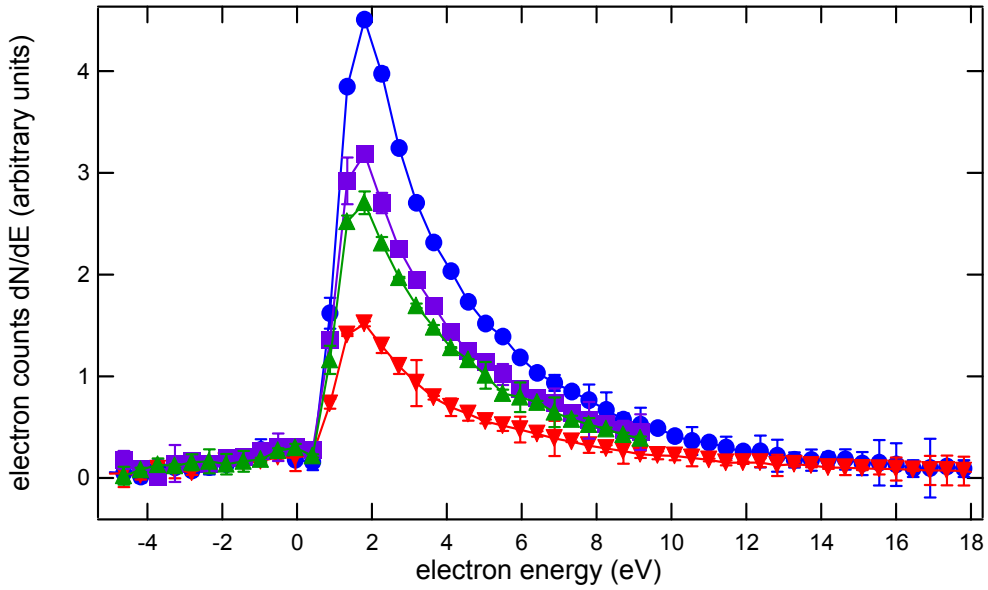

FIG. 4.20. SE spectra of a positively biased gold sample with the inner grid grounded. Grid bias steps were 0.5 V, E_0=1 keV, and I_0≈30 nA. The sample was biased positively to 0 V (●), 1.5 V (■), 2 V (▲), and 5 V (▼). Increasing the sample potential decreased the amplitude of the SE peak, but not the positions, all occurring at 1.8±0.5 eV.

potential could escape from the sample, thus contributing to the total measured SE population. Another way of viewing this is only sample SE's at the higher-energy tail of the uncharged SE distribution could be measured as a part of the SE spectrum. Furthermore, for those SE's that escaped, their kinetic energies were diminished by an amount corresponding to the sample potential.

From these observations, an approximate method for determining positive sample surface potentials, with the inner grid grounded in our detector, was devised. By right shifting the suppressed SE spectra such that the distribution tails lined up, the sample potentials could be determined by noting energy shift required to line up the spectra. This technique is illustrated in Fig. 4.21 for the data shown in Fig. 4.20. After lining up the higher-energy tails of the spectra, the shifts of the SE peaks with respect to their original measured

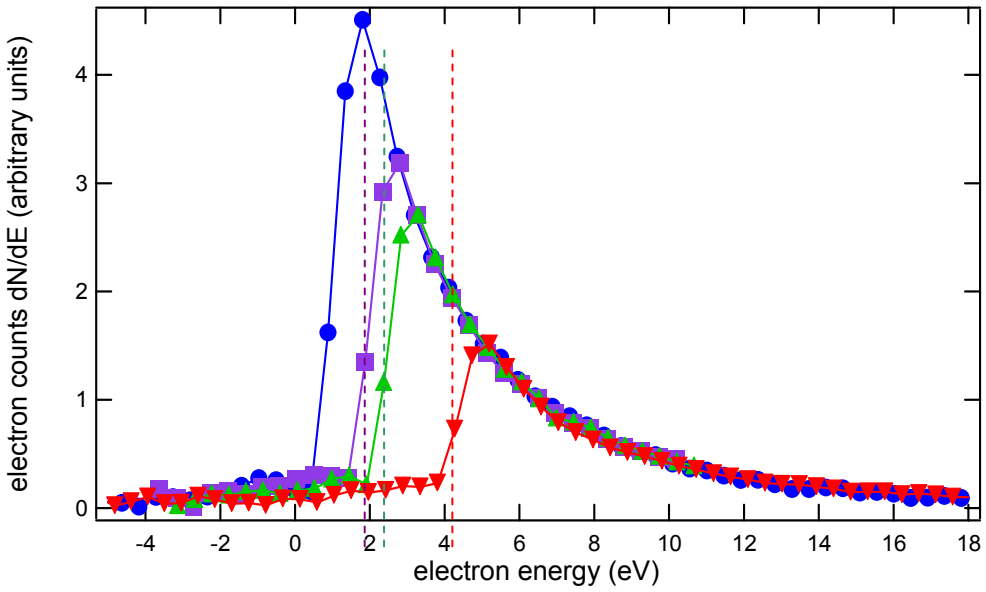

FIG. 4.21. SE spectra of a biased gold sample with the inner grid grounded and electron energy spectra shifted to the right so the higher energy tails lined up. Dashed lines indicate the right-shifted cutoff point of the spectra. This offered a method for determining positive sample surface potentials by measuring the left cutoff point of the SE distributions, suppressed by the positive potentials. Surface potential data obtained from these spectra are summarized in Table 4.4. Error bars have been omitted for clarity.

positions (1.8 eV for all curves) were used to determine the applied potential. For the case of this gold sample, the actual applied sample potential was known such that the accuracy of the method could be assessed. The results of this method are summarized in Table 4.4.

As can be seen from Table 4.4, in general, it was observed the predicted sample potentials were low by ~30 percent. This occurred since a significant portion of the measured SE spectrum was composed of inner grid SE's (not sample SE's), since the two spectra could not be separated by our detector in this biasing configuration. Hence, the inner-grid SE distribution artificially inflated the area under the sample SE spectral curve (pushed the higher-energy tail to the right), and diminished the magnitude of the shift required to line up the spectra (refer to Fig. 4.21). Finally, it should be noted in comparing SE spectra using this method, it was important to maintain a constant incident beam current such that the

magnitudes of the spectra would not be further inflated (deflated) by rising (lowering) incident electron currents.

In order to more directly observe the effects of a positive surface potential on SE emission spectra, the inner grid was electrically tied to the suppression grid. Again, the suppression grid biasing step was 0.5 V, and the incident beam energy was E_0=1 keV. Figure 4.22 shows SE emission spectra for the gold sample biased to +5 V and to -5 V with this detector biasing configuration. Furthermore, in this configuration, it was possible to observe negative sample potentials by observing the right shifting of the sample SE peak. Additionally, the inner grid SE peak (usually at 1.8 eV) was absent for reasons explained above. From these spectra, it was observed the sample SE peak shifted to the left to -3.3 eV when the sample was biased positively (to +5 V), and to the right to +6.4 eV when the sample

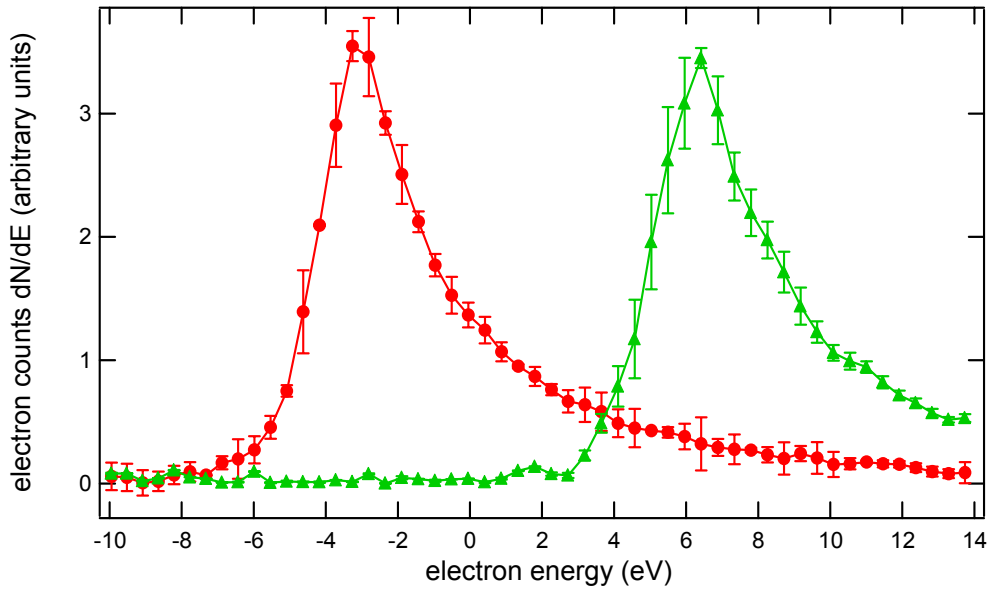

FIG. 4.22. SE spectra with the inner grid tied to the suppression grid on a biased gold sample at +5 V (●) and -5 V (▲). Grid bias steps were 0.5 V, E_0=1 keV, and I_0≈30 nA. With the inner grid tied to the suppression grid, the measurements of both positive and negative sample potentials were made possible by monitoring the shifting of the SE peak position. Surface potential data obtained from these spectra are summarized in Table 4.4.

was biased negatively (to -5 V). Hence after accounting for the inherent SE kinetic energy of 1.8 eV, the sample potentials were estimated to be +5.1 V and -4.6 V. These results were accurate to the known applied potentials (±5 V) to within 2 percent and 8 percent respectively.

Shown in Fig. 4.23 are four additional SE emission spectra with the inner grid grounded, and the sample biased negatively to -2 V, -5 V, -10 V, and -15 V. Again, the suppression grid biasing step was 0.5 V, and the incident beam energy was and E_0=1 keV. This figure further demonstrates the shifting SE spectra in response to the applied negative surface potentials. From the spectra, it was observed the sample SE's gained kinetic energy, and the SE peak maxima right-shifted to values of 4.6 eV, 6.9 eV, 11.9 eV, and 16.9 eV (for

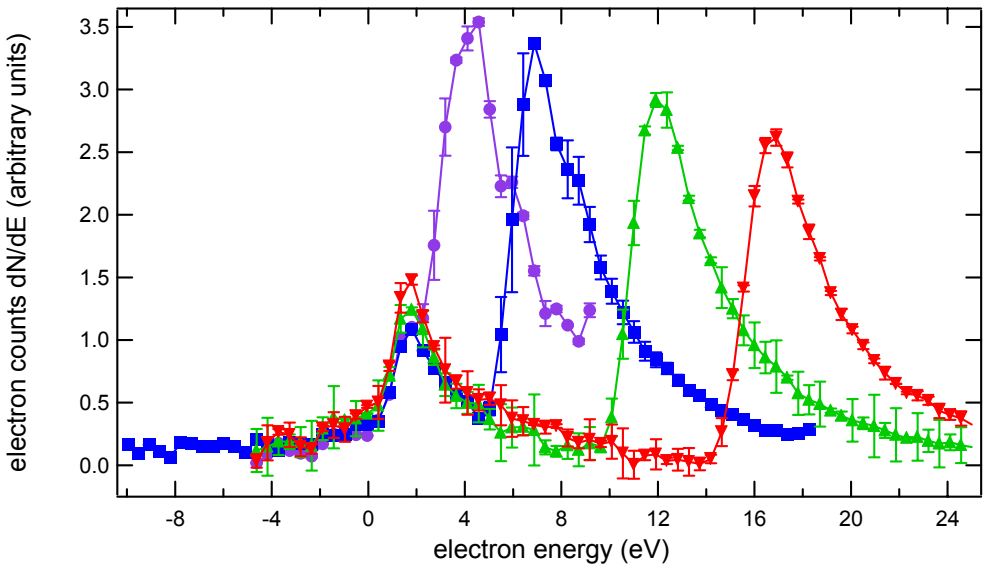

FIG. 4.23. SE spectra with the inner grid grounded on a negatively biased gold sample. Grid bias steps were 0.5 V and E_0=1 keV. The applied sample bias potentials were -2 V (●), -5 V (■), -10 V (▲), and -15 V (▼). The sample potential was determined by the position of the SE peak maxima measured with respect to the grounded grid peak (occurring at 1.8 eV). Surface potential data obtained from these spectra are summarized in Table 4.4.

the applied potentials given above). Again, after having accounted for the inherent SE kinetic energy of 1.8 eV, the sample SE peak positions provided estimates for the negative sample

potential as -2.8 V, -5.1 V, -10.1 V, and -15.1 V. Hence, except for the -2 V bias, sample potentials determined using this method were accurate to within 2 percent. For the -2 V potential, the inner-grid SE distribution inflated the sample SE distribution, thereby increasing the area under the sample SE distribution, and pushing the peak to higher energies.

Table 4.4 (above) summarizes all gold-sample SE spectral results. To summarize, the SE spectral methods involved measuring shifts in the sample SE spectra with respect to a reference potential of 1.8 eV, taken from the inner grid SE peak. These measured shifts were then compared with known applied potentials on the sample in order to test the accuracy of the spectra data. By comparing all SE spectral methods, it was observed that for measuring negative sample potentials, the grounded inner biasing scheme was the most accurate for sample potentials magnitudes >5 V. However, at potentials near 2 V, the sample SE distribution could not be separated from the inner grid SE distribution, leading to errors of ~40 percent. At these lower potentials, it became beneficial to modify the detector biasing scheme by tying the inner grid (along with the sample stage) to the suppression grid. This eliminated the inner-grid SE distribution, and hence increased the accuracy of determining small sample potentials near 2 V. As can be seen from Table 4.4, this biasing scheme also provided the most accurate estimates for positive sample potentials at +5 V. However, presently this biasing configuration is limited by the maximum applied potential that can be supplied to the inner grid. In future work, the inner grid will be rewired such that it can be isolated from the stage, and can be biased *ex situ* to values exceeding ±100 V (see Section 6.1.1).

Finally, it must be mentioned although these DC SE spectral methods provided ways to measure steady-state sample potentials, significant charging occurred by irradiating the insulator samples with a continuous electron beam. For this reason, this method was only used on insulators after all other pulsed-yield measurements were taken. As discussed further

in Section 4.6, this method was also useful for determining insulator crossover energies, and was also used later to evaluate insulator surface potentials as a function of incident energy (see Section 5.1).

4.6 Other Methods for Determining Yield Crossover Energies

In this dissertation, several methods were explored for measuring the insulator crossover energies, E_1^{σ} and E_2^{σ}, energies for which the net charging of an insulator material is zero. Also, at these energies, the total yields are unity. Specifically, four methods were explored for determining the crossover energies, E_1^{σ} and E_2^{σ}, and were applied to both conductor and insulator samples. A short description of each method is outlined below.

4.6.1 The Yield Curve Method

The first method was the most straightforward, and involved fitting the total yield curves with the models presented in Section 2.3.2. Specific methods for measuring pulsed electron yields on insulators are described in Sections 4.1 and 4.2, and involved the use of a pulsed incident electron source and the low-energy electron flood gun. Alternatively, for conductors, total yield curves could be measured using a continuous incident electron source and the DC measurement setup (refer to Section 3.2). For a demonstration of this method, pulsed total and SE yields for conducting titanium are fitted with various yield models in Fig. 4.24. Table 4.5 compares estimates for the crossover energies for both total and SE yields resulting from the various model fits. Similar insulator data is provided in Sections 5.1-5.3.

4.6.2 The Sample Current Method

With the electron beam energy initially set at $E_1^{\sigma}<E_0< E_2^{\sigma}$, the sample current (for DC measurements on conductors) or displacement current (for pulsed measurements on insulators)

was monitored as the incident beam energy was adjusted toward either crossover energy (decreased to find E_1^{σ} or increased to find E_2^{σ}). Initially, for $E_1^{\sigma}<E_0<E_2^{\sigma}$, the sample current was positive, but as the crossover energy was traversed, the current would approach 0 nA, and eventually become negative. By performing a linear fit to the sample current (or integrated charge for pulsed measurements) as a function of beam energy, the total-yield crossover energies could be determined. Linear fits to the integrated pulsed sample current as a function of incident energy are illustrated once again on a conducting titanium sample in Fig. 4.25. Similar results for insulators are provided in Sections 5.2 and 5.3.2. In taking this data, it was important to keep the electron beam current constant such that sample current depended only on beam energy. Additionally, for insulators, the low-energy electron flood gun was used between pulses to neutralize any latent positive surface charge induced by the incident electron source. Finally, this method was only effective in determining the total (not SE) crossover energies since measured sample displacement currents represented the sum of incident, SE, and BSE currents that could only be differentiated with the use of the suppression grid.

4.6.3 The DC-Spectral Method

This method worked only for insulator materials, and depended on the steady-state charging behavior of dielectric materials under electron beam bombardment. A continuous

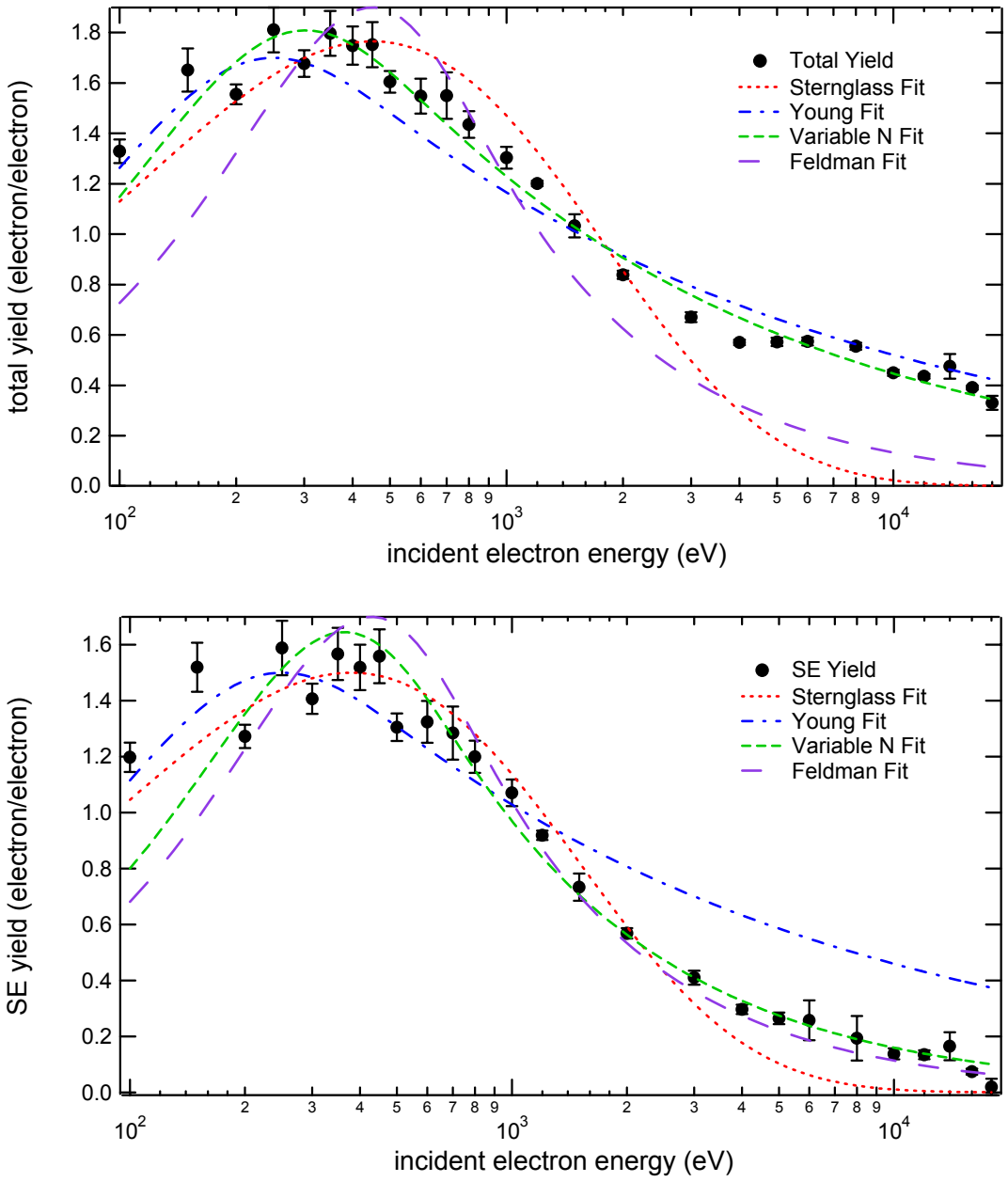

FIG. 4.24. Various fitting models to total (top) and SE (bottom) pulsed-yield curves for titanium. Note the logarithmic energy scale. Estimates for the crossover energies for these models are summarized in Table 4.5. Detailed descriptions of these four models are summarized in Section 2.3.2.

TABLE 4.5. Comparisons of E_1 and E_2 values from pulsed-yield measurements of titanium using various yield-curve fitting models. The crossover energies for both the total and SE yields are shown. Wide variations existed for the crossover energies between the different models. Detailed descriptions of these models are given in Section 2.3.2.

Fitting Model	Total-yield E_1^{σ} (eV)	Total-yield E_2^{σ} (eV)	SE-yield E_1^{δ} (eV)	SE-yield E_2^{δ} (eV)
Sternglass	78	1719	91	1201
Young	64	1550	82	1084
Variable N	82	1600	130	961
Feldman	142	1228	154	1040

incident electron source of <50 nA was used to measure DC-electron energy spectra on the insulator (see Sections 5.1 and 5.2). Regardless of the incident energy, under a DC-electron beam the insulator quickly charged to steady state where no net current arrived at or left the sample (except at E_1^{σ} and E_2^{σ} where the net current remained at zero). Once this steady-state condition was met, the total yield was equal to unity (Reimer, 1985), and depending on the incident energy, the corresponding surface potential became either positive (for energies between the crossover energies) or negative (for energies below E_1^{σ} or above E_2^{σ}). As described in Section 4.5, the DC-SE emission spectra, particularly the position of the SE emission peak, could be used to measure the steady-state surface potential. Hence, starting out in the energy regime of $E_1^{\sigma}<E_0<E_2^{\sigma}$, the incident energy was increased (decreased) towards E_2^{σ} (E_1^{σ}), and the evolution of the surface potential was monitored using the position of the sample SE peak. The beam energy associated with the initial right-shifting of the sample SE peak (indicated by a separation of the sample SE peak from the inner grid reference peak, as shown in Section 4.5) was taken to be the crossover energy. As with the sample current method, this method was only effective in determining the total (not SE)

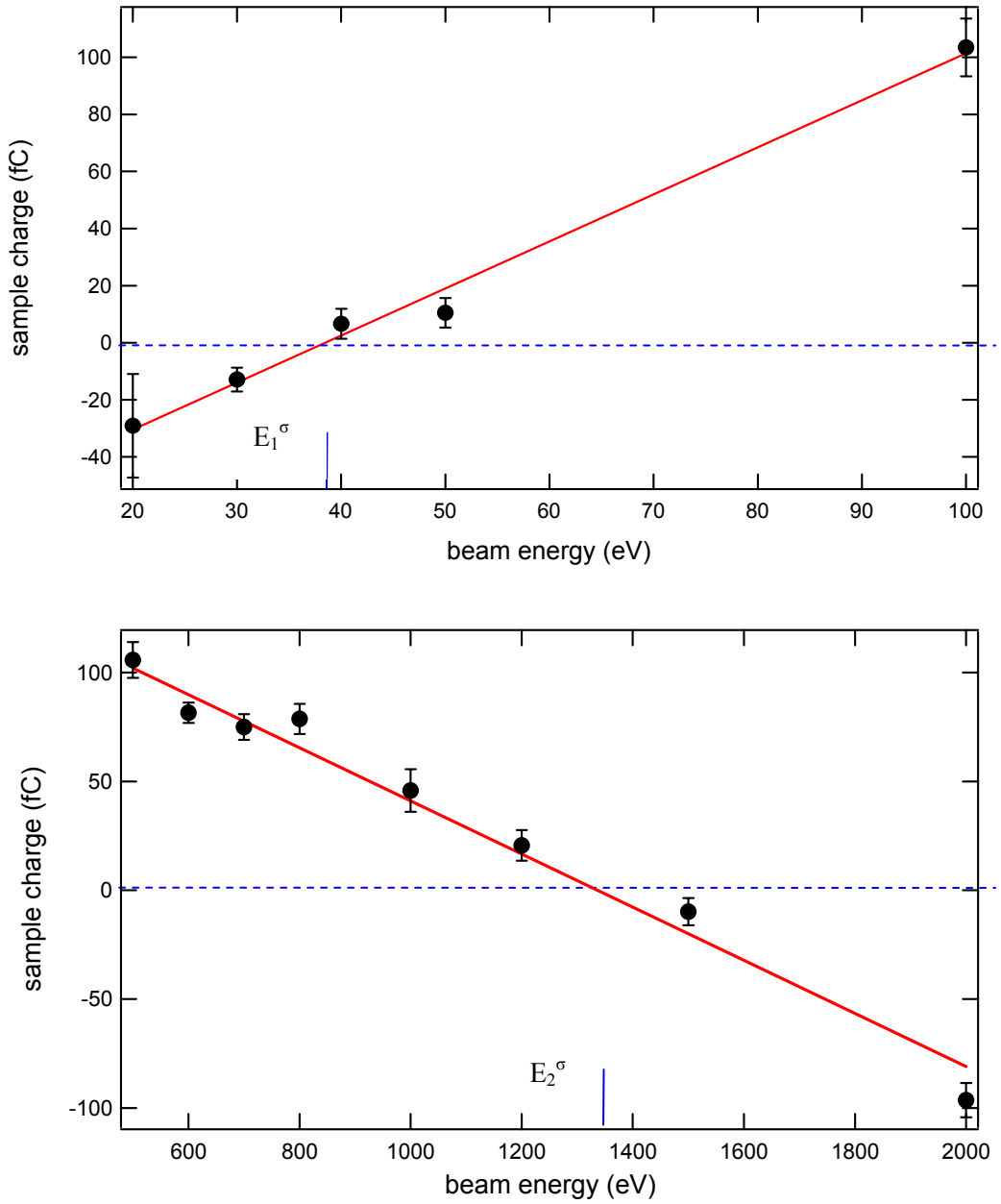

FIG. 4.25. Linear fits to the integrated sample displacement current as a function of incident beam energy for titanium. This method was used to find E_1^{σ} (top) and E_2^{σ} (bottom), the energies for which the sample displacement current was zero. This method yielded E_1^{σ}=38±1 eV and E_2^{σ}=1340±70 eV.

crossover energies. Further results for this method in determining total-yield crossover energies on insulators are provided in Section 5.2.

4.6.4 The Mirror Method

This method worked only for insulator materials for determining the total-yield second crossover energy, and depended on the negatively charged surface potentials of insulators under electron beam bombardment. A defocused (~1 cm) continuous incident electron beam at an energy beyond E_2^{σ} (generally 2-5 keV, depending on the sample thickness and dielectric strength) was used (radiation times were several minutes) to charge the insulator samples uniformly to a negative potential of several hundred volts. During the charging process, it was important not to exceed the beam energy threshold corresponding to the electrical breakdown of the insulator that depended on the dielectric strength and thickness of the material (see Section 5.2 for examples of the effects of dielectric breakdown).

When charged negatively with a high-energy electron beam, the surface potential, V_s, of an ideal infinite-resistance insulator material will adjust such that the landing energy of incident electrons becomes equal to E_2^{σ}, thus satisfying the steady-state condition of $\sigma=1$. The relationship between the landing energy (E_2^{σ} at steady state), the beam energy, and the surface potential is governed by Eq. (2.34) in Section 2.3.6 with the landing energy, E_L, set equal to E_2^{σ}:

$$E_2^{\sigma} = E_0 - \left|eV_s\right|. \tag{4.7}$$

In writing Eq. (4.7), it was assumed the effects of radiation-induced conductivity could be neglected (see Section 2.3.6). However, for most thin-film insulators, some leakage current will occur, either through the bulk or across the surface, which must be accounted for.

As a first approximation, the thin-film insulator can be treated as a planar capacitor (with the conductor substrate and charged surface acting as the electrodes) that discharges in an ohmic fashion through the bulk of the insulator. The RC-time constant, τ_{RC}, for discharging insulator can be written as:

$$\tau_{RC} = \rho \varepsilon_r \varepsilon_0 , \tag{4.8}$$

where ρ is the material resistivity, ε_r is the relative dielectric constant, and ε_o is the permitivity of free space. The decaying surface potential can then be estimated as a function of time as:

$$V_s(t) = V_{s0} \cdot e^{-t/\tau_{RC}} , \tag{4.9}$$

where V_{s0} is the initial sample potential induced by electron beam irradiation, and V_s is the decayed potential after a time interval, t. Using Eqs. (4.7) through (4.9), one needs only to determine the original sample potential (V_{s0}) induced by E_0 to calculate E_2^{σ}. Note this potential decay can be measured directly using a non-contacting surface charge probe; this forms the basis for the charge storage decay method for determining thin-film insulator resistivity developed by Frederickson (Dennison *et al*., 2003a; Swaminathan *et al*., 2003; Frederickson and Dennison, 2003). However, the FATMAN vacuum chamber used in these studies was not yet equipped with a non-contacting potential probe, so indirect methods for determining V_s were employed.

The surface potentials were determined following the mirror effect, encountered in SEM imaging (where a negatively charged insulator reflects the probing electron beam, Vallayer *et al*., 1999) and an experimental procedure similar to that of Wong *et al.* (1997). The samples were first irradiated with a defocused (~1 cm) electron beam at energies above E_2^{σ} to uniformly charge the samples to V_{s0} (as described above). Then, a low-amplitude (~100 nA), pulsed probing electron beam, with a much smaller diameter (~1 mm) was used to probe the surface potential of the insulator sample. In doing this, it was assumed that by using a

low-amplitude pulsed probe beam, the surface potential would not be significantly altered since the incident pulsed beam would be repelled from the charged surface area. Then, by slowly increasing the probing beam energy, E_{probe}, (generally, in 100 eV increments) the kinetic energy of the incident electrons would eventually overcome the potential barrier of the sample. This critical beam energy was marked by a sudden rise in the sample displacement current as shown in Fig. 4.26, and at this point, the surface potential was assumed to be equal to $V_s=E_{probe}/e$. Continuing on in energy, the sample displacement current remained large for higher energies exceeding the surface potential since electrons could reach the surface.

This procedure (both radiation and probing) was often repeated at a given irradiation energy to ensure the measured surface potential remained consistent. Once the surface potential was determined, E_2^{σ} was calculated from Eq. (4.7) after correcting for any suspected leakage current [using Eqs. (4.8) and (4.9)] that had transpired during the time of the probing experiment. Then, the irradiation energy was increased (generally in 200-500 eV increments), and E_2^{σ} was determined for progressively higher surface potentials to test the dependence of E_2^{σ} on incident energy. Based on previous work, it was expected E_2^{σ} would depend on both incident energy and incident current (refer to Sections 2.3.7 and 2.3.8), especially when the dielectric strength of the insulator material was exceeded, in which case, the insulator would not maintain a high surface potential, and Eqs. (4.8) through (4.9) could not be used to determine E_2^{σ}. Further details on the implementation of this technique on RTV-silicone are provided in Section 5.2.

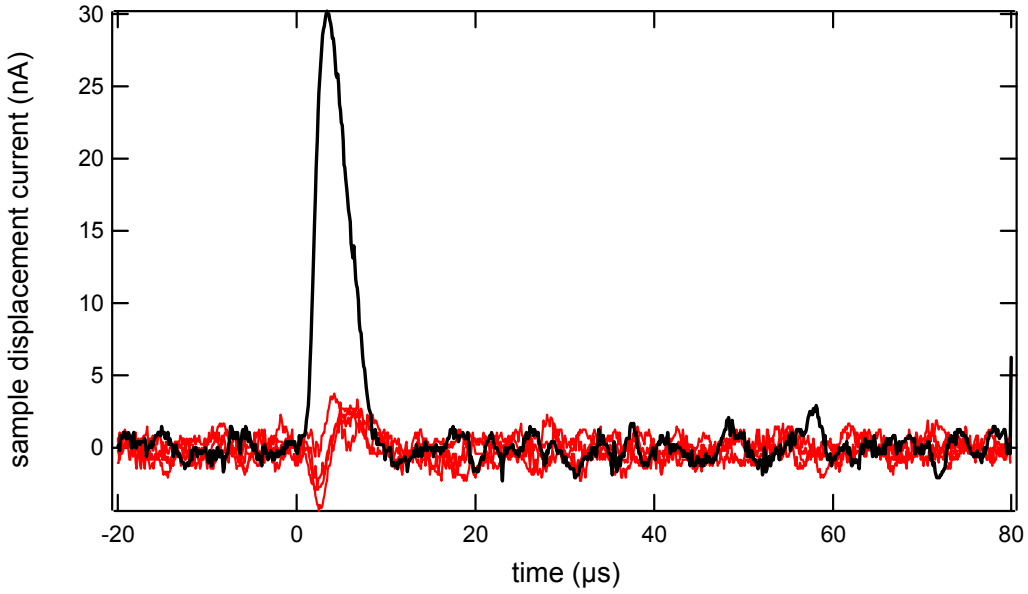

FIG. 4.26. Sample displacement currents for an RTV-silicone adhesive insulator on a copper substrate. The measured displacement currents were in response to a probing pulsed electron beam of 5 μs at 100 nA after being irradiated with a 2.5 keV electron beam. Red traces were displacement currents for 900 eV, 1000 eV, 1100 eV, and 1200 eV pulses, while the black trace was the displacement current for a 1300 eV pulse. Once the probing pulse overcame the surface potential barrier induced by a high-energy electron beam, the displacement current suddenly rose in magnitude.

A comparison of total-yield crossover energies for titanium, determined from fitting the total yield curve and from the sample current method, are provided in Table 4.6. Of these two methods, the sample current method was considered to be most accurate since variations >20 percent existed between fitting models for both E_1^{σ} and E_2^{σ} (refer to Table 4.5), but sample displacement current fit uncertainties were <5 percent. Furthermore, the sample displacement current method was not affected by current losses (and correction factors) associated with our detector apparatus (refer to Section 4.3). Similar comparisons of methods for determining E_1^{σ} and E_2^{σ} for insulating RTV-silicone and Kapton^{TM}-aluminum insulator samples are provided in Sections 5.2 and 5.3.2. Future work at USU will focus on further reducing the systematic uncertainties for all these methods (refer to Section 6.2.2).

TABLE 4.6. Comparison of the total-yield crossover energies determined using the yield curve and sample current methods for titanium. Other methods could only be used on insulator materials. The best model to the DC and pulsed-yield curve data (see Fig. 4.24 and Table 4.5) was used for the yield curve method. Sample displacement current results were obtained from Fig. 4.25.

Method	E_1^{σ} (eV)	E_2^{σ} (eV)
Fitted DC-Yield Data (Variable N Model)	70	1386
Fitted Pulsed-Yield Data (Variable N model)	82	1600
Sample Displacement Current	38	1340

Finally, a few limitations inherent to the methods described above should be noted. First, although in principle the yield curve, sample current, and DC-spectral methods could be used to find E_1^{σ}, the minimum operating energy (~50 eV) of the low-energy STAIB electron gun exceeded E_1^{σ} for most materials. It was possible to obtain current emission from the gun below 50 eV; however, the magnitude of the beam current was low, and the beam spot was large (>10 mm), which impeded directing the beam through the detector aperture. This had the largest impact on the yield-curve approach; it required that model fits to E_1^{σ} had to be extrapolated to low energies where there was no measured yield data. Section 6.1.1 outlines proposed instrumentation changes to the FATMAN chamber, which will facilitate the measurement of yield values at lower energies <50 eV. Second, in implementing the DC-spectra and mirror methods, samples were exposed to prolonged electron radiation that could induce sample charging, which might permanently alter electron emission properties, even after neutralization methods were employed. Consequently, in performing all tests on insulators, precautions were taken to minimize the exposure of the samples to the incident electron source, by not performing DC measurements (DC spectra or mirror measurements) until all other pulsed-yield measurements had been made.

CHAPTER 5

EXPERIMENTAL RESULTS ON INSULATORS

Electron emission data for four insulator materials used in spacecraft construction are presented in this chapter. The chapter includes data on a chromic-acid anodized aluminum disk in Section 5.1, four RTV-silicone thin film adhesives on copper substrates in Section 5.2, and Kapton™ on aluminum in Section 5.3. In addition to presenting pulsed total, SE, and BSE electron yields on these insulators, various techniques (described in earlier sections) are presented to demonstrate the measurement of other aspects of insulator charging behavior induced by electron beam irradiation. Specific aspects of insulator charging that are covered are the steady-state yield behavior of insulators under continuous electron bombardment; the evolution of electron yields and surface potentials as a function of electron fluence; the effectiveness of various neutralization methods as a function of incident electron energy; residual surface and bulk charging in response to high-energy electron irradiation, and these effects on electron emissions; shifts in surface potentials and electron emission spectra in response to electron beam irradiation; and direct determination of electron yield crossover energies using insulator charging and electron yield behaviors. Finally, Section 5.4 summarizes experimental data on the insulators, and compares results to other studies found in the literature.

5.1 Chromic-Acid Anodized Aluminum Alloy

The chromic-acid anodized Al2219 alloy sample was obtained from NASA Marshall Space Flight Center (Thomson *et al*., 2003a; Dennison *et al*., 2003d). The material is used throughout the International Space Station body as a structural material and for micrometeriod and orbital debris shielding. The Al2219 alloy sample (2 mm thick, 10 mm diameter with a

1.3 μm chromic-acid anodized surface coating on each side) was taken from a witness sample plate that was created at the same time as the large plates used on the ISS (Schneider, 2003; Thomson *et al*., 2003a; Dennison *et al*., 2003d). The sample was chosen with specific aims in comparing electron emissions data obtained using both the DC- and pulsed-yield measurement setups. Additionally, the evolving sample potentials under both continuous- and pulsed-incident electron beams were studied. Finally, discharging techniques including electron flooding, UV, and visible light irradiation were explored for neutralization effectiveness.

DC-yields were taken first using a continuous electron source at ~20 nA beam current to observe electron yield behavior under severe charging conditions. As shown in Fig. 5.1, for energies ranging from 100 eV to 1500 eV, the insulator quickly charged such that a steady-state condition was established where the total yield reached unity, and no net current flowed to or from the sample. However, after 1500 eV, a transition in the yield values occurred. As shown in Fig. 5.2, at ~1700 eV the sample current suddenly increased, indicating dielectric breakdown of the anodized coating. For this measurement, the exact value of the surface potential at electrical breakdown was not measured, but from the known thickness and dielectric strength for Al_2O_3 (see Table 5.1) was estimated to be ~35 V. Previous measurements on this material at NASA MSFC have demonstrated a breakdown potential ranging from 60-80 V (Schneider, private communication).

After letting the sample sit for a day, the breakdown surface potential was once again explored using a continuous incident electron beam while measuring the SE spectra. The method for determining the surface breakdown potential was to monitor the shifting of the SE emission peak in the electron energy spectrum as explained in Section 4.5. For the case of insulating materials, the incident electron beam was used to both induce a surface potential (dependent on incident energy), as well as to measure the resultant surface potential

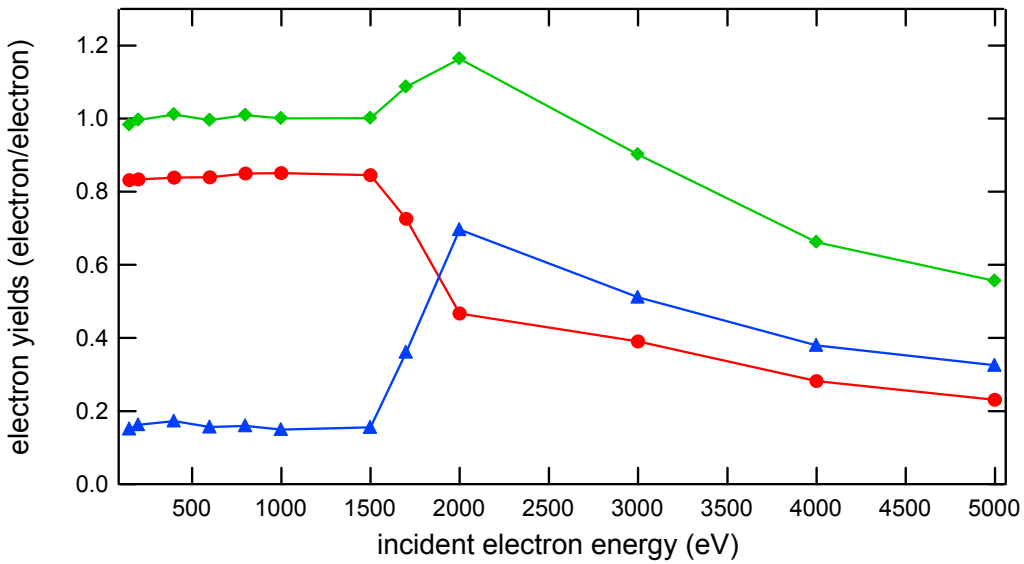

FIG. 5.1. DC-total (♦), SE (●), and BSE (▲) yields for Al2219. The sample remained fully charged, indicated by a constant total yield of one, until E_0=1500 eV, where dielectric breakdown occurred.

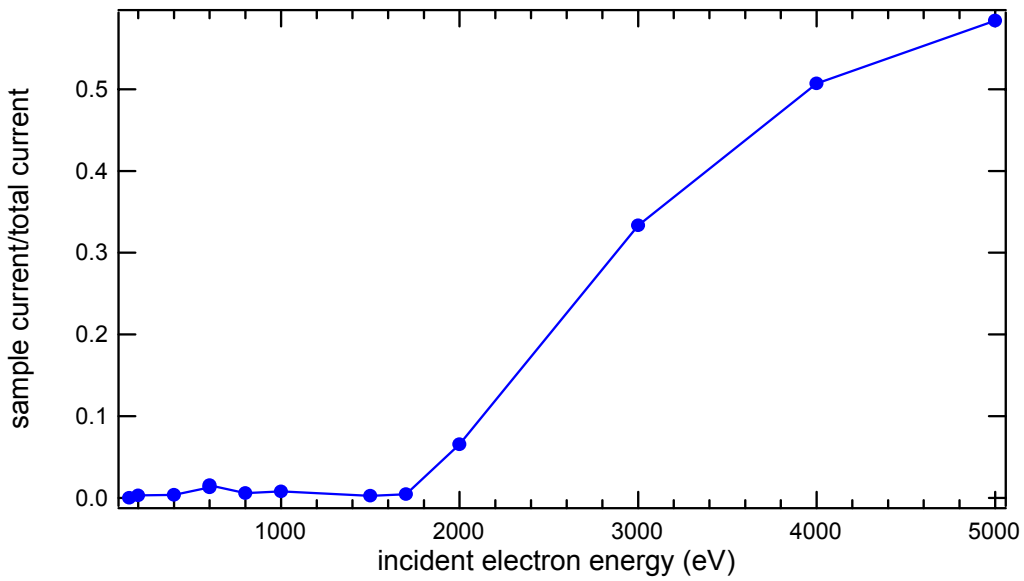

FIG. 5.2. Confirmation of dielectric breakdown of the Al2219 sample indicated by an increase in the DC sample current. The breakdown occurred at ~1700 eV, consistent with the dramatic change in electron yields at this energy (see Fig. 5.1).

TABLE 5.1. Physical and electrical properties for the Al2219 anodized Al sample. The anodized layer thickness was obtained from Schneider (private communication), and resistivity from Goodfellow (2004), dielectric constant from Carruth *et al*. (2001), and dielectric strength from alumina data from the CRC Handbook of Chemistry and Physics (Lide, 2001). The breakdown potential was calculated from the dielectric strength and insulator film thickness.

Film Thick. (μm)	Film Density $(kg/m^3)\cdot 10^3$	Resist. (Ω·cm)	Rel. Diel. Const.	Diel. Strength (MV/m)	Calc. Brkdwn. Pot. (V)
1.3±0.5	3.98	$>10^{14}$	5.0-9.3	13	35

through the SE spectrum. The incident beam energy was increased for each successive spectral measurement (starting from 200 eV up to 1300 eV) until signs of breakdown occurred. As shown in Fig. 5.3, the right shifting of the SE emission peak was used to determine the magnitude of the sample surface potential. From the data in the figure, it can be seen that the sample potential remained negative at energies between E_1^{σ} and E_2^{σ}, and increased in magnitude with increasing incident energy.

The surface potential was not expected to be negative between the crossover energies since the pulsed total electron yield was greater than unity in this energy regime such that positive surface charging should have occurred (refer to Fig. 5.7 below). However, as explained in Section 2.3.8, previous experimental studies on Al_20_3 and MgO have shown the measured polarity of charging induced by a continuous electron beam does not always correspond to that predicted by the pulsed electron yield parameters (Cazaux, 1999; Melchinger and Hofmann, 1995). An explanation for this behavior was provided by Cazaux (1999), who predicted that for metal oxides (e.g., MgO, Al_2O_3), a continuous electron source at energies between the crossover energies would act to lower the steady-state total electron yield from an initial value greater than unity (as measured by pulsed yields) to one below unity, thus reversing the polarity of the surface potential. He attributed this lowering of the

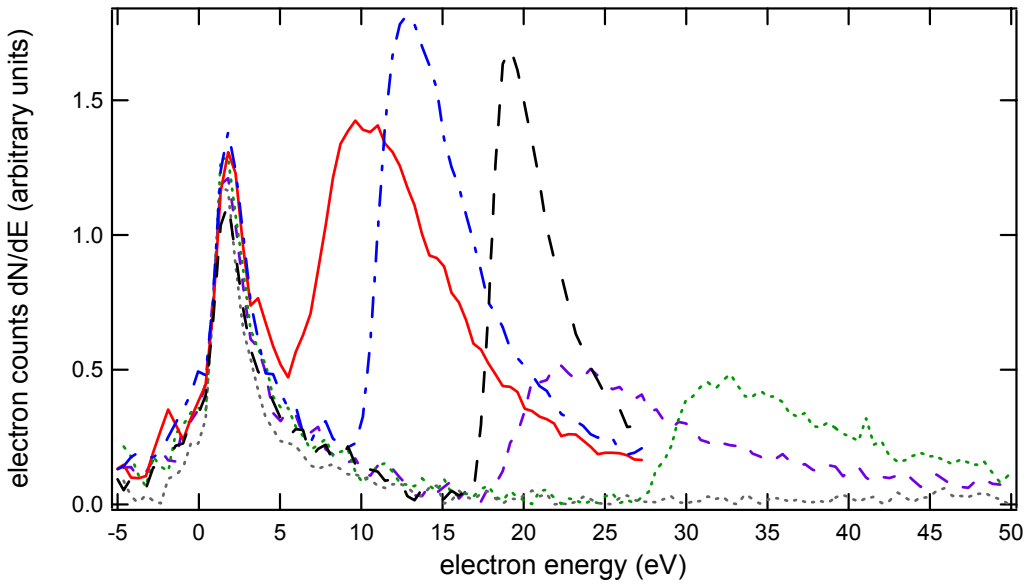

FIG. 5.3. SE DC spectra of Al2219 at different incident beam energies. Spectra showed increasingly negative surface potentials at beam energies of 200 eV (9±1 V) (solid), 500 eV (11±1 V) (dash-dot), 1000 eV (17±1 V) (long dash), 1250 eV (21±2 V) (short dash), 1300 eV (32±2 V) (dot). Decline of SE peak magnitude at 1250 eV indicated dielectric breakdown once more at a surface potential of 21±2 V.

total yield to additional defect creation, through the creation of oxygen vacancies that facilitated electron charge trapping and storage in the insulator bulk. Hence, while under continuous electron irradiation, the dynamic trapping/detrapping rates of the insulator were altered and hindered SE transport such that the steady-state total yield was lowered. Eventually, trapping/detrapping rates and internal charge distributions stabilized such that a negative potential steady-state condition was formed. Hence, for a given energy, negative charging would not continue indefinitely through the continual capture of incident charge.

Given this explanation, it is reasonable to conclude the increasing negative potential, with increasing incident energy, resulted from large concentration of trap centers induced by the continuous-source electron beam (Cazaux, 1999). In this energy regime the incident electron penetration depth would have been comparable to the SE escape depth (refer to Sections 2.3.2 and 2.3.4), $R \sim \lambda_{SE}$ (each on the order of 10 nm) such that only a single-layer

charge distribution would have formed within the anodized layer. The net charge within this layer would be negative (since the surface potential was negative), resulting from trapping of incident electrons and escaping SE's. As the beam energy was increased, the incident electrons pushed further into the material, increasing electron trapping, and thus increasing the magnitude of the negative surface potential. Eventually, the internal charge distributions and associated electric fields stabilized for a given incident energy. It is difficult to quantitatively predict the exact relationship between the evolving surface potential and incident beam energy since these results may also depend strongly on sample history, anodized layer thickness and type (e.g., chromic-acid anodized versus sulfuric acid anodized), and incident current density. Clearly, this charging behavior deserves further investigation (refer to Section 6.2.1).

The magnitude of the negative potential scaled with incident beam energy, up to a critical incident electron energy (initially 1500 eV, then 1250 eV on a subsequent run), where the surface potential became sufficiently high (>20 V) to initiate dielectric breakdown of the thin anodized layer. The negative surface potential scaled with energy since as E_0 was increased, the incident electron penetration depth also increased, thus providing a greater volume (at a greater depth) where additional electrons could be trapped.

As shown in Fig. 5.3, as the beam energy was increased to 1250 eV and 1300 eV the surface potential reached -21±2 V and -31±2 V, respectively and the SE peaks for these energies showed a significant decrease in relative amplitudes, indicative of the electrical breakdown described above. From the SE spectral data, the breakdown surface potential occurred near -21 V (at a beam energy of 1250 eV). This value was slightly lower than the calculated estimates of -35 V, and three to four times smaller than previously measured values (Schneider, private communication). The value may have been slightly lower since the

sample had previously been irradiated and undergone dielectric breakdown from previous testing (refer to Figs. 5.1 and 5.2).

Once dielectric breakdown had occurred, the sample was irradiated for 15 min. at 30 nA at 5 keV beam energy to determine if subsequent SE spectra would be affected. After this irradiation period at 5 keV, the incident beam was once again lowered to 500 and 1000 eV, and SE spectra were measured. As seen in the spectra of Fig. 5.4, the sample potentials (both at 500 eV and 1000 eV) no longer showed dependence on incident beam energy (compare to Fig. 5.3 at 500 and 1000 eV), but remained locked at -8±1 V. This demonstrated the hysteresis of the sample, where residual charge from the high-energy incident beam remained trapped within the insulator, keeping the sample potential at a negative value regardless of subsequent lower-energy electron irradiation between the crossover energies—where positive surface charging should have occurred. The freezing of the surface potential after 5 keV irradiation resulted from electron charge that was trapped to a maximum penetration depth of ~100 nm (refer to Section 2.3.2) below the surface, induced by the high-energy 5 keV incident electron beam. This charge layer created internal electric fields that altered the emission of lower-energy incident electrons that were excited by incident electrons with energies of 500 eV and 1000 eV in a similar fashion.

Before proceeding with pulsed-yield measurements, the sample was allowed to discharge. Based on calculations using the standard resistivity and dielectric constant for alumina (see Table 5.1), the 8 V surface potential, induced by the 5 keV incident beam, was expected to discharge within a time frame ranging from minutes to hours. However, the sample was allowed to sit for one week after irradiating with light from both tungsten and mercury lamps for several hours in an attempt to stimulate photo-induced conductivity. Additionally, the surface was flooded occasionally with the low-energy flood gun at a current

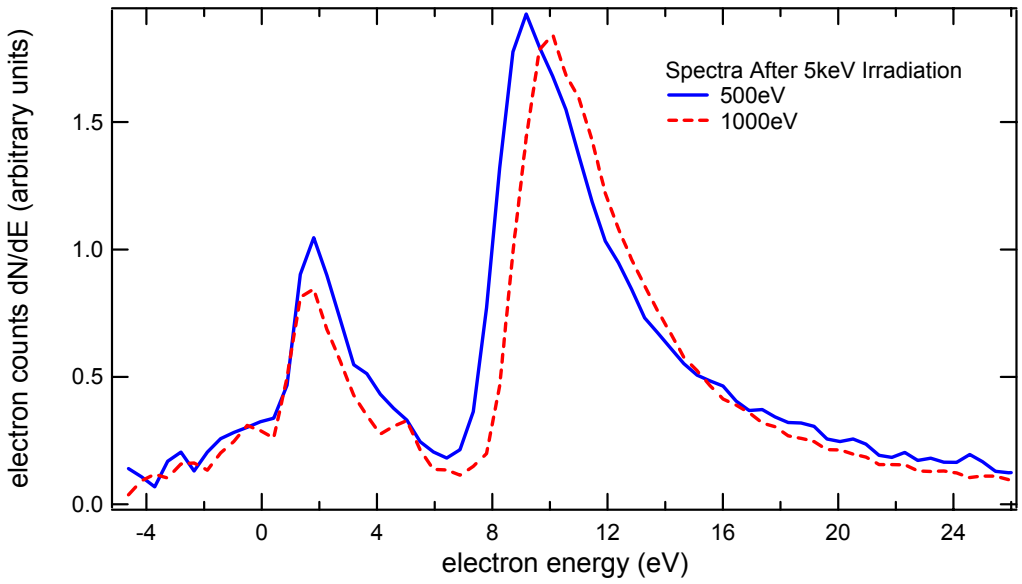

FIG. 5.4. DC-Spectra taken at 500 eV (solid) and 1000 eV (dash) after 5 keV irradiation on Al2219. The SE spectra displayed locked negative surface potentials of 7-9 V resulting from trapped imbedded electron charge induced by prior 5 keV irradiation.

density of 50-500 nA/cm^2 for five minutes to neutralize any positive surface charge (refer to Section 3.5 for information on the neutralization sources).

After this neutralization period, a series of first-pulsed yields were measured to explore the rate of sample charging from a pulsed-electron beam. Three consecutive pulsed-total yield curves (5 μs, 40-60 nA impulses) were taken without implementation of any neutralization techniques, as shown in Fig. 5.5. Each yield point consisted of a single incident pulse, followed by relaxation period of 1-2 min. as the beam energy was adjusted. From the figure, it can be seen after just a few incident pulses, the yield curves were significantly dampened towards unity, even though the incident source was only depositing ~10^6 electrons/pulse over a beam-spot area of ~1 mm^2. This indicated the sample was not relaxing between each incident pulse, but was instead accumulating charge with each measurement. The dampening occurred such that below ~700 eV (between the crossover energies) the yields

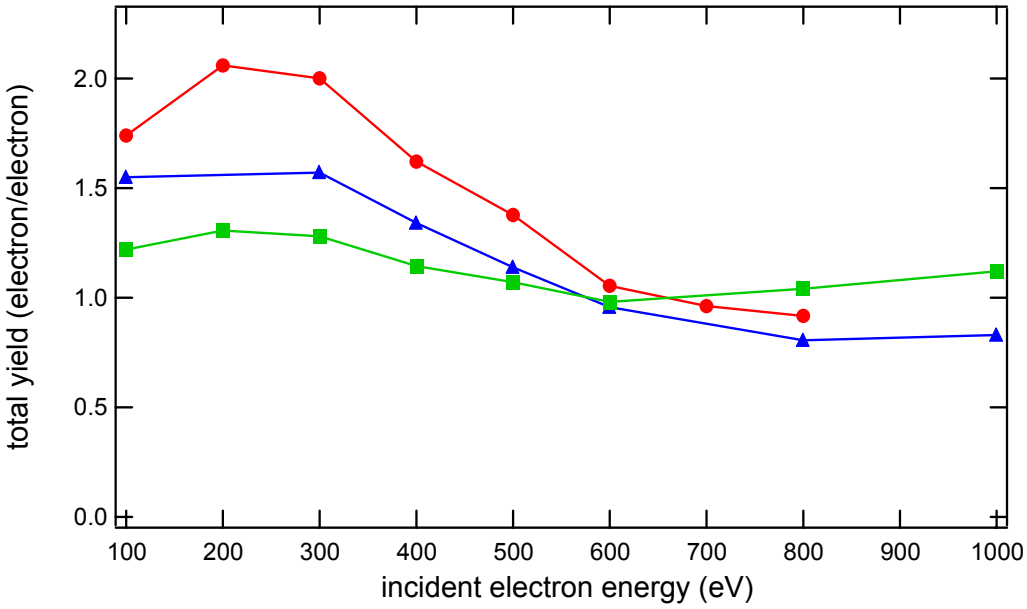

FIG. 5.5. Three consecutive yield curves for Al2219 with no sample neutralization. Each data point consisted of one pulse (~10^6 electrons/pulse). No neutralization methods were used. The first (●), second (▲), and third (■) yield curves quickly flatten towards unity as the sample charged.

decreased towards unity with consecutive pulses, while above 700 eV (above E_2^{σ}), the yields increased towards unity. This behavior is characteristic of the two charging energy regimes, where between the crossover energies, an insulator will charge positive to suppress SE emission in order to reach a steady-state condition, while above E_2^{σ}, an insulator will charge negative such that the landing energy of incident beam will be equal to E_2^{σ} (and the total yield equal to unity), again reaching a steady-state condition. For example, treating the sample as a standard parallel plate capacitor (with an area of the beam spot), the amount of deposited charge in one pulse was estimated to change the surface potential by only ~100 mV/pulse positive. However, a significant portion of SE's are emitted with energies less than 10 eV (see, for example, the SE spectra given in Section 2.1) such that a cumulative positive surface potential of just 1 V can significantly suppress escaping SE's (refer to Section 2.3.6). Therefore, small changes in the positive surface potential could potentially have had large

effects on electron yields (Nickles *et al*., 2000). These results substantiate the use of neutralization techniques (in addition to a pulsed electron beam) in measuring insulator electron yields. After these initial pulsed measurements, the neutralization sources were turned on (as before), and the sample was once again allowed to sit for several days to discharge.

To further explore the rates of sample charging and the evolution of the total electron yields, as well as the discharging effectiveness of the electron flood gun and UV neutralization sources, the sample was pulsed repeatedly at a constant energy of E_0=500 eV (using single 5 μs, 40-60 nA impulses). Between each incident pulse, the sample was not allowed to discharge, but was allowed instead to charge under continued incident electro irradiation. Then, once the sample approached a charged steady-state potential, the different neutralization sources were tested for their neutralization effectiveness. The first pulsing sequence consisted of 30 pulses. Then, the electron flood gun was turned on for five minutes (the flood gun deposited a total electron fluence of $\sim 1 \cdot 10^{-4}$ C/mm^2). After the flood gun was utilized, a second pulsing sequence was taken. Then, the sample was irradiated with a mercury gas lamp for 15 minutes. Then, a third yield sequence was measured, and the sample was irradiated with a tungsten filament lamp for 15 minutes. Finally, a fourth pulsing sequence was measured.

As can be seen from Fig. 5.6, for the initial pulsing sequence, the total electron yield decayed asymptotically towards unity (the steady-state condition) with repeated pulsing, consistent with the flattening of yield data in Fig. 5.5. However, after flooding the sample with the electron flood gun, the total yield was restored to its original uncharged value in the second pulsed-yield sequence (within the error in yield values), and then once again declined at roughly the same charging rate towards unity with repeated pulsing. In the third and fourth

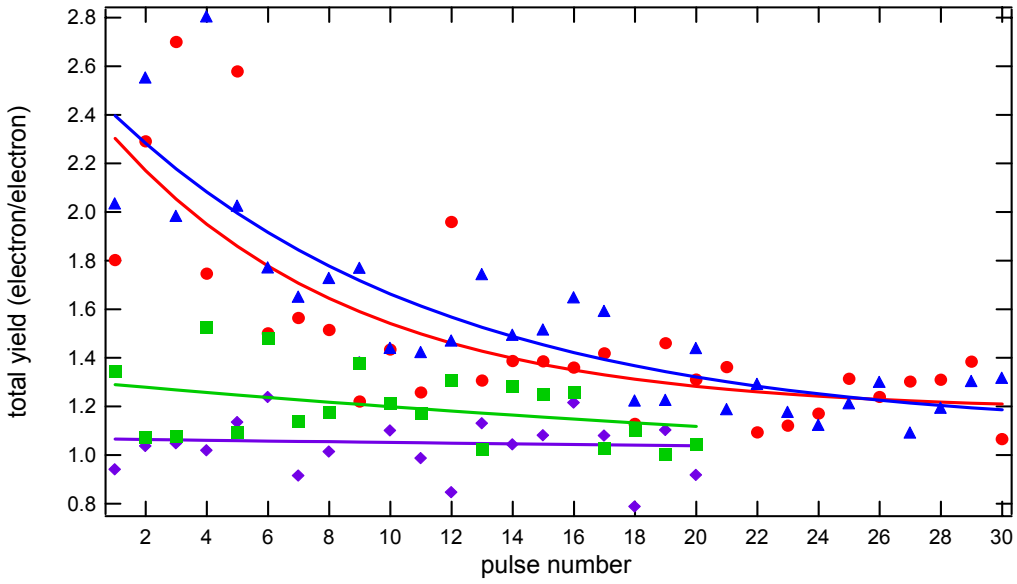

FIG. 5.6. Dampening of total yields at 500 eV as a function of electron pulses (5 μs pulses with amplitude 50 nA) for Al2219, along with exponential fits. First yield sequence (●) and sequence following electron flooding (▲) produced similar yield decay curves indicating that flooding discharged the sample effectively. Yield sequences following mercury (■) and tungsten filament (♦) lamp irradiation remained close to unity, indicating ineffective neutralization.

sequence, it was observed that the mercury and tungsten lamps did not appear to be effective in neutralizing the sample for this incident energy. In summary, these results showed in the energy regime between the crossover energies, the flood gun was very effective for neutralizing positive surface potentials; however, the mercury- and tungsten-lamp sources were not. Further validation of these conclusions is provided in Section 5.3.3 for the Kapton™-aluminum sample.

It can also be seen from Fig. 5.6 that for the first yield sequence, it took >30 pulses for the sample to arrive at a steady-state condition. Each incident pulse consisted of $<10^{-13}$ C/mm^2 of incident charge. Hence, it was concluded that for E_0=500 eV (energy regime of $E_1^{\sigma}<E_0<E_2^{\sigma}$), the sample reached a steady-state condition after ~10^{-12} C/mm^2 of incident electron charge. In comparison, simulations from Meyza *et al.* (2003) predicted total yields

from alumina should reach a steady-state condition after roughly 10^{-13} C/mm^2 in the energy regime of $E_1^{\sigma}<E_0<E_2^{\sigma}$ (at E_0=1000 eV). Hence, steady state estimates from our data were an order of magnitude higher than the simulations of Meyza *et al.* (2003). Further testing along these lines should be conducted at different incident energies.

After exploring the effectiveness of the different neutralization techniques, the sample was once again allowed to discharge for a week, and then a total-yield curve for anodized aluminum was measured from 100 to 5000 eV, and fitted with various electron-yield models as outlined in Section 2.3.2. Flood gun neutralization was alternated with electron beam pulsing to ensure adequate neutralization. Additionally, yields were taken in order of increasing beam energy since it had already been observed in the DC measurements that high-energy incident electrons could deposit negative charge that would remain trapped in the sample and influence subsequent yield measurements. Results for the fits are shown in Fig. 5.7. Yield parameters are summarized in Table 5.2.

It must be noted in comparison to Figs. 5.3 and 5.4, the pulsed yields between E_1^{σ} and E_2^{σ} were positive—indicative of positive charging in this energy regime. However, the surface potentials induced by a continuous electron source were clearly negative. As explained earlier, the discrepancy in these results can be attributed to the slow buildup of trapped internal charge distributions and electric fields induced by a continous electron source as compared to a pulsed electron source.

As can be seen from the Fig. 5.7, in general, the models did not provide accurate fits to the insulator data. They either undershot σ_{max}, or missed the tail of the higher energy yields. This may be attributed to the fact these models do not account for the electronic structure of insulators; nor do they accommodate the insulator's longer SE escape depths that act to increase the maximum electron yield data (as compared to conductor materials). These issues

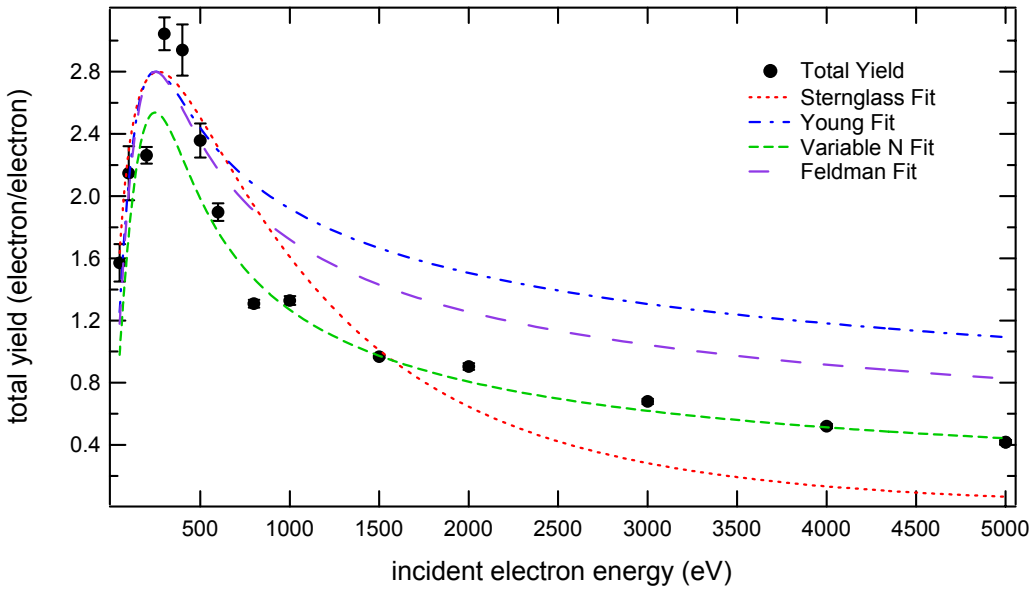

FIG. 5.7. Total pulsed electron yield curve for Al2219 with electron flood gun neutralization. In contrast to Fig. 5.5, reliable absolute total yields were obtained by flooding the sample between yield measurements. This yield curve for Al2219 (5 μs pulses with amplitudes 50 nA, each data point was the average of 10 pulses) is fitted with various analysis models described in Section 2.3.2. Yield parameters from these fits are provided in Table 5.2.

TABLE 5.2. Summary of measured total electron yield parameters for Al2219 using various yield-curve fitting models. The maximum total yield, σ, maximum yield energy, E_{max}^{σ}, and first and second crossover energies, E_1^{σ} and E_2^{σ} are shown. Wide variations existed for the crossover energies between the different models. Derivations for these models are given in Section 2.3.2. The measured surface breakdown potential is also listed, taken from the SE spectral data of Fig. 5.3.

Fitting Model	σ_{max}	E_{max}^{σ} (eV)	E_1^{σ} (eV)	E_2^{σ} (eV)	Meas. Brkdwn. Pot. (V)
Sternglass	2.80±0.03	266±3	15	1511	~21
Young	2.80±0.03	250±8	38	>5000	
Variable N	2.54±0.04	249±7	51	1440	
Feldman	2.80±0.03	250±7	41	3293	

were discussed in Sections 2.3.2, and were studied to some extent in Section 5.3.2. Also, it is suggested an improved insulator model be developed in future work, sensitive to the energy dependence of the SE escape depth, as discussed in Section 6.2.3.

From the best fits and estimates to the yield data, yield parameters were extracted and are summarized in Section 5.4, along with yield parameters obtained from other sources found in the literature. The models were found to provide a better fit to important electron yield parameters when the energy range was shortened. For this reason, for the tabulated data in Section 5.4, the Variable N model was used to estimate the electron yield parameters over the shortened energy range of 100-1200 eV. Finally, it must be mentioned the yield data was obtained after extensive electron irradiation, and will need to be measured again (along with BSE and SE yield discrimination and at higher energies) in the near future on a virgin anodized aluminum sample. Pulsed yields on a fresh sample may vary compared to those obtained on this sample.

5.2 RTV-Silicone Adhesives on Copper

Two sets of thin-film RTV coated copper samples were tested: the first set included two NuSil CV-1147 (samples 1 and 2) controlled volatility silicone coatings used to bond solar cells to Kapton™ sheeting on the International Space Station (Dennison *et al*., 2003c); the second set included two DC 93-500 (samples 5 and 6) silicone space-grade encapsulant coatings used to bond cover glass materials to solar cells on the International Space Station (ISS) (Dennison *et al*., 2003c). Both RTV materials were relatively volatile; concerns that these materials would produce contamination layers on ISS surfaces prompted the investigation of these thin-film materials on a conducting substrate (Dennison *et al*., 2003c).

Similar contamination layers have been shown to potentially have a large impact on the charging of spacecraft surfaces (Dennison *et al*., 2001).

The thin-film samples were prepared by McDonald Douglass Corporation, where the coatings were sprayed onto 10 mm dia. copper substrates (one side only), and were vacuum baked at 65 °C for 1 hr at ~10^{-3} Torr. The bake out procedure was designed in part to mimic conditions the materials would experience in the space environment and also reduced possible outgassing of volatile components in the USU vacuum chamber during electron emission measurements (Dennison *et al*., 2003c). No cleaning methods at USU were used for the DC 93-500 or NuSil CV-1147 samples before introduction to vacuum. Table 5.3 shows the thicknesses and electrical properties of the RTV coatings. Thicknesses were determined using a depth of field method with a microscope at 100 x magnification (Dennison *et al*., 2003c). The relative dielectric constants and bulk resistivity were measured using a standard impedance analyzer by the manufacturer (see Table 5.3). *Ex situ* measurements of the volume resistivity of the thin-film silicone samples were also measured at USU using the ASTM—or capacitor resistance method—and ranged between 2-5·10^{15} Ω·cm (Dennison *et al*., 2003a; Swaminathan *et al*., 2003). Further descriptions of each of the samples are given in Dennison *et al*. (2003c).

These insulator samples were studied primarily to determine accurate methods for measuring the total yield second crossover energy, E_2^{σ}. These methods are discussed in Section 4.6, and included modeling the total yield curve, monitoring the pulse sample displacement current as a function of incident energy, measuring shifts in the DC SE spectra, and the pulsed-probing mirror method. In implementing these four methods, the order of measurements was planned carefully to minimize charging errors. For example, negative charge build-up (up to several hundreds or thousands of volts) induced by beam energies

TABLE 5.3. Physical and electrical properties for the RTV-silicone samples. RTV sample thicknesses, resistivities, dielectric constants, dielectric strengths are from Dennison *et al.* (2003c). The breakdown potential was calculated from dielectric strength and insulator film thickness.

Sample	Mat.	Film Thick. (μm)	Film Density $(kg/m^3)\cdot 10^3$	Resist. (Ω·cm)	Rel. Diel. Const.	Diel. Strength (MV/m)	Calc. Brkdwn. Pot. (V)
RTV 1	CV-1147	34±3	1.14	10^{15}	2.6	22	743
RTV 2	CV-1147	30±3	1.14	10^{15}	2.6	22	644
RTV 5	DC93-500	49±3	1.03	10^{15}	2.6	19	917
RTV 6	DC93-500	26±3	1.03	10^{15}	2.6	19	499

beyond E_2^{σ}, can be very difficult to dissipate. Consequently, precautions were taken to minimize sample exposure to the high-energy (>1 keV) incident electrons until all lower-energy (<1 keV) measurements were made. This was done by initially taking pulsed-yield and pulsed-sample current measurements (in order of increasing incident energies), followed by DC-spectra at energies near E_2^{σ}, and lastly, the mirror method technique (that induced significant negative charging). Details of the measurements follow.

Initially, a pulsed-yield curve (10 pulses/yield point with a puling period of 1 s) followed by a DC-yield curve (incident beam current ~30 nA) were taken on sample 2 to observe the general charging behavior of the sample under electron beam irradiation. No neutralization methods were employed during these measurements. As shown in Fig. 5.8, both pulsed- and DC-yields went to unity after repeated measurements, consistent with the steady-state charging condition observed with the Al2219 sample. Deviations from unity on the order of 10-20 percent were attributed to irregular radiation time periods and leakage currents beyond the dielectric strengths of the materials. However, while measuring DC-yields at 2 keV (30 nA beam current), it was noticed the DC sample current remained below

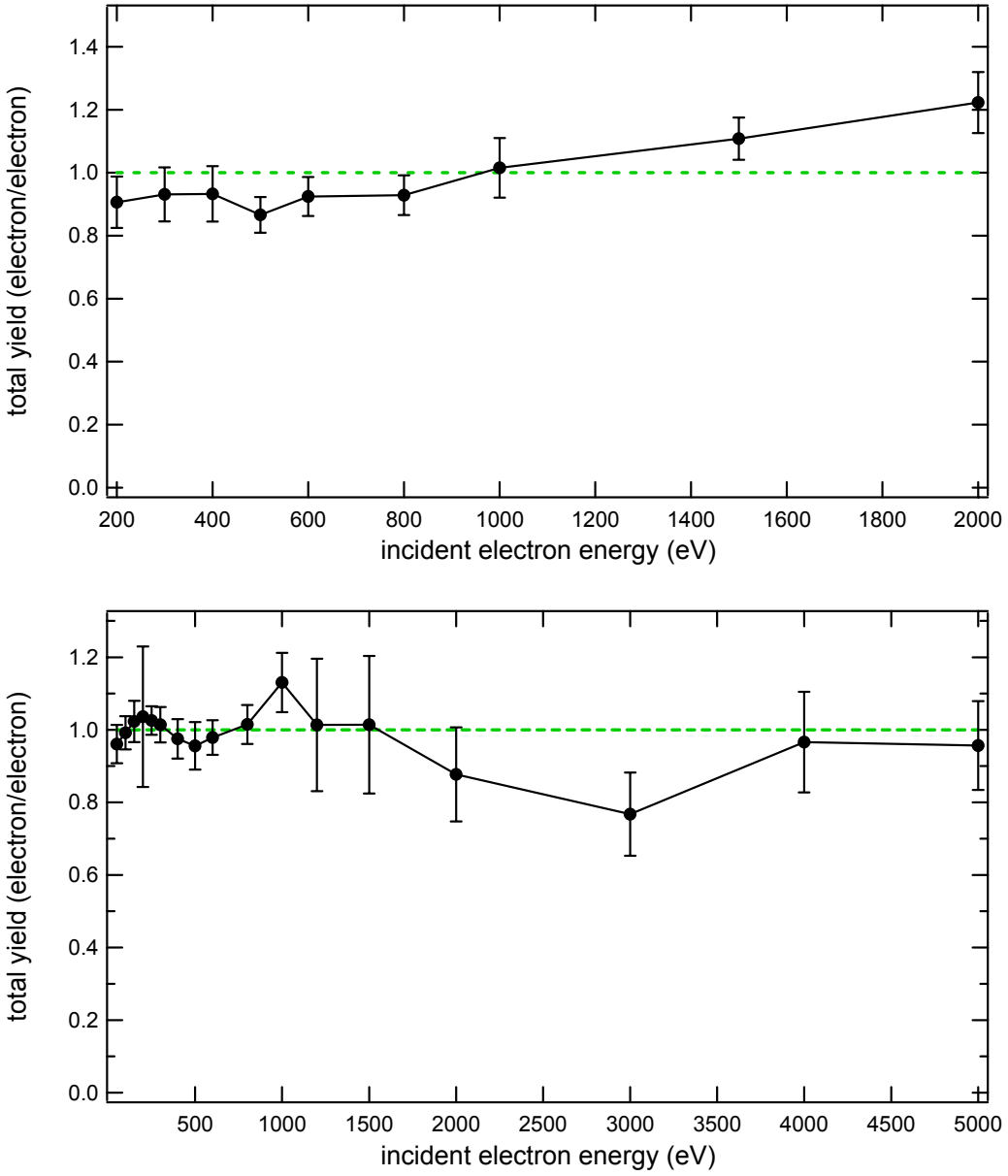

FIG. 5.8. Plots of DC (top) and pulsed (bottom) total yields of CV-1147 sample 2. Each yield point was the average of 10 pulsed-yield measurements (5 μs pulse with amplitude ~30 nA with standard errors as the error bars. No neutralization was used after each pulse such that total yields quickly approached unity.

the measured noise level of ±1 nA, and showed no signs of dielectric breakdown. This gave initial indications the RTV insulator films possessed sufficient bulk resistance and dielectric strength to perform further DC-spectral and mirror-method (see Section 4.6) measurements at ~2 keV-beam energies.

Pulsed-yields as a function of incident energy were taken on samples 1 and 6 using 5 μs, ~30 nA incident pulses (~10^6 electrons/mm^2 per data point). Ten pulsed measurements were averaged for each data point, with flooding performed between each incident pulse. The pulsed-yield measurements were started at beam energies of 100 eV, and then increased up to 1 keV (yields beyond 1 keV were not taken until after DC-spectral measurements to avoid premature negative charging beyond E_2^{σ}). In contrast to yields on sample 2, these samples were neutralized with the flood gun after each incident electron pulse, and exhibited total yield curves consistent with other uncharged insulators. The yield curves along with several semi-empirical models are shown in Fig. 5.9. Yield parameters extracted from these models are summarized in Table 5.4. The origins of these models are explained in Section 2.3.2. Unlike the Al2219 sample, the models provided an adequate fit to the data over the energy range of 100 eV to 5 keV.

Also recorded with the pulsed-yield data were sample displacement current data. These data were integrated to obtain values of sample charge, and plotted as a function of incident beam energy (see Fig. 5.10). As explained in Section 4.6, the energy associated with the sample charge of 0 C was taken as E_2^{σ}.

When the total yield curves began to approach unity (and sample displacement currents approached 0 nA), close to E_2^{σ}, for samples 1 and 6, the electron gun was switched from pulsed to continuous-emission mode, and DC-spectra were taken (at ~30 nA incident beam current) on the samples as the beam energy was increased. Spectra were taken for each

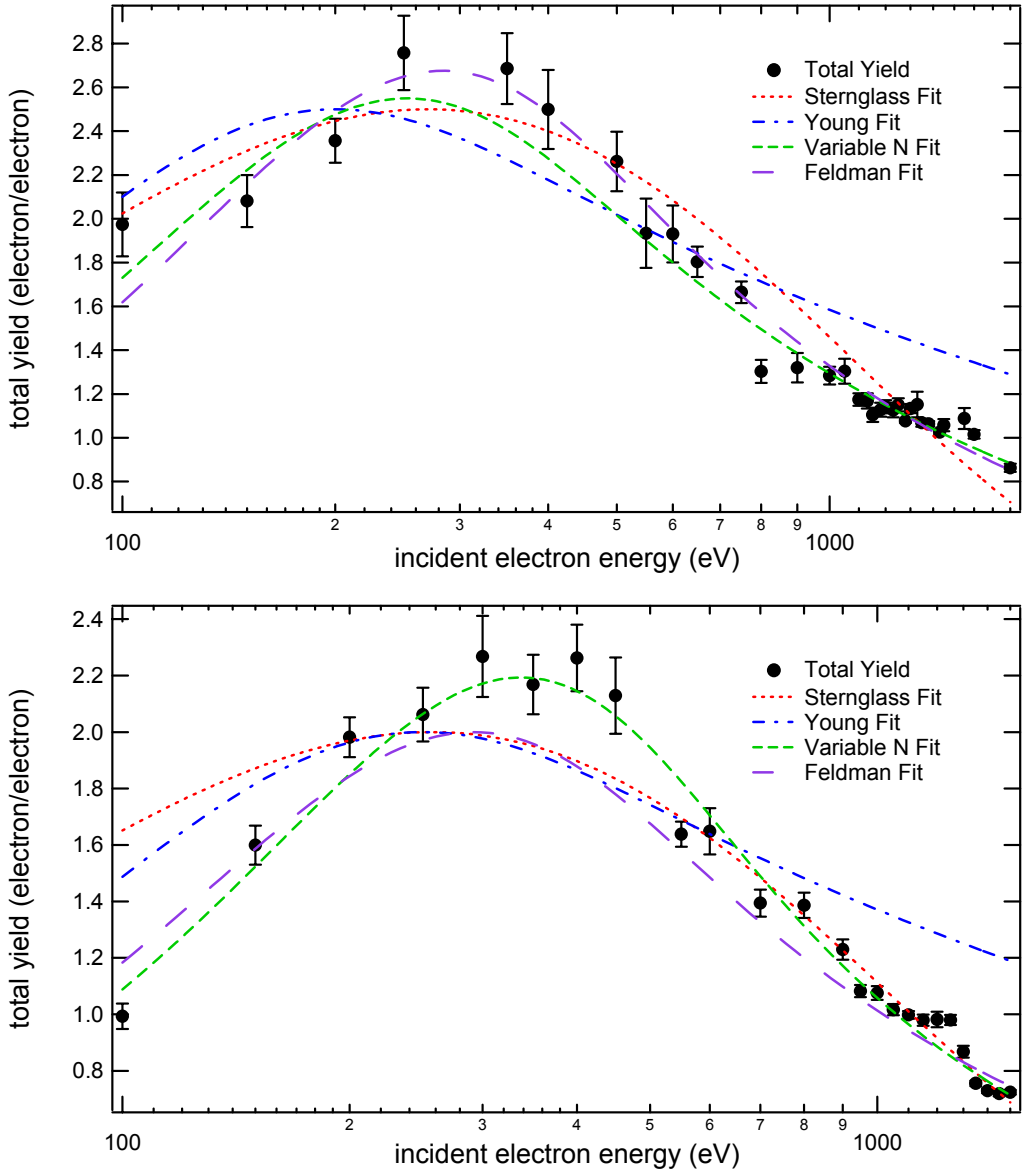

FIG. 5.9. Semi-log plots of the pulsed-yield curve versus beam energy for CV-1147 sample 1 (top) and DC 93-500 sample 6 (bottom). Flood gun neutralization was used after each pulse. Each yield point was the average of 10 pulsed-yield measurements (5 μs pulse with amplitude ~30 nA) with standard errors as the error bars. Shown also are various model fits to the data (described in Section 2.3.2). Yield parameters from these fits are summarized in Table 5.4.

TABLE 5.4. Summary of measured total electron yield parameters for samples 1 and 6 using various yield-curve fitting models. Wide variations existed for the crossover energies between the different models. Some models did not produce meaningful results over the fitted energy range (indicated by dashes). Derivations for these models are given in Section 2.3.2.

Fitting Model	σ_{max}	E_{max}^{σ} (eV)	E_1^{σ} (eV)	E_2^{σ} (eV)	n^{σ}
Sample 1 CV-1147					
Sternglass	2.5±0.1	271±4	--	1410±50	--
Young	2.5±0.1	200±11	--	--	1.35
Variable N	2.6±0.1	250±10	40±20	1490±40	1.64
Feldman	2.7±0.1	284±6	50±20	1450±50	--
Sample 6 DC 93-500					
Sternglass	2.00±0.02	257±3	--	1110±40	--
Young	2.00±0.02	250±6	45±30	--	1.35
Variable N	2.20±0.03	338±6	90±10	1060±30	1.28
Feldman	2.00±0.02	292±5	80±10	1020±40	--

progressive beam energy until E_2^{σ} was traversed, and double-peak SE emission spectra (as described Sections 4.5 and 4.6) were observed due to negative sample charging. This transition in the electron emission spectra for increasing beam energy are shown in Fig. 5.11. For both samples, the double sample SE peak emerged at energies between 1200-1300 eV.

When pulsed-yield, sample current, and DC-spectral measurements were completed, mirror-method potential measurements were taken on all samples for E_0=2 keV, 2.3 keV, 2.5 keV, and 3 keV (measurements were always taken in order of increasing beam energy on a given sample). The RTV samples were irradiated with a defocused (~10 mm diameter for uniform charging) electron beam at 100 nA for 5 minutes for each beam energy. This irradiation was done with the low-energy electron gun with a filament current of I_f=1.52 A (for ~100 nA emission), and grid/focus settings of 4.5/8.4 for 2-2.5 keV, and 4.9/7.5 for 3 keV to achieve a widened beam spot to produce uniform negative charging across the surface. Also, during this irradiation period, DC sample current was monitored to check for dielectric

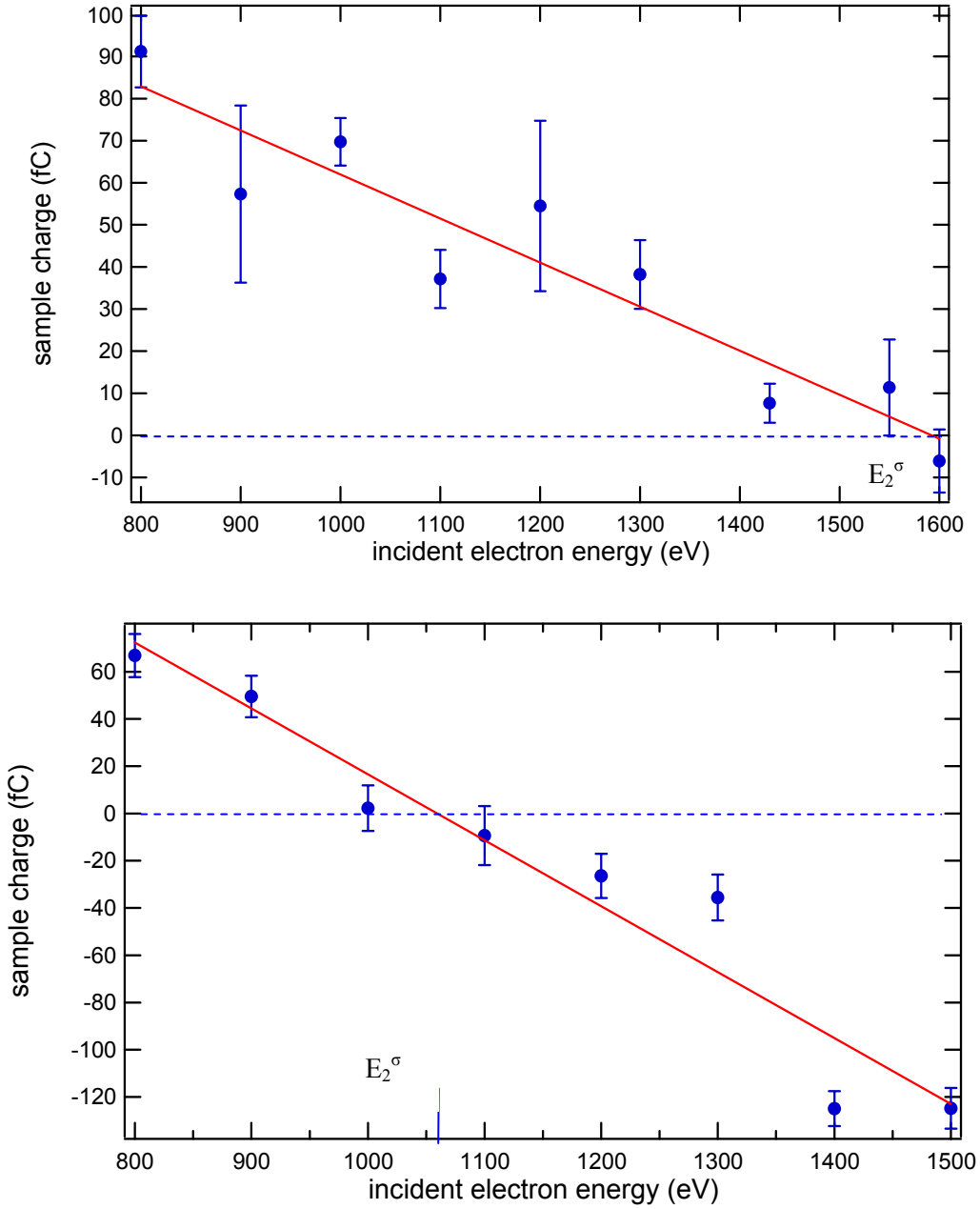

FIG. 5.10. Integrated sample displacement current versus beam energy for CV-1147 sample 1 (top) and DC 93-500 sample 6 (bottom). Flood gun neutralization was used after each pulse. Each yield point was the average of 10 pulsed-yield measurements (5 μs pulse with amplitude ~30 nA) with standard errors as the error bars. A sample charge value of 0 C marked the second crossover energy, E_2^σ. Linear fits to the data yielded for sample 1: intercept=167±18 fC, slope=-0.11±0.01 fC/eV; and sample 6: intercept=296±36 fC, slope=-0.28±0.03 fC/eV. Values for E_2 obtained from this method are given in Table 5.6.

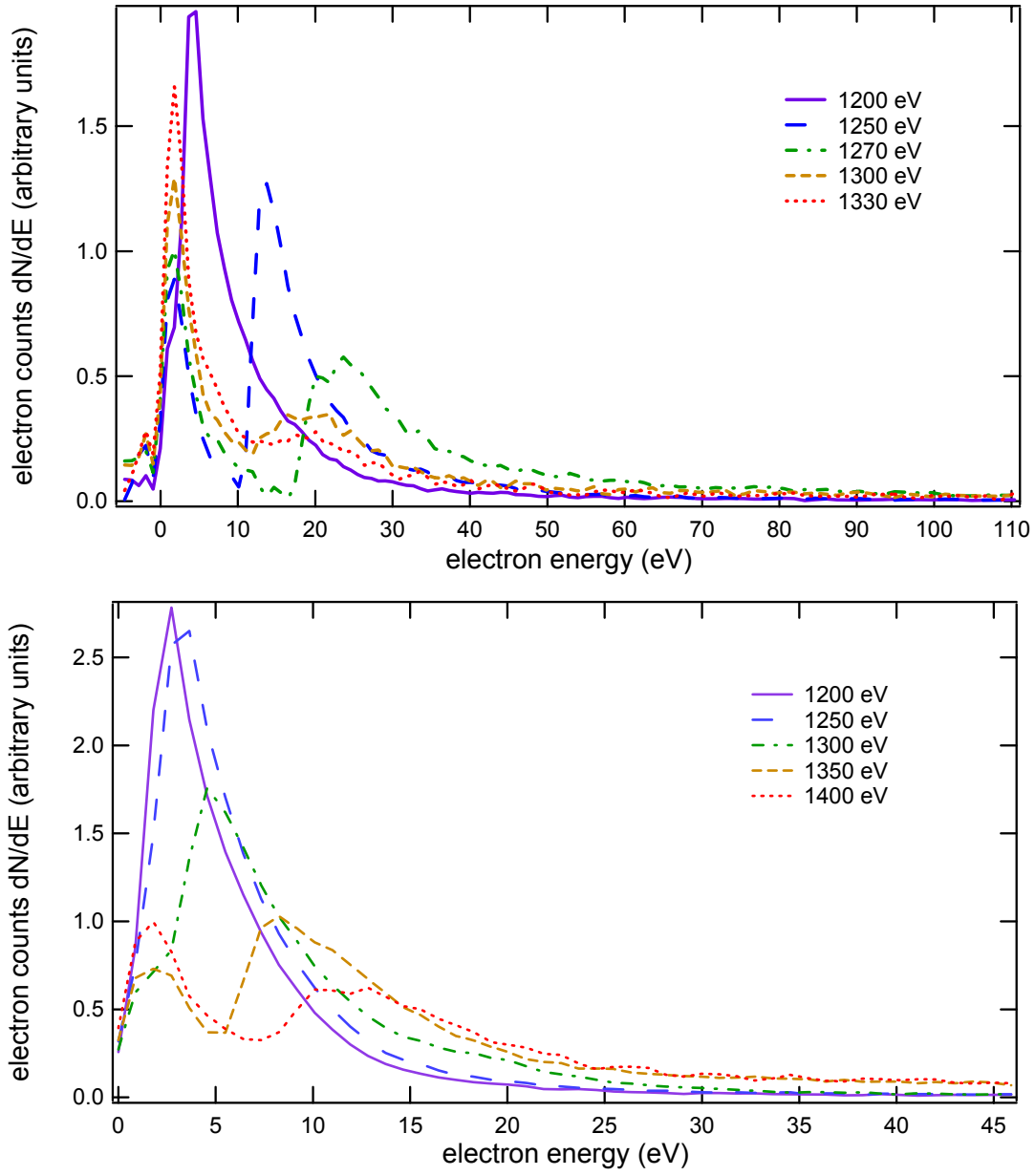

FIG. 5.11. Evolving SE energy spectra for RTV-silicone sample 1 (top) and sample 6 (bottom) for increasing incident electron beam energies. The 1st peak in the spectra is caused by SE emission from the inner grid of the detector housing. The 2nd peak is the true SE peak of the sample. The emergence and right shifting trend of the 2nd peak was caused by a negative sample potential induced by the incident electron energy exceeding E_2^{σ}. These spectra indicated a crossing of E_2^{σ} (and sample negative charging) at 1200-1250 eV for sample 1 and 1250 to 1300 eV for sample 6.

breakdown of the insulators. At these incident energies, sample current was found to be lower than the noise level ±1 nA, except for sample 6 (see below).

After this irradiating period, the electron gun was suppressed temporarily, and the beam energy was decreased to a value below the suspected sample potential, eV_s. Then, a pulsed probe electron beam (diameter <1 mm) consisting of three pulses (three pulses were used for noise-reduction averaging of the signals), each ~100 nA in magnitude and 5 μs duration, were used to probe the surface potential of the insulator film as outlined in Section 4.6. For the probing electron beam, the low-energy settings were the same as for pulsed-yield measurements (see Section 3.3), except the filament current was increased to 1.52 A to achieve ~100 nA pulse magnitudes. Shown in Fig. 4.26 in Section 4.6 is a plot of the sudden rise in sample displacement current in response to the incident probe beam energy, where the critical energy was reached and the sample potential barrier was breached. Sample potentials determined by the probing electron beam, induced by different initial irradiation energies, are summarized in Table 5.5.

Mirror-method results for measured surface potentials along with calculated values for E_2^{σ} were calculated using Eqs. (4.7) through (4.9). Using the manufacturer material specification data, provided in Table 5.3, estimates for the leakage RC time constant, τ_{RC}, were calculated to be 240 seconds. [from Eq. (4.8)] for all RTV samples. In comparison, probing measurements lasted anywhere from 60 to 180 seconds. Consequently, during the course of an experiment, the sample surface potentials decreased by an amount determined by Eq. (4.9). After making these corrections, the second crossover energies were calculated using Eq. (4.7) as described further in Section 4.6. Results for calculated surface potentials and second crossover energies for different values of E_0 are summarized in Table 5.5.

From the data in Table 5.5, it can be seen E_2^{σ} values derived at higher E_0 (>2.5 keV) were typically inconsistent with respect to values derived from E_0=2.0 keV, and were also prone to large errors. It is conceivable electrical breakdown (in the form of small sustained arcs through the bulk of the films) occurred at higher-energy electron irradiation, as indicated by * in Table 5.5. Dielectric breakdown potentials of the four samples were calculated based on dielectric strength values (see Table 5.3). As seen in Table 5.5, (with the exception of sample 6, see below for further discussions), E_2^{σ} values were consistent for each sample for surface potentials, V_s, lower than the calculated breakdown potentials. This observation provides some evidence the mirroring method approach to finding E_2^{σ} was obfuscated by low breakdown potentials of thin-insulating films, and may be a more suitable method for finding the crossover energies of thicker samples.

Finally, in contrast to the other RTV samples, the surface potential of sample 6 did not rise with increasing radiation energy, and stayed at relatively low potentials between 150 V to 300 V, as shown in Table 5.5. As mentioned earlier, for sample 6, a sample current of ~2 nA was measured at beam energies ranging from 2-3 keV. It was speculated the sample had undergone dielectric breakdown (prematurely) at beam energies <2 keV. This assumption was consistent with the fact sample 6 had been prepared with the thinnest RTV coating (compared to the other three samples), and should therefore have demonstrated the lowest breakdown potential (see Table 5.3). Other samples displayed similar breakdown behavior at higher beam energies. For example, when E_0 was pushed to 5000 eV at 30 nA for sample 1, the sample current suddenly rose >20 nA. Then, upon decreasing E_0 to energies as low as 800 eV (keeping the incident current at ~30 nA), the sample remained open to current conduction on the order of 4 nA). Although the electrical breakdown of sample 6 did not influence pulsed-yield, sample current, or DC-spectral estimates for E_2^{σ} (since these measurements were

TABLE 5.5. Mirror method results for RTV sample surface potentials and E_2^{σ} at different irradiation energies. E_2^{σ} was calculated from Eqs. (4.7) and (4.9) using the measured surface potential, V_s and a RC time constant of 240 seconds as determined from Eq. (4.8). Variations in E_2^{σ} resulted from uncertainties in the measurement time interval of 60-180 seconds. E_0 values indicated with a * induced surface potentials,V_s, exceeding the sample dielectric breakdown potential (shown in Table 5.3), and therefore produced inaccurate estimates for E_2^{σ} (also indicated by *). Sample 6 appeared to have already undergone electrical breakdown at E_0 <2 keV.

Sample	E_0 (eV)	V_s (V)	E_2^{σ} (eV)
RTV 1	2000	475 ± 25	1200±200
	2500*	775 ± 25	1150±300*
	3000*	875 ± 25	1500±400*
RTV 2	2000	500 ± 100	1100±200
	2300*	850 ± 100	800±400*
	2500*	1250 ± 50	300±550*
	3000*	1800 ± 100	-100±800*
RTV 5	2000	290 ± 10	1500±100
	2300	525 ± 25	1400±200
	2500	625 ± 50	1400±300
	3000*	1140 ± 10	1000±500*
RTV 6	2000*	175 ± 25	1700±100*
	2500*	150 ± 50	2200±100*
	3000*	250 ± 50	2500±100*

taken before mirror method measurements), E_2^{σ} values derived from the mirror method were inconclusive for this sample.

Table 5.6 summarizes all estimates for E_2^{σ} as determined from the four methods described above. Of the four techniques, the DC spectral measurements were considered to be a more precise method for determining E_2^{σ} since SE emission energies were very sensitive to sample potentials of even a few volts (causing the double-peaks in Fig. 5.11). However, there were concerns continuous electron-beam bombardment could have altered electron yields, including E_2^{σ}, resulting from charge deposition in the bulk of the material. From the table it can be observed, in general, that two pulsed methods for determining E_2^{σ} were consistent for both materials to within 6-7 percent. Furthermore, the two DC methods were consistent to

TABLE 5.6. Estimates for E_2^{σ} for RTV-silicone samples obtained from different methods. These methods included the total yield model, sample current, spectral, and mirror-method techniques. Uncertainties in the mirror method data were obtained from the calculated surface potential decay over a measurement period of 60-180 seconds (see Eqs. (4.7) through (4.9)).

Sample	Material	Tot. Yld E_2^{σ} (eV)	Sample Current E_2^{σ} (eV)	DC-Spectral E_2^{σ} (eV)	Mirror Meth. E_2^{σ} (eV)
RTV 1	CV-1147	1490±40	1600±300	1225±25	1200±200
RTV 2	CV-1147	No data	No data	No data	1100±200
RTV 5	DC93-500	No data	No data	No data	1400±400
RTV 6	DC93-500	1060±30	1000±200	1275±25	Data not conclusive

within 2 percent for CV-1147 (mirror method data was not available for DC93-500). However, pulsed and DC results differed by 25-33 percent for CV-1147 and by 17-22 percent for DC93-500. Additionally, the differences between pulsed and DC results were not systematic. Pulsed results for CV-1147 were higher than DC results, while they were lower for DC93-500. Hence, for these samples, no consistent trends could be drawn between second crossover energies and electron irradiation history.

By comparing results for these two sample types, it can be seen pulsed-yield measurement and sample current estimates for E_2^{σ} differed by 400-600 eV (CV-1147 displayed higher E_2^{σ} values), while DC measurements did not vary substantially. This result can also be observed by the overall higher pulsed yields for the CV-1147 sample than DC93-500 samples, displayed in the total yield curves (see Fig. 5.9) and higher fitted E_2^{σ} values (summarized in Table 5.4). These results may indicate under continuous electron bombardment, the two sample types reached a steady-state condition with very similar internal charge distributions, producing similar surface potentials and electron emission properties. However, in the uncharged cases, measured with a pulsed electron beam and flood gun neutralization, electron emissions varied, with the CV-1147 sample displaying higher total electron yields.

5.3 Kapton™ on Aluminum

5.3.1 Sample Description and Electron Irradiation History

The Kapton™-aluminum sample was sold by Sheldahl Technical Materials (2004) for applications as a low-emissivity conductive thermal control material for spacecraft. The polyimide substrate was 8 μm thick, manufactured by DuPont under the trade name Kapton™. The back surface of the Kapton™ film was coated with a ~0.1 μm evaporated aluminum film. The overall sample thickness measured at USU was 8±0.5 μm, in agreement with the thickness provided by the sample supplier. The physical and electrical properties of Kapton™ were obtained from Sheldahl (2004) and are listed in Table 5.7.

A (10.0 ± 0.1) mm diameter sheet of the material was mounted on a (10.0 ± 0.1) mm diameter Cu cylinder using a conductive UHV adhesive. The sample was wiped clean using methanol prior to insertion into the vacuum chamber. The UHV environment had a typical base pressure of ~$2 \cdot 10^{-9}$ Torr and an operating pressure of ~$5 \cdot 10^{-9}$ Torr for incident electron measurements on the sample. The sample was not ion sputtered since this would have induced unknown insulator charging and possible damage to the Kapton™ layer.

The purpose for studying this sample was to obtain accurate pulsed total, SE, and BSE electron yields (only total yields had been obtained on previously measured insulators, see Sections 5.1 and 5.2) both for comparison with literature results (Willis and Skinner, 1973; Levy *et al*., 1985; Krainsky *et al*., 1981; Kishimoto *et al*., 1990), and also to provide updated electron emissions data for spacecraft charging databases (Dennison *et al*., 2003d). Along with the yield curves, the crossover energies were determined using methods explored on previous materials (refer to Sections 4.6 and 5.2). Additionally, our UV discharging apparatus was tested (along with the electron flood gun) to determine its effectiveness in neutralizing

charged insulators (refer to Section 3.5 for a description of the UV apparatus). By employing

TABLE 5.7. Physical and electrical properties for the Kapton™-aluminum sample. The breakdown potential was calculated from the dielectric strength and insulator film thickness.

Film Thick. (μm)	Surface Rough. (nm)	Density $(kg/m^3)\cdot 10^3$	Resist. $(\Omega\cdot cm)$	Rel. Diel. Const.	Diel. Strength (MV/m)	Brkdwn. Pot. (V)
8±0.5	45±10	1.42±0.02	$1.5\cdot 10^{17}$	3.4	303	2400

both flood gun and UV neutralization techniques, we also intended to test the repeatability of pulsed electron yields after several pulsed-yield/neutralization cycles. Finally, with this sample, we intended to study insulator charging rates as a function of incident electron energy and electron flux, both to provide a useful guide for future measurements, as well as to provide data for insulator charging models.

As has been shown in Sections 5.1 and 5.2, sample electron irradiation history plays an important role in the electron emission properties of insulators. As a general rule, in order to minimize the effects of electron irradiation on electron emission properties, low-energy pulsed data was taken first, followed by higher-energy pulsed data. This was done to reduce the depth of trapped charge inside the insulator. Furthermore, DC yields and spectra were measured only after all pulsed yields had been acquired. This general measurement sequence was followed for the Kapton™-aluminum sample, as well as for the other insulator samples. Nevertheless, part the reason for studying this sample was to determine the effects of electron irradiation on subsequent electron emission properties. Hence, as is described in the next section, a series of yield curves were measured to determine the effects of previous electron irradiation on electron emission properties. The sequence of yield measurements on the Kapton™-aluminum sample went as follows:

1. The first set of measurements on this sample included total and BSE yield curves measured over the positive-charging energy regime of E_0=100-1200 eV. Ten pulses, each 5 μs at ~35 nA, were averaged for each yield data point, and the electron flood gun was triggered between each incident pulse to neutralize any positive surface charging. For this initial yield curve set, the incident electron energy was kept below 1200 eV (near E_2^{σ}) to avoid negative charging. Also, total electron yields were measured in order of increasing beam energy in order to minimize the effects of increasing depth penetration of high-energy electrons. Data for this first yield set is described in Section 5.3.2.
2. After measuring this initial total and BSE yield curve set, the sample was allowed to discharge for two days. The estimated discharge relaxation time was determined from the resistivity and relative dielectric constant values provided by the manufacturer (refer to Table 5.7), where the RC time constant was estimated to be ~13 hrs (refer to Eq. (4.8) in Section 4.6). After this two day relaxation time period, a second set of total and BSE yield curves were measured between E_0=100-1200 eV, and results were compared to the first set. This data is presented along with the first yield set in Section 5.3.2. Along with this second yield curve set, the charging behavior as a function of cumulative charge was measured through repeated pulsing between 200-1200 eV. Results for these studies are discussed in Section 5.3.4. Immediately following this second yield curve set, a third total and BSE yield curve set was measured. This data is also described in Section 5.3.2.
3. Following the measurement of these three initial yield curve sets, a pulsed SE spectrum was taken at E_0=400 eV, and was fitted with the Chung and Everhart model (refer to Section 2.3.5 for a further description of this model). An evaluation of this

spectrum, along with comparisons to a pulsed SE spectrum taken later, is provided in Section 5.3.2.

4. After taking the three yield curves and pulsed spectrum, two additional total yield curves were measured from 200-1000 eV to compare results using different pulse widths and data acquisition methods (data acquisition methods are described further in Section 4.2). For the fourth yield curve, 5 μs pulses were used, and the collector and sample currents were sent both to the oscilloscope and to two of the integrator circuits. For the fifth yield curve, 10 μs pulses were used with the same oscilloscope and integrator measurement configuration. This was done to assess the systematic errors associated with analyzing total electron yields using the charge integration circuitry versus waveform storage and computational analysis. Data analysis for these measurements is presented in Section 5.3.3.
5. After letting the sample discharge for one day, total and BSE yields were measured beyond E_2^{σ} at incident energies ranging from E_0=1.5-5 keV using the STAIB gun. Since negative charging occurred in this energy regime, it was expected the low-energy flood gun would not be effective in neutralizing the insulator surface, leading to negative charging that would exceed several hundreds of volts. Furthermore, as was already shown in Section 5.1, irradiating insulators at incident energies $>E_2^{\sigma}$ can alter subsequent electron emission properties significantly. Hence, it was expected that lower-energy electron yields would be changed after irradiating at these energies. Results and analysis for this yield set are described in Section 5.3.2.
6. After measuring yields at incident energies ranging from 1.5-5 keV, a sixth total and BSE yield curve set was measured for E_0=100-1200 eV for comparison with the first five yield curves measured previously. It was expected this yield set would show

variations resulting from irradiating the sample at the higher energies. A variation that occurred and is worth mentioning here is the initial total electron yields at E_0=100 eV and 200 eV were roughly half their normal values (compared to the first yield set), and sample displacement currents were <10 percent their normal values. However, backscattered yield values were typical for these energies. However, upon increasing E_0 to 300 eV the sample displacement currents suddenly rose, and more typical total yield values were restored for all other incident energies from E_0=300-1200 eV. This yield behavior indicated negative sample charging exceeded -200 V, resulting from the previous electron irradiation at incident energies, E_0=1500-5000 eV. The negative sample potential was sufficient in magnitude to cause the majority of incident electrons to be repelled from the sample for E_0<200 eV due to the mirroring effect (refer to Sections 4.6 and 5.2). However, at E_0>300 eV, the beam was able to overcome the negative surface potential, and reach the sample surface. This caused the negative sample to once again charge positive such that the electron flood gun could be used to neutralize the surface. Results and analysis are for this yield set are described further in Section 5.3.2.

7. After this sixth yield curve, several neutralization tests were performed to compare the effectiveness of the UV neutralization sources with the electron flood gun for incident energies $E_1^{\sigma}<E_0<E_2^{\sigma}$, as well as $E_0>E_2^{\sigma}$. These tests consisted of pulsing the sample with the incident electron beam repeatedly, and then employing either the UV or flood gun neutralization techniques. UV neutralization was explored since the electron flood gun did not effectively discharge negative sample surface potentials induced by incident electron energies of $E_0>E_2^{\sigma}$, and it has been reported in the literature that UV will induce photoconductivity in Kapton^{TM} (Levy *et al*., 1985). As discussed further

below in Section 5.3.3, the results of the effectiveness of UV neutralization for pulsed yields were unsuccessful due, in part, because of the obstruction of the detector apparatus, UV source intensity, and UV source energy.

8. Following these discharging tests, the sample was allowed to discharge for two additional days, and a seventh total yield curve was measured for E_0=100-1200 eV for comparison with the previous six yield sets measured in this energy regime. Data for this yield curve is presented along with the others in Section 5.3.2.
9. To observe how these repeated measurements affected the SE energy distribution, a second pulsed spectrum at E_0=400eV was measured for comparison with the spectrum measured previously at the same incident energy (the previous spectrum was taken after the three initial pulsed-yield curve sets as described above). Data for both yield curves is presented in Section 5.3.2.
10. After completing these measurements, the sample was once again allowed to discharge for three days, and then the Kimball electron gun was used to measure total and BSE yields at high incident energies ranging from 6 keV to 18 keV. Three yield curves were measured in this energy regime: the first and third were taken using 5 μs incident pulses, and the second was taken using 20 μs incident pulses. Different pulse durations were used to compare different electron yield analysis methods that included the charge-integration and pulse-profile methods (refer to Section 4.2 for a further description of these methods). This yield data is presented in Section 5.3.2, and a study of the comparisons of the different pulse measurement methods is presented in Section 5.3.3.
11. Once all pulsed yields had been measured on the Kapton^{TM} sample, the electron gun was turned to continuous emission mode, and the evolution of the DC steady-state

total yields were monitored as a function of total incident electron fluence and energy. This data is presented in Section 5.3.5.

5.3.2 Electron Yield Behavior

This section is divided into three main discussions that describe different aspects of the electron yield behavior of the Kapton™ sample. First, the modeled total, SE, and BSE yield parameters for repeated measured yield curves (refer to sample history discussion in Section 5.3.1) are presented, with a discussion of the effects of sample history on evolving SE yield parameters and SE spectra. Second, the total, SE, and BSE yield curves for Kapton™ are presented, and modeled over the extended energy range of E_0=100 eV to 18 keV, with a discussion of the yield behavior dependence on incident energy. Finally, the total-yield crossover energies of the Kapton™ sample are determined using the sample displacement current method (refer to Section 4.6) for comparison with the crossover energies determined from the modeled yield curve.

Shown in Fig. 5.12 are the first, second, third, sixth and seventh repeated total yield curves described above in Section 5.3.1. Fig. 5.13 shows the first, second, third and sixth repeated BSE yield curves (BSE yields were not measured for the seventh measurement). The raw total and BSE data have been adjusted using the correction factors described in Section 4.3. In order to evaluate changes to the electron emission yield parameters due to repeated pulsing, the maximum yields, σ_{max}, energies, $E_{max}{}^{\sigma}$ and $E_2{}^{\sigma}$, and power coefficient, n^{σ}, were determined by fitting the total yields with the Variable N model over the measured energy range (the Variable N model was used over other methods since it provided the best overall fits, refer to Section 2.3.2). The fits to the total yield data are also shown in Fig. 5.12, and total-yield fit parameters are provided in Table 5.8. As can be seen from the table, in most cases, fitted results for $E_1{}^{\sigma}$ (and $E_1{}^{\delta}$) were inconclusive since experimental data did not extend

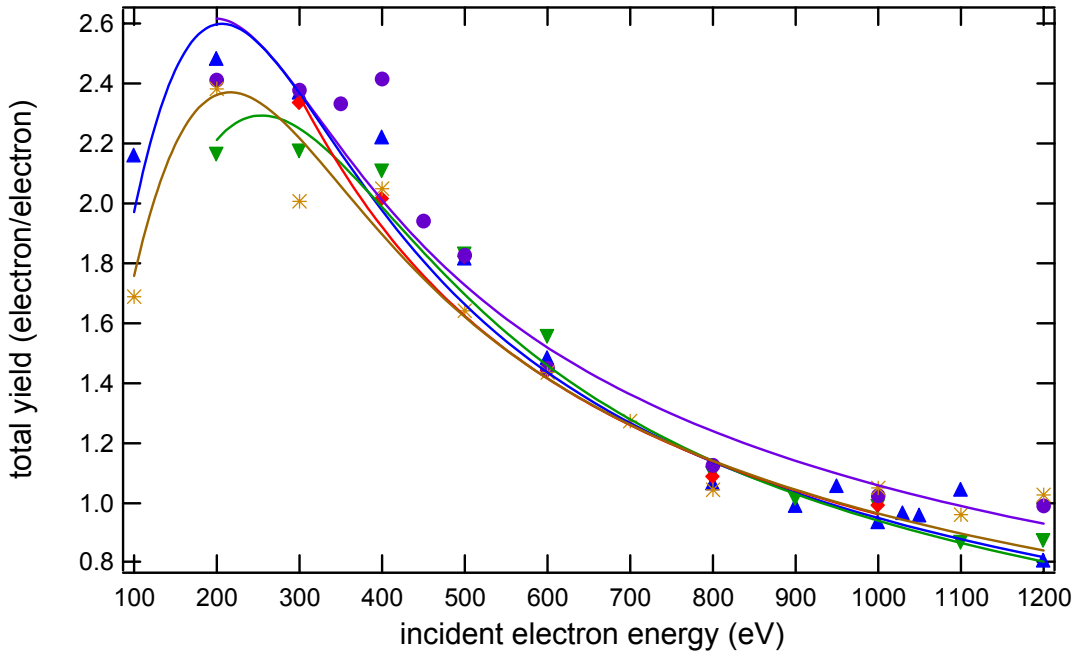

FIG. 5.12. Consecutive total yield curves for Kapton^{TM}-aluminum. The yield curves were taken with ten pulses/measurement, and with flooding between each incident pulse. Error bars have been excluded for visual clarity. The order of the yields curves goes as follows: first (●), second (▲), third (▼), sixth (♦), and seventh (*). Each yield curve was fitted over the energy range shown using the Variable N model (see Section 2.3.2) to determine the total yield parameters. Fit results are summarized in Table 5.8.

below the first crossover energy (the STAIB gun did not operate well at these incident energies, refer to Section 3.4). Also, it must be mentioned here for the sixth yield run, the total yield data was only fitted over the energy range of E_0=300-1200 eV. Total yield data points at E_0=100 and 200 eV were excluded from the fit since they were abnormally low as a result of negative charging from irradiating the sample at energies of E_0=1.5-5 keV prior to taking the sixth yield set (see the discussion above on sample history provided in Section 5.3.1 for further details). To determine differences in the BSE yield trend, the BSE yield data were fitted with linear functions. These fits are shown in Fig. 5.13, and fit results are presented in Table 5.9. From the BSE yield fits, no consistent trends in the slope or intercept were

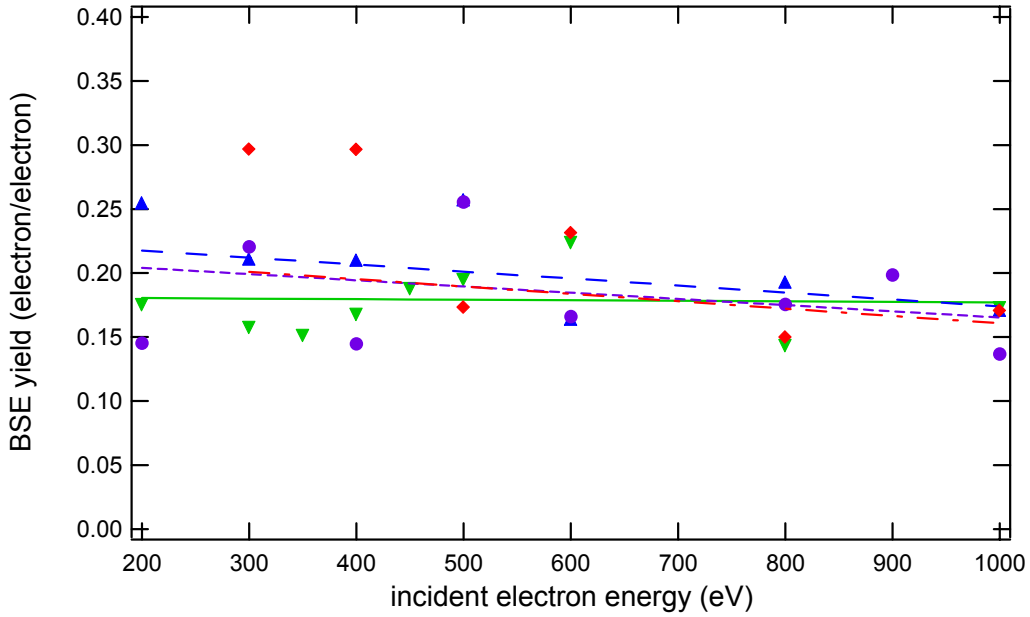

FIG. 5.13. Consecutive BSE yield curves for Kapton™-aluminum in the energy range $E_1^{\sigma}<E_0<E_2^{\sigma}$. The yield curves were taken with ten pulses/measurement, and with flooding between each pulse. Error bars have been excluded for visual clarity. The order of the yields curves goes as follows: first (●, solid line), second (▲, long-dash line), third (▼, short-dash line), and sixth (♦, dash-dot line). Linear fits to the data revealed no significant alterations in BSE yield parameters with repeated measurements. Fit parameters are given in Table 5.9.

observed resulting from repeated electron irradiation. This indicated BSE yields were not strongly affected by sample electron irradiation history in the energy range of $E_1^{\sigma}<E_0<E_2^{\sigma}$ using the pulsed electron beam setup. This makes sense, since pulsed BSE yields in the energy range of $E_1^{\sigma}<E_0<E_2^{\sigma}$ should not be altered significantly by the small positive surface potentials (0-10 V) that occur in this energy regime.

From the corrected total and BSE yield data, SE yields were calculated from the difference between the total and BSE yields (refer to Section 3.3). Similar to the total yields, the SE yields were also fitted with the Variable N model to obtain δ_{max}, E_{max}^{δ}, E_2^{δ} and n^{δ}, and are summarized in Table 5.8. Furthermore, Table 5.10 provides calculated maximum incident electron penetration depths, R, as well as mean SE escape depths, λ_{SE} for each of the fitted SE

TABLE 5.8. Summary of repeated total and SE yield parameters for Kapton™-aluminum fitted with the Variable N model. SE yields were calculated as the difference of the total and BSE yields for runs where BSE yields were measured (refer to Figs. 5.12 and 5.13). Only the second and seventh yield sets provided sufficient data to perform E_1^{σ} parameter extrapolations.

Total Yield Sequence	Sample History	σ_{max}	E_{max}^{σ}	E_1^{σ}	E_2^{σ}	n^{σ}
1st	New	2.6±0.2	199±23	--	1086	1.57±0.03
2nd	Relaxed 2 Days	2.6±0.1	206±11	25	939	1.44±0.03
3rd	No Relaxation	2.3±0.1	254±12	--	933	1.39±0.03
6th	After 5 keV Irradiation	2.9±0.1	164±139	--	952	1.50±0.06
7th	Relaxed 2 Days	2.4±0.1	216±14	36	955	1.51±0.04
SE Yield Sequence	Sample History	δ_{max}	E_{max}^{δ}	E_1^{δ}	E_2^{δ}	n^{δ}
1st	New	2.4±0.1	228±18	--	815	1.32±0.04
2nd	Relaxed 2 Days	2.3±0.1	254±13	--	748	1.17±0.04
3rd	No Relaxation	2.1±0.1	259±12	--	765	1.24±0.04
6th	After 5 keV Irradiation	2.2±0.5	212±60	--	770	1.40±0.06

TABLE 5.9. Summary of repeated BSE yield parameters for Kapton™-aluminum, fitted with linear functions. Within the error, BSE data fit parameters displayed no clear dependence on electron exposure, sample relaxation time, or pre-irradiation energy.

Yield Sequence	Sample History	Fitted Intercept (electron/electron)	Fitted Slope (BSE yield/eV)
1st	New	0.18±0.01	$(-4.3\pm5.5)\cdot10^{-6}$
2nd	Relaxed 2 Days	0.23±0.04	$(-5.4\pm5.3)\cdot10^{-5}$
3rd	No Relaxation	0.21±0.02	$(-4.8\pm2.5)\cdot10^{-5}$
6th	After 5 keV Irradiation	0.22±0.05	$(-5.7\pm5.4)\cdot10^{-5}$

yield curves. To obtain λ_{SE}, the ratio of R/λ_{SE} was first calculated using Eqs. (2.14) and (2.15), along with the fitted power law coefficient, n^{δ} (refer to Fig. 2.5 in Section 2.3.2). Then, the maximum incident electron penetration depth, R, was calculated at the maximum-yield incident electron energy, E_{max}^{δ} using Eq. (2.12) and the fitted power law coefficient (refer to

TABLE 5.10. Calculation of mean SE attenuation depth and maximum incident electron range for Kapton^{TM}-aluminum as determined from the Variable N model. Calculated SE escape depths were consistent with known sample history and internal electric fields resulting from electron irradiation.

SE Yield Sequence	Sample History	R/λ_{SE}	R at $E_{max}{}^{\delta}$ (nm)	λ_{SE} (nm)
1st	New	1.9	12	6.1
2nd	Relaxed 2 Days	3.0	16	5.5
3rd	No Relaxation	2.4	15	6.2
6th	After 5 keV Irradiation	No Soln.	9	No Soln.

Fig. 2.4 in Section 2.3.2). Having obtained R, the mean SE escape depths were then determined using the ratio, R/λ_{SE}.

The SE yields were expected to be more sensitive to sample electron irradiation history than the BSE yields. Although the positive surface potential was continually being neutralized, internal trapped electron/hole charge distributions remained beneath the surface that could affect the transport and escape of low-energy SE's (refer to Section 2.3.6 for further discussions). It was expected the fitted SE yield parameters would be sensitive to these charging effects. The discussion that follows in the next paragraph highlights the changes in the SE yield parameters with respect to the first SE yield curve parameters (parameters are given in Tables 5.8 and 5.10). These changes are explained in terms of the sample electron irradiation history provided in Section 5.3.1.

It was assumed the set of first SE yield parameters would more truly represent the uncharged SE emission properties of the Kapton^{TM} sample since, before measuring this first yield curve, the sample had not been previously irradiated with electrons. For this reason, relative changes in the SE yield parameters were referenced with respect to the first SE yield parameter set. As described in the previous section, the first three yield curve sets were measured in the incident energy regime, $E_1{}^{\sigma}<E_0<E_2{}^{\sigma}$, where net positive charging would have

occurred. In this energy regime, internal charge distributions would have resembled those outlined by the charging Scenarios I-III presented in Section 2.3.7 (refer to Fig. 2.12), where an SE depletion region formed beneath the surface (anywhere from 0-50 nm), resulting in a net positive surface potential. Between each incident pulse, this surface potential would have been neutralized with the flood gun (by depositing a thin electron charge layer on the surface), but the SE depletion region would have continued to grow with continued incident electron irradiation. Hence, strong internal electric fields would have developed that pointed from the positive SE depletion region towards the flooded (electron rich) surface. This internal electric field would have accelerated incident electrons further into the sample, and inhibited the transport of SE's towards the surface (refer to Sections 2.3.7-2.3.8 and Meyza *et al*., 2003). Hence, in this energy regime, one would expect an overall decrease in the SE yields with repeated pulsed-yield measurements. This overall lowering of the SE yield curve would cause both δ_{max}, and E_2^{δ} to decrease with repeated yield measurements. Furthermore, one would expect the maximum incident electron penetration depth, R, to increase, while the mean SE escape depth should decrease.

By comparing the first SE yield curve parameters with both the second and third yield curve parameters in Table 5.8, it was observed the data agreed fairly well with the expected trends described above. Specifically, compared to the first SE yield curve, δ_{max} displayed a drop of 4 percent and 13 percent for the second and third yield curves, respectively. Additionally, E_2^{δ} decreased by 8 percent and 6 percent for the second and third yield curves, respectively. Also, the fitted n^{δ} parameter dropped by 11 percent and 6 percent for the second and third yield curves, respectively. As was shown in Section 2.3.2, the fitted parameter, n, is related to the ratio of the maximum incident electron penetration depth, and mean SE escape length, R/λ_{SE}. From Table 5.10, it can be seen that compared to the first yield curve, the

calculated maximum incident electron penetration depth, R at E_{max}^{δ}, increased by 33 percent and 25 percent for the second and third yield curves, respectively. These increases were consistent with the notion internal electric fields (pointing towards the surface) accelerated penetrating electrons to greater depths. Finally, the mean SE escape depth, λ_{SE}, decreased by 10 percent between the first and second yield curves (again, consistent with the direction of the internal electric fields), but the change in λ_{SE} between the first and third yield curves was insignificant.

As described in Section 5.3.1, the sixth yield curve was measured after the sample had been irradiated with incident electrons in the energy regime $E_0>E_2^{\sigma}$ (specifically, electron yields had been measured from E_0=1.5-5 keV). In this energy regime, negative charging would have occurred that were expected to reverse the SE yield parameter trends observed for the second and third yield curves. Specifically, after irradiating the sample at $E_0>E_2^{\sigma}$, internal charge distributions were expected to resemble those described in the charging Scenario IV, presented in Section 2.3.7 (refer to Fig. 2.12). This charging scenario is dominated by a negative incident electron deposition region extending as far as 1 μm into the insulator (refer to Fig. 2.4 in Section 2.3.2), which causes the insulator surface potential to go negative. This negative charge distribution also changes the overall direction of the internal electric field (directed into the sample) as compared to the first three yield curves described above, which causes subsequent incident electron penetration depths to decrease in the decelerating field, and subsequent SE attenuation lengths to increase due to electric-field-assisted transport. Hence, for the sixth yield curve, the SE mean escape depth, λ_{SE} should increase, while the incident electron penetration depth, R, should decrease as compared to values obtained for the first yield curve. It is hard to predict the effects this charging scenario will have on the overall SE yield curve behavior. The first inclination is to assume the overall SE yield curve would

increase, causing the parameters δ_{max} and E_2^{δ} to increase. However, as was already explained in the sample history outline of Section 5.3.1, initial total electron yields at E_0=100 eV and 200 eV were roughly half their normal values (compared to the first yield set) for the sixth yield run until the incident electron energy became sufficient to overcome the negative surface potential and reach the sample surface. At this point, the sample would have resumed positive charging, but the negative incident electron deposition region would have remained deeper in the material. Hence, the internal charge distribution would have been quite complex, and predicting its impact on SE yield behavior is quite difficult.

By comparing the sixth SE yield curve parameters with the first yield curve Table 5.8, it was observed, compared to the first SE yield curve, δ_{max} and E_2^{δ} were both lower by 8 percent. As discussed above, the internal charge distributions that would have led to the observed decrease in these yield parameters are not known. However, the parameter, n, increased by 6 percent, indicative of a smaller R/λ_{SE} ratio. From Table 5.10, it can be seen that the calculated maximum incident electron penetration depth, R, was lower by 25 percent, consistent with the notion internal electric fields had reversed direction in the sample (as compared to the first three yield curve measurements), inhibiting the penetrating of incident electrons into the material. Finally, the mean SE escape depth, λ_{SE}, was not calculated since the ratio, R/λ_{SE}, did not have a solution for the modeled SE yield parameter, n^{δ} (refer to Table 5.8 and Fig. 2.5 in Section 2.3.2). However, as mentioned, the increase in n^{δ} as compared to the first yield curve, was indicative of a smaller R/λ_{SE} ratio, and hence, a larger λ_{SE} value. This further supports the notion the internal electric fields increased λ_{SE} by accelerating SE's towards the surface, as discussed above.

Finally, the data presented above offers evidence the SE yields were altered by repeated pulsed-yield measurements. However, future measurements on Kapton^{TM} and

additional insulator materials need to be repeated to verify these charging trends further. Specifically, once instrumentation improvements are made, as discussed in Section 6.1, electron emission measurements at USU should become more accurate both in the positive and negative charging regimes, and this will allow us to better determine the relationships between internal charging and electron emission behavior.

In addition to monitoring SE yields after repeated measurements, two SE spectra were measured: the first spectrum was measured after the third yield curve, and the second spectrum was measured after the seventh yield curve. These two spectra are shown in Fig. 5.14. Both spectra were fitted with the Chung and Everhart model (refer to Section 2.3.5). From the fits, the material-parameter, k and surface potential-barrier term, χ, were determined, and found to be identical to within the fitting error, with $k=(1.2\pm0.3)\cdot10^{-8}$ $C\cdot eV^3$, $\chi=3.7\pm0.3$ eV for the first spectrum and $k=(1.0\pm0.3)\cdot10^{-8}$ $C\cdot eV^3$, $\chi=3.8\pm0.4$ eV for the second. Small differences in the fitted k values were attributed to the slightly higher amplitude of the first spectrum due to larger incident electron pulse magnitudes. These results indicated as long as the insulator's surface potential was discharged using effective neutralization techniques (i.e., the electron flood gun), the internal charge distributions induced by previous electron irradiation would not alter the escaping SE energy distribution significantly. This is consistent with the models presented in Section 2.3.6, where alterations in the SE spectra were found to only depend on changes in the surface potential barrier (electron affinity and surface potential), since ultimately, an SE escaping into the vacuum will only respond to the surface electric fields (and not internal electric fields) of the insulator.

Once repeated electron yield curves had been measured on the Kapton^{TM} sample, the total and BSE yields from the three initial yield sets, as well as the seventh yield set, between 100-1200 eV were averaged (and errors combined) to produce total, SE, and BSE electron

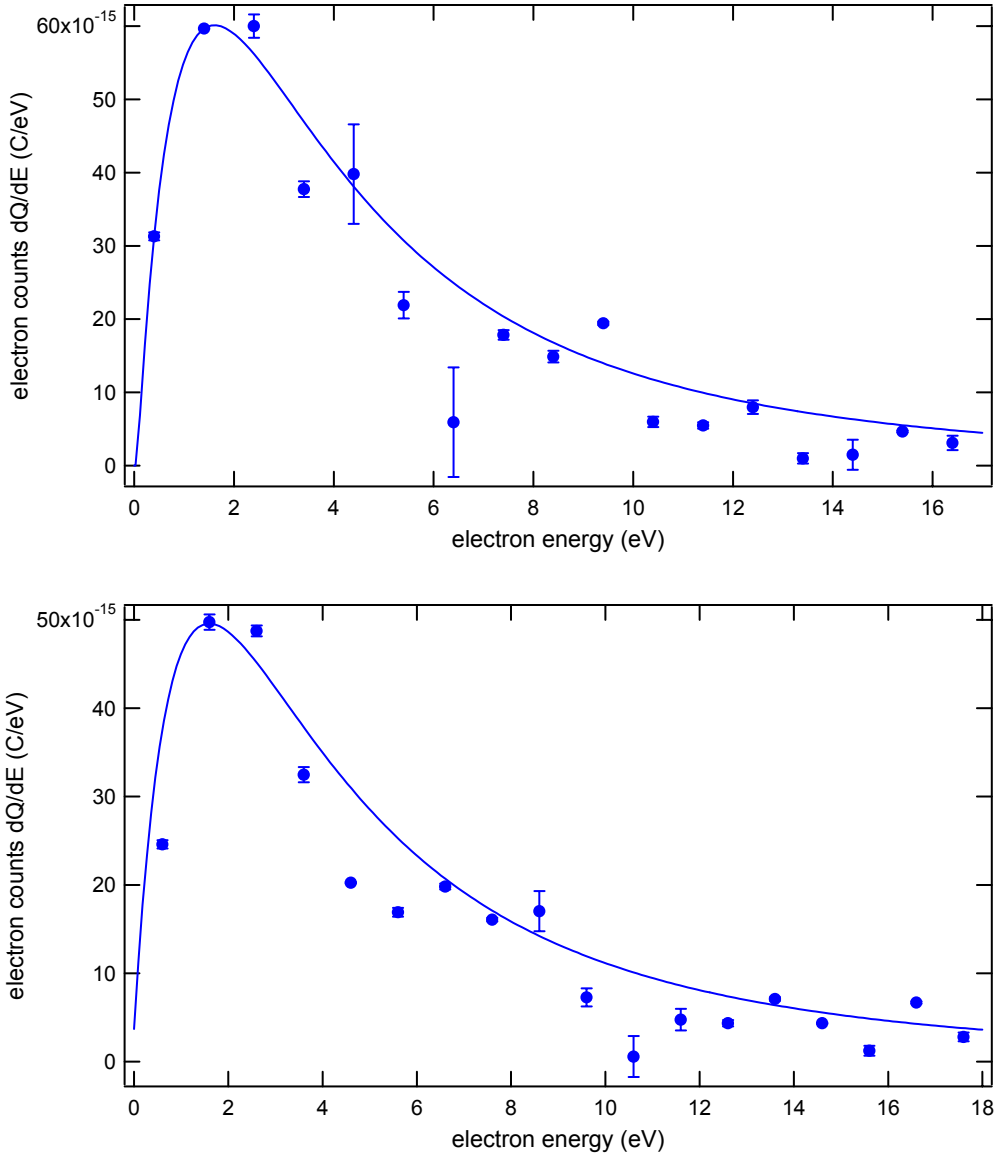

FIG. 5.14. Pulsed SE spectra on Kapton^{TM}-aluminum for the virgin sample (top) and after having undergone repeated testing (bottom). The incident electron energy was E_0=400 eV. Each data point consisted of ten pulses of 5 μs in duration and ~35 nA in magnitude. Flooding was used between each incident pulse. Data were fit with the Chung and Everhart model (refer to Section 2.3.5). Fitting parameters did not vary between the two spectra, indicating that the sample SE distribution remained unchanged after repeated electron irradiation.

yield curves for the Kapton™ sample in the energy regime of $E_1^{\sigma}<E_0<E_2^{\sigma}$. This data was combined with data taken in the energy regime of $E_0>E_2^{\sigma}$, which consisted of data measured with the STAIB gun (E_0=1.5-5 keV) and Kimball gun (E_0=6-18 keV). As discussed in Sections 5.3.1 and 5.3.3, three yield data sets were measured with the Kimball gun, and were averaged. The appropriate correction factors were then applied to the raw data over the extended energy range to correct for detector and stage losses (refer to Section 4.3 for explanations for pulsed and DC correction factors). These final yield curves are shown in Fig. 5.15.

It must be noted for $E_0>E_2^{\sigma}$, although the electron flood gun was still employed between each incident pulse, the gun was not expected to neutralize negative surface charging. However, it was believed negative charging in the pulsed setup would not significantly alter total electron yields, since, as has been mentioned previously, each incident pulse was expected to alter the surface potential by no more than 1 V. As can be seen from Fig. 5.15, for $E_0>E_2^{\sigma}$, the total electron yields did not appear to be strongly altered by repeated electron pulsing, since, within the data error, the total yields decreased smoothly with increasing incident energy (as they should for $E_0>E_2^{\sigma}$). However, from the data for $E_0>E_2^{\sigma}$, it was observed the SE and BSE yields were significantly altered with repeated pulsing. Specifically, once E_2^{σ} was traversed (between 950-1000 eV), the BSE yields jumped in magnitude by a factor of three to values that approached total yields, and the SE yields approached zero. This jump was attributed to the fast negative charging mechanism described in Section 2.3.6, where upon crossing E_2^{σ}, the insulator surface potential charged negatively beyond 50 V, accelerating escaping SE's to energies >50 eV. Consequently, the major fraction of the total electron yield was comprised of electrons with energies >50 eV, which were therefore registered as BSE's by our detector. Also, as expected for $E_0>E_2^{\sigma}$, the electron flood gun had

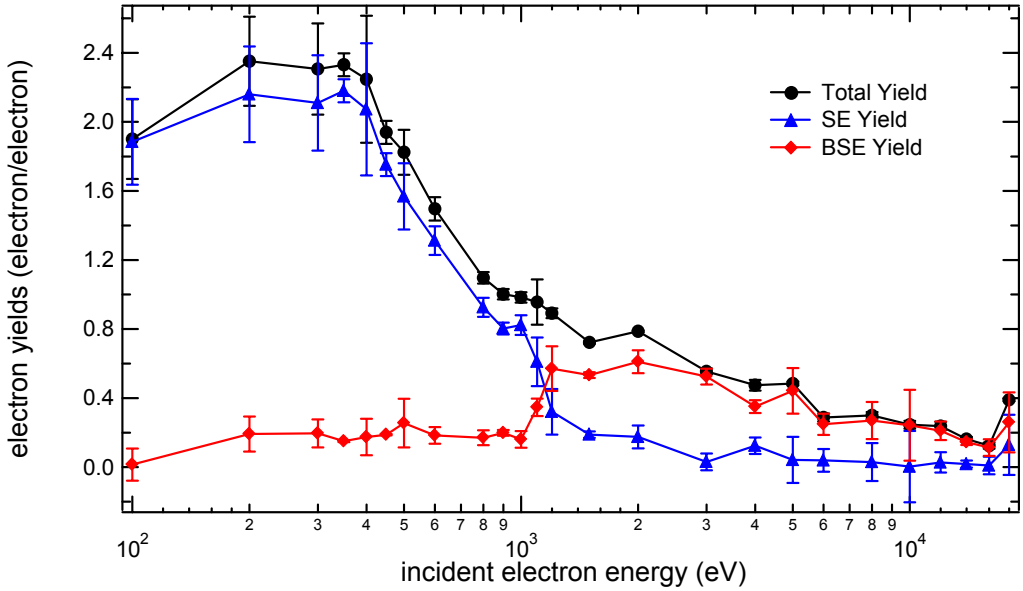

FIG. 5.15. Combined pulsed total, SE, and BSE yield curves for Kapton^{TM}-aluminum. BSE yields increased and SE yields decreased past E_2^{σ}, due to the additional energy given to escaping SE's by increasing negative surface potentials.

no noticeable effect on neutralizing these negative surface potentials, and restoring uncharged SE and BSE yield behavior. Hence, for $E_0>E_2^{\sigma}$, although the total electron yields remained accurate, the measured SE and BSE yields were not. Future efforts at USU will concentrate on developing UV neutralization techniques capable of neutralizing negative charging for $E_0>E_2^{\sigma}$. Once we have developed such neutralization techniques, we will be able to measure accurate SE and BSE yields beyond E_2^{σ} (refer to Section 6.1).

The combined total and SE yields over the range of E_0=100 eV to 18 keV were fitted with electron emission models, as shown in Fig. 5.16. Fitted results are summarized in Table 5.11. In general, the fitting models were poor over the extended energy range of 100 eV to 18 keV (especially as compared to fits over the 100 eV to 1200 eV energy range), being either weighted by the higher-energy data or lower-energy data near the yield maximum. Fit results for SE yields over the extended energy range were further in error due to the drop in measured

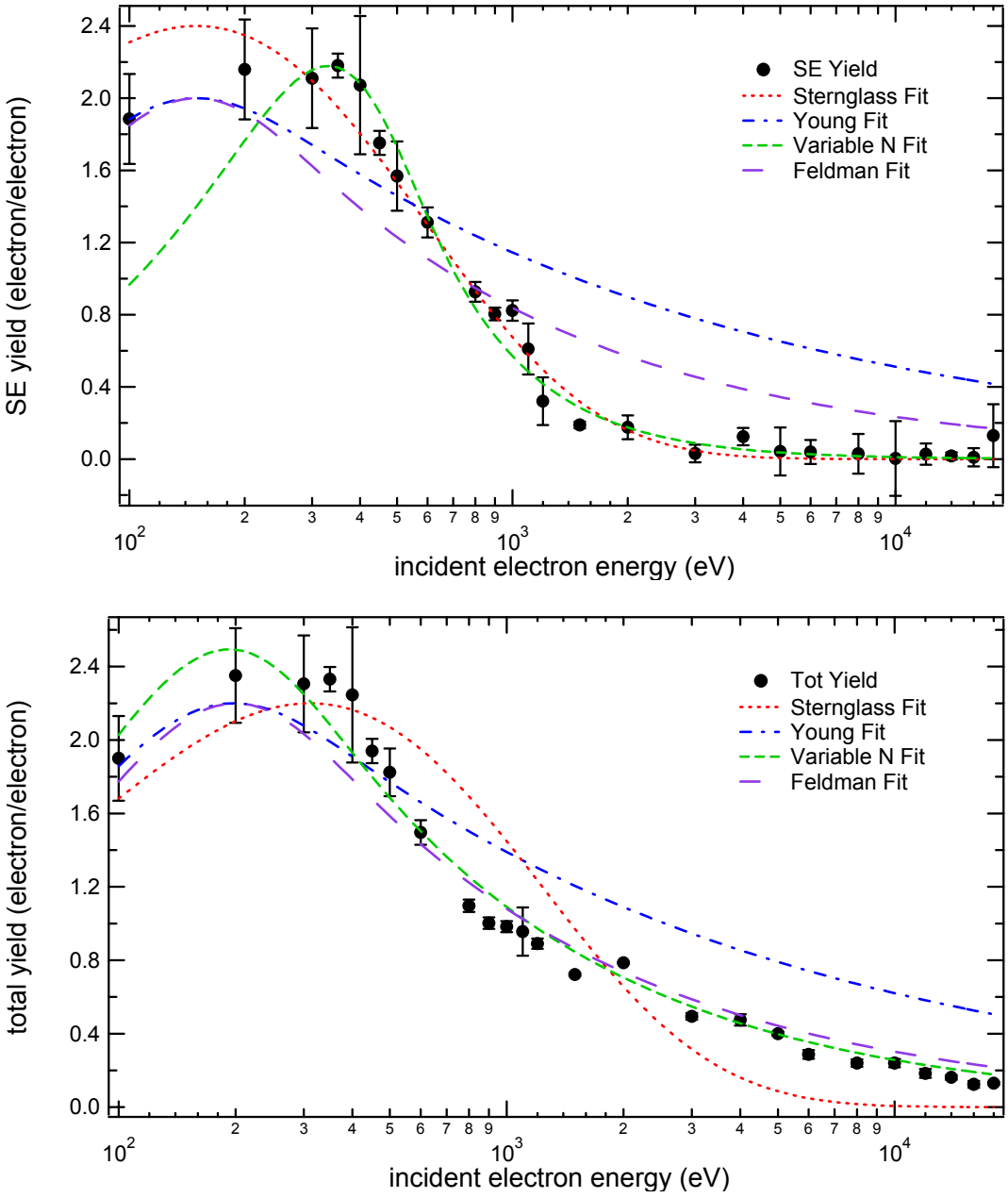

FIG. 5.16. Various models applied to the SE yield (top) and total yield (bottom) curves. Models are described in Section 2.3.2. SE yield parameters from the fits are summarized in Table 5.11. In general, the fits were poor over the extended energy range from 100 eV to 18 keV.

TABLE 5.11. Summary of measured total and SE electron yield parameters for Kapton™-aluminum resulting from the yield-curve fitting models in Fig. 5.16. Estimates for yield parameters varied widely since models provided poor fits over the fitted energy range. Explanations for these models are given in Section 2.3.2.

Total Yield Fitting Model	σ_{max}	E_{max}^{σ} (eV)	E_1^{σ} (eV)	E_2^{σ} (eV)	n^{σ}
Sternglass	2.2	311	3	1463	--
Young	2.2	198	-1	2561	1.35
Variable N	2.5	193	8	1101	1.68
Feldman	2.2	200	21	1105	1.8
SE Yield Fitting Model	δ_{max}	E_{max}^{δ} (eV)	E_1^{δ} (eV)	E_2^{δ} (eV)	n^{δ}
Sternglass	2.4	150	-236	758	--
Young	2.0	149	-72	1474	1.35
Variable N	2.2	331	104	720	0.86
Feldman	2.0	150	-33	726	1.8

SE yields for $E_0>E_2^{\sigma}$. Model extrapolations for E_1^{δ} and E_1^{σ} varied widely, and in half the cases were negative in value (non-physical solutions). Fitted values for E_{max}^{δ}, E_{max}^{σ} E_2^{δ}, and E_2^{σ} also displayed wide variation between the fitting models. Due to the errors associated with fitting the entire yield curve, the lower-energy fits shown in Fig. 5.12, along with their fitting parameter given in Table 5.8, were considered to be much more accurate.

Finally, as discussed in Section 4.6 and as demonstrated in Section 5.2, an accurate method for determining the total-yield crossover energies, E_1^{σ} and E_2^{σ} is to monitor the sample displacement current as a function of incident electron energy. This method was used on the Kapton™ sample to more accurately determine the total-yield crossover energies, for comparison with the crossover energies determined from the modeled total yield curves (data provided in Table 5.8). As shown in Fig. 5.17, the integrated sample displacement current was plotted as a function of incident beam energy, and the crossover energies were taken as the vertical-axis zero crossing (refer to Section 4.6 for further explanation of this technique). Results for this method are summarized in Table 5.12. For E_1^{σ}, sample charge data were taken

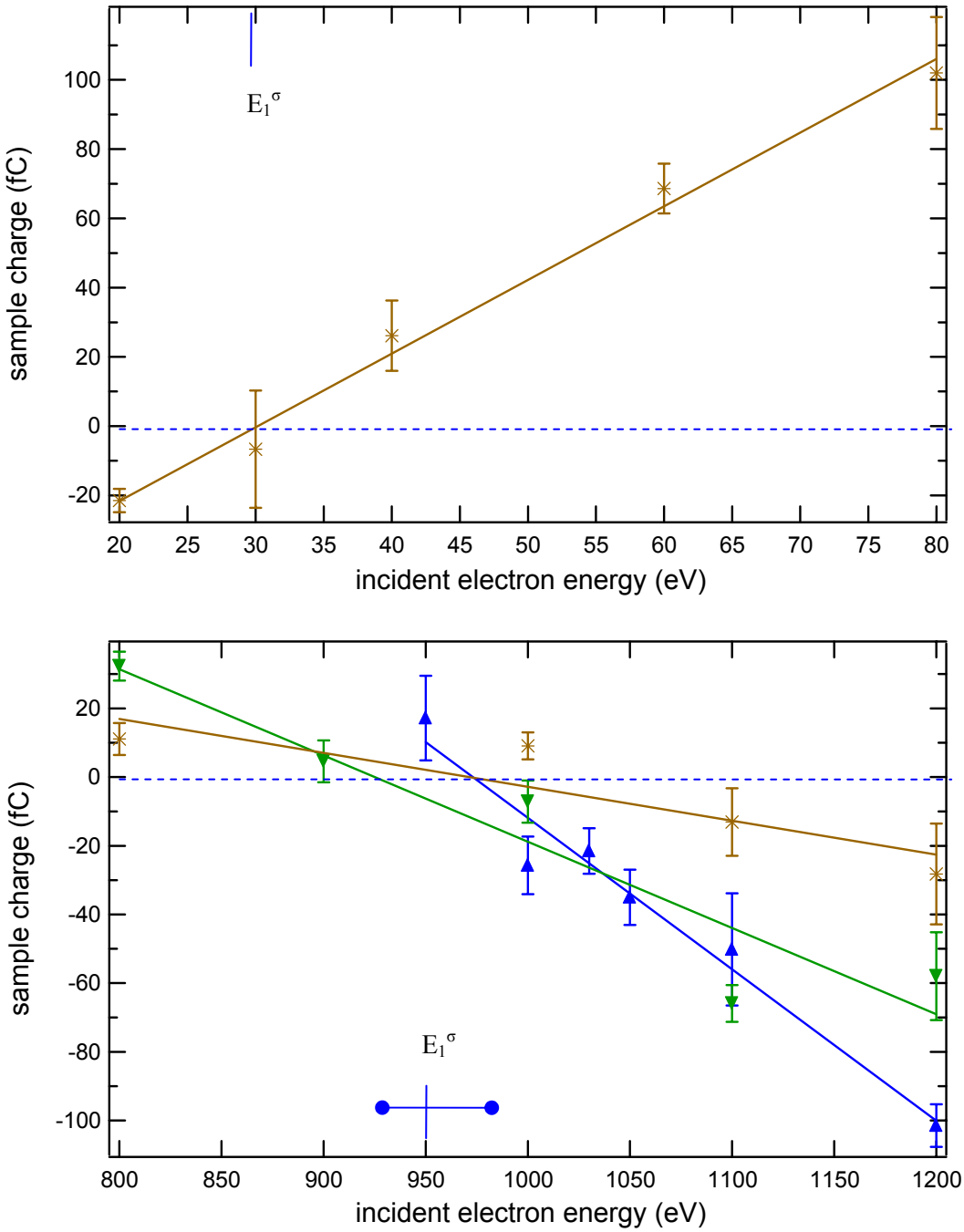

FIG. 5.17. Integrated sample displacement current as a function of beam energy for Kapton™-aluminum crossover energies. Data came from the second (▲), third (▼), and seventh (*) yield data sets. Fits for E_1^{σ} (top) gave a value of 30.1±0.1 eV, while fits for E_2^{σ} (bottom) gave second run: 974±1 eV, third run: 928±1 eV, and seventh run: 970±1.

TABLE 5.12. Estimates for E_1^{σ} and E_2^{σ} for Kapton^{TM}-aluminum obtained from the fitted total yield and sample current methods. Fitted total yield values for E_1^{σ} and E_2^{σ} were taken from Table 5.8. Fitted sample current values were taken from Fig. 5.17. Both methods were consistent to within the error of the fitted values, and were considered to be much more accurate than fitted values obtained from the extended yield curve in Table 5.11.

Fitted E_1^{σ} (eV)	Sample Current E_1^{σ} (eV)	Fitted E_2^{σ} (eV)	Sample Current E_2^{σ} (eV)
31±6	30.1±0.1	973±29	957±25

from the seventh yield set, producing E_1^{σ}=30.1±0.1 eV. For E_2^{σ}, data were chosen from the second, third, and seventh yield data sets, and produced the following values: second set 974±1 eV; third set 928±1 eV; and seventh set 970±1 eV. By comparing Tables 5.8 and 5.12, it can be observed the results obtained by the sample current method were consistent with those obtained from fitting the total yield curves to within 4 percent.

5.3.3 Pulsed-Yield Analysis Methods and UV and Floodgun Neutralization Studies

This section is comprised of two major discussions. The first discussion addresses the relative accuracy of total electron yields, measured using both the STAIB and Kimball electron guns, and analyzed using various methods discussed in Section 4.2. The second discussion presents data on the effectiveness of the electron flood gun and UV neutralization sources for neutralizing both positive and negative charging in the energy regimes $E_1^{\sigma}<E_0<E_2^{\sigma}$ and $E_0>E_2^{\sigma}$.

As discussed in the sample history in Section 5.3.1, the fourth and fifth total yield curves with E_0=200-1000 eV were measured to compare results using different pulse widths and yield-calculation methods. For the fourth yield curve, 5 μs pulses were used (from the STAIB gun), and the collector and sample currents were sent both to the oscilloscope and to two of the integrator circuits. This was done to compare electron pulse charge values obtained

using the computational integration method versus the integrator circuitry. For the fifth yield curve, collector and sample currents were again sent to both the oscilloscope and integrator circuits, only 10 μs pulses (from the STAIB gun) were used. Total electron yields were then calculated using each of these measurement configurations, and are plotted in Fig. 5.18. As can be seen in the figure, overall agreement between the different measurement configurations was good throughout the energy range to within the error of the measurements. Only the fifth yield curve (10 μs pulses), which was computationally integrated, showed variations at E_0=400 eV, 600 eV, and 1000 eV exceeding 20 percent as compared to the other data curves. This occurred perhaps due to inappropriate DC offset correction boundaries for the longer pulses in the Labview VI analysis (refer to Sections 4.2 and Thomson, 2003d).

In a similar fashion, the Kimball electron gun was used to measure total yields from 6-18 keV, using different measurement and analysis schemes. Specifically, three yield curves were measured: the first and third were taken using 5 μs incident pulses, and the second was taken using 20 μs incident pulses. The different pulse durations were used to compare the charge-integration and pulse-profile electron yield analysis methods (refer to Section 4.2). Since the Kimball electron gun emitted regular square-wave pulse profiles (as opposed to the STAIB gun, as explained in Section 3.4), and since the pulse duration (20 μs) exceeded the combined rise/fall response time (~4 μs) of the ammeters, it was possible to calculate total yields using the ratios of the collector and sample pulse current maxima (referred to as the pulse-profile method as discussed further in Section 4.2). These yield values were compared with the more typical charge-integration analysis method (refer to Section 4.2) for the 5 μs and 20 μs pulses, and are shown in Fig. 5.19. From the figure, it can be seen the charge-integration method for the 20 μs pulses produced yield data points at 8 keV and 10 keV, which were higher than the other methods by ~20 percent. Once again, the yield values obtained

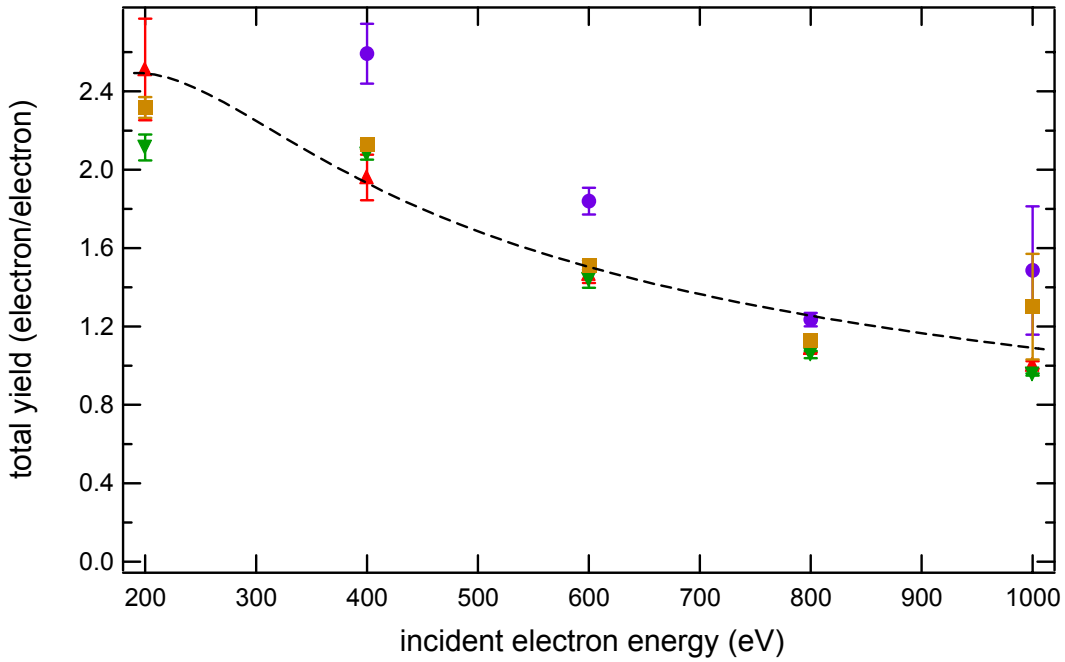

FIG. 5.18. Comparison of STAIB gun electron total yields measured and analyzed using the charge-integration method for 5 μs and 10 μs incident pulses. The Variable N model (dashed line) is included as a guide to the eye. The graph key is as follows: fourth yield set oscilloscope 5 μs (▲), fourth yield set integrator circuit 5 μs (▼), fifth yield set oscilloscope 10 μs (●), and fifth yield set integrator circuit 10 μs (■). Only the oscilloscope 10 μs data varied by more than 20% (at 400 eV and 600 eV) compared to the other data.

from the charge integration method for the longer pulse durations were attributed to inadequate DC offset correction prior to signal integration in the Labview analysis (as was the case with the integration of longer STAIB gun pulses, shown in Fig. 5.18). Hence, the data presented here demonstrates total yield values obtained using different electron yield measurement and analysis schemes (i.e., integration circuitry versus computational integration measurements and charge integration versus pulse profile yield analysis) produced results that showed overall consistency over a wide energy range. However, additional data needs to be acquired, and improvements need to be made towards the computational charge integration method of longer pulse durations, in order to further validate the consistency of electron yields using longer pulse durations and different analysis methods.

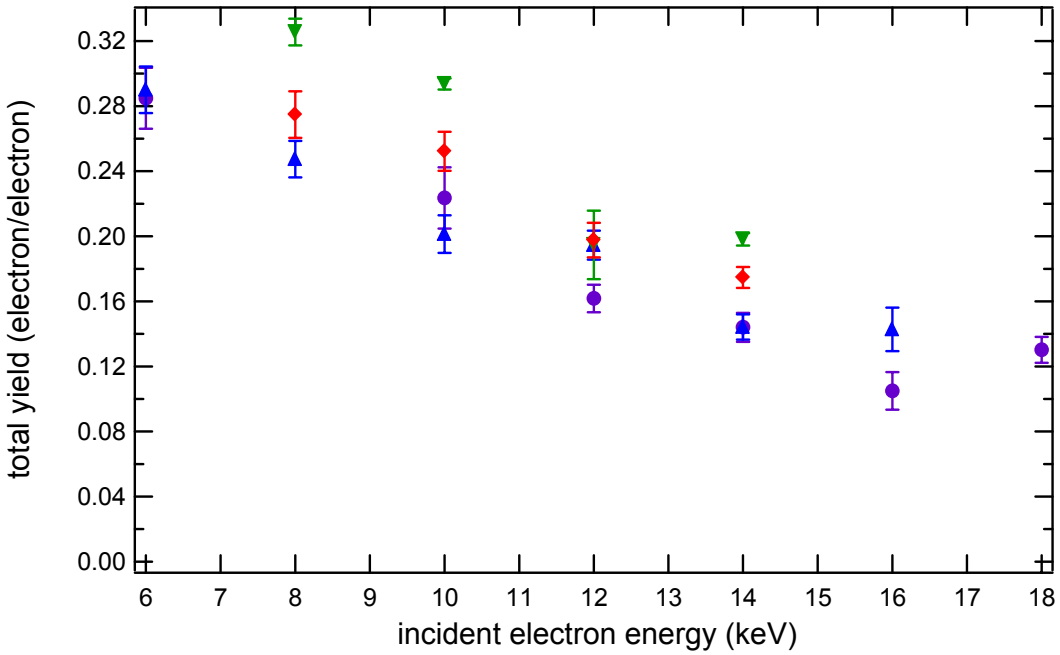

FIG. 5.19. Comparison of repeated Kimball gun electron yields measured by the charge integration and pulse-profile methods. The charge-integration method was used for the first (5 μs pulse width), second (20 μs pulse width), and third (5 μs pulse width) yield sets, and the pulse-profile method was only used for the second (20 μs pulse width) yield set. The graph key is as follows: first-run integrated 5 μs (●), third-run integrated 5 μs (▲), second-run integrated 20 μs (▼), and second-run pulse-profile method 20 μs (♦). Similar to the STAIB yield results (Fig. 5.18), the charge integration analysis of the longer-duration pulses produced data that was higher for some measurements.

In addition to testing various yield measurement and analysis methods on this sample, different charge neutralization techniques, including the electron flood gun and UV neutralization sources, were compared in different energy regimes. Specifically, the electron flood gun, as well as two UV neutralization sources (i.e., a mercury lamp and UV diode array), were tested both for $E_1^{\sigma}<E_0<E_2^{\sigma}$ (positive charging) and $E_0>E_2^{\sigma}$ (negative charging). Section 3.5 gives a more detailed description of the characterization of the flood gun and UV neutralization sources. Fig. 5.20 shows a series of pulsed total yields and integrated sample displacement currents at E_0=400 eV used to monitor positive sample charging for $E_1^{\sigma}<E_0<E_2^{\sigma}$ (refer Section 4.5 for an explanation of this method for monitoring insulator charging). By

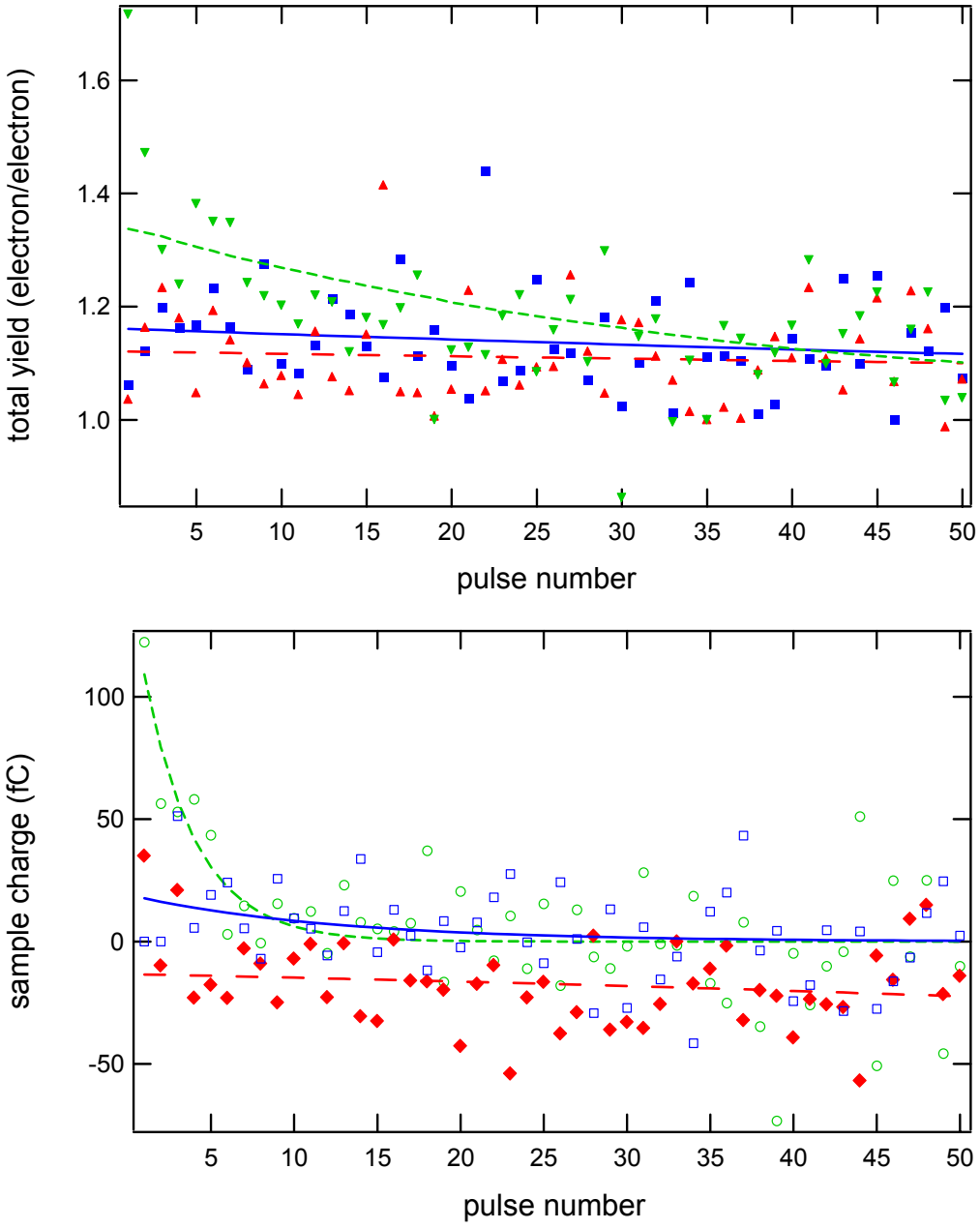

FIG. 5.20. Total yield (top) and integrated sample displacement current (bottom) plots at 400 eV, showing effectiveness of various neutralization techniques. Previous to taking these data, the sample was fully charged with a 400 eV electron beam. Then, a series of pulsing sequences were used to test the effectiveness of various neutralization sources that included: allowing the sample to sit for 10 min. (■); irradiation with a mercury lamp for 10 min. (▲); low-energy electron flooding for 2 min. (▼and ○); irradiated for 10 min. with a UV photdiode array (♦); and allowed to sit overnight (□).

measuring multiple series of decaying yield curves, the effectiveness of the UV sources versus low-energy electron floodgun neutralization techniques were explored. Initially, the sample was pulsed repeatedly at E_0=400 eV until the sample became fully charged (as determined by the convergence of the total yields towards a steady-state value). Then, as shown in the top graph of Fig. 5.20, different neutralization techniques were implemented to determine their discharging effectiveness on subsequent total yields. For example, once the sample had reached steady state through repeated electron pulsing, the sample was allowed to sit for 10 min. Then another electron pulsing sequence was measured, and did not reveal any recovery of the original uncharged electron yield value. Next, the mercury lamp (see Section 3.5 for details) was used to irradiate the sample for 10 minutes. Again, upon measuring another electron pulsing sequence, no recovery of the uncharged yield was observed. Finally, the sample was flooded with the electron flood gun for 2 min., and a third yield sequence was measured, displaying nearly full recovery of the initial uncharged yield value. After this pulsing sequence, the sample was once again flooded for 2 min. to restore the insulator surface potential to ~0 V.

In performing the UV neutralization procedure described above, it was necessary to swing the detector apparatus out of the way in order to irradiate the sample surface with the UV source. In doing so, it was decided changing the position of the detector and sample for UV irradiation introduced yield measurement errors associated with repositioning the detector and sample towards the electron beam. Hence, it was decided to move the detector out of the way for all subsequent UV discharging measurements (to avoid intermittently moving the detector for electron gun pulsing and UV neutralization), and to monitor sample charging through sample displacement current measurements (instead of total yield measurements). In

this way, the sample position would remain stationary and the electron irradiated area would not change between electron pulsing and UV discharging sequences.

After making these measurement alterations, the pulse sequence measurements described above were resumed, and are shown in the bottom graph of Fig. 5.20. First, the sample was once again pulsed with the electron beam until it reached a charged steady-state condition (it had previously been neutralized using the flood gun). Then, the sample was irradiated with a UV diode array source for 10 min (refer to Section 3.5 for a description of the UV diode array). Then, another electron pulsing sequence was measured, and revealed a negative sample displacement current, attributed to a net electron current into the sample. It was not clear why this displacement current was negative. Finally, the sample was allowed to discharge overnight before one last pulsing sequence was measured. This sequence also revealed no neutralization effects. These results indicated for the positive charging regime of $E_1^{\sigma}<E_0<E_2^{\sigma}$, the flood gun provided the only effective method for neutralizing the Kapton^{TM} sample in a timely manner.

Next, a similar procedure to that described above was performed at 5 keV ($E_0>E_2^{\sigma}$) to test the effectiveness of the electron flood gun and UV sources in neutralizing negative charge. From previous measurements (refer to Section 5.3.2 above), it had already been determined the electron flood gun was not effective in neutralizing negative charge since the low-energy electrons were repelled from the negative sample potential. However, based on previous studies reported in the literature, it was believed the UV sources might be effective in neutralizing negatively charged insulators (Bass *et al*., 1998; Levy *et al*., 1985). To test this notion, the sample was pulsed repeatedly (as above), first without UV irradiation, and then while being irradiated continuously with the UV diode source. From the data shown in Fig. 5.21 it was observed the displacement current from the sample, while being irradiated

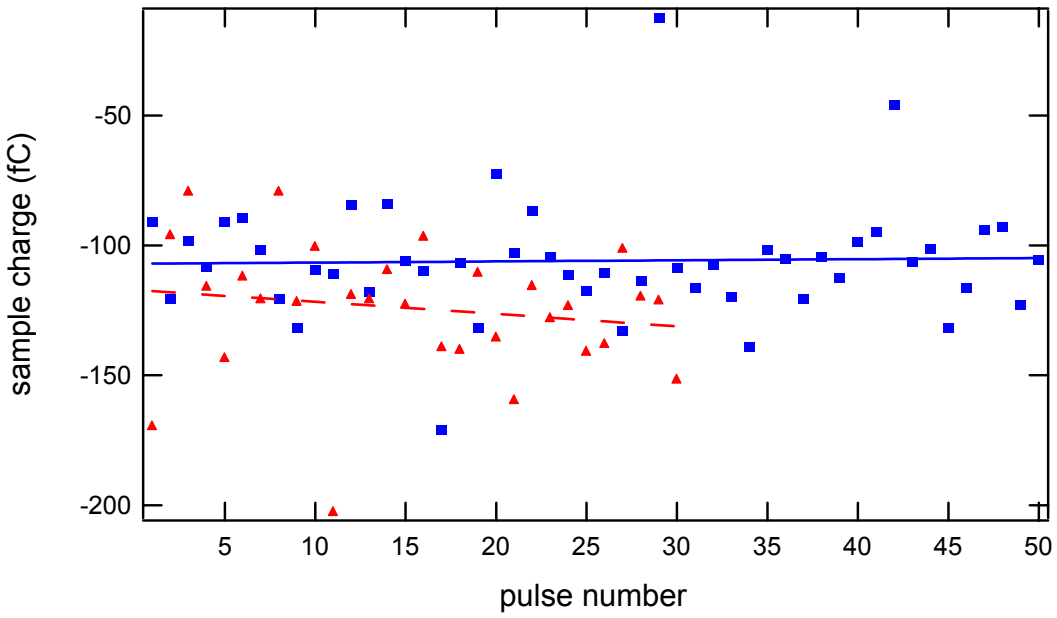

FIG. 5.21. Integrated sample displacement current using a pulsed beam at 5000 eV with (▲) and without (■) UV diode irradiation. The sample was pulsed while continually being irradiated with the UV diode source.

with the UV diode source, was more negative than for the sequence without UV irradiation, and displayed a decrease in displacement current with repeated pulsing. This was consistent with the 400 eV sequences, where the UV diode appeared to induce negative sample electron current. However, the reasons for the negative sample displacement current were not clear.

Overall, it was hard to assess the effectiveness of the UV neutralization technique for $E_0>E_2^{\sigma}$ since charging effects on sample displacement currents in this energy regime were minimal, even without UV neutralization. This was attributed to the slow negative charging mechanism discussed in Section 2.3.6 where, although rising negative surface potentials can significantly affect SE and BSE yields, the total yields (and sample displacement currents) are not influenced heavily until the potential reaches a sufficient magnitude to alter the landing energies of incident electrons. It can take thousands of pulses at $\sim 10^{-13}$ C/pulse for this

charging mechanism to significantly affect total electron yields or sample displacement currents with our pulsed-measurement setup (refer to Section 5.3.4 below).

In summary, the low-energy electron flood gun neutralization was shown to be very effective in neutralizing positive charging for $E_1^{\sigma}<E_0<E_2^{\sigma}$, but ineffective for neutralizing negative charging for $E_0>E_2^{\sigma}$. UV surface neutralization was found to be ineffective for discharging Kapton^{TM} for both positive and negative charging regimes, although the UV diode array seemed to have some effects of inducing a negative electron sample displacement current into the sample, perhaps due to UV radiation induced conductivity. The UV discharge method was ineffective for two reasons: first, the intensity of the UV source was significantly diminished when irradiated onto the sample through the closest chamber view port; second, the maximum energies of the mercury lamp and LED-array UV radiation sources were too low. It has been reported in the literature that photon energies >3.5 eV are needed to discharged insulator materials (Bass *et al*., 1998). However, as was shown in Section 3.5, the energy spectrum for our UV sources did not extend (significantly) above 3.5 eV. Clearly, more work needs to be conducted to establish an effective UV-source technique for discharging insulators. As described in Section 6.1.1, plans are underway to permanently mount a UV source into the detector apparatus. This will not only improve the UV flux intensity at the sample surface, but will also improve the reproducibility of insulator discharging since the detector apparatus will not need to be moved in order to irradiate the sample surface. Additionally, we will acquire UV sources that will possess energy spectra extending above 4 eV. Developing an effective UV neutralization source is essential to our efforts since this will allow us to measure accurate SE and BSE yields at incident energies $>E_2^{\sigma}$, where negative charging occurs. As demonstrated in Section 5.3.2, this will eliminate SE and BSE yield errors associated with the fast negative charging mechanism. Furthermore,

it will eliminate the less significant errors associated with the slow negative charging mechanism, where the growing negative surface potential decreases the landing energy of incident electrons, causing the total yields to increase slowly until a steady-state condition is reached, where the total yields are equal to unity (refer to Section 2.3.6 for further discussions of these charging mechanisms).

5.3.4 Pulsed Charging Rates

The evolution of total and BSE yields were studied as a function of both incident electron fluence and energy. This was done in a manner similar to the discharging studies described above in Section 5.3.3, where the electron yield and sample displacement current were monitored for repeated incident electron pulses. These measurements were performed both with and without electron flooding (for neutralization) between each incident pulse. These measurements were also performed in both positive and negative charging energy regimes, at incident energies ranging from 200 eV to 14000 eV. Data for total, BSE, and sample displacement currents are shown in Figs. 5.22 through 5.25, plotted against the cumulative incident charge [converted from incident pulse number as calculated from Eq. (2.44)]. In general, for $E_1^{\sigma}<E_0<E_2^{\sigma}$, the unflooded pulsed total yield and sample displacement current data approached their asymptotic values exponentially (near unity for total yields and 0 C for sample charge data) with repeated pulses. For $E_0>E_2^{\sigma}$, evolution of the unflooded versus flooded total yield data and sample displacement current were comparable. This was expected, since as explained in more detail in Section 2.3.6, total yields should approach their steady-state value rapidly for the positive charging regime, $E_1^{\sigma}<E_0<E_2^{\sigma}$, but very slowly for the negative charging regime, $E_0>E_2^{\sigma}$.

The pulsed yield and sample charge data were fitted using Eqs. (2.52) and (2.57), also shown in Figs. 5.22 to 5.25. When performing these fits, the steady-state values (unity for

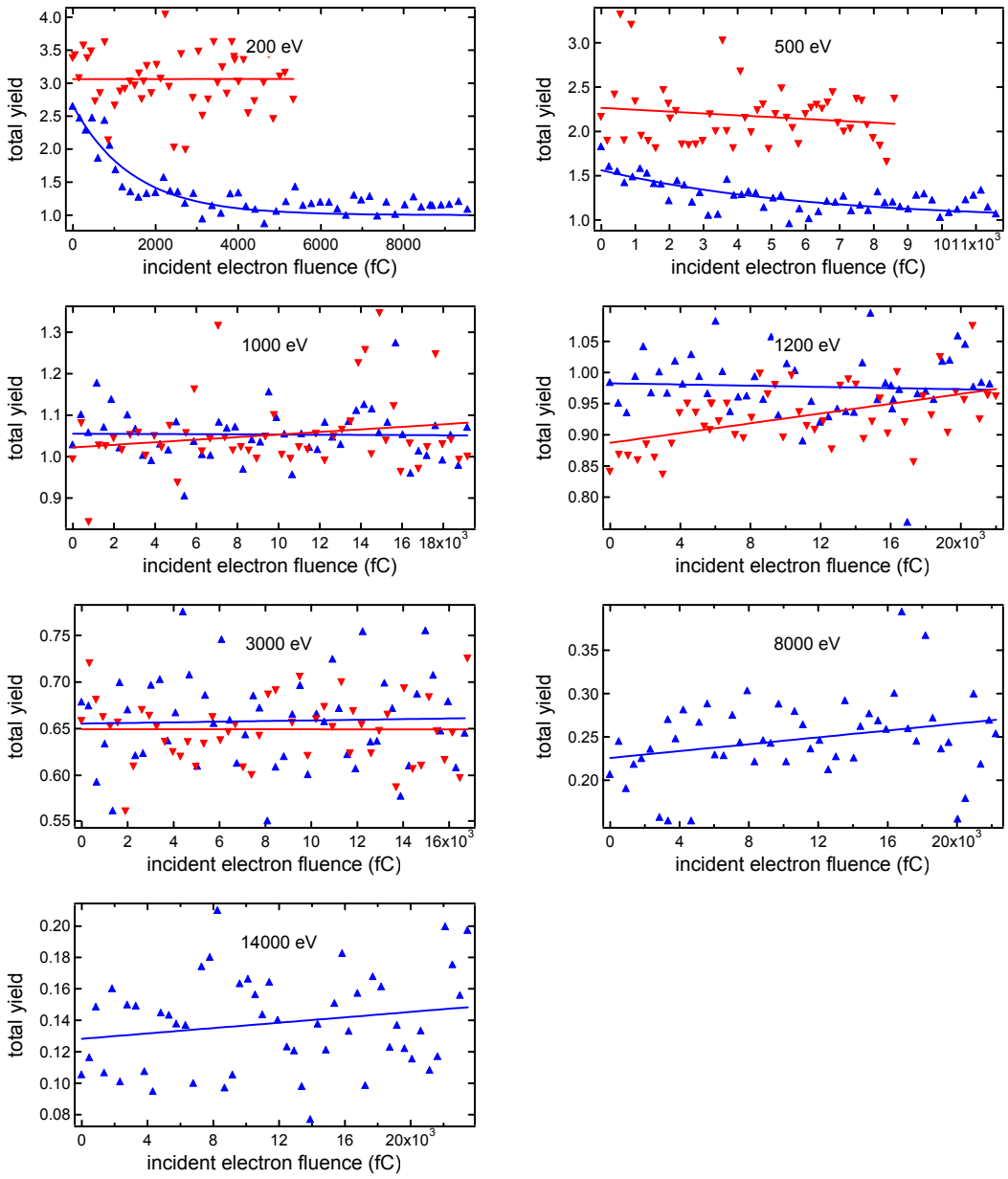

FIG. 5.22. Pulsed total yields as a function of cumulative incident electron charge at different incident beam energies for Kapton™ on aluminum. Data were taken both without flooding (▲) and with flooding (▼) between incident pulses. Linear and exponential fits were performed for all non-flooded data, while only linear fits were performed for flooded data (refer to Section 2.3.9 for fitting models). Flooding data was not taken for 8 and 14 keV data. Fit parameters are summarized in Table 5.13.

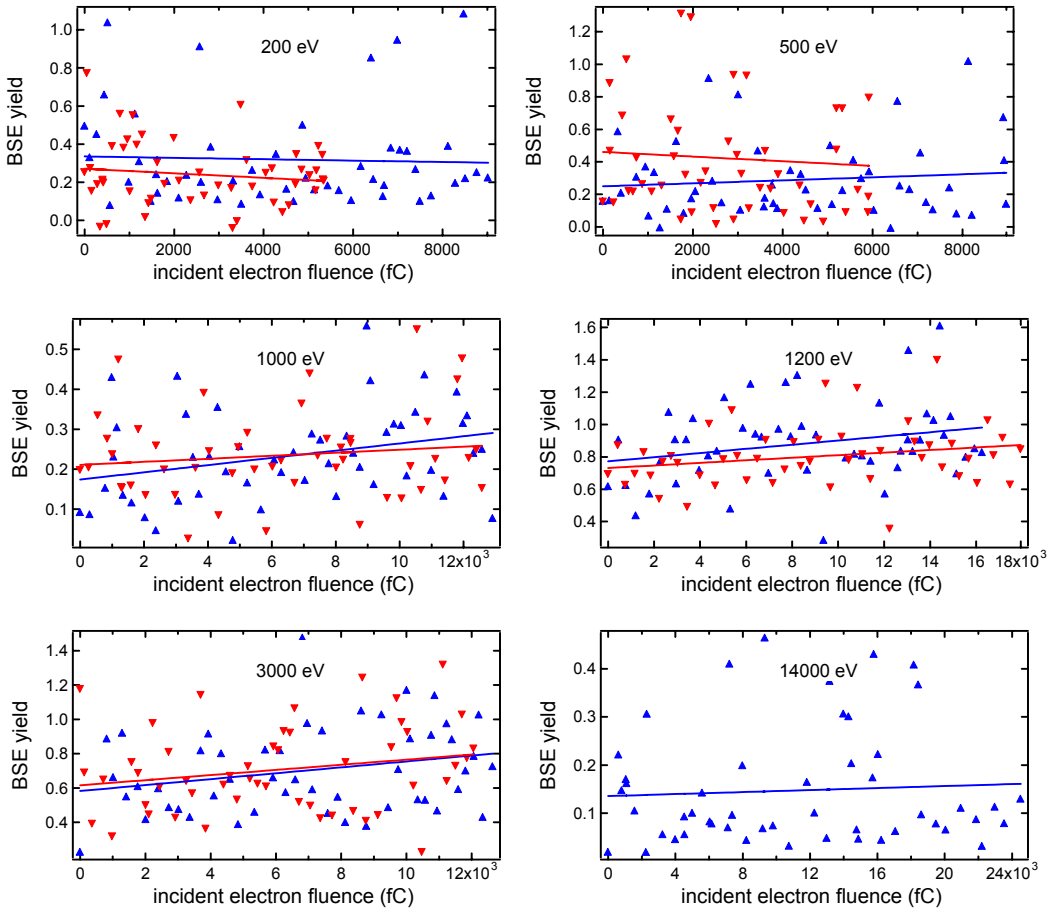

FIG. 5.23. Pulsed BSE yields as a function of cumulative incident electron charge at different incident beam energies for Kapton™ on aluminum. Data were taken both without flooding (▲) and with flooding (▼) between incident pulses. Linear fits were performed for all data. Flooding data was not taken for 14 keV data. Fit parameters are summarized in Table 5.14.

total yields and zero for sample charge) were fixed such that only the initial magnitude, σ_0, and exponential decay constant, α, were allowed to vary. By doing this, leakage currents associated with radiation-induced conductivity were assumed to be neglected (see Section 2.3.6). Additionally, linear fits were performed to the data since for $E_0>E_2^{\sigma}$, as well as for BSE yields, the samples approached steady state slowly, and linear slopes were sufficient to describe the evolution of yields and sample charge. Results from the exponential and linear

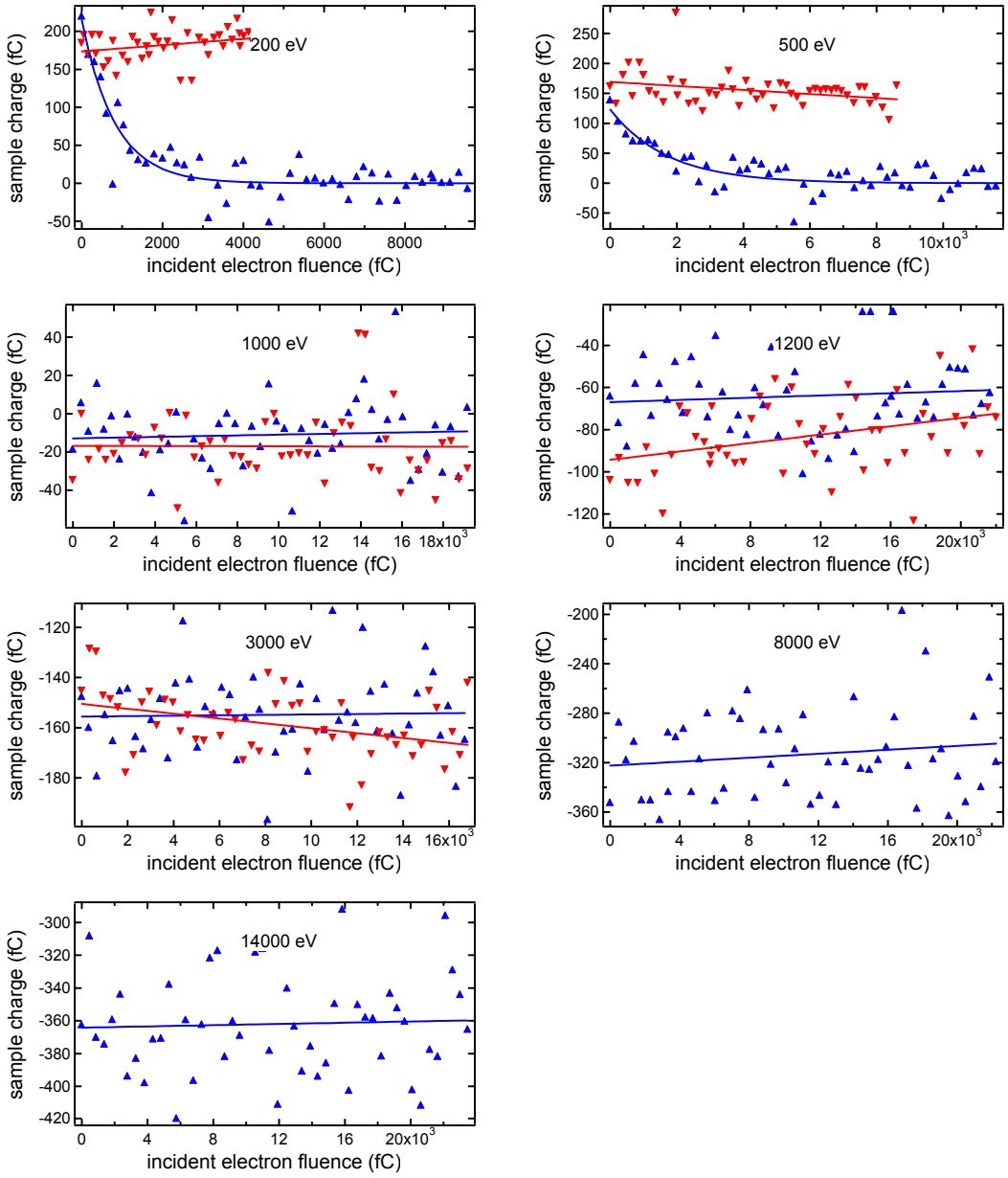

FIG. 5.24. Integrated sample displacement current taken from pulsed total yields as a function of cumulative incident electron charge at different incident beam energies for Kapton™ on aluminum. Data were taken both without flooding (▲) and with flooding (▼) between incident pulses. Linear and exponential fits were performed for all non-flooded data, while only linear fits were performed for flooded data (refer to Section 2.3.9 for fitting models). Flooding data was not taken for 8 and 14 keV data. Fit parameters are summarized in Table 5.15.

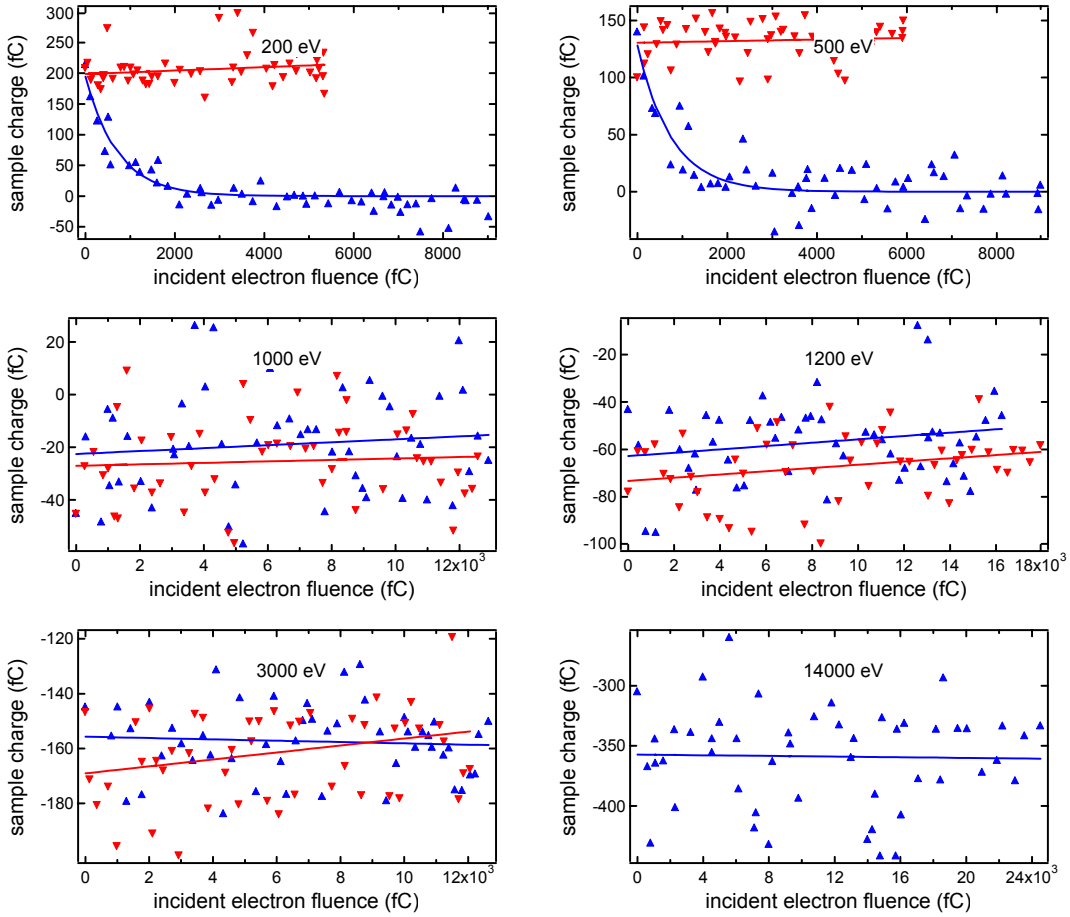

FIG. 5.25. Integrated sample displacement current taken from pulsed BSE yields as a function of cumulative incident electron charge at different incident beam energies for Kapton™ on aluminum. Data were taken both without flooding (▲) and with flooding (▼) between incident pulses. Linear and exponential fits were performed for all non-flooded data, while only linear fits were performed for flooded data (refer to Section 2.3.9 for fitting models). Flooding data was not taken for 14 keV data. Fit parameters are summarized in Table 5.16.

data fits are summarized in Tables 5.13 to 5.16.

From Figs. 5.22, 5.24, and 5.25, it can be seen for $E_1^{\sigma}<E_0<E_2^{\sigma}$, the total yield and integrated sample displacement current started at their positive uncharged values, and then decayed rapidly towards their steady-state values. As described by Eq. (2.31), and as demonstrated in Section 2.3.9, the decay was rapid since positive surface potentials quickly

TABLE 5.13. Pulsed-total yield fit parameters from Fig. 5.22. All non-flooded data were fit with linear and exponential functions (refer to Section 2.3.9 for fitting models). Flooded data for 8 keV and 14 keV yields were not measured.

Energy (eV)		Init. Yld.	Slope (fC^{-1})	Init. Yld.	Exponent (fC^{-1})
200	Flood	3.1±0.1	$(0.0\pm3.9)\cdot10^{-5}$	--	--
	No Flood	1.8±0.1	$(-9.6\pm1.6)\cdot10^{-5}$	2.7±0.1	$(6.9\pm0.8)\cdot10^{-4}$
500	Flood	2.3±0.1	$(-2.1\pm1.9)\cdot10^{-5}$	--	--
	No Flood	1.4±0.0	$(-3.1\pm0.6)\cdot10^{-5}$	1.6±0.1	$(1.7\pm0.2)\cdot10^{-4}$
1000	Flood	1.0±0.0	$(3.1\pm2.2)\cdot10^{-6}$	--	--
	No Flood	1.1±0.0	$(-0.2\pm1.6)\cdot10^{-6}$	1.1±0.0	$(0.4\pm2.9)\cdot10^{-5}$
1200	Flood	0.89±0.01	$(3.9\pm0.9)\cdot10^{-6}$	--	--
	No Flood	0.98±0.02	$(-0.5\pm1.2)\cdot10^{-6}$	0.98±0.01	$(-1.7\pm5.3)\cdot10^{-5}$
3000	Flood	0.65±0.01	$(0.0\pm1.0)\cdot10^{-6}$	--	--
	No Flood	0.66±0.01	$(0.3\pm1.4)\cdot10^{-6}$	0.66±0.01	$(1.0\pm4.1)\cdot10^{-6}$
8000	Flood	--	--	--	--
	No Flood	0.23±0.01	$(1.9\pm0.9)\cdot10^{-6}$	0.23±0.01	$(2.7\pm1.3)\cdot10^{-6}$
14000	Flood	--	--	--	--
	No Flood	0.13±0.01	$(8.6\pm6.2)\cdot10^{-7}$	0.13±0.01	$(9.9\pm7.2)\cdot10^{-7}$
14000	Flood	--	--	--	--
	No Flood	0.19±0.00	$(9.8\pm3.6)\cdot10^{-8}$	0.19±0.00	$(1.2\pm0.4)\cdot10^{-7}$

TABLE 5.14. Pulsed-BSE yield fit parameters from Fig. 5.23. All data were fit with linear functions. BSE yield data was not taken at 8 keV. Flooded BSE data for 14 keV yields was not measured.

Energy (eV)		Init. Yld.	Slope (fC^{-1})
200	Flood	0.27±0.03	$(-1.2\pm0.9)\cdot10^{-5}$
	No Flood	0.34±0.05	$(-3.7\pm9.5)\cdot10^{-6}$
500	Flood	0.46±0.07	$(-1.4\pm2.0)\cdot10^{-5}$
	No Flood	0.25±0.05	$(9.3\pm8.9)\cdot10^{-6}$
1000	Flood	0.21±0.02	$(3.8\pm2.9)\cdot10^{-6}$
	No Flood	0.17±0.02	$(9.0\pm2.9)\cdot10^{-6}$
1200	Flood	0.73±0.04	$(7.9\pm3.5)\cdot10^{-6}$
	No Flood	0.77±0.05	$(1.3\pm0.5)\cdot10^{-5}$
3000	Flood	0.62±0.05	$(1.5\pm0.7)\cdot10^{-5}$
	No Flood	0.58±0.05	$(1.7\pm0.7)\cdot10^{-5}$
14000	Flood	--	--
	No Flood	0.14±0.02	$(1.0\pm1.7)\cdot10^{-6}$

TABLE 5.15. Pulsed-sample displacement current fit parameters from total yields from Fig. 5.24. All non-flooded data were fit with linear and exponential functions (refer to Section 2.3.9 for fitting models). Flooded data for 8 keV and 14 keV sample current were not measured.

Energy (eV)		Init. Chrg. (fC)	Slope (unitless)	Init. Chrg. (fC)	Exponent (fC^{-1})
200	Flood	174±5	$(4.1\pm1.6)\cdot10^{-3}$	--	--
	No Flood	76±11	$(-1.0\pm0.2)\cdot10^{-2}$	215±17	$(1.2\pm0.2)\cdot10^{-3}$
500	Flood	169±7	$(-3.4\pm1.4)\cdot10^{-3}$	--	--
	No Flood	58±8	$(-6.2\pm1.1)\cdot10^{-3}$	123±13	$(5.8\pm0.9)\cdot10^{-4}$
1000	Flood	-17±5	$(-0.2\pm4.4)\cdot10^{-4}$	--	--
	No Flood	-13±5	$(1.9\pm4.6)\cdot10^{-4}$	-13±5	$(1.6\pm4.2)\cdot10^{-5}$
1200	Flood	-94±5	$(9.9\pm3.6)\cdot10^{-4}$	--	--
	No Flood	-67±5	$(2.6\pm4.1)\cdot10^{-4}$	-67±5	$(4.0\pm6.4)\cdot10^{-6}$
3000	Flood	-151±3	$(-9.7\pm3.4)\cdot10^{-4}$	--	--
	No Flood	-156±5	$(0.8\pm4.8)\cdot10^{-4}$	-156±5	$(0.5\pm3.1)\cdot10^{-6}$
8000	Flood	--	--	--	--
	No Flood	-322±10	$(7.9\pm7.7)\cdot10^{-4}$	-323±10	$(2.6\pm2.4)\cdot10^{-6}$
14000	Flood	--	--	--	--
	No Flood	-364±9	$(1.9\pm6.3)\cdot10^{-4}$	-364±9	$(0.5\pm1.7)\cdot10^{-6}$
14000	Flood	--	--	--	--
	No Flood	-1594±12	$(3.9\pm2.1)\cdot10^{-4}$	-1594±12	$(-2.4\pm1.3)\cdot10^{-7}$

TABLE 5.16. Pulsed-sample displacement current fit parameters from BSE yields from Fig. 5.25. All non-flooded data were fit with linear and exponential functions (refer to Section 2.3.9 for fitting models). BSE sample current data was not taken at 8 keV. Flooded data for 14 keV sample current was not measured.

Energy (eV)		Init. Chrg. (fC)	Slope (unitless)	Init. Chrg. (fC)	Exponent (fC^{-1})
200	Flood	199±7	$(2.8\pm2.2)\cdot10^{-3}$	--	--
	No Flood	72.4±9.7	$(-1.3\pm0.2)\cdot10^{-2}$	194±14	$(1.4\pm0.2)\cdot10^{-3}$
500	Flood	43±7	$(-6.6\pm1.4)\cdot10^{-3}$	--	--
	No Flood	130±4	$(0.7\pm1.2)\cdot10^{-3}$	128±13	$(1.3\pm0.2)\cdot10^{-3}$
1000	Flood	-27±4	$(2.8\pm5.8)\cdot10^{-4}$	--	--
	No Flood	-23±5	$(5.6\pm7.2)\cdot10^{-4}$	-23±6	$(3.3\pm3.8)\cdot10^{-5}$
1200	Flood	-73±4	$(6.8\pm3.6)\cdot10^{-4}$	--	--
	No Flood	-63±5	$(7.1\pm4.9)\cdot10^{-4}$	-63±5	$(1.3\pm0.9)\cdot10^{-5}$
3000	Flood	-169±5	$(1.3\pm0.7)\cdot10^{-3}$	--	--
	No Flood	-156±4	$(-2.4\pm5.1)\cdot10^{-4}$	-156±4	$(-1.6\pm3.2)\cdot10^{-6}$
14000	Flood	--	--	--	--
	No Flood	-357±11	$(1.4\pm8.3)\cdot10^{-4}$	-357±11	$(-0.4\pm2.3)\cdot10^{-6}$

screened out a significant portion of the SE spectrum. However, in this energy regime, when surface flooding was implemented between each incident pulse, these charging effects were significantly diminished such that the total yield and sample charge data did not change significantly with cumulative incident charge. It can be seen from Figs. 5.22 through 5.25, for the energy regime of $E_1^{\sigma}<E_0<E_2^{\sigma}$, steady-state charging was reached within 10 pC/mm^2 of incident charge. It can also be seen from Fig. 5.22 total yields near E_2^{σ} (E_0=1000 eV) did not change significantly with repeated pulsing for either the flooded or unflooded cases, and remained very close to unity. This occurred since little net charge accrued on the sample near E_2^{σ}, and the sample steady-state surface potential was close to 0 V.

For $E_0>E_2^{\sigma}$, in general, the unflooded total yield and sample displacement current slowly increased with cumulative incident charge towards steady state. The slow steady-state behavior for $E_0>E_2^{\sigma}$ resulted since the growing negative surface potentials diminished the landing energy of incident electrons. However, as explained in Section 2.3.6, in order to reach steady state, the surface potential needed to grow in magnitude such that the landing energy of the incident electrons was equal to E_2^{σ}. Depending on the incident energy, this would require a surface potential of several hundreds to thousands of volts. Finally, as can be seen from the figures and tables, in this energy regime, flooding had little or no effect on the measured data since, as explained above, negative surface potentials repelled flooding electrons away from the sample surface, rendering this technique inadequate for neutralization in the energy regime of $E_0>E_2^{\sigma}$.

As shown in Fig. 5.23, the behavior of BSE yields with consecutive pulse number was significantly different than total yield and sample displacement current data. In general, for both positive and negative charging regimes, the changes in BSE yields with repeated pulsing were small, and flooding and non-flooding data were similar. This occurred since, for

$E_1^{\sigma}<E_0<E_2^{\sigma}$, the positive surface potential needed to reach 50 V before BSE's would begin to be attracted back towards the insulator surface, but needed to rise to several hundreds of volts (up to E_0) before all BSE's were recaptured. Hence, in this energy regime, it was expected that BSE yields would decrease slowly with repeated pulsing. The unflooded data was inconclusive, showing a slight decrease in BSE yields for E_0=200 eV, and a slight increase for E_0=500 eV.

For $E_0>E_2^{\sigma}$, it was expected the measured BSE yields would at first rise somewhat rapidly as SE's were accelerated beyond 50 eV by the growing negative surface potential. This has been referred to as the fast negative charging mechanism in Section 2.3.6 and in Section 5.3.2, where SE's gained energy and contributed to the measured BSE yields until the BSE yield magnitudes became equal to the measured total yield, where all escaping electrons exhibited energies >50 eV. This effect was also observed in the measured yields for E_0>1 keV, as shown in Fig. 5.15. After proceeding through this charging mechanism, the BSE yields were expected to increase along with the total yields at a much slower rate (referred to as the slow negative charging mechanism in Section 2.3.6) as the growing negative surface potentials decelerated incident electrons until the landing energies were close to E_2^{σ}, where the steady-state condition would be achieved. As shown in Fig. 5.23, the charging trends for BSE yield data for $E_0>E_2^{\sigma}$ (1.2 keV, 3 keV, and 14 keV data) were consistent with the slow charging mechanism behavior, showing a consistent (but slow) increased in BSE yields with consecutive pulses. Flooded and unflooded data were similar for 1.2 keV and 3 keV data since the flood gun was not effective for neutralizing negative surface charging. Furthermore, for $E_0>E_2^{\sigma}$, the magnitudes of the BSE yields were abnormally high (comparable to the total yield values as shown in Figs. 5.23 and 5.15), lending further evidence that the sample had already transitioned through the fast negative charging mechanism (from previous electron

irradiation), and the increase in BSE yields shown in Fig. 5.23 was attributed to the slow negative charging mechanism.

It must be noted, although pronounced charging effects were absent for BSE yields, they were still present in the BSE sample charge data as shown in Fig. 5.25, particularly for $E_1^{\sigma}<E_0<E_2^{\sigma}$. This occurred since the inner detector grid completely shielded the emitted electrons from the retarding potentials (in this case -50 V) of the suppression grid. Hence, the energy dependent decay constants summarized in Tables 5.13, 5.15, and 5.16 were generally in agreement, to within an order of magnitude, regardless of whether they were taken from total yield, total-yield sample displacement current, or BSE sample displacement current data. The consistency of the decay constant between total yield and sample displacement current fits was also in agreement with the models presented in Section 2.3.9, where it was shown the same charge decay constant governs both total electron yield and sample displacement current charge-decay curves.

It was noticed the fitted decay constants, provided in Tables 5.13, 5.15, and 5.16, displayed a dependence on incident energy. To test this relationship, the total yield and total-yield sample displacement decay constants (from Tables 5.13 and 5.15) were averaged, and plotted as a function of energy as shown in Fig. 5.26. These averaged decay constants are also summarized in Table 5.17. From Fig. 5.26, it can be seen the decay constants for $E_1^{\sigma}<E_0<E_2^{\sigma}$ decreased with increasing energy, and approached a value close to zero near E_2^{σ}. Furthermore, the decay constant at E_0=1200 eV was incredibly noisy and negative (nonphysical) since near E_2^{σ}, the accuracy of the calculated total yields (and hence the fitted decay parameters) decreased due to small measured sample displacement and collector signals. However, for other energies in the range of $E_0>E_2^{\sigma}$, the decay constant remained small and positive. The details of the functional relationship of $\alpha(E_0)$ and E_0 were not known,

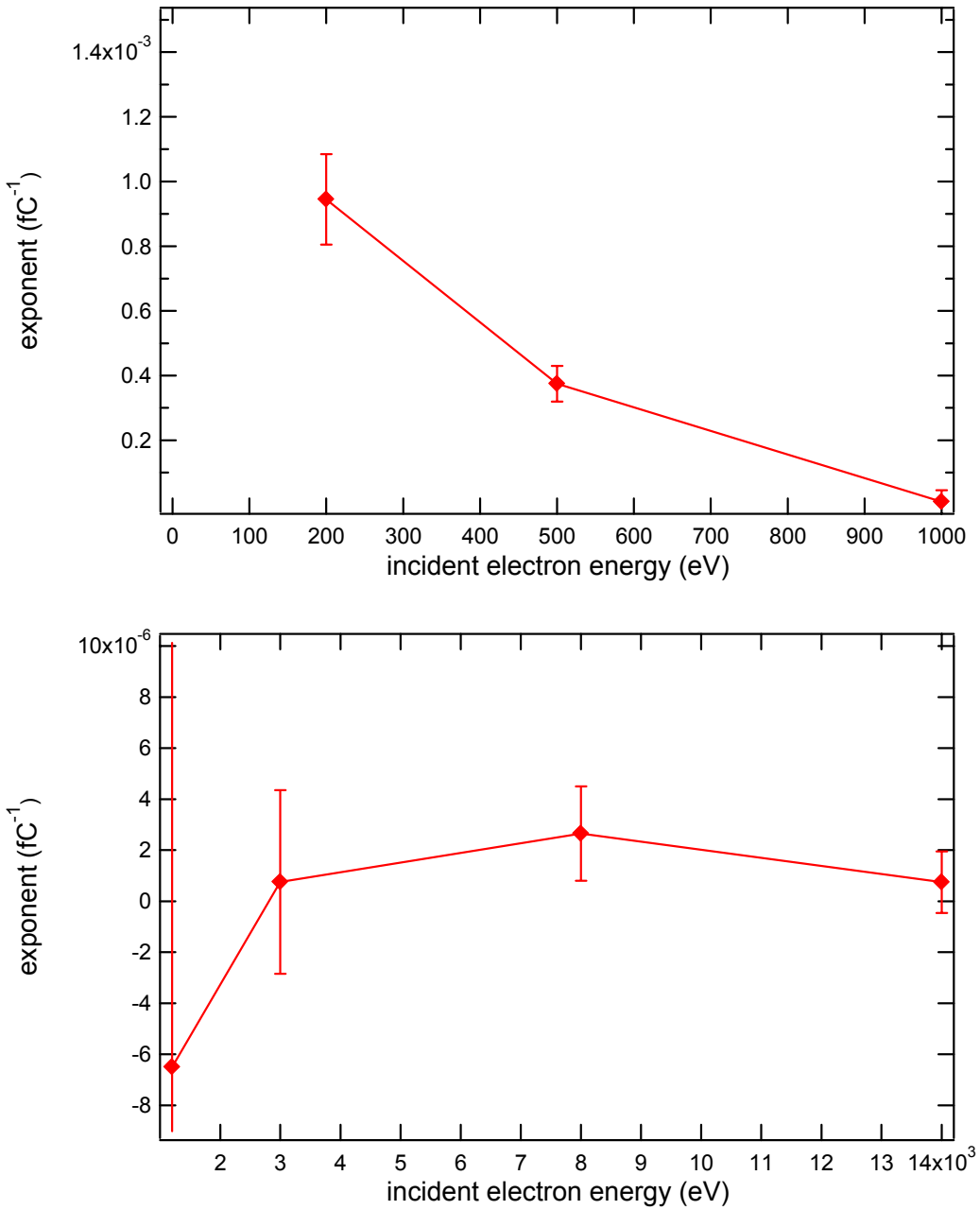

FIG. 5.26. Total yield and sample charge decay constant plotted as a function of beam energy. The decay constants were averaged from Tables 5.13 and 5.15, and fitted errors were combined (error bars). The decay constant magnitude underwent a large transition near E_2^{σ} such that two graphs (one before and one after E_2^{σ}) were used to demonstrate the energy dependence. (Top) The decay before E_2^{σ} decreased with increasing energy, and approached zero near E_2^{σ}. (Bottom) after E_2^{σ}, the decay constant grew once again, but remained small and slightly positive.

TABLE 5.17. Summary of fitted charge decay parameters for different incident energies. Tabulated are the averaged fitted charge decay parameters, α (plotted in Fig. 5.26), and the calculated incident charge densities required to bring the insulator total yields to within 20 percent of their steady state values. Also shown are the mean incident charge per pulse, Q_0, and the mean incident current peak per pulse, $\bar{I}_0$, for the total yield decay curve, and the associated DC time constants, ξ, for the peak currents.

Energy (eV)	α (fC^{-1})	Q_{0N}/A_0 (pC/mm^2)	Q_0 (fC)	$\bar{I}_0$ (nA)	ξ (s)
200	$(9.5\pm1.4)\cdot10^{-4}$	2.3±0.4	196±5	39±1	$(2.7\pm0.4)\cdot10^{-5}$
500	$(3.8\pm0.6)\cdot10^{-4}$	2.9±0.5	237±3	47±1	$(5.6\pm1.9)\cdot10^{-5}$
1000	$(1.0\pm3.6)\cdot10^{-5}$	--	391±4	78±1	$(1.3\pm1.0)\cdot10^{-3}$
1200	$(-0.6\pm2.9)\cdot10^{-5}$	--	443±15	89±3	--
3000	$(0.7\pm3.6)\cdot10^{-6}$	710±590	341±4	68±1	$(2.0\pm1.7)\cdot10^{-2}$
8000	$(2.7\pm1.9)\cdot10^{-6}$	500±310	454±11	91±2	$(4.1\pm1.8)\cdot10^{-3}$
14000	$(0.7\pm1.2)\cdot10^{-6}$	2000±1200	480±5	96±1	$(1.4\pm0.9)\cdot10^{-2}$

but qualitative trends were consistent with arguments made in Section 2.3.6 through 2.3.8. Specifically, $\alpha(E_0)$ (or the charging rate) decreased as E_0 increased for $E_1^{\sigma}<E_0<E_2^{\sigma}$ since SE's were excited further into the material, thus making it harder for SE's to escape. This both decreased the total yield values beyond E_{max}^{σ}, and also decreased the charging rate as E_0 approached E_2^{σ}. At E_2^{σ}, the charging rate was expected to be small, since at this incident energy, the sample had arrived at a steady-state condition with the surface potential being close to 0 V. Finally, for $E_0>E_2^{\sigma}$, the charging rate was driven by the slow negative charging mechanism (as explained above, the sample had already progressed through the fast mechanism), and the steady-state condition was driven by the deceleration of incident electrons by rising negative sample potentials, and the slow creep of the total yields towards unity as the incident electron landing energies continued to decrease (refer to Section 2.3.6). Furthermore, the charge decay rate leveled off for $E_0>E_2^{\sigma}$ to a more-or-less constant value (for E_0=3-14 keV) since the electron emission properties no longer changed significantly as a function of incident energy (refer to Fig. 5.16).

Using the averaged charge decay constants shown in Fig. 5.26, the cumulative incident charge fluence required to bring the insulator to a steady-state condition for the energy regime of $E_1^{\sigma}<E_0<E_2^{\sigma}$. This was done by calculating the cumulative charge required to bring the total yields to within 20 percent (σ=1.2) of their equilibrium values (σ=1) using Eq. (2.52). An arbitrary threshold (in this case, 20 percent) was chosen since the total yields exponentially approached their steady-state conditions at an ever decreasing rate. The cumulative charge was then converted to a measure of charge density by simply dividing by the approximate beam spot area of 1 mm^2. These values are also provided in Table 5.17, along with error estimates taken from the charge decay constant errors. Incidentally, the beam spot area did not stay entirely constant as a function of incident energy (it could have varied by as much as a factor of 4), and hence may have added an undetermined amount of error to these estimates. As a part of the proposed future work in Section 6.1.2, it is suggested a full beam-spot characterization be performed as a function of incident energy to improve the accuracy of the charge density calculations.

From this data, it can be seen for $E_1^{\sigma}<E_0<E_2^{\sigma}$, a steady-state condition was achieved very rapidly, within 2.3 pC/mm^2 and 2.9 pC/mm^2 for E_0=200 eV and 500 eV, respectively. For E_0=1000 eV and 1200 eV, no solutions existed for the calculated steady-state charge. This was the case since E_0 was already very close to E_2^{σ}, and the total yields were already within 20 percent of their steady-state values. These calculated cumulative charge values for E_0=200 eV and 500 eV were consistent with the charge decay plots shown in Figs. 5.22 and 5.24. Unfortunately, similar experimental data for the steady-state incident charge for $E_1^{\sigma}<E_0<E_2^{\sigma}$ does not exist in the literature for comparison. The closest comparisons come from simulations performed by Meyza *et al.* (2003) for anodized aluminum, where the steady-state conditions at E_0=1000 eV (this value was well below E_2^{σ} in their simulations) were achieved

after ~10^{-13} C/mm^2 (within an order of magnitude of our measurements). The discrepancies between our experimental results and the simulation results may be attributed to insulator material differences (a metal oxide versus polymer).

As was done with the positive charging data above, for $E_0>E_2^{\sigma}$, the charge decay constants from Table 5.17 were used to perform exponential fits to the cumulative charge required to bring the total yields to within 20 percent (σ=0.8) of their steady-state values. These calculations were also performed using Eq. (2.52) from Section 2.3.9, and provided estimates for the incident charge required to bring the sample to a steady-state condition for the slow negative charging mechanism. From the fits, it was found the steady-state conditions were reached after 0.7±0.6 nC, 0.5±0.3 nC, and 2.0±1.2 nC for 3 keV, 8 keV, and 14 keV, respectively. Since the beam spot area was ~1 mm^2, this equated to incident charge densities of 0.7±0.6 nC/mm^2, 0.5±0.3 nC/mm^2, and 2.0±1.2 nC/mm^2. It should be mentioned the errors for the steady-state charge values were quite large since the extrapolation to steady-state condition was performed using a very small portion of the overall charge decay data. Still, these results were consistent with other experimental studies reported by Song *et al.* (1996), as well as simulations conducted by Meyza *et al.* (2003) and Kotera and Suga (1988) in the energy regime of $E_0>E_2^{\sigma}$. For example, Song *et al.* (1996) reported steady-state conditions on PMMA polymer after irradiating with 0.2-0.7 nC of incident charge in the energy range of 5-20 keV (irradiation was with a DC electron source at 10^{-11} A). Meyza *et al.* (2003) calculated a steady-state condition at 30 keV that occurred after 3 nC/mm^2 of incident charge on alumina. Finally, Kotera and Suga (1988) calculated steady-state conditions on PMMA polymer after irradiating with 0.1-4 nC of incident charge at 20 keV. Hence, although charge decay data for Kapton^{TM} did not exist in the literature, our data was in good agreement with experimental data and simulations found on other insulator materials in this energy regime.

In order that the pulsed charge decay studies of this dissertation could be compared more easily to DC charging studies reported in the literature (only a few experimental DC charging studies exist, and all are for $E_0>E_2^{\sigma}$), the charge decay constants reported in Table 5.17 were converted to corresponding charge time constants, ξ. This was done by methods developed in Section 2.3.9, by first calculating the mean charge per incident pulse, and then the mean peak current per pulse using Eqs. (2.46) and (2.47). Then, the charge-decay time constants, ξ, corresponding to the mean incident current pulses were calculated using Eq. (2.60). Results for these calculations are also summarized in Table 5.17. Referring to Table 5.17, an interpretation of these results goes as follows: at E_0=200 eV, using an incident DC current of I_0=39 nA (current density of ~39 nA/mm^2), the insulator sample would be within 37 percent (37 percent comes by setting $t=\xi$ in the exponential function) of its steady-state yield condition at t=27 μs. Likewise, at E_0=14000 eV at 96 nA, the sample yield would be within 37 percent of their steady-state values at t=14 ms.

It must be mentioned, caution should be taken in applying the time constant, ξ, to DC results reported in the literature, since, as can be seen from Eq. (2.60), its value not only depends on incident energy, but also depends on the value chosen for the incident current. However, the charge-decay constant, α, is not dependent on the incident current (or incident charge). Hence, in comparing pulsed-charge decay results to DC-current decay results in the literature, a new time constant must be calculated for each incident DC-current being compared. An example is given as follows: Song *et al*. (1996) reported a PMMA sample irradiated at I_0=10 pA at E_0=15 keV (other Kapton^{TM} data does not exist in the literature) arrived at a steady-state potential within ~50 s. In order to compare our pulsed charge decay results for Kapton^{TM} to these DC-current measurements, our measured charge decay constant for 14 keV (taken from Table 5.17 as $0.7\cdot10^{-6}$ fC^{-1}) was used to calculate a corresponding

charge-decay time constant at I_0=10 pA using Eq. (2.60). This calculation yielded a value ξ=143 s, in agreement with the reported result for PMMA to within a factor of three.

Using the decay constants from Fig. 5.26, along with the fitted total and BSE yield parameters from Tables 5.13 and 5.14, the evolving positive surface potentials were calculated as a function of incident electron fluence for the energy regime $E_1^{\sigma}<E_0<E_2^{\sigma}$, as shown in Fig. 5.27. These calculations were made by first calculating the evolving SE yields from the fitted evolving total and BSE yields for unflooded data at E_0=200 eV, 500 eV, and 1000 eV (refer to Figs. 5.22 and 5.23), as shown in the top graph of Fig. 5.27. Then, the positive surface potentials as a function of incident electron fluence were calculated using Eq. (2.61) from Section 2.3.9. From the top graph in Fig. 5.26, it can be seen the initial SE yields decreased with increasing incident energy, consistent with the SE yield curve data of Fig. 5.15. However, the values of the steady-state SE yields increased with increased incident energies since the steady-state surface potentials were lower for higher incident energies (near E_2^{σ}), thus allowing more SE's to escape. From the bottom graph in Fig. 5.27, it can be seen the steady-state positive potentials for 200 eV, 500 eV, and 1000 eV approached 6.6 V, 3.3 V, and 0.3 V, respectively. The steady-state surface potentials for E_0=200 eV were higher than for 500 eV and 1000 eV since the initial total yields were higher; hence, the sample gave up more electron charge with continued incident pulsing. Furthermore, the surface potential at 1000 eV should be close to 0 V since the incident energy was very close to E_2^{σ} (refer to Table 5.12).

For $E_0>E_2^{\sigma}$, it has already been explained the sample had transitioned through the fast negative charging mechanism. Hence, the fast negative charging mechanism could not be analyzed using Eq. (2.62) and the arguments laid out in Section 2.3.9, as was done for the positive charging mechanism (as discussed in Section 6.2, this could be a subject of future investigation at USU). However, surface potential analysis was performed on data for $E_0>E_2^{\sigma}$

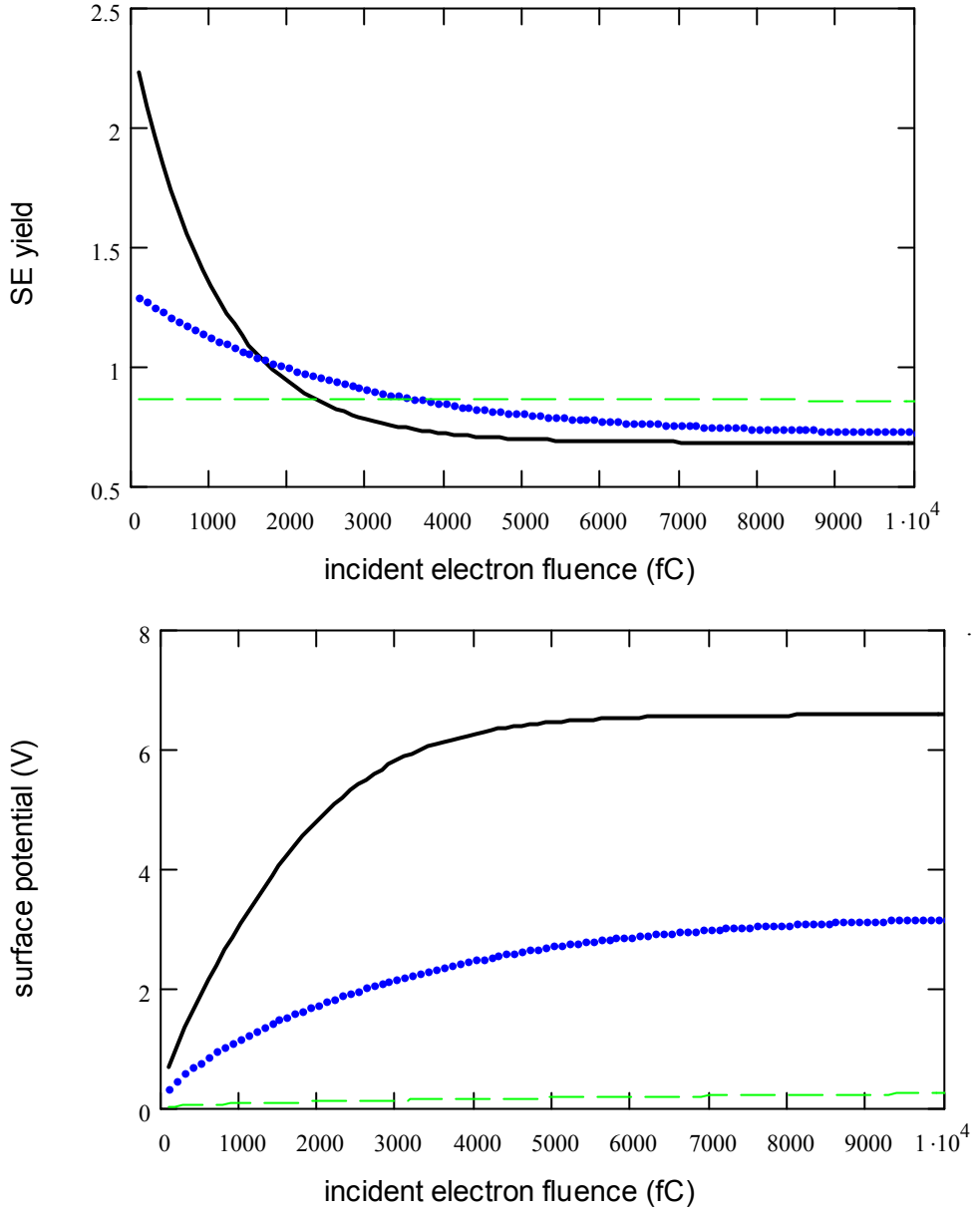

FIG. 5.27. Evolving SE yields (top) and positive surface potentials (bottom) for E_0=200 eV (solid line), 500 eV (dot), and 1000 eV (dash). SE yields were calculated from fitted total and BSE yields shown in Figs. 5.22 and 5.23. Evolving positive surface potentials were calculated using Eq. (2.61) from Section 2.3.9.

using the slow negative charging mechanism (refer to Section 2.3.6). To do this, the evolving negative surface potentials were evaluated using a technique set forth by Reimer (1985) using Eq. (2.34). As the sample continued to charge negatively, the magnitude of the negative surface potential continued to increase, thus decelerating incident electrons and decreasing their landing energy, E_L. This decrease in landing energy caused the total yields to increase with continued pulsing as shown in Fig. 5.22 for 3-14 keV. Hence, changes in the landing energy could be ascertained indirectly by monitoring the rise in the total yield values with continued electron pulsing. This was done by tracing the rise in the total yields (obtained from the slopes of the charge decay data from Table 5.13 for 3-14 keV) along the total yield curve of Fig. 5.16 to determine the corresponding incident electron landing energies. Once the landing energies were obtained, the surface potential was calculated using Eq. (2.34). From these calculations, the change in the surface potential was calculated to be on the order of V_s=0 kV, 2 kV, and 3 kV for E_0=3 keV, 8 keV, and 14 keV, respectively. However, it quickly became apparent these surface potential estimates were quite inaccurate, and the inaccuracies stemmed from inherent flaws of the method. For example, it can be seen from the yield curve of Fig. 5.16, the accuracy of the total yield values (obtained from Fig. 5.22) must be quite good to obtain accurate estimates for the incident electron landing energies since the slope of the total yield curve is so shallow in this energy regime. Very small changes in the total yield will equate to very large changes in the corresponding calculated landing energies. For example, a quick calculation from the total yield curve of Fig. 5.16 revealed at incident energies >10 eV, variations of the total yield on the order of 5 percent (on the order of our measurement uncertainty) would translate to changes in the landing energy by 1 keV. Hence, unless the accuracy of our total yield measurements can be reduced to within just a couple percent, other methods (such as the mirror method approach or a surface potential probe as

discussed in Sections 4.5 and 4.6) may be better suited for determining the high negative surface potentials resulting from the slow negative charging mechanism in the energy regime of $E_0>E_2^{\sigma}$.

5.3.5 Steady-State Total Yield Behavior

As mentioned in Section 5.3.1, once all pulsed yields had been measured on the Kapton^{TM} sample, the electron gun was turned to continuous emission mode, and the evolution of the steady-state total yields were monitored as a function of total incident electron fluence and energy. In making these measurements, the incident beam current varied between 20-40 nA (depending on the beam energy). The sample was irradiated for up to 30 minutes (cumulative incident charge densities ranged from 10-60 $\mu C/mm^2$) for each incident energy, and the total yields were plotted as a function of total incident electron charge (incident current multiplied by irradiation time) as shown in Fig. 5.28. For $E_1^{\sigma}<E_0<E_2^{\sigma}$, no clear dependence existed between the total yields and incident charge. However, for $E_0>E_2^{\sigma}$, total yields consistently decreased (slowly) with continued incident electron irradiation. The rate of decrease was only between 1-4 percent over 30-60 μC of incident charge, but the trend was very consistent for each steady-state yield set taken beyond E_2^{σ}. From the data, it did not appear the slope magnitudes depended on incident energy, but the initial magnitudes of the steady-state yields did. This data was consistent with predictions from Cazaux (1999) that steady-state yields should decrease with continued incident electron irradiation due to additional defects and electron trapping that are created by the incident beam (see Section 2.3.6). Furthermore, Liehr *et al*. (1986) reported similar decreases in electron yield parameters with continued electron irradiation on Polyethylene, finding a decrease in E_2^{σ} by 26 percent after irradiating with 20 mC of incident charge. Clearly, this behavior warrants further investigation, and, as discussed in Section 6.2.3, will studied in the future at USU.

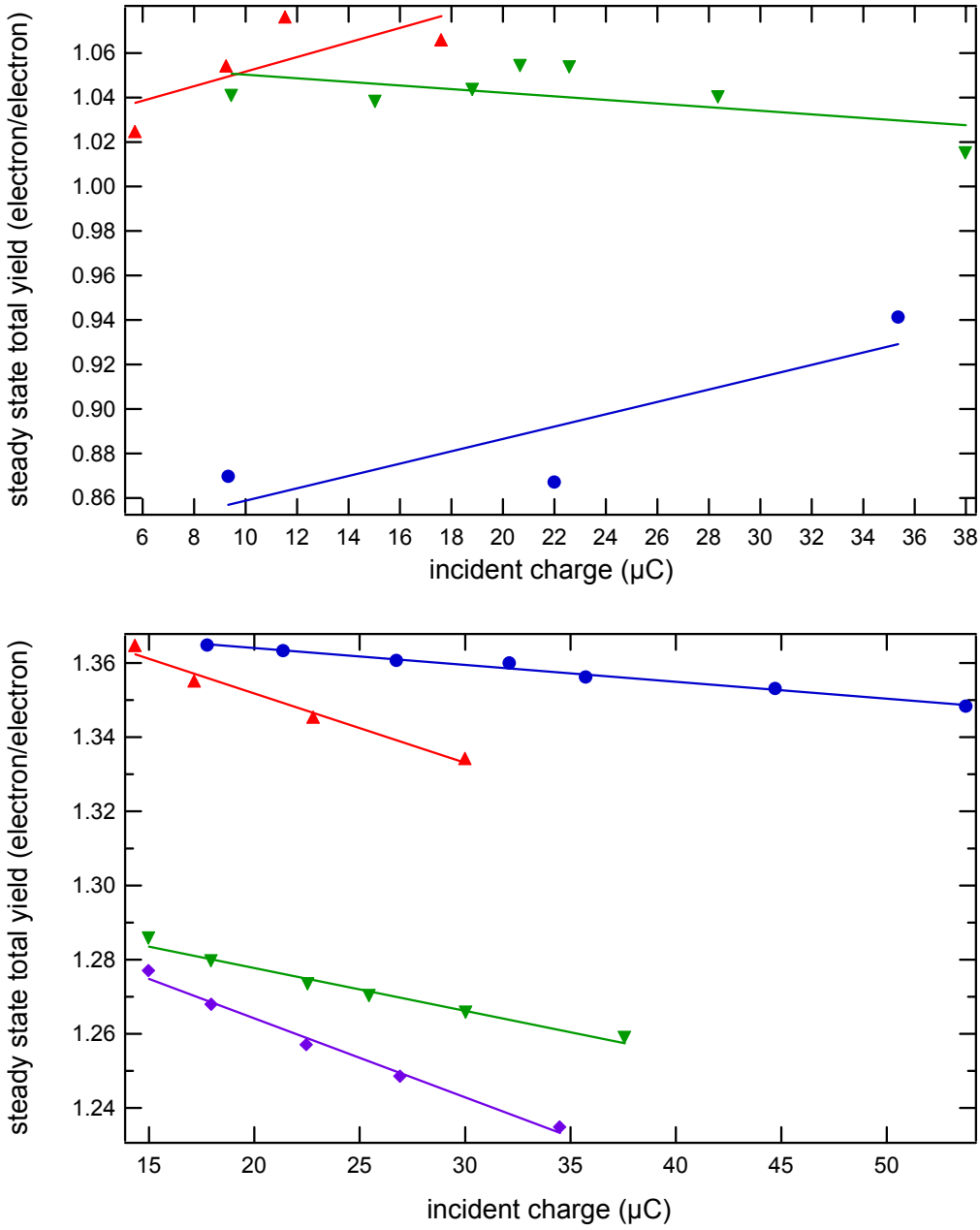

FIG. 5.28. Dependence of evolving steady-state total yields with incident energy and electron fluence. (Top) Steady-state yields below E_2^{σ} for E_0=200 eV (●), 500 eV (▲), and 600 eV (▼). (Bottom) Steady-state yields above E_2^{σ} for E_0=1200 eV (●), 1500 eV (▲), 1700 eV (▼), and 1800 eV (♦). For $E_1^{\sigma}<E_0<E_2^{\sigma}$ the initial yield, as well as the slopes, showed no clear trends with incident energy. For $E_0>E_2^{\sigma}$, the initial yield values displayed a dependence on incident energy (decreasing with increasing energy), and yields continued to decrease with continued electron beam irradiation.

5.4 Summarization of Insulator Yield Results

In this section, a summary of the total and SE yields measured in this dissertation work are compared with those found on similar materials in the literature. In scanning the literature, it was found no other total yield data existed for Al2219 aluminum oxide and RTV-silicone as shown in Tables 5.18 and 5.19). However, both total and SE yield data was available for Kapton^{TM}-aluminum in the literature as shown in Table 5.20. Hence, for Al2219 and for RTV-silicone samples, materials similar in chemical composition were chosen for comparison. For example, for Al2219, data was gathered for Al6061, ceramic, alumina, and sapphire (refer to Table 5.18). For RTV-silicone, the most similar material found was DC-704 silicone-based diffusion pump oil made by Dow Corning (refer to Table 5.19).

From the literature, it was found for anodized Al2219, that our values for E_{max} and E_2^{σ} were less than those reported in the literature by more than a factor of three, while σ_{max} values were comparable (refer to Table 5.18). From these comparisons, it was concluded even though the materials found in the literature had similar chemical compositions, wide variations existed in electron yield parameters due to differences in chemical bonding structure. Total yield data for the RTV-silicone and diffusion pump oil was surprisingly similar to that of silicone-based diffusion pump oil as shown in Table 5.19. Our values for all parameters (σ_{max}, E_{max} and E_2^{σ}) were slightly higher than those reported for diffusion pump oil.

From Table 5.20, it can be seen our results for Kapton^{TM} were found to be more in agreement with those reported in the literature. However, our values for σ_{max}, E_2^{σ}, δ_{max}, and E_2^{δ} were higher than the values reported in other studies. Our data was most consistent with data reported by Levy *et al.* (1985), where values for σ_{max}, E_{max}^{σ}, and E_2^{σ} agreed to within 15 percent, 0.5 percent, and 24 percent, respectively. For Kapton^{TM}, SE yield data was only

TABLE 5.18. A summary of experimental electron yield parameters for Al2219 anodized aluminum. For this study, fitted parameters were taken from the Variable N model over the energy range of 100-1200 eV for better fitting accuracy. The fitted power coefficient, n, was 1.58.

Researcher	Materials Details	σ_{max}	E_{max}^{σ} (eV)	E_1^{σ} (eV)	E_2^{σ} (eV)	δ_{max}	E_{max}^{δ} (eV)	E_1^{δ} (eV)	E_2^{δ} (eV)
Krainsky *et al*., 1981	Anodized 6061-as received	--	--	--	--	3.00	679	59	--
Wong et al., 1997	"ceramic" sapphire	--	--	--	6200	--	--	--	--
Seiler, 1967	alumina	2.6-4.7	600	--	--	--	--	--	--
This Study	1 μm chomic acid anodized Al2219	3.1	198	32	1440	--	--	--	--

TABLE 5.19. A summary of experimental electron yield parameters for RTV-silicone samples. Literature data was for Dow Corning DC-704 diffusion pump oil. For this study, fitted parameters were taken from the Variable N model fits provided in Section 5.2.

Researcher	Materials Details	σ_{max}	E_{max}^{σ} (eV)	E_1^{σ} (eV)	E_2^{σ} (eV)	δ_{max}	E_{max}^{δ} (eV)	E_1^{δ} (eV)	E_2^{δ} (eV)
(Ishikawa and Goto, 1967)	DC-704 D.P.O.	2.0	200	--	900-1000	--	--	--	--
This Study	CV-1147	2.6	253	41	1487	--	--	--	--
This Study	DC93-500	2.2	338	91	1060	--	--	--	--

TABLE 5.20. A summary of experimental electron yield parameters for Kapton™. For this study, Variable N fitted parameters were taken from the first yield data sequence from Section 5.3.2.

Researcher	Materials Details	σ_{max}	E_{max}^{σ} (eV)	E_1^{σ} (eV)	E_2^{σ} (eV)	δ_{max}	E_{max}^{δ} (eV)	E_1^{δ} (eV)	E_2^{δ} (eV)
Willis and Skinner, 1973	10-80 μm (substrate not given)	2.1	150	30	500	--	--	--	--
Levy *et al*., 1985	50 μm (substrate not given)	2.2	~200	--	~825	--	--	--	--
Krainsky *et al*., 1981	50 μm on Al	1.75	212	67	738	1.62	222	75	651
Kishimoto *et al*., 1990	"few" μm on Al	1.49	180	--	--	--	--	--	--
Yong *et al*., 1998	2 μm (substrate not given)	--	--	--	--	--	--	--	~600
This Study	10 μm on Al	2.6	199	--	1086	2.4	228	--	861

reported in one other study (Krainsky *et al*., 1981). In comparison to this study, our estimates for δ_{max}, E_{max}^{δ}, and E_2^{δ} were found to be higher by 33 percent, 3 percent, and 24 percent, respectively.

CHAPTER 6

PROPOSED FUTURE WORK

A summary of proposed future work is outlined in this chapter, and can be broken into two main sections. Section 6.1 is composed of three subsections that list upgrades to the pulsed-yield instrumentation and measurement setup, which will offer increased accuracy and speed to the present pulsed-yield data acquisitioning process, and will also expand electron yield measurement capabilities. Section 6.2 is composed of three subsections that list future measurements of new insulator materials, a continuation of measurements and techniques explored in this dissertation, and measurements and analysis aimed at exploring the internal charge distributions that result from electron irradiation. These proposed studies follow from the experimental work of this dissertation and will progress the understanding of insulator charging and electron emissions. It should be noted, some of the ideas presented in this chapter originated from enlightening discussions that took place with J.R. Dennison and Vladimir Zavyalov, and are included here to serve as a more complete compilation for future efforts.

6.1 Instrumentation and Computer Upgrades

6.1.1 Detector-Apparatus Upgrades

A prioritized list (highest to lowest priority) of instrumentation upgrades related to the detector apparatus and sample/stage assembly include:

1. *Widening the detector aperture*: the present detector aperture is 0.5 cm in diameter. Optimization of the incident beam onto the sample is critical for accurate electron yield measurements (Nickles, 2002). Presently, there are difficulties related to directing the electron gun through the small aperture tube, which can result in

systematic errors in electron yield measurements, particularly for insulators. For example, with conductors, optimization can be performed by maximizing the amplitudes of sample and collector currents (while minimizing the stage current) by moving the sample stage and detector apparatus with the electron beam in continuous-emission mode. This requires the irradiation of samples for several seconds. However, for insulators this same optimization procedure cannot be used since charging occurs very quickly (see Sections 5.1 to 5.3). Instead, for insulators, the electron gun and detector aperture have to be first visually aligned, and then several incident pulses are used to optimize the electron beam through the aperture tube (see Section 4.1). This often requires several incident pulses before the collector current pulse is maximized, and in this time, the insulator material undergoes charging. Although the flood gun can be used to then neutralize the insulator, the sample has already undergone charging that could subsequently alter electron yields. Widening the aperture of the detector to 0.7 cm dia. would loosen the tolerances for angular and translational sample stage settings, making the beam alignment easier for both DC and pulsed measurements. Current losses through the widened aperture would remain minimal, and could be corrected for by determining the corresponding correction factors (see Section 4.3, Section 6.2.2, and Nickles, 2002).

2. *Modification of detector apparatus to electrically isolate the inner grid from the stage*: presently, the inner grid (sitting between the suppression grid and sample) is electrically tied to the sample stage assembly via the detector housing. Consequently, the DC-spectral method for determining positive sample potentials was limited in its effectiveness (see Section 4.5) since the inner grid screened out the positive suppression grid potentials required to pull SE's from the positively charged sample

surface. An improvement to the present detector design would be to electrically isolate the inner grid inside the detector housing such that it could be biased independent of the suppression grid or stage assembly. The electrical insulation between the inner grid and sample stage assembly should be sufficient to withstand electrical potentials >1000 V to accommodate for future electron energy spectrum studies. This alteration would also offer a more accurate method for monitoring positive surface potentials using the DC-spectral method described in Section 4.5. It may also provide the option to improve the energy resolution in spectral measurements by adding another more radial symmetric suppression grid to the detector.

3. *Mounting an additional electron flood gun into the detector housing*: the electron flood gun presently sits adjacent to the sample in the sample block (see Section 3.5). This design was originally chosen so the flood gun could reside inside of the detector apparatus without making further alterations to the detector housing. This design has been both cost effective and relatively easy to implement, but suffers from a few drawbacks. First, the flood gun (filament, Wehnelt can, and anode) is powered through the same ribbon cable that carries sample and stage current signals out of the chamber. The cable has a total of 21 lines, each rated at 1 A. A total of six lines must be used to safely power the filament (operated at 1-2.5 A). Two additional lines are used to bias the Wehnelt can and anode. At least 11 of the other lines are used to carry sample and stage current signals. Consequently, with the present design, only one flood gun (and therefore only one insulator sample) can be measured at any given time, and the vacuum must be broken to replace insulator samples. A better design would involve the installation of a single flood gun into the detector housing, pointing

towards the sample. The flood gun could be wired with 22 AWG Kapton™-coated wire, rated at 5 A per line, and would rotate freely with the swiveling detector. Associated electron yield correction factors would need to be calculated to account for current losses within the detector to the flood gun. However, this design would allow multiple insulators to be measured without breaking vacuum, and only one flood gun would need to be built to neutralize all samples. Additionally, with the implementation of crude focusing capabilities (using an annular electrostatic lens), the gun could be used for low-energy (<100 eV) DC-yield measurements that would allow direct determination of the first crossover energies for most insulator and conductor materials. Presently, the STAIB gun is used to probe E_1^{σ} and E_1^{δ}, but the minimum operating energy of the gun is ~80 eV such that accurate determination of E_1^{σ} and E_1^{δ} <80 eV is not attainable for many materials (refer to Section 4.6).

4. *Mounting of a UV source inside the detector housing*: it would useful to install a UV light source (such as LED's or a fiber optic cable leading outside the chamber) into the detector housing for photo-induced discharging of insulator materials. Presently, these studies can only be made by swinging the detector apparatus away from the samples, and then irradiating the samples with lamps through the vacuum chamber port windows. This has not only been extremely time consuming, but in using this method, there was no guarantee the electron beam was properly optimized through the aperture tube after the detector was returned to its position over sample. Furthermore, the tests performed to examine the effectiveness of present UV discharging setup on Kapton™ did not produce noticeable results (see Section 5.3.3). However, it has been reported in the literature that UV radiation >4 eV is effective in neutralizing some insulators (Bass *et al*., 1998; Levy *et al*., 1985), so continued UV discharging

experiments on Kapton™ and other insulators are warranted (see discussion in Section 6.2.2). Installation of a UV source inside the detector housing would allow UV discharging without moving the sample stage or detector apparatus. As with the flood gun, correction factors would need to be calculated for current losses associated with the internal UV source. Additionally, the light sources or fiber optics would need to be designed for UHV compatibility. The insulating glass bulbs would need to be coated with a transparent conductor coating (such as ITO) to eliminate insulator charging and resulting distortion of electric fields inside the detector apparatus. Furthermore, fiber optics, lenses, and windows would need to be transparent to UV wavelengths. Fiber optics could also be used to deliver light from a monochromated light source or solar simulator source presently used for UV-induced electron emissions in the FATMAN chamber. Finally, a fiber optic cable might also be used as a bore scope to view the sample inside the enclosed detector housing for visual inspection.

5. *Installation of an additional Faraday cup on detector apparatus:* mounting an additional Faraday cup on the outside of the detector, near the detector aperture, would allow quick measurement of the incident beam current without moving the detector, using instead electrostatic deflection of the electron guns. A small phosphor screen could also be mounted above or below the detector aperture tube for facilitation in the alignment of the electron and ion beams.
6. *Sample heating capabilities:* sample heating capabilities would provide an additional discharging technique for insulators. A resistance heater with an integrated thermocouple could be mounted to the underlying sample block. However, temperatures could not exceed ~200° C, since the stage wiring insulation (Kapton™)

may melt. However, even temperatures of ~200° C have been shown in the literature to accelerate sample discharging times by altering insulator conductivity, particularly in polymer materials (Vigouroux *et al*., 1985).

7. *Installation of a non-contacting electrostatic charge transfer probe*: presently, the FATMAN chamber is not equipped with a method for directly measuring insulator sample surface potentials. Sample charging has been measured using indirect methods involving DC and pulsed electron emission spectra, the pulsed probing technique, and evolution of electron yields and sample displacement current (see Sections 4.5 and 5.1-5.3). A non-contacting potential probe would offer an additional (and more direct method) to study evolving surface potential and its effects on electron yields. The probe could be built similarly to the one used in the charge storage chamber (Dennison *et al*., 2003a; Swaminathan *et al*., 2003; Swaminathan, 2004), where an *in situ* charge transfer probe is installed on a horizontal translational arm that can be brought up to the sample surface. A non-contacting surface potential TREK probe could then used *ex situ* to measure the potential of the charge transfer probe, which can be calibrated to correspond to the actual sample potential (Swaminathan, 2004).

6.1.2 FATMAN Vacuum Chamber Upgrades

A list of additional instrumentation upgrades and modifications to be implemented into the FATMAN chamber include:

1. *Further reduction of pulsed system noise*: further system noise reduction could be achieved by mounting the pulsed ammeter circuitry closer to the UHV chamber, and by shortening all current-signal carrying triaxial cabling. In conducting the initial noise diagnostics, it was determined the cable length can significantly affect systems

noise to levels that rival the electron pulse signals. Presently, the triaxial cabling that carries the current signals are ~2 m in length. By mounting all electronics near the chamber, cable lengths could be reduced by half (if not more), and this may improve the present signal/noise ratio obtainable with the present setup. Additionally, switching to simple LCD computer monitors in the lab may help reduce electromagnetic noise since it has been observed computer monitors in the vicinity of the signal cables can add to the noise level.

2. *Addition of solar simulator lamp*: along with a UV source mounted inside the detector apparatus, it would be beneficial to equip the FATMAN chamber with an intense solar simulator lamp. Such a lamp would allow a direct measure of the photon-induced electron yields over a broader UV frequency spectral band (3-7 eV) for comparison with the electron yields that are presently measured with the monochromated source (Dennison *et al*., 2002; Dennison *et al*., 2003b, 2003d). Additionally, this would provide an additional discharging source for negatively charged insulators, which could be directed to the sample using fiber optic cabling (refer to the discussion in Section 6.1.1)
3. *Modulation of incident electron beam and flood gun*: it may possible to modulate the pulsed incident electron beam and use lock-in amplification to significantly increase the signal-to-noise ratio in pulsed-yield measurements. However, a technique would need to be devised to limit sample charging in the presence of repeated electron pulsing such as lowering the incident electron current to the order of 0.1-1 nA (such that 100-1000 pulses could be used before inducing significant charging), and by alternating the pulsed electron beam with pulsed low-energy flood gun bursts (Dennison, private communication).

4. *Electron gun beam spot-size characterization as a function of incident energy*: although reasonable estimates for the beam spot size were obtained using the phosphor-screen sample, a more careful beam characterization study should be conducted to accurately determine the spot sizes as a function of incident energy for both the STAIB and Kimball electron guns. This could be done using the knife-edge technique, where the electron beam is directed into a Faraday cup, and the intensity is measured as a sharp edge is moved across the electron beam. Variations in the beam spot size caused errors in the charge-decay analysis as a function of incident electron current density in Section 5.3.4.

6.1.3 Computer Upgrades

A list of upgrades to the present computer automation and analysis includes:

1. *Computer, DAC card, and Labview software upgrades and online documentation:* Labview 5.0 is currently used to automate the measurement procedure on a computer driven by a 166 MHz Pentium-processor. It would greatly improve interfacing, computational, and analysis capabilities to purchase a new computer and DAC card, and to upgrade the Labview software to version 7.0.
2. *Frequency filtering of pulsed signals using Labview software or electronic filters*: the frequency band of the measured pulsed signals ranges from ~100 kHz to 1 MHz. The presence of high-frequency noise on the order of ±10 nA has been observed in the pulsed measurements. This noise originates from other nearby instrumentation, from signal-carrying cables, and the signal measuring instrumentation. Since it is not possible to eliminate all these noise contributors, it might improve the signal-to-noise ratio to implement signal frequency filters either electronically or in Labview signal

processing. Both high-pass and low-pass filtering electronics might be used to eliminate unwanted noise.

3. *Computer automation of electron gun controllers*: Section 4.1 provided time constraints associated with each step in the general pulsed-yield measurement procedure. In future work, pulsed-yield measurements can be further streamlined by automating electron gun controller settings such as the energy, filament, grid and focus knob settings using computer interfacing (Dennison, 2003e; Sim, 2003). This would allow a complete yield curve (over the gun's operating energy range) to be measured with minimal operator input, and would therefore reduce errors and time constraints associated with manual operation.
4. *Angular control of sample stage with stepper motors:* Automating the angular control of the sample stage using a stepper motor would streamline pulsed-yield measurements, particularly in experiments when multiple samples are being studied. It could also provide more precise alignment of the sample stage and detector with electron beams during the optimization process (discussed further in Section 4.1).

6.2 Future Measurements and Analysis

A list of proposed measurement and analysis studies include three main categories: i) new materials studies, ii) improved measurement and analysis techniques, and iii) charge distribution and three-stage SE emission measurements and modeling. These proposed studies are listed in the subsections below in order of suggested priority.

6.2.1. New Materials Study

Several recommended new materials studies are provided as follows:

1. *The study of additional insulator materials*: now that a pulsed-yield setup has been designed and built, continued pulsed electron yield studies can be conducted on numerous insulators. USU is now equipped with state-of-the-art instrumentation for making these types of measurements. Furthermore, the resulting data would alleviate the deficit of electron emissions data in existing current databases. An extensive list of samples proposed to be tested at USU is provided in Dennison *et al.* (2002, 2003d).
2. *Collaborative electron emission validation with other researchers*: it would be advantageous to perform parallel testing of identical insulator materials with other researchers in the spacecraft charging community. This would provide further validation of our techniques and facility, and provide further confidence in materials databases used by the international spacecraft charging community. Furthermore, teaming with other researchers would provide the capability to extend our electron yield studies to higher incident energies (up to several MeV), as well as over a wide spectrum of incident energies (Levy *et al*., 1985; Jbara *et al*., 2001; Cazaux *et al*., 1991).
3. *The negative charging of metal oxides for* $E_1^{\sigma}<E_0<E_2^{\sigma}$: As measured in this dissertation, and as hypothesized by Cazaux (1999), Al_2O_3 and other metal oxide materials charge negatively under a continuous source electron beam, even in the positive charging regime between the crossover energies (where the crossover energies are predicted by the pulsed beam technique). Spacecraft, including the International Space Station, are constructed from these anodized aluminum materials, and these results suggest the polarity of charging may not follow charging models based on pulsed-yield measurements. These results deserve further study to determine the negative charging magnitude and rates as a function of incident beam energy and

electron fluence. Such charging studies could be performed using the shifting-SE spectral method outlined in Section 4.5. Such spectral shifts could be systematically measured at different incident energies, and at regular time (or incident fluence) intervals, as was done by Jbara *et al*., (2001) in the energy regime of $E_0 > E_2^{\sigma}$. Finally, the resulting DC-beam steady-state potentials could be compared to resulting surface potentials obtained by the pulsed-beam method described in Section 5.3.4.

4. *Negative-electron-affinity materials*: recent studies have shown some carbon and doped-diamond materials exhibit very high electron-emission properties due to their negative-electron affinity properties (Yater *et al*., 1997, 1998, 2003; Yater and Shih, 2000, 2001; Shih *et al*., 1997). This facilitates both SE transport and escape within the material, since high local electric fields in the bulk of the insulator draw SE's toward the surface. Additionally, once SE's reach the surface no escape energy barrier exists since the vacuum level energy lies below the conduction band minimum. Such materials offer promise in the field of electron multiplier detection, and may also have useful applications in the field of spacecraft charging. Additionally, from a physics standpoint these materials are interesting since, by measuring the SE energy spectrum, they provide a full view of the insulator's hot-electron energy distribution in the conduction band (Zavyalov, private communication). This permits the study of the full SE spectra with respect to energy loss mechanisms (e.g. electron-phonon, electron-hole pair production, and electron-plasmon losses). The facility at USU is particularly well suited for the continuation of electron emission studies of these materials. The studies could begin by measuring the total, SE, and BSE yields and SE spectra of oxygen- or hydrogen-treated carbon nanotubes, which exhibit negative electron affinity behavior (Kim *et al*., 2002; Yi *et al*., 2001).

6.2.2 Continuation of Electron Emission Measurements and Analysis

Continuation and improvement of measurement and analysis techniques follow from those explored in this dissertation work, and include:

1. *Completion of detector-apparatus characterization and correction factors*: As outlined in Section 4.3, total-yield correction factors were determined from data on numerous insulator materials. Specifically, two correction factors were determined; one was related to the detector apparatus, and the other was related to errors associated with the exclusion of the stage current signal from total yield measurements. As explained in Sections 4.2 and 4.3, the pulsed stage signal was excluded from the pulsed-yield calculations due to the large noise level present in the stage circuit [it should be noted since the initial writing and defense of this dissertation, the stage-signal noise has been significantly reduced, and the pulsed stage current is now being used in pulsed-yield calculations (Sim, private communication). In regards to the detector-apparatus correction factor, the total-yield correction factor was empirically determined on both insulator and conductor materials at E_2^{σ} by comparing total yield values to sample current for both DC and pulsed setups (refer to Section 4.3). Regardless of material type, the detector correction factor was determined to be accurate to within 2 percent. Continued empirical studies need to be conducted to expand upon and validate the correction factors provided in Section 4.3 for total, SE, and BSE yields. First, the empirical methods of this dissertation only provided correction factors for the total yields, not for the SE and BSE yields. Hence, we have proposed additional experimental studies in our laboratory involving photon and electron-induced electron emissions to

empirically determine SE and BSE correction factors (Dennison, private communication). Furthermore, although the total-yield correction factors were determined for $E_0=E_2^{\sigma}$ to within our target accuracy of 5 percent (refer to Section 4.3), these specific tests could not ensure the total-yield correction factor was independent of incident energy. Hence, experimental methods must also be devised to determine the possible energy dependence of total, SE, and BSE correction factors. Finally, if the detector apparatus is modified, as proposed in Section 6.1.1, an additional set of correction factors will need to be determined to accommodate for these alterations. Along these lines, it would be incredibly useful to devise a calibration standard that could be inserted or removed into the FATMAN chamber to empirically determine these correction factors, and to accommodate all future detector-apparatus modifications. The details of such a calibration standard are not presented in this dissertation, but could involve the use of a flood-gun electron source (operated both at low energies, <50 eV, and higher energies, >50 eV) mounted in a sample block to simulate an electron-emitting sample. By characterizing the emitted current, and by measuring resulting currents to all detector surfaces, associated SE and BSE loss corrections could be characterized for any given detector design modification. In summary, continued empirical correction factor studies and methods need to be conducted that can determine total, SE, and BSE corrections in a redundant fashion, using independent measurement techniques. Such studies are critical to our goal of determining absolute total, SE, and BSE yields with minimal systematic errors at Utah State University.

2. *Further exploration of methods to accurately determine insulator crossover energies*: as described in Section 4.6 and demonstrated in Sections 5.1 to 5.3, alternate methods

existed to directly measure insulator total-yield crossover energies (other than fitting the total yield curve) that included monitoring DC SE spectra, mirror method surface potentials, and sample displacement current polarity measurements. Further exploration and improvements upon these methods can be made by disconnecting the inner grid from the sample stage assembly for SE spectral peak monitoring (refer the discussion above in Section 6.1.1 of proposed detector upgrades), by using thicker insulators to eliminate leakage current in the mirror method measurements (see Section 5.2), and by installing a flood gun with focusing capabilities in the detector housing from low-energy yield and sample displacement current measurements (see the discussion above in Section 6.1.1 of proposed instrumentation upgrades). Such instrumentation modifications will reduce the systematic errors associated with each of these methods (refer to Sections 4.6, 5.1, 5.2, and 5.3). Furthermore, the value of E_1^{σ} could be explored using the DC spectral method. Also, the TREK probe (described in Section 6.1.1 of proposed instrumentation upgrades above) could provide a measurement of the surface potentials near the crossover energies to test for charge polarity reversal. Finally, to fully demonstrate these methods, a more extensive study of the crossover energies of various insulators should be conducted using each of the methods described above. For each insulator, the crossover energies should be measured using these various pulsed and DC methods, and scrutinized based on material properties, electron irradiation history, and measurement method.

3. *UV-source discharging studies*: in the experimental studies presented in this dissertation, the effectiveness of photo-induced neutralization methods on insulators were not obvious due in large part to the *ex situ* UV source setup and its relatively low intensity and low-frequency spectrum cutoff of the sources (see Sections 3.5 and

5.3.3). Once a UV source is mounted inside the detector apparatus (see the discussion above in Section 6.1.2 of proposed instrumentation upgrades), the effectiveness of UV neutralization (as reported in the literature) can be monitored more efficiently and accurately. Also, the intensity of the source at the sample will be greater due to the close proximity of the source. Furthermore, the high-frequency cutoff limit of the source will be extended since the UV will be propagating in a vacuum rather than in an oxygen-rich environment. These studies can also be extended to explore the relationships between discharging rates of different materials as a function of both incident electron energy and incident photon energy and radiation fluence.

4. *Extension of Chung and Everhart model to insulators*: From Chung and Everhart (1974), an expression for the escaping SE energy distribution for conductors is given by:

$$\frac{dN}{dE} = \frac{S(E)\lambda(E)}{4}\left[1-\left(\frac{E_F+\varphi}{R}\right)\right], \tag{6.1}$$

where S(E) is the number of SE's excited by primaries per unit energy in the energy interval E+dE, λ(E) is the mean SE escape length, E_F is the Fermi energy, and φ is the conductor's work function. Baroody (1950) and Quinn (1962) further applied this model to conductors by calculating values for S(E) and λ(E) such that Eq. (6.1) was shown to reduce to Eq. (2.23) (Davies, 1999). In this dissertation, the liberty was taken to extend this model to insulators, assuming many parts of this model have analogues in insulator theory. For example, the conductor SE mean escape depth, dominated by electron-electron scattering, was replaced by the longer insulator SE mean escape depth, dominated by electron-phonon scattering. Furthermore, for conductors, the work function provides a surface energy barrier that suppresses SE escape, whereas with charged insulators, the electron affinity, χ, and surface potential,

V_s, suppress SE escape. Hence, the SE energy distributions for both conductors and insulators appear to be very similar, and have both been fitted with the Chung and Everhart model in this dissertation (see Sections 2.1 and 5.3.2). However, it would be beneficial to perform a thorough review of previous literature, particularly of Chung and Everhart (1974), Baroody (1950), and Quinn (1962), to make any necessary alterations and interpretations to the Chung and Everhart model as applied specifically to dielectric material SE distribution theory. Such alterations could involve differences in the conductor and insulator SE production terms, S(E), mean SE escape depth, $\lambda(E)$, electric-field assisted SE transport, as well as the associated surface escape terms of electron affinity, χ, and surface potential, V_s.

6.2.3 Insulator Charging and Electron Yield Mechanism Studies

As described in Section 2.3.2, the three-stage model of SE emission is composed of production, transport, and emission components. However, the physical mechanisms for SE creation, migration, and escape are more complicated for insulators than for conductors, since electron and hole charges become trapped on the surface and in the bulk of the insulator. This can lead to electric-field assisted (or repressed) SE emissions through a complicated interplay between migrating SE's and trapped charges. This can lead to a number of anomalous experimental observations, which are not predicted by the present SE theory. For example, as demonstrated in Section 5.1, experimental observations have shown metal oxides can charge in a direction not predicted by their pulsed total electron yield curve. Furthermore, in Section 5.3.2, it was shown SE yield parameters for Kapton^{TM} will fluctuate from previous electron irradiation. Hence, continued experimentation and modeling is essential to understanding the

nature of the internal charge distributions of insulator materials. Proposed measurements and analysis for such studies are provided as follows:

1. *Pulsed charging rates of electrons yields and sample displacement currents*: following up on the work of Section 5.3.4, the continued study of evolving pulsed electron yields and sample displacement currents as a function of cumulative electron fluence could provide important information on insulator steady-state behavior and internal charge distributions. In this dissertation work, the total yield decay rates as a function of incident electron fluence were studied both for positive and negative charging regimes. Specifically, three charging regimes were identified (refer to Sections 2.3.6 and 2.3.9) and studied (refer to Sections 5.1 and 5.3.4): the first was the positive charging regime for incident electron energies of $E_1^{\sigma}<E_0<E_2^{\sigma}$; the second was the fast negative charging regime for $E_0>E_2^{\sigma}$; and the third was the slow negative charging regime for $E_0>E_2^{\sigma}$. A fourth negative charging regime for the incident electron range, $E_0<E_1^{\sigma}$ was not studied due to the present limitations of our electron sources (refer to Section 3.4). These studies could be continued to include more accurate and thorough investigations of the total yield and sample displacement current decay rates as a function of incident energy, incident electron fluence, material type, and sample thickness. Since the rates of charging are directly related to both the amount and depth of deposited (or emitted) charge, these studies could be used to study the dynamic behavior of charge polarity and internal charge distributions. Furthermore, these tests could be used to validate and improve available charge modeling codes (Meyza *et al*., 2003; Cazaux, 1986, 1999; Melchinger and Hofmann, 1995; Frederickson and Brautigam, 2003; Frederickson *et al*., 2003; Frederickson and Dennison, 2003). Finally, this work may ultimately be related to the charge storage

resistivity studies being performed at USU (Dennison *et al*., 2003a; Swaminathan *et al*., 2003; Swaminathan, 2004). Work by Frederickson (Frederickson and Brautigam, 2003; Frederickson *et al*., 2003; Frederickson and Dennison, 2003) has demonstrated the use of correct resistivity values is critical to accurately predict electrostatic discharge of spacecraft materials. In these studies, the leakage current and resistivity of an insulator has also been found to depend on the internal and surface charge distribution of the insulator. As discussed in Section 6.1, several improvements could be made to the yield-measuring instrumentation to improve the accuracy and speed of these types of measurements.

2. *Monitoring of evolving surface potentials from pulsed incident electron irradiation*: as discussed in Sections 2.3.6 and 2.3.9, and as demonstrated in Section 5.3.4, the evolving positive and negative surface potentials under a pulsed-incident electron source can be determined by monitoring the evolving SE yields. Specifically, Eq. (2.61) allowed the calculation of evolving positive surface potentials for $E_1^{\sigma}<E_0<E_2^{\sigma}$ in terms of the evolving SE yields and electron affinity. Furthermore, Eq. (2.62) allowed the calculation of the fast negative charging potentials for $E_0>E_2^{\sigma}$. Finally, Eq. (2.34) allowed the calculation of the slow negative charging potentials for $E_0>E_2^{\sigma}$ (although errors of this method were found to be quite substantial in Section 5.3.4). In all the literature reviewed, the pulsed method provided the only known method for measuring evolving surface potentials and charging rates for $E_1^{\sigma}<E_0<E_2^{\sigma}$. Furthermore, for $E_0>E_2^{\sigma}$, no data existed on the fast negative charging rates and potentials, and very little data existed on the slow charging rates, especially for polymers (refer to Section 5.3.4 for further literature comparisons). Our laboratory is uniquely equipped with the instrumentation and experience for the continuation of

these novel charging-rate characterization studies of numerous insulators, dependent on material type, incident electron energy, and incident electron fluence.

3. *Systematic study of the differences in E_2^{σ} as determined by pulsed vs. DC methods:* in Section 5.2, it was shown differences between E_2^{σ}, as determined by pulsed versus DC methods, can vary by more than 30 percent. However, for the RTV-silicone samples studied, these differences were not consistent with other studies that show a decrease in E_2^{σ} with continued electron bombardment (Jbara *et al*., 2001; Liehr *et al*., 1986). Instead, pulsed results for CV-1147 were higher than DC results, while they were lower for DC93-500. Nevertheless, the magnitudes of the discrepancies resulting from these two measurement methods needs to be studied further and reported in the literature. This information is important to the SEM and spacecraft charging communities, since generally, no distinction has been made for E_2^{σ} as determined by pulsed vs. continuous-source methods. For example, data presented in the spacecraft charging community has traditionally been determined using pulsed methods to minimize charging effects on the electron yield curve. However, results presented in the SEM community have typically been made using a continuous electron source, since in this community, it has only been desirous to find the energy corresponding to negligible charging (E_2^{σ}) for insulator imaging. Hence, on a variety of insulator materials, it would be beneficial to study the differences in E_2^{σ} as determined using pulsed versus DC methods, and determine possible dependencies on measurement methodology and incident electron fluence. Furthermore, it would be informative to perform a systematic study on the effects of sample history and previous higher-energy ($>E_2^{\sigma}$) incident electron irradiation on the measured values of E_2^{σ}.

4. *Steady-State Surface Potentials as a Function of Incident Electron Energy*: A study of the energy-dependent steady-state surface potentials for numerous insulators would greatly benefit both the spacecraft charging and electron microscopy communities. This could be performed by irradiating insulator materials with a continuous electron source until a steady-state current condition is achieved. Then, several methods could be utilized to measure surface potentials, and include: using a non-contacting surface potential TREK probe (see Section 6.1.1 above); monitoring shifting SE spectral peaks for positive and negative charging (refer to Section 4.5); utilizing the pulsed-probing mirror method for high negative potentials for $E_0>E_2^{\sigma}$ (method discussed in Section 4.6 and demonstrated in Section 5.2); and calculating surface potentials using the steady-state yield and uncharged SE spectrum (refer to the discussion in Section 2.3.6). By characterizing steady-state surface potentials as a function of material type, incident energy, and total electron fluence, scientists and engineers would be able to select materials for spacecraft design based on their maximum steady-state charging magnitudes. Additionally, in the field of electron microscopy, scientists would be able to predict electron-beam energy dependent steady-state surface potentials better.
5. *Measurement of the steady-state DC yield decay with continued electron irradiation*: in Section 5.3.5, it was shown on Kapton™ the steady-state total electron yields continued to evolve with incident electron irradiation. No clear pattern was identified for evolving yields at incident energies of $E_0<E_2^{\sigma}$, but for $E_0>E_2^{\sigma}$, total yields decreased by 1-4 percent when exposed to continued incident electron charge of 30-60 μC. Although these changes were small, they were consistent for numerous incident energies $>E_2^{\sigma}$, and should therefore be studied further by increasing the intensity of the incident electron beam, and by irradiating insulator samples for longer periods of

time. By repeating these types of measurements using a constant incident electron beam current, a systematic study could be performed to determine a characteristic steady-state yield decay rate dependent on electron fluence, material type, and incident electron energy.

6. *Mirror method charge storage decay studies*: the pulsed probing mirror method offers a way to monitor the charge decay, or resistivity, time constant of negatively charged insulator materials. This could be done by irradiating the insulator to some unknown negative potential using an incident beam at $E_0>E_2^{\sigma}$. Then, the decaying surface potential could be monitored as a function of time using the pulsed probing technique described in Section 4.6. Finally, with this data, the charge-decay time constant, τ_{RC}, could be fitted using Eq. (4.9). These measurements could be directly compared with similar measurements taken with a TREK probe in the charge storage resistivity studies being performed in our other lab at USU (Dennison *et al*., 2003a; Swaminathan *et al*., 2003; Swaminathan, 2004).
7. *Decay of the pulse plateau in current-profile measurements*: as a complimentary study to the pulsed charge decay studies, it would be beneficial to also measure charging rates of insulator materials using an incident pulse with a duration exceeding 100 μs such that the decay of the pulse plateau could be monitored as a function of time. These results could be compared with the calculated decay time constants calculated in Section 5.3.4. This method is considered a more direct approach for determining a charge-decay data time. This method was not performed in this dissertation due to time constraints, and since at the present time, the plateau decays can only be monitored using the Kimball gun over the incident energy range of 5-20 keV (beyond

E_2^{σ} for most insulators) since the STAIB gun did not exhibit the uniform pulse-profile emission required to perform this technique (refer to Section 3.4).

8. *Partial-population analysis of material spectra*: based on the literature results presented in Section 2.3.4, there appears to exist a clear SE energy dependence associated with the mean SE escape depth, λ_{SE}. However, current SE emission models assign one mean escape depth to the SE exponential escape term, as shown in the escape and transport probability functions given by Eqs. (2.6) through (2.14) in Section 2.3.2. As demonstrated in Section 5.3.2, these models are not sufficient to adequately model insulator SE yield data over extended incident energy regimes ranging from 0-20 keV. As proposed by Zavyalov (2003a), including the energy dependence of $\lambda_{SE}(E)$ into an improved SE yield model might offer vast improvements in fitting insulator SE yields over extended energy regimes. Unfortunately, in the literature, there is a vast deficit of both experimental and simulated data that can relate the SE mean escape depth to SE energy. The functional form of $\lambda_{SE}(E)$ in regards to fundamental material and electronic parameters could be the subject of future research at USU. One such study might proceed as follows: the SE spectrum is a measure of the hot-electron energy distribution of an insulator material, with a portion of the lower-energy electron distribution (at the conduction band minimum) filtered out by surface potential barriers. For insulators, this surface barrier involves both the band gap energy and the electron affinity (see Sections 2.3.3-2.3.8). Hence, the SE spectrum provides information on the partial populations of hot electrons in different SE energy regimes that are dominated by different energy-loss mechanisms. For example, SE's with energies less than the material band gap energy are susceptible to electron-phonon inelastic scattering, but not electron-hole pair creation (see Section

2.3.4). Alternatively, SE's with energies greater than the band gap energy may be susceptible to electron-hole pair creation, electron-plasmon interactions, and electron-phonon inelastic scattering. Consequently, each segment of the hot-electron energy distribution (or SE spectrum) can have its own associated mean-free-path and stopping power term, and ultimately a characteristic mean escape that depends entirely on SE energy. An intriguing study suggested by Zavyalov (private communication) would be to measure of the partial population of SE yields as a function of SE energy. This could be done by using different suppression grid biases (e.g., in 1 V increments up to 50 eV) and then fitting the partial SE yield curves with available SE models (refer to Section 2.3.2) to solve for the mean SE escape depth, λ_{SE}. Hence, the population of SE's (determined by the partial SE yield), as well as their associated SE energy dependence on λ_{SE} could be determined, corresponding to different energy-loss mechanisms in the SE energy distribution. The relationships found could also serve as a complimentary study for the theoretical and computational methods used to determine the mean escape depths (refer to discussions in Section 2.3.4). This information could ultimately be used to construct a more sophisticated insulator SE yield model that includes an energy dependent mean SE attenuation length that is sensitive to the energy loss mechanisms of SE's throughout the energy spectrum (Zavyalov, private communication; Dennison, private communication; Sim, private communication).

9. *Internal charge distribution modeling of insulator surface potentials and electron yield parameters*: as demonstrated in this study, insulator electron emissions, as well as surface potentials, can be altered by continued electron radiation, resulting from charge distributions on the surface and inside the bulk of the insulator material (see

Sections 2.3.7-2.3.8, 5.3.2, and 5.3.4). As demonstrated in Section 5.3.5, electron yield parameters continued to evolve even after insulator surface potentials had been neutralized. In past electron yield models, the charge distribution resulting from incident electrons has been assumed to take on the simplest of spatial distributions such as a single-layer or double-layer distribution. It would be very informative to utilize a bulk charging model as presented by Cazaux (1986, 1999), Cazaux *et al*. (1991), Meyza *et al*. (2003), Melchinger and Hofmann (1995), Frederickson and Brautigam (2003), Frederickson *et al*. (2003), and Frederickson and Dennison (2003) to quantitatively map out internal charge distributions and electric fields for all applicable energies (0 eV to 30 keV), applicable to the studies performed at Utah State University. Once the internal charge distributions are modeled, the internal electric fields can be calculated, as well as the resulting potentials on the surface of the insulator. These surface potentials could then be experimentally validated by methods set forth above. Finally, until recently, the measured internal charge distribution could only be inferred experimentally from surface potential measurements and alterations to the measured SE yields. However, recent experimental studies in Japan have demonstrated the direct measurement of charge distributions inside the bulk of insulators resulting from high-energy electron irradiation (Miyake *et al*., 2003; Osawa *et al*., 2003; Usui *et al*., 2003). Collaboration with these groups might allow for the direct comparison of measured surface potentials and altered electron yields with experimentally determined internal charge distributions at a given incident beam energy. Furthermore, direct measurement of the internal charge distribution would provide essential information on the SE creation and transport mechanisms, as well as on the internal charge diffusion and recombination rates in insulator materials.

Possible collaborative studies could include the measurement of electron yields and associated internal charge distributions for different insulators as a function of electron fluence, incident energy, and previous electron irradiation.

10. *Continued literature review*: additional literature related to insulator electron transport, emissions, and charging that warrants further investigation are for MgO (Cazaux, 1999; Cazaux *et al*., 1991; Liehr *et al.,* 1986; Jbara *et al*., 2001; Vallayer *et al*., 1999), Al_2O_3 (Meyza *et al*., 2003; Melchinger and Hofmann, 1995; Liehr *et al.,* 1986; Jbara *et al*., 2001; Mizuhara *et al.,* 2002; Vallayer *et al*., 1999; Belhaj *et al*., 2000; Toth *et al*., 2002; Wong *et al*., 1997), SiO_2 (Glavatskikh *et al*., 2001; Vigouroux *et al*., 1985; Wolters and van der Schoot, 1985; Yong *et al*., 1998; Arnold *et al*., 1994; Cartier and McFeely, 1991; DiMaria and Fischetti, 1988; McFeely *et al*., 1990; Wong *et al*., 1997), PMMA and polyethylene (Song *et al*., 1996; Akkerman and Akkerman, 1999; Liehr *et al.,* 1986; Bass *et al*., 1998; Kotera and Suga 1988), Teflon™ (Gross *et al*., 1976, 1977, 1979, 1984; Jbara *et al*., 2001; Wong *et al*., 1997), Kapton™ (Levy *et al*., 1985; Arakawa *et al*., 1981), PET (Wong *et al*., 1997; Toth *et al*., 2002), alkali halides (Boutboul *et al*., 1996, 1998, 1999; Akkerman *et al*., 1992, 1994; Henke *et al*., 1979), and doped Diamond, carbon nanotubes and negative electron affinity materials (Yater *et al*., 1997, 1998, 2003; Yater and Shih, 2000, 2001; Mearini *et al*., 1994, 1995; Krainsky and Asnin, 1998; Yi *et al*., 2001; Kim *et al*., 2002).

CHAPTER 7

SUMMARY AND CONCLUSIONS

The main focus of this dissertation research has been the experimental study of the electron-induced electron emission and charging properties of insulators using newly-developed state-of-the-art equipment and measurement techniques (Thomson *et al*., 2003a). Of key importance to this work has been the measurement of accurate uncharged insulator electron yields and charging behavior (Thomson *et al.*, 2003b). These experimental investigations on material electron emission properties were performed in an ultra-high vacuum chamber with numerous sample characterization and measurement capabilities (Dennison *et al.,* 2003b). These included SEM imaging, Auger electron spectroscopy, electron-, ion-, and photon-induced electron emission measurement apparatus. Furthermore, separate DC and pulsed electron sources and electronics existed for measuring electron yields of conducting and insulating materials. These capabilities have offered vast improvements in comparison to previous electron emission studies reported in the literature prior to the development of ultra-high vacuum technology. The measurement of absolute total, SE, BSE electron emission properties of insulators and conductors provides important new data for the spacecraft charging models. This work is also important to other applications, which include scanning electron microscopy, surface spectroscopy methods, particle detectors, plasma fusion devises, dielectric arcing, and flat panel displays (Shih *et al*., 1997; Reimer, 1985; Seiler, 1983; Belhaj *et al*., 2000; Schwoebel and Brodie, 1995; Auday *et al*., 2000).

Key advances in this research study were: i) the development of novel state-of-the-art methods and instrumentation for measuring electron yields and emission spectra from insulating materials, particularly for low-fluence pulsed-beam techniques; ii) new or greatly improved measurements of electron emission properties of a number of thin-film insulators,

relevant to spacecraft charging applications; and iii) extensive measurements and development of basic models to quantitatively describe the effects of charge buildup on electron emission properties.

7.1 Summarization of Dissertation Sections

In Section 2.1, a basic description of the electron yields and energy spectra were presented, characteristic to nearly all conductor and insulator materials. This included definitions of total electron, secondary electron, and backscattered electron yields along with their associated curve parameters. Section 2.2 provided an extensive literature review of experimental electron yield measurements on insulator materials, with a summarization of the measurement techniques used to minimize sample charging. It was found most of these studies employed pulsed incident electron sources to provide incident charge/pulse ranging from 10^4 to 10^8 electrons/mm^2 per pulse. In cases where the incident pulse charge threshold of ~10^7 electrons/pulse was exceeded, the samples were found to have been heated during measurements to temperatures >500° C to increase the insulator conductivity to dissipate unwanted charging effects (Krainsky and Lesny, 1998; Johnson and McKay, 1953; Johnson, 1948). In some cases, the use of a low-energy electron floodgun was employed to neutralize the insulator surface between pulses, with claims the neutralization was effective throughout the incident beam energy range (Krainsky *et al*., 1980, 1981). Expanding upon these prior methods, this dissertation work used pulsed-electron sources for measuring insulator electron yields along with a compact electron flood gun as a primary method of neutralization. Our pulse sources delivered ~10^6 electrons/mm^2 per pulse (~10^{13} C/mm^2 per pulse), and were found, in some cases, to produce significant charging after just a few pulses (refer to Section 5.1 and 5.3.4).

Section 2.3.2 through 2.3.5 provided an overview of existing secondary electron yield and energy spectrum models, with an emphasis on dielectric materials. From this review, expressions for the incident electron stopping power and range, SE escape depth, SE escape probability coefficient, SE yield curves, and SE energy spectrum were presented from the literature. Where provided in the literature, these models were related specifically to insulator electronic properties. For example, the escape probability coefficient was related to the electron affinity and energy bandgap through the works of Alig and Bloom (1978). Furthermore, insulator surface potentials were related to such quantities as the evolving SE yield (refer to Section 2.3.6) for both positive and negative charging regimes of $E_1^{\sigma}<E_0<E_2^{\sigma}$ and $E_0>E_2^{\sigma}$. Also, theoretical and Monte Carlo calculation data were gathered on the mean SE attenuation length, which is dependent on electron-phonon and electron-plasmon interactions. It was found from these data the SE attenuation length was highly dependent on the SE energy; from this we concluded insulator models based on a single SE attenuation length may not be sufficient to fully model SE yield data. As a suggestion for future studies, an improved model could be based upon the energy dependence of the SE attenuation depth, providing better fits to insulator SE yield data (see Section 6.2.3).

In Section 2.3.8, a review of insulator charging models was presented. These models are used to predict evolving bulk and surface potentials due to bulk insulator charging resulting from incident electron irradiation. Based on the recent works of Cazaux (1999) and Melchinger and Hofmann (1995), the dynamic double layer model (DDLM) was outlined. This simple DDLM model is able to predict evolving surface potentials and electron yields as a function of incident electron fluence and energy. Of key importance, included in the work of Cazaux (1999), was an explanation for the evolution of negative surface potentials, measured on metal oxides, for $E_1^{\sigma}<E_0<E_2^{\sigma}$ under continuous electron irradiation, when

positive charging is predicted from the pulsed total electron yields. As described in more detail in Section 2.3.8, this anomalous charging behavior resulted from incident electron-induced electron trap creation. Experimental evidence of this charging behavior has been measured by Melchinger and Hofmann (1995) and Cazaux *et al*. (1991), and was also measured in this dissertation on an anodized aluminum sample (see Section 5.1).

In addition to these DDLM models, a very recent charging model by Meyza *et al*. (2003) was explored and summarized in Section 2.3.8 that demonstrated the formation of more complicated internal charge distributions resulting from incident electron bombardment. As with the DDLM models, this model also accurately predicted measured surface potentials in different incident energy charging regimes, demonstrating the direction of the internal electric fields were dependent on the incident electron energy and flux.

Finally, in Section 2.3.9, a quantitative development of evolving electron yields and sample displacement currents in response to repeated incident electron pulsing was presented. This charging model was intended to be applied to the dynamic charging of insulators prior to reaching steady state. Furthermore, from arguments presented in Section 2.3.6, an expression for the evolving surface potential as a function of incident electron fluence was derived in terms of the fractional change in the evolving SE yields (refer to Section 2.3.6 and 2.3.9). This development was later used to model evolving electron yields, sample displacement currents, and surface potentials as a function of incident electron charge and energy for Kapton^{TM}-on-aluminum in Section 5.3.4.

A general description of the USU equipment and facilities used to measure electron emission properties was presented in Section 3.1. A more detailed description of the DC-data acquisitioning setup used to make conductor yield measurements was provided in Section 3.2 and in other sources (Nickles, 2002; Dennison *et al*., 2003b). Measuring insulator yields

required the development of electron-source pulsing capabilities, as well as state-of-the-art fast-response, optically isolated electron current detection equipment that was synchronized with electron gun pulsing, integrator circuitry, digital storage oscilloscope capture, flood gun neutralization, and computer data acquisition (refer to Sections 3.3-3.5). Of key importance were the fast, low-noise ammeters designed and built by Zavyalov (2003), with amplifications ranging from $1 \cdot 10^8$-$2 \cdot 10^6$ V/A, and response times of 1-10 μs (refer to Section 3.3, Thomson *et al*., 2003b, and Zavyalov, 2003 for more details). Additionally, integrator circuitry and/or a digital storage oscilloscope were used to capture the electron current signals. Further areas of instrumentation development included the development of effective neutralization methods, including a compact, low-energy electron flood gun that was found to be extremely effective in regulating surface potentials at beam energies of $E_1^{\sigma}<E_0<E_2^{\sigma}$. Additional UV neutralization sources were characterized and tested on insulators, but were later found to not be effective in neutralizing either positive or negative charge due to their low-energy photon spectrum and low flux levels. Further details on the discharging instrumentation are provided in Section 3.5 and Section 5.3.3. Finally, both DC and pulsed measurement setups, data compression, and analysis were fully computer automated using Labview (refer to Thomson, 2003d for more details).

The general procedure used for pulsed-yield measurements was outlined in Section 4.1. This section also included important measurement time constraints that may justify the further procurement of lab equipment and development of data acquisition automation in order to streamline insulator and conductor yield measurements in our lab (Dennison, private communication; Sim, private communication). Section 4.2 provided a more in-depth discussion of yield procedures, along with descriptions of alternative methods for pulsed-yield measurements and analysis. Two specific methods deserve further mention. The charge

integration method was used for short pulse widths of ~5 μs (the pulse width limited by the response time of the ammeters), and involved integrating current pulse signals with respect to the time to obtain total electron charge. The pulse profile method could be used for pulse widths >10 μs (the charge integration method could also be used on longer pulses), and involved finding the current pulse peak maxima.

A crucial part of this dissertation was to reduce the systematic error of total, BSE and SE yield measurements to within 5 percent. Previous calculations by Nickles (2002) provided estimates for correction factors associated with electron losses in our detector apparatus. Furthermore, as discussed in Section 4.3, empirical methods were used in this dissertation to determine total yield correction factor for many different conductor and insulator materials. These correction factors were specific to our detector apparatus, and were applicable to both pulsed-yield and DC-yield setups. Empirically determined correction factors in this dissertation work were found to be consistent for many measured materials to within 2 percent.

In Section 4.4, the pulsed-yield setup was validated on a conducting titanium sample by comparing pulsed yields and DC yields on the same sample. Overall agreement was determined to be within 10 percent for energies ranging from 100 eV to 14 keV. Finally, in Section 4.4, the total pulsed-yield fractional error was determined as both a function of incident pulse magnitude and number of pulses. This provided a means to predict the random uncertainties of total, BSE, and SE yields using the pulsed-yield setup.

In Section 4.5 different experimental methods were explored to determine the charging behavior of insulators resulting from incident electron irradiation. Several non-contacting methods for monitoring evolving surface potentials were investigated and developed. These involved pulsed techniques such as the evolution of pre-steady-state

electron yields and sample displacement currents, the pulsed probe mirror method (described in more detail in Section 4.6), measuring shifts in the DC SE emission spectrum, calculation of the steady-state surface potential using the steady-state SE yield (derived more fully in Section 2.3.6), and calculation of the evolving surface potential using the evolving SE yields prior to steady state (derived more fully in Sections 2.3.6 and 2.3.9). Measuring the shift in the DC SE spectra was effective for monitoring both positive (for $E_0<E_2^{\sigma}$) and negative (for $E_0>E_2^{\sigma}$) surface potentials resulting from continuous electron irradiation. Methods, such as monitoring shifts in the SE spectra and calculating evolving potentials from evolving SE yields, were very sensitive to small fluctuations in the insulator surface potential (resolution <1 V) as compared to other more conventional methods for measuring insulator surface potentials (compare to TREK probe measurements in Swaminathan, 2004). Finally, there was not time in this dissertation work to fully explore and compare these methods for a variety of insulator materials at varying incident energies. Hence, further studies are warranted at USU (refer to Section 6.2.3).

Section 4.6 described alternative methods that were explored to measure the total yield first and second crossover energies, quantities important to spacecraft charging and SEM applications. This involved the standard method for determining the crossover energies by fitting the pulsed total and SE yield curves with fitting models (models were presented in Section 2.3.2). Another method that was explored for the pulsed-yield setup included finding the energy for which the sample displacement current went to 0 nA (this method was suggested by Corbridge, private communication). Of these two pulsed methods, the second method was considered to be the most direct and accurate method for determining the crossover energies since it did not suffer from additional errors associated with the fitting models (see for example Sections 5.1 to 5.3.2). For insulators, these pulsed methods were

minimally invasive in the sense only small amounts of charge (~10^6 electrons/mm^2) were deposited during the measurement procedure.

Other continuous-source methods were explored for determining E_2^{σ} with the DC yield setup. These involved the DC-spectral method (similar to that described in Section 4.5), where shifts in the SE spectral peak were used to determine E_2^{σ}. Also, the mirror method was used to determine E_2^{σ} in a manner similar to that presented by Wong *et al.* (1997), although it was found this method suffered from errors associated with radiation-induced conductivity, leakage currents, and dielectric breakdown (refer to Sections 4.6 and 5.2). These drawbacks were either not apparent or were not mentioned in the works of Wong *et al.* (1997), but introduced significant errors in our investigations (see Section 5.2). Consequently, the DC-spectral method was considered to be most accurate for determining E_2^{σ} using a continuous incident electron source. Finally, most efforts in this dissertation were focused on finding E_2^{σ} rather than E_1^{σ} simply because our electron guns did not operate effectively at incident energies <100 eV. However, once our electron sources are modified to operate at lower energies, the methods described above could be used to determine E_1^{σ}.

The accurate determination of the insulator crossover energies is important in scanning electron microscopy to image insulator materials without inducing significant material charging (Girard *et al*., 1992; Wong *et al*., 1997). Also, in previous studies, it has been shown E_1^{σ} may play an important role in Snapover spacecraft charging, where it is believed to be related to the threshold potential of the Snapover event of high-powered solar arrays (Thomson, 2001). Furthermore, E_2^{σ} can be critical in determining the steady potential for spacecraft materials of samples bombarded with energies $E_0>E_2^{\sigma}$ as approximated by Eq. (2.34). E_2^{σ} is also critical in determining the polarity of insulator charging relevant to arc discharging of solar cell arrays on the International Space Station [refer to Section 5.2 on

RTV-silicone solar cell adhesives, as well as Dennison *et al.* (2003c); Thomson *et al*. (2003a)].

In Chapter 5, electron yield data for three insulator materials used in spacecraft construction were presented. In addition, various other electron yield parameters were explored that included methods for determining total and SE yield parameters, the dynamic evolution of electron yields, sample displacement currents and surface potentials, and the effectiveness of electron flooding and UV neutralization methods.

Section 5.1 presented data on an Al2219 chromic acid anodized aluminum disk. Pulsed measurements on Al2219 showed charging was positive for $E_1^{\sigma}<E_0<E_2^{\sigma}$ (~1400 eV), and occurred very rapidly, even at low electron fluences of $\sim 10^6$ electrons/pulse over a ~1 mm^2 area. For example, it was found at 500 eV, steady-state total yields were reached within $\sim 10^{-12}$ C/mm^2 of incident charge. However, when irradiated with a continuous source at E_0=200-1200 eV, the direction of charging was found to be negative, counter to our pulsed-yield measurements. Furthermore, the magnitude of the negative potential scaled with incident beam energy, up to a critical incident electron energy (~1700 eV), where the surface potential became sufficiently high (>20 V) to initiate dielectric breakdown of the thin anodized layer. An explanation for this negative charging behavior under continuous electron irradiation was provided by Cazaux (1999), who conjectured for metal oxides (e.g., MgO or Al_2O_3), a continuous electron source at $E_1^{\sigma}<E_0<E_2^{\sigma}$ would act to lower the total electron yields from an initial value greater than unity (as measured by pulsed yields) to one below unity, thus reversing the polarity of the surface potential. Cazaux attributed this lowering of the total yield to the creation of oxygen vacancies that facilitated electron charge trapping and storage in the insulator bulk. Hence, while under continuous electron irradiation, the dynamic trapping/detrapping rates of the insulator were altered, and acted to hinder SE transport such

that the total yield was lowered. This caused the surface potential to measure negative at energies where it should have been positive. Additional experimental studies on metal oxide materials need to be conducted to determine the nature of the trapping/detrapping rates as a function of incident electron fluence and energy.

Furthermore, for the Al2219 sample, it was found after irradiating the sample with high incident energies of E_0=5 keV, the trapped charge in the sample maintained the surface potential at a negative value on the order of 10 V, even while being irradiated with an electron beam at energies of 500 eV and 1000 eV. Hence, in contrast to measurements made prior to irradiating at E_0=5 keV, the negative surface potential no longer scaled with incident energy.

Section 5.2 presented data on the pulsed electron yields and the second crossover energies, E_2^{σ} for four RTV-silicone thin film samples. These four samples consisted of two types of RTV-silicone adhesive: CV-1147 and DC93-500. Four approaches were explored for determining the second crossover energies: i) the pulsed-total yield approach; ii) the sample displacement current method; iii) the DC-spectral approach; iv) and the mirroring method (these methods are explained in more detail in Sections 4.5 and 4.6). The mirror method was considered to be the least accurate method for determining E_2^{σ}, due to leakage currents and sample dielectric breakdown. The DC-spectral approach and sample displacement current approaches were assumed to be more accurate (to within ±25 eV) for determining E_2^{σ}. However, it has been shown in the literature, and in this dissertation work, continued electron irradiation (as in the DC-spectral approach) can alter electron emission properties of materials (refer to Sections 5.1, 5.3.2, as well as Jbara *et al*., 2001, and Liehr *et al*., 1986). For the RTV-silicone samples, E_2^{σ} data resulting from pulsed versus DC differed by 25-33 percent. However, these differences were not consistent with other studies that show a decrease in E_2^{σ} with continued electron bombardment (Jbara *et al*., 2001; Liehr *et al*., 1986). Instead, pulsed

results for CV-1147 were higher than DC results, while they were lower for DC93-500. Further studies need to be conducted to explore the differences associated with the pulsed and DC approaches (refer to Section 6.2.3).

Section 5.3 presented total, SE, and BSE pulsed yields on Kapton^{TM}-aluminum. To observe the effects of sample history, numerous pulsed-yield curve sets were measured and presented in Section 5.3.2. It was observed the fitted yield parameters, namely the maximum incident electron penetration depth, R, as well as the mean SE escape length, λ_{SE}, fluctuated in a manner consistent with the charging models presented in Sections 2.3.7 and 2.3.8. Specifically, the calculated values for R increased and λ_{SE} decreased after irradiating in the energy regime of $E_1^{\sigma}<E_0<E_2^{\sigma}$, consistent with the notion internal electric fields (pointing towards the surface) accelerated penetrating electrons to greater depths, and inhibited SE transport towards the surface (refer to Sections 2.3.7-2.3.8 and Meyza *et al*., 2003). Furthermore, after the sample was charged negatively with energies $E_0>E_2^{\sigma}$, the direction of the internal electric field was reversed such that the calculated maximum penetration depth, R, decreased.

Additionally, from the pulsed-yield data presented in Section 5.3.2, it was observed for incident energies beyond E_2^{σ} the BSE yields increased in value by a factor of three (as compared to BSE yield values below E_2^{σ}) to values equal to the total yields (within the measurement uncertainty), and the measured SE yields decreased toward zero. This occurred as growing negative sample potentials accelerated SE's to energies >50 eV, such that they were registered as BSE's by our detector apparatus. This was termed the fast negative charging mechanism in Section 2.3.6, and the rates of SE yield decay and growing surface potentials can be modeled as a function of incident charge by Eqs. (2.33) and (2.62). Furthermore, although the electron flood gun was found to be extremely effective in

neutralizing positive surface potentials for $E_1^{\sigma}<E_0<E_2^{\sigma}$, it was found to be ineffective in mitigating this negative charging behavior beyond E_2^{σ}. Additionally, UV surface neutralization sources were found to be ineffective for discharging Kapton^{TM}-aluminum on the time scales of 10 min., due in part to the low intensity of the sources and relatively low energy of the UV radiation. Consequently, in future experimental studies, an effective means for neutralizing negative surface potentials needs to be developed such that BSE and SE yields are not distorted beyond E_2^{σ}. As explained in Section 6.1.1, such a method could be the insertion of a UV diode source or fiber optic into the detector housing, with radiation energy spectra that extend beyond 4 eV.

Section 5.3.4 provided extensive total and BSE yield and sample charge data used to monitor the dynamic charging behavior of the Kapton^{TM} sample as a function of electron fluence. This was done for numerous incident energies both below and above E_2^{σ}. In general, both total yield and sample charge data exponentially approached their asymptotic values (near unity for total yields and 0 C for sample charge data) with consecutive incident pulses. For $E_1^{\sigma}<E_0<E_2^{\sigma}$, the total yield and sample charge started at positive uncharged values, and then decayed rapidly toward their steady-state values (within 10 pC/mm^2). The total yield decay was rapid since positive surface potential suppressed a significant portion of escaping SE's, as discussed further in Section 2.3.6 and 2.3.9. For $E_0>E_2^{\sigma}$, in general, the unflooded total yield and sample charge data slowly increased as the sample approached its negative steady-state potential. The decrease in the charging rate (as compared to data taken for $E_1^{\sigma}<E_0<E_2^{\sigma}$) resulted primarily because the magnitude of the steady-state negative potential is significantly increased beyond E_2^{σ}, and the ultimate steady-state condition is governed by Eq. (2.34). Furthermore, since the electrical potential induced by a single incident pulse is only a fraction of 1 V, it can take hundreds of pulses to progress toward the steady-state surface

potential. For $E_0>E_2^{\sigma}$, it was observed BSE yields also increased slowly with pulsed incident electron charge. This occurred since the BSE yields had already approached total yield values through the fast negative charging mechanism (refer to Section 2.3.6), and hence were similarly controlled by the ultimate steady-state condition and slow charging rates of the total yields.

From the fitted evolving total and BSE yields, the evolving SE yields were calculated as a function of cumulative incident charge for $E_1^{\sigma}<E_0<E_2^{\sigma}$. Furthermore, the evolving positive surface potentials were calculated using Eq. (2.61) from Section 2.3.9, and converged to steady-state potentials ranging from 0-10 V in the positive charging regime. Also, the change in the negative surface potentials for $E_0>E_2^{\sigma}$ due to the slow negative charging mechanism were calculated using Eq. (2.34) from the rise in the total yield values with incident pulsed charge. However, errors for this method were found to be quite significant. Finally, steady-state charge values and time constants were determined from the charge decay measurements for each incident energy, and were found to be in agreement with those found in the literature.

In addition to monitoring the dynamic evolution of electron yields prior to steady state, the continued evolution of the total yields long after steady state was monitored as a function of total incident electron fluence and energy in Section 5.3.5. For $E_1^{\sigma}<E_0<E_2^{\sigma}$, their existed no clear dependence between the steady-state total yields and incident charge. However, for $E_0>E_2^{\sigma}$, total yields consistently decreased slowly with incident electron charge at the rate 1-4 percent over 30-60 μC of incident charge. These data were consistent with predictions from Cazaux (1999) that steady-state yields should decrease with incident electron irradiation due to additional defects and electron trapping that are created by the incident beam (refer to Section 2.3.8). It was unclear whether the rate of decrease depended on beam energy.

Also, it was unclear how long this evolution process would continue. Clearly, these findings deserve further investigation (refer to Section 6.2.3).

The best estimates of total and SE yield parameters from Chapter 5 are summarized in Section 5.4 and compared to findings in the literature. Of the samples we studied, only Kapton^{TM}-aluminum had a full-yield parameter data set for comparison available in the literature. For Al2219 and the RTV-silicone samples, other materials similar in chemical composition were chosen for comparison. Overall, our results for Kapton^{TM}-aluminum were found to be most consistent with data presented in Levy *et al*. (1985), although the method used for total yield measurement from this study was not certain. For aluminum oxides, total-yield parameters varied widely, depending strongly on the crystalline structure of the reported materials. Results for RTV-silicone were found to be most consistent with studies on silicone-based pump oil.

A summary of proposed future work is summarized in Chapter 6. Section 6.1 lists upgrades to the pulsed-yield instrumentation and measuring setup, which will offer increased accuracy and speed to the present pulsed-yield data acquisitioning process, and also expand yield measurement capabilities. Section 6.2 lists future insulator measurement and analytical studies that follow from the experimental work of this dissertation.

7.2 Key Experimental Findings

Several key findings were reported in this dissertation work including the design and development of state-of-the-art instrumentation for pulsed-yield measurements, novel techniques for measuring electron emission parameters, charging parameters, and resulting surface potentials, experimental evaluation of theoretical and experimental claims made in the

literature, and experimental results that open new avenues for both theoretical and empirical studies. These key findings are summarized as follows:

1. *Electron transport models and multiple mean escape depths*: In Section 2.3.4, the SE mean attenuation depths as a function of SE energy for three alkali halides were calculated from displacement probabilities presented in the literature (Akkerman *et al*., 1994). These data were based on the Monte Carlo computational mean-free path and stopping powers of low-energy electrons subject to electron-phonon energy loss mechanisms in solids. From these calculations, it was found λ_{SE} was strongly dependent (increased) with electron energy over the range of 0-6 eV; an energy range spanning the vast majority of the SE energy distribution. Beyond 6 eV, $\lambda_{SE}(E)$ approached a material-dependent asymptotic value. Furthermore, λ_{SE} was calculated beyond the band gap energy of the insulators by Kanaya *et al*. (1978), dominated by electron-plasmon interactions, and plotted at the minimum plasmon excitation energy (ranging from 13-16 eV for the materials). These computational results lend credence to conjectures made by Zavyalov (private communication) that a single λ_{SE} mean escape value is not sufficient to adequately describe SE transport in insulators, as is assumed in current SE yield models [refer to Eqs. (2.13) through (2.16)]. An improved semi-empirical model for insulator yields should be developed that incorporates not only an energy-dependent SE transport term, but other insulator electronic properties. For example, as presented in Sections 2.3.4 and 2.3.5, work has already been performed by Alig and Bloom (1978) to relate other SE yield parameters to insulator properties such as the band gap energy and electron affinity [see, for example, Eqs (2.19) through (2.22)]. Unfortunately, very little computational work has been done, and virtually no experimental data exists on the low-energy electron

transport lengths in insulators, such that at the present time, developing a representative and universal energy-dependent SE transport model may be difficult.

2. *Enhanced laboratory capabilities and instrumentation*: In the last two years at USU, the sophistication, sensitivity, and versatility for making low-level, fast current electron emission measurements on insulators has reached a level that is unprecedented in the reported literature. This is due in large part to the innovative isolated ammeter design and construction performed by Zavyalov (2003). With ammeter amplification ranging from $2 \cdot 10^6$-$1 \cdot 10^8$ V/A, response times of 1-10 μs, and 2 kV optical isolation, numerous electron yield measurement schemes have become possible in our laboratory, which include independent sample, collector, suppression grid, and stage biasing and signal measurement capabilities. Furthermore, included in this design was the development of a compact electron flood gun source that was both inexpensive and easily integrated into our sample stage/detector apparatus. Moreover, a pulsed-yield measurement methodology has been developed that involves alternating pulsed incident electrons with flood gun neutralization in a fully automated fashion. This minimizes sample charging effects (refer to pulsed yields presented in Chapter 5), and allows the measurement of insulator total, SE, and BSE yield curves and spectra in a timely manner (refer to Section 4.1). These developments have made our lab one of the most capable, versatile, and accurate electron emission measuring facilities presently available.

3. *Absolute yield calculation*: An integral part of this dissertation was to verify the absolute accuracy of total, SE, and BSE yield measurements. Accurate electron yield parameters are crucial for accurately predicting spacecraft charging potentials using present simulation programs such as NASCAP 2K. As described in Section 4.3,

previous yield measurements have been measured in poor vacuum environments, and systematic errors associated with yield detection apparatus have not been adequately studied or corrected. Therefore, it has been a goal in our laboratory to fully characterize our detector apparatus, both through experimentation and calculation, to correct for electron current losses that alter absolute electron yields measurements. Our target has been to reduce the systematic errors of our total, SE, and BSE measurements to within 5 percent uncertainty. The calculation of detector apparatus correction factors was first performed by Nickles (2002), and has since been scrutinized by experimental methods presented in Section 4.3. Through these efforts, our group has arrived at a set of DC and pulsed-yield correction factors that bring the absolute values of our measured yields to within our target accuracy. A summary of the current state-of-the-art of facilities and capabilities at USU is provided in Thomson *et al*. (2003b) and Dennison *et al*. (2003b). A more detailed description of calibration methods for accurate absolute electron yield measurements and the associated pulse yield electronics and charge neutralization methods is in preparation for publication. Chapter 6 details proposed instrumentation upgrades, along with empirical studies, which can be used to further increase the accuracy of our pulsed electron yields.

4. *Measurement of new insulator electron emissions data*: From this dissertation work, new insulator materials used in spacecraft material construction have been studied (refer to Chapter 5). These include chromic anodized aluminum alloy Al2219, RTV-silicone adhesive, and Kapton^{TM} on aluminum substrate, all used on the International Space Station. Further results for these materials are published in Thomson *et al*. (2003a) and in Dennison *et al*. (2003d). A more extensive list of proposed materials

for study is provided in Dennison *et al*. (2003b). Although total, SE, and BSE electron yield data on Kapton^{TM} has been measured previous to this dissertation work (refer to Section 5.4), the results presented for aluminum alloy Al2219 and RTV-silicone are new to the literature, and are important additions to spacecraft materials charging databases.

5. *Quantitative studies of the effectiveness of charge neutralization studies*: Although previous experimental studies have claimed to measure the uncharged pulsed total, SE, and BSE insulator yields, these claims have never been justified by demonstrating the evolution of electron yields with incident electron pulses, and the effectiveness of neutralization sources. In this dissertation work, quantitative studies were conducted to test the effectiveness of different neutralization sources, including an electron flood gun and UV sources, over different incident electron energy regimes. In general, it was found the flood gun was extremely effective in neutralizing positive surface potentials for $E_1^{\sigma}<E_0<E_2^{\sigma}$, along with associated effects on total, SE, and BSE yields. However, the flood gun was found to be ineffective for negative surface potential neutralization at $E_0>E_2^{\sigma}$. In particular, although the total electron yields were not affected significantly by rising negative surface potentials [since the long-term charging rate beyond E_2^{σ} is very slow as controlled by Eq. (2.34)], the magnitude of the SE and BSE yields were very sensitive to surface potential changes as a growing number of SE's were accelerated to energies >50 eV (refer to Sections 2.3.6, 2.3.9, 5.3.2, and 5.3.4 for further discussions and data on these charging mechanisms). The floodgun was found to be ineffective in mitigating these charging distortions. Furthermore, UV irradiation was not found to be effective over time scales of 10 minutes, most likely due to the low-energy spectra of the sources (refer to Sections 3.5

and 5.3.3). These results are in contradiction to previous experimental studies in the literature that have claimed insignificant charging distortions over energy ranges of 100 eV to 5000 eV (above and below E_2^{σ}), along with the effective implementation of a floodgun electron source for $E_0>E_2^{\sigma}$ (Krainsky *et al.,* 1980, 1981). It is not clear why these discrepancies existed between our work and those in the literature, but further experimental investigation is warranted as outlined in Section 6.2.2.

6. *Effects of electron irradiation history and internal charge distributions SE emission parameters*: This dissertation presents experimental data demonstrating trends in the SE yield parameters in response to electron irradiation history on a Kapton™-aluminum sample in Section 5.3.2. These effects were observed even when proper surface neutralization methods were employed in the positive charging regime, $E_1^{\sigma}<E_0<E_2^{\sigma}$. Specifically, the SE maximum yield, maximum energy, calculated incident electron penetration depth, and calculated mean SE escape depth were found to change in a manner consistent with conjectured internal charge distributions and the resulting direction of internal electric fields, dependent on electron irradiation energy. Speculations of the energy-dependent charge distributions, as well as the resulting changing SE yield parameters, were in agreement with the charging model simulations presented by Meyza *et al*. (2003). These internal charge distributions created internal electric fields that either acted to accelerate or decelerate penetrating incident electrons and escaping SE's, thus altering yield parameters even when the surface potential was neutralized to 0 V. When the insulator was pre-irradiated in the positive charging energy regime, $E_1^{\sigma}<E_0<E_2^{\sigma}$, a positive electron depletion region built up beneath the surface that increased the maximum incident electron penetration depth, and decreased the mean SE escape depth. Alternatively, when the insulator

was pre-irradiated in the negative charging energy regime, $E_0>E_2^{\sigma}$, a negative incident electron deposition region built up that decreased the maximum penetration depth, and increased the mean SE escape depth. The data offered intriguing new evidence SE yield parameters respond to electron irradiation history in a manner consistent with modeled internal charge distributions. Additional data needs to be taken for different insulators to further verify these findings (refer Section 6.2.).

7. *Novel methods for determining the steady-state surface potentials for insulators:* As discussed in Sections 2.3.6, 4.5, and 4.6, and as demonstrated in Sections 5.1, 5.2, and 5.3.4, numerous new methods for determining the steady-state surface potentials for insulators, resulting from electron beam irradiation, were explored in this dissertation. Specifically, three methods were discussed. The first method was introduced for the first time in this dissertation work, and involved combining the uncharged pulsed SE spectra with steady-state SE yield data (measured using a DC incident electron source) to calculate the steady-state positive surface potential for $E_1^{\sigma}<E_0<E_2^{\sigma}$. This method was discussed in Section 2.3.6, but was not demonstrated experimentally due to lack of time and data, and hence warrants further investigation (refer to Section 6.2.3). The second method for determining steady-state surface potentials involved monitoring shifts in the SE spectral peak under continuous electron irradiation, both for positive charging ($E_1^{\sigma}<E_0<E_2^{\sigma}$) and negative charging ($E_0>E_2^{\sigma}$). This method was discussed further in Section 4.5 and was demonstrated for negative potentials on anodized aluminum and RTV-silicone in Sections 5.1 and 5.2. This method has been demonstrated elsewhere in the literature in the energy regime of $E_0>E_2^{\sigma}$, but has not yet been demonstrated for positive charging for $E_1^{\sigma}<E_0<E_2^{\sigma}$ (Jbara *et al*., 2001). Moreover, as discussed in Section 6.1.1, once modifications are made to the detector

apparatus by electrically isolating the inner grid from the stage, positive surface potentials can be measured with additional accuracy (resolution of <1 V), and results can be compared to methods presented in Section 2.3.6. The third and final method involved using a pulsed-probing incident electron beam to monitor the magnitude of high negative potentials (>100 V) and was referred to as the mirroring method. This method was explained further in Section 4.6 and was demonstrated in Section 5.2, where it was also used to determine the total-yield second crossover energy of RTV-silicone. A downfall to this method was it was only accurate to within ±300 V due to problems associated with leakage currents and the dielectric strength of thin-film insulators. Hence, in future studies, this method may prove to be feasible only for thick insulator materials.

8. *Novel methods for determining insulator SE- and total-yield crossover energies*: This dissertation reports the first systematic study comparing different approaches for determining E_2^{σ} using both pulsed and DC methods (refer to Sections 4.6, 5.2, and 5.3.2). The DC methods for determining total crossover energies included monitoring the shifts in DC spectra, as well as the pulsed-probing mirror method (refer to Sections 4.5, 4.6, 5.1, and 5.2). The pulsed methods for determining the total and SE yield crossover energies included fitting the pulsed SE and total yield curves (refer to Section 2.3.2, 5.2, and 5.3.2), and fitting the sample displacement current as a function of incident energy (refer to Sections 4.6, 5.2, and 5.3.2). It must be noted the pulsed-probing mirror method, as well as the pulsed sample displacement current method, have not been demonstrated elsewhere in the literature. In Section 5.2, significant differences were observed between E_2^{σ} values determined by pulsed versus DC methods. Furthermore, recent experimental evidence suggests measured E_2^{σ} values

are dependent on electron dose, and will hence vary according to the measurement method (Jbara *et al*., 2001; Liehr *et al*., 1986). It can be deduced from these studies pulsed measurements for E_2^{σ} should be higher than for DC measurements, since continued electron irradiation will cause an increasing number of internal electron trapping sites that act to lower the overall total yields (and hence, decrease E_2^{σ}). For our studies on RTV-silicone, although it was found pulsed E_2^{σ} values differed from DC values by 20-30 percent, the differences between pulsed and DC results were not consistent. Specifically, pulsed results for CV-1147 were higher than DC results, while for DC93-500, they were lower. Nevertheless, these differences need to be further explored on many other materials since they could have important implications to other spacecraft charging and SEM investigations. For example, in both the SEM and spacecraft charging communities, measured E_2^{σ} values have been treated as an electron-fluence independent parameter. No discrimination has been made for the methods used to determine E_2^{σ}. In the spacecraft charging community, pulsed-yield measurements of electron yield parameters, such as E_2^{σ}, have been inappropriately applied to space environments that exhibit continuous electron currents. Likewise, pulsed-yield values for E_2^{σ} may not be adequate to accurately predict the non-charging energies of insulators for SEM applications.

9. *Anomalous charging trends for aluminum oxide*: As reported in Section 5.1, when a continuous incident electron source with energies $E_1^{\sigma}<E_0<E_2^{\sigma}$ was incident on anodized aluminum, negative charging resulted (as measured by the DC spectral method) instead of positive charging, as predicted by the pulsed total yield curve. Additionally, this surface potential grew in magnitude with increasing energy until the dielectric breakdown potential was reached. This anomalous charging behavior for

metal-oxide materials has been explained by Cazaux (1999), has been measured in other recent experimental studies (Melchinger and Hofmann, 1995; Cazaux *et al*., 1991), and is attributed to the lowering of total electron yields resulting from electron irradiation-induced defect creation. These results further emphasize the differences in insulator electron emission properties and charging behavior, resulting from either pulsed or continuous-source measurement methods. These results may also be of importance to the spacecraft charging community since anodized aluminum is a common material used in spacecraft construction (including the International Space Station). Present charging models based on pulsed-yield data are not able to predict this type of negative charging behavior for $E_1^{\sigma}<E_0<E_2^{\sigma}$. For example, from the pulsed uncharged yield results presented in Section 5.1, charging models would predict a resulting surface potential of a few volts positive for incident energies $E_1^{\sigma}<E_0<E_2^{\sigma}$. However, ours and other recent studies have shown under continuous electron emission, the charging on aluminum oxide will not follow pulsed-yield data projections, but will instead be driven to a negative potential that scales with the incident energy up to the arcing potential of the anodized layer. Proposed further testing of these results is outlined in Section 6.2.1.

10. *Dynamic evolution of electron yields, sample displacement currents, and surface potentials*: In this dissertation work, the dynamical evolution of total, BSE, and SE yields and sample displacement currents were systematically monitored as a function of both incident electron fluence and energy as the sample approached steady state. The charge decay rates were studied both for positive and negative charging, and were sensitive to incident electron charge densities of $<10^6$ electrons/mm^2. Specifically, three charging regimes were identified (refer to Sections 2.3.6 and 2.3.9) and studied

(refer to Sections 5.1 and 5.3.4): the first was the positive charging regime for incident electron energies of $E_1^{\sigma}<E_0<E_2^{\sigma}$, the second was the fast negative charging regime for $E_0>E_2^{\sigma}$, and the third was the slow negative charging regime for $E_0>E_2^{\sigma}$. A fourth negative charging regime for the incident electron range, $E_0<E_1^{\sigma}$ was not studied due to the present limitations of our electron sources. The Chung and Everhart model (Chung and Everhart, 1974) was extended to charging insulator materials to model the evolution of the SE yields and surface potentials as a function of cumulative incident charge (refer to Sections 2.3.6, 2.6.9, and 5.3.4). Specifically, mathematical expressions were developed for the evolving positive and fast negative surface potentials for $E_1^{\sigma}<E_0<E_2^{\sigma}$ and $E_0>E_2^{\sigma}$ as a function of the evolving fractional SE yield data (ratio of the charged SE yield versus the uncharged SE yield, as measured in Section 5.3.4) and electron affinity of the insulator material. Conversely, the fractional SE yield was calculated as a function of the electron affinity and evolving surface potential (refer to Sections 2.3.6 and 2.3.9). Similar expressions do not exist elsewhere in the literature. These analyses were then used to evaluate the evolving total, BSE, and SE yields (and evolving SE yields were calculated from the evolving total and BSE) measured for Kapton^{TM} in Section 5.3.4. By fitting the electron yields (as they approached steady state) as a function of cumulative charge, a characteristic exponential decay parameter (that characterized the energy-dependent charging rate of the insulator) was extracted from the fits. This charging parameter was found to be energy dependent (but charge independent), decreasing with incident energy for $E_1^{\sigma}<E_0<E_2^{\sigma}$, and slightly positive for $E_0>E_2^{\sigma}$. These results were consistent with positive and negative charging mechanisms described in Section 2.3.6 and 2.3.9. Using this charge decay constant, the cumulative charge required to bring the insulator

to a steady-state condition was calculated and was found to agree well with experimental results and simulations reported in the literature (refer to Section 5.3.4 for more details). From the charge decay parameters, energy-dependent charge time constants were calculated for comparison with DC-current charge decay studies presented in the literature for $E_0>E_2^{\sigma}$. Comparisons were made with what data could be found, and were in good agreement. Using these methods, further studies need to be conducted to explore the energy- and flux-dependence of dynamical charging rates for numerous other insulator materials as discussed in Section 6.2.3. Furthermore, improvements could be made to the methodology and instrumentation to improve the accuracy of these measurements. These studies will lead to new and important findings on the energy- and material-dependent charging rates of insulators, and will provide vital information for internal charge modeling simulations.

11. *Long-term evolution of steady-state electron yields*: Finally, as shown in Section 5.3.5, long after the sample had come to a steady-state condition, the total electron yields were shown to continue to decrease with continued incident electron irradiation. Specifically, for $E_0>E_2^{\sigma}$, total yields decreased by 1-4 percent when exposed to continued incident electron charge of 30-60 μC. In the literature this type of long-term evolution has been predicted based on continued internal charging and electron trap defect creation (Cazaux, 1999; Meyza *et al*., 2003; Melchinger and Hofmann, 1995), although data demonstrating these trends as a function of incident charge and for numerous incident energies has not yet been measured. In future studies, these measurements could be taken for numerous insulators, leading to an associated steady-state yield decay rate dependent on both material type and incident electron energy.

These key findings offer new avenues for experimental and theoretical research in the field of insulator electron emissions and charging, as well as important information applicable to spacecraft charging, electron imaging, electron sources, and particle detection research. Available equipment, measurement, and analysis techniques demonstrated in this dissertation work are superbly tailored to perform future experimental studies at USU.

REFERENCES

Akkerman A., and E. Akkerman, "Characteristics of electron inelastic interactions in organic compounds and water over the energy range 20–10000 eV," J. Appl. Phys. **86** (10), 5809-5816 (1999).

Akkerman, A., T. Boutboul, A. Breskin, F. L. Chechik, and A. Gibrekhterman, "Low-energy electron transport in alkali halides," J. Appl. Phys. **76** (8), 4656- 4662 (1994).

Akkerman, A., A. Gibrekhterman, A. Breskin, and R. Chechik, "Monte Carlo simulations of secondary electron emission from Csl, induced by l-10 keV x rays and electrons," J. Appl. Phys. **72** (11), 5429-5436 (1992).

Alig, R. C., and S. Bloom, "Secondary electron escape probabilities," J. Appl. Phys. **49** (6), 3476-3480 (1978).

Arakawa, E. T., M. W. Williams, J. C. Ashley, and L. R. Painter, "The optical properties of kapton: measurement and applications," J. Appl. Phys. **52** (5), 3579- 3582 (1981).

Arnold, D., E. Cartier, and D. J. Dimaria, "Theory of high-field electron transport and impact ionization in silicon dioxide," Phys. Rev. B, **49** (15), 10278-10297 (1994).

Auday, G., P. Guillot, and J. Galy, "Secondary emission of dielectrics used in plasma display panels," J. Appl. Phys. **88** (8), 4871-4874 (2000).

Baroody, E. M., "A theory of secondary electron emission from metals," Phys. Rev. **78**, 780-787 (1950).

Bass, A. D., P. Cloutier, and L. Sanche, "Measurements of charge accumulation induced by monochromatic low-energy electrons at the surface of insulating samples," J. Appl. Phys. **84** (5), 2740-2748 (1998).

Battye, F. L., J. G. Jenkin, J. Leisegang, and R. C. G. Leckey, "Photoelectron determination of the attenuation of low-energy electrons in Al_2O_3," Phys. Rev. B **9** (7), 2887-2893 (1974).

Belhaj, M., S. Odof, K. Msellak, and O. Jbara, "Time-dependent measurement of the trapped charge in electron irradiated insulators: Applications to Al_2O_3-sapphire," J. Appl. Phys. **88** (5), 2289-2294 (2000).

Boutboul, T., A. Akkerman, A. Breskin, and R. Chechik, "Electron inelastic mean free path and stopping power modeling in alkali halides in the 50 eV–10 keV energy range," J. Appl. Phys. **79** (9), 6714-6721 (1996).

Boutboul, T., A. Akkerman, A. Breskin, and R. Chechik, "Escape length of ultraviolet induced photoelectrons in alkali iodide and CsBr evaporated films: measurements and modeling," J. Appl. Phys. **84** (5), 2890-2896 (1998).

Boutboul, T., A. Akkerman, A. Gibrekhterman, A. Breskin, and R. Chechik, "An improved model for ultraviolet- and x-ray-induced electron emission from CsI," J. Appl. Phys. **86** (10), 5841-5849 (1999).

Carruth Jr., M. R., T. Schneider, M. McCollum, M. Finckenor, R. Suggs, D. Ferguson, I. Katz, R. Mikatarian, J. Alred, and C. Pankop, "ISS and space environment interactions without operating plasma contactor," AIAA Paper 2001-0401, Proceedings for the 39th Aerospace Sciences Meeting and Exhibit, Reno, NV (2001).

Cartier, E., and F. R. McFeely, "Hot-electron dynamics in SiO_2 studied by soft-x-ray induced core-level photoemission," Phys. Rev. B **44** (19), 10689-10705 (1991).

Cazaux, J., "Some considerations on the electric field induced in insulators," J. Appl. Phys. **59** (5), 1418-1430 (1986).

Cazaux, J., "Some considerations on the secondary electron emission δ, form e^- irradiated insulators," J. Appl. Phys. **85** (2), 1137-1147 (1999).

Cazaux, J., K. H. Kim, O. Jbara, and G. Salace, "Charging effects of MgO under electron bombardment and nonohmic behavior of the induced specimen current," J. Appl. Phys. **70** (2), 960-965 (1991).

Chang, W. Y., N. Nickles, R. E. Davies, and J. R. Dennison, "Utah State University ground-based test facility for study of electronic properties of spacecraft materials," Proceedings of the 6th Spacecraft Charging Technology Conference, Air Force Research Laboratory Science Center, Hanscom Air Force Base, MA (2000a).

Chang, W. Y, J. R. Dennison, J. Kite, and R. E. Davies, "Effects of evolving surface contamination on spacecraft charging," Proceedings of the 38th American Institute of Aeronautics and Astronomics Meeting on Aerospace Sciences, Reno, NV (2000b).

Chang, W. Y., J. R. Dennsion, and P. Judd, "Measurements of electronic properties of conducting spacecraft materials with application to the modeling of spacecraft charging," Proceedings of the 38th American Institute of Aeronautics and Astronomics Meeting on Aerospace Sciences, Reno, NV (2000c).

Chung, M. S., and T. E. Everhart, "Simple calculation of energy distribution of low-energy secondary electrons emitted from metals under electron bombardment," J. Appl. Phys. **45** (2), 707-709 (1974).

Corbridge, J, J. R. Dennison, and N. Nickles, "Effects of bandgap on secondary electron emission for graphitic carbon semiconductors," American Physical Society Annual March Meeting, Austin, TX (2003).

Davies, R. E., *Measurement of Angle-resolved Secondary Electron Spectra*, PhD Dissertation, Utah State University, 1999.

Davies R. E., and J. R. Dennison, "Evolution of secondary electron emission characteristics of spacecraft surfaces," J. Spacecr. Rockets, **34**, 571-574 (1997).

Dekker, A. J., "Secondary electron emission," Solid State Phys. **6**, 251-311 (1958).

Dennison, J. R., W. Y. Chang, N. Nickles, J. Kite, C. D. Thomson, J. Corbridge, and C. Ellsworth, "Final report part III: materials reports," NASA Space Environments and Effects Program Grant, "Electronic Properties of Materials with Application to Spacecraft Charging," Available in electronic format through NASA SEE as part of the SEE Charge Collector Knowledgebase (2002).

Dennison, J. R., J. Kite, W. Y. Chang, and R. E. Davies, "Absolute and differential spacecraft charging as a result of evolving surface contamination," Proceedings of the 7th Spacecraft Charging Technology Conference, Noordwijk, Netherlands (2001).

Dennison, J. R., J. Kite, C. D. Thomson, J. Corbridge, R. Berry, and C. Ellsworth, "Final report part IV: additional materials reports," NASA Space Environments and Effects Program Grant, Electronic Properties of Materials with Application to Spacecraft Charging, 2003d (Available from J. R. Dennison at PHYSJRD@cc.usu.edu).

Dennison, J. R., A. R. Frederickson, and P. Swaminathan, "Charge storage, conductivity and charge profiles of insulators as related to spacecraft charging," Proceedings of the 8th Spacecraft Charging Technology Conference, Huntsville, Al (2003a).

Dennison, J. R., C. D. Thomson, J. Kite, V. Zavyalov, and J. Corbridge, "Materials characterization at Utah State University: facilities and knowledgebase of electronic properties of materials applicable to spacecraft charging," Proceedings of the 8th Spacecraft Charging Technology Conference, Huntsville, Al (2003b).

Dennison, J. R., C. D. Thomson, and J. Corbridge, "Electronic properties of ISS materials," Boeing Company Final Report, Contract No. M/C H014-B419, 2003c (Available from J. R. Dennison at PHYSJRD@cc.usu.edu).

DiMaria D. J., and M. V. Fischetti "Vacuum emission of hot electrons from silicon dioxide at low temperatures," J. Appl. Phys. **64** (9), 4683-4691 (1988).

Dionne, G. F., "Effects of secondary electron scattering on secondary emission yield curves," J. Appl. Phys. **44** (12), 5361-5364 (1973).

Dionne, G. F., "Origin of secondary electron yield curve parameters," J. Appl. Phys. **46** (8), 3347- 3351 (1975).

Feldman, C., "Range of 1-10 keV electrons in solids," Phys. Rev. **117**, 455-459 (1960).

Fitting, H. J., "The energy loss of transmitted and backscattered electrons," J. Phys. D. **8**, 1480-1486 (1975).

Frederickson, A. R., C. E. Benson, and J. F. Bockman, "Measurement of charge storage and leakage in polyimides," Nucl. Instrum. Methods **208** (7), 454-460 (2003).

Frederickson, A. R. and D. H. Brautigam, "Mining CRRES IDM pulse data and CRRES environmental data to improve spacecraft charging/discharging models and guidelines; final report and fourth quarterly report," 2003 (Available from J. R. Dennison at PHYSJRD@cc.usu.edu).

Frederickson A. R. and J. R. Dennison, "Measurement of conductivity and charge storage in insulators related to spacecraft charging," IEEE Trans. Nucl. Sci. **50** (6), 2284-2291 (2003).

Fridrikhov, S.A and A. R., Shul'man, "An investigation of the secondary electron emission by certain dielectrics at low primary electron energies," Sov. Phys. Solid State **1**, 1153-1159 (1960).

Girard, P., P. Charpenel, and H. Martin, "Determination of the noncharging electron-beam energy on insulators," J. Appl. Phys. **71** (6), 2871-2876 (1992).

Glavatskikh, I. A., V. S. Kortov, and H. J. Fitting, Self-consistent electrical charging of insulating layers and metal-insulator-semiconductor structures," J. Appl. Phys. **89** (1), 440-448 (2001).

Goodfellow Corporation, Aluminum-oxide technical data sheet, Available on the internet at: http://www.goodfellow.com, 2004.

Goto, K., and K. Ishikawa, "Secondary electron emission from diffusion pump oils II. δ-η analysis for DC-705," J. Jap. Appl. Phys. **7** (3), 227-231 (1968).

Grais, K. I., and A. M. Bastawros, "A study of secondary electron emission in insulators and semiconductors," J. Appl. Phys. **53**, 5239-5242 (1982).

Gross, B., G. M. Sessler, and J. E. West, "TSC studies of carrier trapping in electron- and γ-irradiated Teflon," J. Appl. Phys. **47** (3), 4303-4306 (1976).

Gross, B., G. M. Sessler, and J. E. West, "Location of charge centroid in electron-beam-charged polymer films," J. Appl. Phys. **48** (10), 4303-4306 (1977).

Gross, B., G. M. Sessler, H. von Seggern, and J. E. West, "Hole transit in Teflon films," Appl. Phys. Lett. **34** (9), 555-557 (1979).

Gross, B., H. von Seggern, and J. E. West, "Positive charging of fluorinated ethylene propylene copolymer (Teflon) by irradiation with low-energy electrons," J. Appl. Phys. **56** (8), 2333-2336 (1984).

Henke, B. L., J. Liesegang, and S. D. Smith, "Soft-x-ray-induced secondary-electron emission from semiconductors and insulators: models and measurements," Phys. Rev. B **19** (6) 3004-3021 (1979).

Holliday, J. E., and E. J. Sternglass, "Backscattering of 5-20 keV electrons from insulators and metals," J. Appl. Phys. **28**, 1189-1193 (1957).

Ishikawa, K., and K. Goto, "Secondary electron emission from diffusion pump oils I," J. Jap. Appl. Phys. **6** (11), 1329-1335 (1967).

Jbara, O., M. Belhaj, S. Odof, K. Msellak, E. I. Rau, and M. V. Andrianov, "Surface potential measurements of electron-irradiated insulators using backscattered and secondary electron spectra from an electrostatic toroidal spectrometer adapted for the scanning electron microscope applications," Rev. Sci. Instrum. **72** (3), 1788-1795 (2001).

Johnson, J. B., "Secondary electron emission from targets of Barium-Strontium Oxide," Phys. Rev. **73** (9), 1058 (1948).

Johnson, J. B., and K. G. McKay, "Secondary electron emission of crystalline MgO," Phys. Rev. **91** (3), 582-587 (1953).

Jonker, J. H. L., "The angular-distribution of the secondary electrons of nickel," Philips Res. Rep. **6**, 372-387 (1951).

Kanaya, K., S. Ono, and F. Ishigaki "Secondary electron emission from insulators," J. Phys. D: Appl. Phys. **11**, 2425-2437 (1978).

Kim, W. S., W. Yi, S.G. Yu, J. Heo, T. Jeong, J. Lee, C. S. Lee, J. M. Kim, H. J. Jeong, Y. M. Shin, and Y. H. Lee, "Secondary electron emission from magnesium oxide on multiwalled carbon nanotubes," Appl. Phys. Lett. **81** (6), 1098-1100 (2002).

Kishimoto, Y., T. Ohshima, M. Hashimoto, and T. Hayashi, "A consideration of secondary electron emission from organic solids," J. Appl. Polym. Sci. **39**, 2055-2066 (1990).

Kishimoto, Y., T. Hayashi, M. Hashimoto, and T. Ohshima, "Secondary electron emission from polymers and its applications to the flexible channel electron multiplier," J. Appl. Polym. Sci. **21**, 2721-2733 (1977).

Kotera, M., and H. Suga, "A simulation of keV electron scatterings in a charged up specimen," J. Appl. Phys. **63** (2), 261-268 (1988).

Krainsky, I. L., and V. M. Asnin, "Negative electron affinity mechanism for diamond surfaces," Appl. Phys. Lett. **72** (20), 2574- 2576 (1998).

Krainsky, I. L., and G. G. Lesny, "Simple device for monitoring secondary electron emission of materials in the pulse mode," Rev. Sci. Instrum. **69** (4), 1916-1917 (1998).

Krainsky, I., W. Lundin, W. L. Gordon, and R. W. Hoffman, *Secondary Electron Emission Yield Annual Report for Period July 1, 1979 to June 30, 1980*, Case Western Reserve University, Cleveland, OH, 1980 (unpublished).

Krainsky, I., W. Lundin, W. L. Gordon, and R. W. Hoffman, *Secondary Electron Emission Yield Annual Report for Period July 1, 1980 to June 30, 1981*, Case Western Reserve University, Cleveland, OH, 1981 (unpublished).

Levy, L., D. Sarrail, and J. M. Siguier, "Conductivity and secondary electron emission properties of dielectrics as required by NASCAP," Proceedings of the Third European Symposium on Spacecraft Materials in Space Environment, Noordwijk, The Netherlands, (1985).

Lide, D. R., *CRC Handbook of Chemistry and Physics, 82nd ed.* (CRC Press, Boca Raton, FL, 2001).

Liehr, H., P. A. Thiry, J. J. Pireaux, and R. Caudano, "Characterization of insulators by high-resolution electron-energy-loss spectroscopy: Application of a surface-potential stabilization technique," Phys. Rev. B **33** (8), 5682-5697 (1986).

Lye, R. B., and A. J. Dekker, "Theory of secondary emission," Phys. Rev **107** (44), 977-981 (1957).

McFeely, F. R., E. Cartier, J. A. Yarmoff, and S. A. Joyce, "Low-energy-electron escape lengths in SiO_2," Phys. Rev. B **42** (8), 5191-5200 (1990).

Mearini, G. T., I. L. Krainsky, J. A. Dayton, Jr., Y. Wang, C. A. Zorman, J. C. Angus, and R. W. Hoffman, "Stable secondary electron emission observations from chemical vapor deposited diamond," Appl. Phys. Lett. **65** (21), 2702-2704 (1994).

Mearini, G. T., I. L. Krainsky, J. A. Dayton, Jr., Y. Wang, C. A. Zorman, J. C. Angus, R. W. Hoffman, and D. F. Anderson, "Stable secondary electron emission from chemical vapor deposited diamond films coated with alkali-halides," Appl. Phys. Lett. **66** (2), 242-244 (1995).

Melchinger, A., and S. Hofmann, "Dynamic double layer model: Description of time dependent charging phenomena in insulators under electron beam irradiation," J. Appl. Phys. **78** (10), 6224-6232 (1995).

Meyza, X., D. Goeuriot, C. Guerret-Piecourt, D. Treheux, and H. J. Fitting, "Secondary electron emission and self-consistent charge transport and storage in bulk insulators: application to alumina," J. Appl. Phys. **94** (8), 5384-5392 (2003).

Miyake, H., Y. Tanaka, and T. Takada, "Characteristic of charge accumulation in glass materials under electron beam irradiation," Proceedings of the 8th Spacecraft Charging Technology Conference, Huntsville, AL, (2003).

Mizuhara, Y., J. Kato, T. Nagatomi, Y. Takai, and M. Inoue, "Quantitative measurement of surface potential and amount of charging on insulator surface under electron beam irradiation," J. Appl. Phys. **92** (10), 6128-6133 (2002).

Mueller, C. W., "The secondary electron emission of pyrex glass," J. Appl. Phys. **16**, 453-458 (1945).

Nickles, N. E., *The Role of Bandgap in the Secondary Electron Emission of Small Bandgap Semiconductors: Studies of Graphitic Carbon*, Ph.D. Dissertation, Utah State University, 2002.

Nickles, N., R. E. Davies, and J. R. Dennison, "Applications of secondary electron energy and angular distributions to spacecraft charging," Proceedings of the 6th Spacecraft Charging Technology Conference, Hanscom Air Force Base, MA, (2000).

Nunes de Oliveira, L., and B. Gross, "Space-charge-limited currents in electron-irradiated dielectrics," J. Appl. Phys. **46** (7), 3132-3138 (1975).

Osawa, N., S. Takahashi, Y. Tanaka, T. Takada, R. Watanabe, N. Tomita, V. Griseri, L. Levy, and C. Laurent, "Measurement of bulk charge in dielectric materials irradiated by electron beam in vacuum environment," Proceedings of the 8th Spacecraft Charging Technology Conference, Huntsville, AL, (2003).

Ozturk, N., and W. Williamson, Jr., "Monte Carlo simulation of keV electron transport in solid media," J. Appl. Phys. **74** (7), 4723-4728 (1993).

Pines, D., *Elementary excitations in solids*, (Westview Press, New York, 1999).

Quinn, J. J., "Range of excited electrons in solids," Phys. Rev. **126**, 1453 (1962).

Reimer, L., *Scanning Electron Microscopy. Physics of Image Formation and Microanalysis*, (Springer-Verlag, New York, 1985).

Reimer, L., and H. Drescher, "Secondary electron emission of 10-100 keV electrons from transparent films of Al and Au," J. Phys. D. **10**, 805-815 (1977).

Schwoebel, P. R., and I. Brodie, "Surface-science aspects of vacuum microelectronics," J. Vac. Sci. Technol. B **13** (4), 1391-410 (1995).

Seiler, H., "Secondary electron emission in the scanning electron microscope," J. Appl. Phys. **54** (11), R1-R18 (1983).

Sheldahl, Inc., Aluminum Coated (one side) Polyimide Product Bulletin, (online). Available on the internet at: http://www.sheldahl.com, 2004.

Shih, A., J. Yater, P. Pehrsson, J. Butler, C. Hor, and R. Abrams, "Secondary electron emission from diamond surfaces," J. Appl. Phys. **82** (4), 1860-1867 (1997).

Song, Z. G., C. K. Ong, and H. Gong, "A time-resolved current method for the investigation of charging ability of insulators under electron beam irradiation," J. Appl. Phys. **79** (9), 7123-7128 (1996).

Sternglass, E. J., "Secondary electron emission and atomic shell structure," Phys. Rev. **80**, 925-926 (1950).

Sternglass, E. J., *An Experimental Investigation of Electron Back-Scattered and Secondary Electron Emission From Solids*, Ph.D. Dissertation, Cornell University, 1953.

Swaminathan, P. V., *Measurement of Charge Storage Decay Time and Resistivity of Spacecraft Insulators*, MS Thesis, Utah State University, 2004.

Swaminathan, P. V., A. R. Frederickson, J. R. Dennison, A. Sim, J. Brunson, and E. Crapo, "Comparison of classical and charge storage methods for determining conductivity of thin film insulators," Proceedings of the 8th Spacecraft Charging Technology Conference, Huntsville, AL, (2003).

Thomas, S., and E. B. Pattison, "Range of electrons and contribution of backscattered electrons in secondary production in aluminum," J. Phys. D. **3**, 349-357 (1970).

Thomson, C. D., *Experimental Investigation of Snapover: The Sudden Increase of Plasma Current Drawn to a Positively Biased Conductor When Surrounded by a Dielectric*, MS Thesis, Utah State University, 2001.

Thomson, C. D., V. Zavyalov, J. R. Dennison, and J. Corbridge, "Electron emission properties of insulator materials pertinent to the international space station," Proceedings of the 8th Spacecraft Charging Technology Conference, Huntsville, AL, (2003a).

Thomson, C. D., V. Zavyalov, and J. R. Dennison, "Instrumentation for studies of electron emission and charging from insulators," Proceedings of the 8th Spacecraft Charging Technology Conference, Huntsville, AL, (2003b).

Thomson, C. D., presented at the Utah State University graduate school Candidacy Exam, Utah State University, Logan, UT, 2003c (Available from C. D. Thomson at CLINT.THOMSON@ATK.COM).

Thomson, C. D., Labview Pulsed Yield Data Acquisitioning Report, 2003d (Available from J. R. Dennison at PHYSJRD@cc.usu.edu).

Toth, M., M. R. Phillips, J. P. Craven, B. L. Thiel, and A. M. Donald, "Electric fields produced by electron irradiation of insulators in a low vacuum environment," J. Appl. Phys. **91** (7), 4492-4499 (2002).

Usui, Y., T. Sakai, M. Ishikawa, T. Isono, Y. Tanaka, T. Takada, R. Watanabe, N. Tomita, and Y. Murooka, "Measurement of charge distribution in electron beam irradiated PMMA using electro-optical effect," Proceedings of the 8th Spacecraft Charging Technology Conference, Huntsville, AL, (2003).

Vallayer B., G. Blaise, and D. Treheux, "Space charge measurement in a dielectric material after irradiation with a 30 kV electron beam: application to single-crystals oxide trapping properties," Rev. Sci. Instrum. **70** (7), 3102-3112 (1999).

Vigouroux, J. P., J. P. Duraud, A. Le Moel, C. Le Gressus, and D. L. Griscom, "Electron trapping in amorphous SiO_2 studied by charge buildup under electron bombardment," J. Appl. Phys. **57** (12), 5139-5144 (1985).

Wargo, P., B. V. Haxby, and W. G. Shepherd, "Preparation and properties of thin film MgO secondary emitters," J. Appl. Phys. **27** (11), 1311-1316 (1956).

Whetten, N. R., "Cleavage in high vacuums of alkali halide single crystals-secondary electron emission," J. Appl. Phys. **35** (11), 3279-3282 (1964).

Whetten, N. R., and A. B. Laponsky, "Secondary electron emission of single crystals of MgO," J. Appl. Phys. **28**, 515 (1957).

Whetten, N. R., and A. B. Laponsky, "Secondary electron emission from MgO thin films," J. Appl. Phys. **30** (3), 432-435 (1959).

Willis, R. F., D. K. Skinner, "Secondary electron emission yield behavior of polymers," Solid State Commun. **13**, 685-688 (1973).

Wolters, D. R., and J. J. van der Schoot, "Kinetics of charge trapping in dielectrics," J. Appl. Phys. **58** (2), 831-837 (1985).

Wong, W. K., J. C. H. Phang, and J. T. L. Thong, "Estimation of the second crossover in insulators using the electrostatic mirror in the scanning electron microscope," Appl. Phys. Lett. **71** (9), 1270-1272 (1997).

Yater, J. E., and A. Shih, "Secondary electron emission characteristics of single-crystal and polycrystalline diamond," J. Appl. Phys. **87** (11), 8103-8112 (2000).

Yater, J. E., and A. Shih, "Secondary electron emission characteristics of C(111) and the observation of double-peaked emission spectra," J. Appl. Phys. **90** (6), 3057-3064 (2001).

Yater, J. E., A. Shih, and R. Abrams, "Electron transport and emission properties of C(100)," Phys. Rev. B **56** (8), R4410-R4413 (1997).

Yater, J. E., A. Shih, and R. Abrams, "Electron transport and emission properties of diamond," J. Vac. Sci. Technol. A **16** (3), 913-918 (1998).

Yater, J. E., A. Shih, J. E. Butler, and P. E. Pehrsson, "Transmission of low-energy electrons in boron-doped nanocrystalline diamond films," J. Appl. Phys. **93** (5), 3082-3089 (2003).

Yi, W., S. Yu, W. Lee, I. T. Han, T. Jeong, Y. Woo, J. Lee, S. Jin, W. Choi, J. Heo, D. Jeon, and J. M. Kim, "Secondary electron emission yields of MgO deposited on carbon nanotubes," J. Appl. Phys. **89** (7), 4091-4095 (2001).

Yong, Y. C., J. T. L. Thong, and J. C. H. Phang, "Determination of secondary electron yield from insulators due to a low-kV electron beam," J. Appl. Phys. **84** (8), 4543-4548 (1998).

Young, J. R., “Penetration of electrons and ions in aluminum,” J. Appl. Phys. **27** (1), 1-4 (1956).

Yu, S., T. Jeong, W. Yi, J. Lee, S. Jin, J. Heo, and D. Jeon, “Double-to single-hump shape change of secondary electron emission curve for thermal SiO_2 layers,” J. Appl. Phys. **79** (20), 3281-3283 (2001).

Zavyalov, V., Pulsed-Yield Ammeter and Integrator Circuitry Report, 2003 (Available from J. R. Dennison at PHYSJRD@cc.usu.edu).

CURRICULUM VITA

Clint D. Thomson
(March, 2004)

EDUCATION:

Ph.D., Utah State University, Logan, UT. May 2005, GPA: 3.91
- NASA Graduate Student Research Fellowship, 2000-2003.
- NASA Group Achievement Award, 2003 (one of fifteen group members).
- NASA Software Author Award, 2003 (one of four group members).

M.S., Utah State University, Logan, UT. August 2001, GPA: 3.96.
- NASA Award for Research Excellence Nominee, 1999 (one of eight group members).
- Rocky Mountain NASA Space Grant, 1999.
- American Physical Society Centennial Meeting Travel Award, 1999.
- School of Graduate Studies Presidential Fellowship, 1998-1999.

B.S., Utah State University, Logan, UT. August 1998, GPA: 3.91, Magna Cum Laude.
- Physics Department's Most Valuable Graduating Senior, 1998.
- College of Science Academic Scholarship, 1997-1998.
- Non-resident Transfer Academic Scholarship, 1996-1997.

EXPERIENCE:

Ph.D. GRADUATE PHYSICS RESEARCH: Spacecraft Material Charging, September 2000 to March 2004.
- Nanoampere-current microsecond-time duration pulsed electron yields of insulators.
- Electron, ion, and photon-induced electron emission measurements of materials.
- Extensive automated data acquisition and analysis of electron and ion spectra.
- Designed and built a miniature centimeter-scale low-energy electron gun.
- Operated, repaired, and maintained ultrahigh vacuum equipment.
- UV source optics and detection, Auger electron spectroscopy apparatus.

M.S. GRADUATE PHYSICS RESEARCH: Spacecraft Plasma Environmental Interactions Study of "Snapover," August 1998 to August 2001.
- Experimental investigation of "snapover" at NASA John H. Glenn Research Center.
- Evaluation of theoretical and computational snapover models with experimental data.
- Proposed practical solutions to high-powered spacecraft power loss problems.
- Laser studies including beam-profile characterization and Fourier optics.
- Scanning tunneling microscopy (STM) of metals.
- Adsorption studies of nitrogen gas on a graphite substrate.
- Surface/bulk resistivity measurements of conductors and semiconductors.

RESEARCH INTERN SCIENTIST: Thiokol Corporation, May 2000 to August 2001.
- Nondestructive ultrasonic measurements and aging surveillance research.
- Computational waveform analysis.

Reports and presentations for interdepartmental, Air Force, and Navy collaborators.

GRADUATE TEACHING ASSISTANT: Utah State University Physics Department, September 1998 to May 2000

Bi-weekly lectures and demonstrations for introductory physics courses.
Instructed computer-interfaced sophomore laboratories.

PUBLICATIONS

Thomson, C.D., V. Zavyalov, J.R. Dennison, and J. Corbridge, "Electron Emission Properties of Insulator Materials Pertinent to the International Space Station," Proceedings of the 8th Spacecraft Charging Technology Conference, Huntsville, Al, (2003).

Thomson, C.D., V. Zavyalov, and J.R. Dennison, "Instrumentation for studies of electron emission and charging from insulators," Proceedings of the 8th Spacecraft Charging Technology Conference, Huntsville, Al, (2003).

Dennison, J.R., C.D. Thomson, J. Kite, V. Zavyalov, and J. Corbridge, "Materials characterization at Utah State University: facilities and knowledgebase of electronic properties of materials applicable to spacecraft charging," Proceedings of the 8th Spacecraft Charging Technology Conference, Huntsville, Al (2003).

Dennison, J.R., C.D. Thomson, and J. Corbridge, "Electronic Properties of ISS Materials," Boeing Company Final Report, Contract No. M/C H014-B419, 2003 (unpublished).

Dennison, J.R., J. Kite, C.D. Thomson, J. Corbridge, R. Berry, and C. Ellsworth, "Final Report Part IV: Additional Materials Reports, NASA Space Environments and Effects Program Grant, Electronic Properties of Materials with Application to Spacecraft Charging," (2003).

Dennison, J.R., W.Y. Chang, N. Nickles, J. Kite, C.D. Thomson, J. Corbridge, and C. Ellsworth, "Final Report Part III: Materials Reports," NASA Space Environments and Effects Program Grant, "Electronic Properties of Materials with Application to Spacecraft Charging," (2002).

Thomson, C.D. "Experimental Investigation of Snapover: The Sudden Increase of Plasma Current Drawn to a Positively Biased Conductor When Surrounded by a Dielectric," M.S. Thesis, Utah State University, (2001).

Dennison, J.R., Chang, W.Y., Nickles, N., Kite, J., Thomson, C.D., and Davies, R.E., "Final Report Part II: Experimental Studies," NASA Space Environments and Effects Program Grant, Electronic Properties of Materials with Application to Spacecraft Charging, (2001).

Thomson, C.D., and Dennison, J.R., "Snapover: Anomalous Plasma Current Collection by Positively Biased Conductors when Surrounded by a Dielectric," *Proceedings of the 6th Rocky Mountain NASA Space Grant Consortium Symposium*, Salt Lake City, UT, (2000).

Dennison, J.R., Chang, W.Y., Nickles, N., Kite, J., and Thomson, C.D., "Final Report Part I: Instrumentation, Methods and Analysis," NASA Space Environments and Effects Program Grant, Electronic Properties of Materials with Application to Spacecraft Charging, (2000).

Thomson, C.D., Dennison, J.R., Davies, R.E., Vayner, B., Galofaro, J., Ferguson, D.C., de Groot, W., "Investigation of the Snapover of Positively Biased Conductors in a Plasma", *Proceedings of the 38th American Institute of Aeronautics and Astronomics Meeting and Exhibit*, Reno, NV, (2000).

Vayner, B.V., Galofaro, J.T., Ferguson, D.C., de Groot, W.A., Thomson, C.D., Dennison, J.R., and Davies, R.E., "A Comprehensive Study of Dielectric-Conductor Junctions in Low Density Plasmas," *Proceedings of the 38th American Institute of Aeronautics and Astronomics Meeting and Exhibit*, Reno, NV, (2000).

Galofaro, J. T., Ferguson, D. C. Vayner, B.V. de Groot, W.A. Thomson, C. D. Dennison J.R. and Davies, R.E. "Inception of Snapover and Gas Induced Glow Discharges," *Proceedings of the 38th American Institute of Aeronautics and Astronomics Meeting and Exhibit*, Reno, NV, (2000).

Vayner, B.V., Galofaro, J.T., Ferguson, D.C., de Groot, W.A., Thomson, C.D., Dennison, J.R., and Davies, R.E., "The Conductor-Dielectric Junction in a Low Density Plasma," NASA Technical Memorandum 1999-209408 Glenn Research Center, Cleveland, OH, (1999).

Thomson, C.D., Dennison, J.R., Davies, R.E., Vayner, B., Galofaro, J., Ferguson, D.C., "Snapover Parasitic Current Collection Mitigation Strategies for High Powered Spacecraft," in preparation.

Thomson, C.D., Dennison, J.R., Davies, R.E., Vayner, B., Galofaro, J., Ferguson, D.C., "Ground-Based Experimental Investigation of Snapover On Conductor/Insulator Samples in a Plasma," in preparation.

PRESENTATIONS

Thomson, C.D., presented at the Utah State University graduate school Candidacy Exam, Utah State University, Logan, UT, 2003.

Thomson, C.D., Zavyalov, V., Dennison, J.R., "Electron-Induced Electron Emission of Insulators Using Short-Duration Low-Amplitude Pulsed Sources," *Presented at the APS March Meeting*, Austin, TX, March 3-7, 2003.

Thomson, C.D., Dennison, J.R., "Electron Emissions from Insulator Materials and a Study of "Snapover"," *Presented at NASA GSRP Orientation*, Huntsville, AL, August 14, 2002.

Thomson, C.D., Chang, W.Y. Dennison, J.R., Nickles, N., "Charged Particle-Induced Secondary and Backscattered Electron Emissions From Insulator Materials," *Presented at the APS March Meeting*, Indianapolis, IN, March 18-22, 2002.

Dennison, J.R, Chang, W.Y., Nickles, N., Thomson, C.D., Kite, J., Davies, R.E., "Ground-based Measurements Simulating Space Environment Interaction of Materials and SEE Spacecraft Charging Materials Database for Spacecraft Charging Modeling," *Proceedings of the URSI 2002 Conference*, University of Colorado, Boulder, CO, January 10, 2002.

Thomson, C.D., "Measurements of the Secondary Electron Yields of Insulators," *Presented at the Surface Science Seminar*, Utah State University, November 29, 2001.

Chang, W.Y., Nickles, N., Dennison, J.R., and Thomson, C.D., "An Improved Database of Electronic Properties of Spacecraft Materials for Modeling of Spacecraft Charging," *Proceedings of the 7th Spacecraft Charging Technology Conference,* Noordwijk, The Netherlands, April 23-27, 2001.

Thomson, C.D., Dennison, J.R., Davies, R.E., Vayner, B.V., Galofaro, J.T., Ferguson, D.C., de Groot, W., "Snapover: Anomalous Current Collection by Positively Biased Conductors when Surrounded by a Dielectric and Immersed in a Plasma," *Presented at the APS March Meeting*, Seattle, WA, March, 2001.

Thomson, C.D., "Raman Scattering," *Presented at the Surface Science Seminar*, Utah State University, November 9, 2000.

Thomson, C.D., "Snapover II–The Rest of the Story", *Presented at the Surface Science Seminar*, Utah State University, December 1, 1999.

Thomson, C.D., "Snapover: Anomalous Current Collection by a Positively Biased Conductor Surrounded by a Dielectric in a Plasma", *Presented at the Surface Science Seminar*, Utah State University, October 13, 1999.

Thomson, C.D., Davies, R.E., Dennison, J.R., Ferguson, D.C., Galofaro, J.T., "Relation of Secondary Electron Emission to Snapover of Dielectric Surfaces Surrounding Biased Conductors in a Plasma", *Presented at the APS Centennial Meeting*, Atlanta, GA, March 20-25, 1999.

Thomson, C.D., "Secondary Electron Emissions and Spacecraft Charging", Senior Project, Utah State University, May, 1998.